

Physics Area - PhD course in Theory and Numerical Simulation of Condensed Matter

Electron-phonon coupling in strongly correlated systems: a Variational Monte Carlo study of the Su-Schrieffer-Heeger Hubbard model

Candidate:

Davide Piccioni

Advisors:

Prof. Federico Becca Prof. Michele Fabrizio

Academic Year 2024-25



Abstract

This thesis investigates the interplay between electron-electron and electron-phonon interactions in low-dimensional lattice models, specifically within the Hubbard model incorporating Su-Schrieffer-Heeger (SSH) coupling with phonons. SSH interactions, which modulate the electron hopping amplitude through lattice displacements, have recently attracted renewed interest due to their potential relevance in strongly correlated materials.

The main objective of this work is to determine whether the inclusion of SSH couplings in the Hubbard model can stabilize superconducting or spin-gapped metallic states, as well as other exotic phases of matter. While the half-filled SSH-Hubbard model has been extensively studied in one dimension and only partially examined in two dimensions, its phase diagram in the doped regime remains largely unexplored. This thesis aims to fill this gap, focusing on the emergence of correlated phases away from half-filling in both one and two spatial dimensions.

We use the variational Monte Carlo method with a trial wave function defined in a hybrid electron-phonon Hilbert space. In addition to Jastrow factors that account for correlation effects, the wave function includes an antisymmetric component that captures backflow-inspired electron-phonon correlations. This approach enables us to accurately model both electron-electron and electron-phonon interactions. Moreover, since the variational method avoids the sign problem, we can simulate the system in the doped regime, an area typically inaccessible to exact quantum Monte Carlo methods (QMC), which are limited to half-filling.

In one dimension, we observe the stabilization of a Luther-Emery liquid, a metallic phase with gapless charge excitations and a finite spin gap, upon doping a Peierls insulating phase. This finding resolves a long-standing debate regarding its realization in SSH chains. Benchmarking with density-matrix renormalization group results confirms the reliability of our approach.

In two dimensions, we investigate the SSH-Hubbard model on the square lattice, obtaining results that are consistent with previous exact QMC studies at half-filling. Upon doping, we observe that SSH phonons can induce s-wave superconductivity in the weakly correlated regime. However, we suggest that the enhancement of d-wave superconductivity by SSH coupling in the strongly correlated regime may significantly depend on the specific implementation of the SSH interaction. In one particular case, we find that d-wave superconductivity is slightly suppressed by SSH coupling. These results are further confirmed by a Hartree-Fock analysis performed in the anti-adiabatic limit.

Overall, this thesis highlights the crucial role of lattice effects in correlated electron systems, shedding light on the distinct contributions of SSH-type couplings in one and two dimensions. Our findings provide new insights into the microscopic mechanisms behind exotic metallic phases and set the stage for further studies of phonon-mediated phenomena in correlated systems.

List of publications

Works on the Su-Schrieffer-Heeger-Hubbard model:

• Davide Piccioni, Francesco Ferrari, Michele Fabrizio, and Federico Becca.

Insulating and metallic phases in the one-dimensional Hubbard-Su-Schrieffer-Heeger model: Insights from a backflow-inspired variational wave function.

Phys. Rev. B 111, 045125 (2025).

• Davide Piccioni, Michele Fabrizio, and Federico Becca.

Superconductivity, bond-order wave, and antiferromagnetism in the square lattice Hubbard-Su-Schrieffer-Heeger model: a variational Monte Carlo study.

In preparation.

Other research contributions:

• Davide Piccioni, Christian Apostoli, Federico Becca, Guglielmo Mazzola, Alberto Parola, Sandro Sorella, and Giuseppe E. Santoro.

Jastrow wave function for the spin-1 Heisenberg chain: The string order revealed by the mapping to the classical Coulomb gas.

Phys. Rev. B 108, 104417 (2023).

• Roberta Favata, Davide Piccioni, Alberto Parola, and Federico Becca.

Interaction-induced phases in the half-filled Bernevig-Hughes-Zhang model in one dimension.

Phys. Rev. B 111, 155105 (2025).

Contents

C	Contents			
1		roduction	9	
	1.1	Summary	11	
		1.1.1 SSH-Hubbard chain at half-filling	11	
		1.1.2 Variational Monte Carlo Ansatz	11	
		1.1.3 1D oSSH-Hubbard model: a variational Monte Carlo study	13	
		1.1.4 Square lattice SSH-Hubbard model at half-filling	13	
		1.1.5 2D oSSH-Hubbard model: a variational Monte Carlo and Hartree-Fock		
		study	14	
2		H-Hubbard chain at half-filling	17	
	2.1	SSH-Hubbard chain	17	
	2.2	Alternative definitions of SSH-Hamiltonians	18	
	2.3	Adiabatic limit	19	
		2.3.1 Non-interacting fermions in the adiabatic limit: U=0	19	
		2.3.2 Interacting fermions in the adiabatic limit: $U>0$	28	
	2.4	Anti-adiabatic limit	28	
		2.4.1 Anti-adiabatic limit for the bSSH chain	29	
		2.4.2 Anti-adiabatic limit for the aSSH chain	30	
		2.4.3 Anti-adiabatic limit for the oSSH chain	30	
		2.4.4 Physical properties in the anti-adiabatic limit for $U=0$	31	
		2.4.5 SSH-Hubbard model in the anti-adiabatic: $U > 0$	31	
	2.5	Finite Phonon mass case	32	
		2.5.1 Early studies on the SSH-Hubbard Model	32	
		2.5.2 Spin-Peierls Heisenberg model in the large- <i>U</i> limit	33	
		2.5.3 Numerical results on SSH-Hubbard model	33	
3	Var	riational wave function for SSH-Hubbard model	35	
	3.1	Simplified SSH Hamiltonian with rescaled phonon coordinates	35	
	3.2	Variational wave function definition	37	
		3.2.1 Slater Determinant with phonon-backflow terms	38	
		3.2.2 Non-interacting bosonic state	39	
		3.2.3 Jastrow factors	39	
	3.3	Variational wave function for 2D SSH-Hubbard model	40	
	0.0	3.3.1 SSH-Hubbard Hamiltonian on the square lattice	40	
		3 3 2 Variational wave function on the square lattice	40	

4	Var	iational Monte Carlo	45
	4.1	Variational principle	45
	4.2	Variational Monte Carlo	46
		4.2.1 Monte Carlo sampling	46
		4.2.2 The Metropolis algorithm	47
		4.2.3 Details about Variational Monte Carlo implementation	47
	4.3	Variational Monte Carlo for electron-phonon systems	48
	1.0	4.3.1 Metropolis algorithm details	48
		4.3.2 Local energy term	49
	4.4	Optimization method: Stochastic Reconfiguration	50
	7.7	4.4.1 Local operators	51
		4.4.2 Gradient descent	51
		4.4.3 Stochastic Reconfiguration	52
		4.4.9 Stochastic reconfiguration	02
5	1D	oSSH-Hubbard model: a variational Monte Carlo study	55
	5.1	Benchmark against DMRG calculations	55
		5.1.1 Details about DMRG implementation	55
		5.1.2 Benchmark results	56
	5.2	Half-filling results	57
		5.2.1 Phase diagram	57
		5.2.2 Static structure factors definition	59
		5.2.3 Mott and Peierls insulating states	60
	5.3	Results away from half-filling	61
		5.3.1 Doping the Mott insulator	61
		5.3.2 Doping the Peierls insulator	62
		5.3.3 Luther-Emery Liquid: Phase Diagram, Phase Separation, and Size Scaling	64
	5.4	Changing the SSH Coupling to prevent sign changes of the hopping amplitude	65
6	_	8	69
	6.1	The Hamiltonians	69
	6.2	Adiabatic limit	70
		6.2.1 Single mode distorsions	71
		6.2.2 Multimode Peierls distortions in the adiabatic limit for the $aSSH$ model .	73
		6.2.3 Excluding multimode distortions for $oSSH$ and $bSSH$ models	75
	6.3	Anti-adiabatic limit	76
	6.4	Finite-frequency phonon results	77
7	nΤ	- CCII II-ll d d .l M + C d II-ut Fl t d	70
7		oSSH-Hubbard model: a variational Monte Carlo and Hartree-Fock study Comparison with DQMC results	79
	7.1	•	80
	7.2	VMC phase diagram at half filling	81
		7.2.1 First order AFM-BOW transition	82
		7.2.2 Phase diagram	84
		7.2.3 AFM-BOW coexistence	84
		7.2.4 Antiferromagnetism at $U = 0 \dots \dots \dots \dots \dots$	87
	7.3	Superconductive instabilities in the anti-adiabatic limit of the square lattice SSH-	
		Hubbard model: a Hartree-Fock study	88
		7.3.1 Hartree-Fock: bSSH-Hubbard model at anti-adiabatic limit	89
		7.3.2 Hartree-Fock: oSSH-Hubbard model at anti-adiabatic limit	93
	7.4	VMC results away from half-filling	97
		7.4.1 s-wave superconductivity at $U = 0$ and large $\lambda \dots \dots \dots \dots$	97

		7.4.2 7.4.3	Weak d-wave superconductivity at $U/t = 10$ and small $\lambda \dots \dots \dots$ Preliminary results at large U/t and large lambda	
8	Con	clusio	ns and Future Perspectives	101
\mathbf{A}	Adi	abatic	and anti-adiabatic limits with simplified SSH Hamiltonian	105
В	Der	ivative	es of a slater determinant depending on continuous coordinates: as	u-
	tom	atic di	ifferentiation	107
	B.1	Wave	function definition and implementation	. 108
		B.1.1	Determinant without pairing terms	. 108
			Determinant with pairing terms	
	B.2		of wave function computation	
	B.3		natic differentiation	
			Types of Automatic Differentiation	
	B.4	First o	order derivatives: Backward automatic differentiation	. 111
	B.5	First o	order derivatives: Forward automatic differentiation	. 112
	B.6	The L	aplacian with Automatic Differentiation: computing the Hessian matrix .	. 113
B.7 Forward Laplacian method: directly computing		Forwa	rd Laplacian method: directly computing the Laplacian	. 114
		B.7.1	Relations among tangents	. 114
		B.7.2	Computing the Laplacian for of the wave function	. 116
Bi	bliog	graphy		117

Chapter 1

Introduction

The electron-phonon interaction plays a central role in condensed matter physics, often inducing significant changes in the low-energy electronic properties of materials. Two key phenomena closely related to electron-phonon coupling are the emergence of superconductivity in various systems [1] and the tendency to favor lattice distortions, which can drive, for example, a metallic system into a Peierls insulating state [2].

Within the Bardeen–Cooper–Schrieffer (BCS) theory of superconductivity [3], the condensation of Cooper pairs allows the system to enter a superconducting state [4]; however, an attractive interaction between electrons is required for such pairing to occur. In conventional superconductors, well described by BCS theory, this attractive interaction originates from the coupling between electrons and lattice vibrations, as indicated by the isotope effect on the critical temperature [5]. The electron-phonon interaction thus produces an effective attraction between electrons, which is responsible for the superconducting instability.

The situation is more complicated in the case of unconventional superconductors. In high-temperature cuprates superconductors, the complex interplay between electron pairing and charge ordering (commonly referred to as "stripes") has been a central topic of investigation over the past decades [6, 7] and continues to represent a crucial element in understanding their unconventional properties. Some experimental observations suggest that electron-phonon coupling may contribute to the superconducting mechanism in cuprates [8, 9], although its role remains debated and likely intertwined with strong electronic correlations.

Peierls insulating states have been observed experimentally in various materials. In the 1970s, several quasi-one-dimensional organic conductors, such as TTF-TCNQ, were synthesized and shown to exhibit Peierls transitions [10, 11]; other inorganic compounds, such as CuGeO₃, are also known to exhibit a Peierls instability [12, 13]. These transitions are characterized by a spontaneous breaking of translational symmetry, leading to a periodic lattice distortion that opens a gap at the Fermi level. Such lattice-distortion instabilities can also compete or coexist with other collective phenomena, making Peierls systems a fertile ground for exploring intertwined orders in low-dimensional materials.

From a computational perspective, the accurate treatment of systems where both electron-electron and electron-phonon interactions are relevant (especially including effects beyond the Born-Oppenheimer approximation) remains a challenging task for *ab initio* methods [14]. In this context, low-energy lattice models provide a valuable alternative to *ab initio* approaches aimed at simulating real materials. Within the framework of such models, one can investigate the fundamental physics emerging from the competition and cooperation between these interactions. The single-band Hubbard model (and its strong-coupling limit, the t-J model) stands as a paradigmatic example, capturing essential aspects of electronic correlations [15, 16].

Phonons can be incorporated into lattice models by introducing harmonic oscillators attached

either on lattice sites or along the bonds, thereby generating acoustic or optical phonon branches. Depending on the physical context, different forms of electron-phonon coupling can be considered, such as Fröhlich, Holstein, and Su–Schrieffer–Heeger (SSH) interactions [17, 18, 19, 20]. The Fröhlich and Holstein couplings are typically associated with polaronic effects in ionic or molecular crystals, where electrons interact with local or long-range lattice vibrations. In contrast, the SSH model—originally developed to describe polyacetylene chains—couples lattice displacements directly to the electron hopping amplitude, making it particularly relevant for systems in which bond modulations play a central role.

Lattice models incorporating electron-phonon interactions can host a remarkably rich variety of quantum phases. In one dimension, a notable example is the Luther–Emery liquid: a metallic state characterized by gapless charge excitations and gapped spin excitations. This phase has been identified, for instance, in the half-filled Hubbard–Holstein chain [21, 22, 23, 24]. In two dimensions, recent studies of the SSH model have uncovered exotic phenomena, including phases that can be mapped onto unconstrained \mathbb{Z}_2 gauge theories [25]. Furthermore, investigations of the half-filled Hubbard–Holstein model on the square lattice have revealed a parameter regime in which superconducting pairing correlations are enhanced [26]. Finally, SSH-type couplings have also been proposed as a potential mechanism to enhance superconductivity in the doped regime of Hubbard-like models [27, 28].

This thesis focuses on the SSH electron-phonon interaction, with particular attention to its effects in the hole-doped Hubbard model. In recent years, growing experimental and theoretical evidence has indicated that SSH-like couplings may be relevant in a broad class of strongly correlated materials, including cuprates [8, 9, 29], nickelates [30], manganites [31], and other transition-metal oxides [32, 33]. Incorporating such couplings into minimal models is therefore essential for capturing the low-energy physics of these systems beyond a purely electronic description.

In one dimension, hole doping a Peierls insulator—characterized by spontaneous dimerization and alternating strong and weak bonds—raises the question of whether a Luther–Emery phase can be stabilized. Although such a metallic phase with gapped spin excitations has been identified in doped Holstein chains at quarter filling [34], its existence in SSH-type models remains debated [35]. Recent density-matrix renormalization group studies have either not observed this phase [36] or focused on doping levels far from the low-doping regime where it is expected to occur [37, 38]. Therefore, investigating the possible emergence of a Luther–Emery phase within the one-dimensional SSH and SSH–Hubbard models remains an open and compelling problem.

In two dimensions, numerical investigations have suggested that a d-wave superconducting phase may emerge in the doped SSH–Hubbard model [39, 40], indicating that SSH couplings could play a significant role in the physics of strongly correlated superconductors. Understanding whether such couplings can enhance or stabilize superconductivity in realistic parameter regimes is crucial, as it could shed light on pairing mechanisms in materials where both strong correlations and bond-modulation effects are present.

1.1 Summary

This thesis explores the physics of interacting electrons coupled to lattice phonons via a Su-Schrieffer-Heeger (SSH) mechanism [19]. We investigate both the one-dimensional (1D) SSH-Hubbard model, whose properties have been often studied in the literature [41, 42, 43], and its two-dimensional (2D) generalization, which, although addressed to some extent in the literature [44, 45, 46, 47], remains relatively unexplored. The phonon degrees of freedom are modeled as quantum harmonic oscillators attached to each site to emulate lattice vibrations. Electron-electron interaction is added by including a standard on-site Hubbard interaction U.

We focus on the behavior of these models at half-filling and upon hole doping. Since exact quantum Monte Carlo (QMC) simulations are free from the sign problem only at half-filling, we adopt a variational approach to access a broader range of physical regimes. Variational Monte Carlo (VMC) thus serves as the central computational method in this thesis. Our goal is to design a trial wave function capable of accurately capturing electron-phonon and electron-electron correlations.

The structure of the thesis is as follows.

1.1.1 SSH-Hubbard chain at half-filling

In Chapter 2, we introduce the SSH-Hubbard model in one dimension, exploring three distinct approaches to implement the SSH coupling: the optical SSH (oSSH), acoustic SSH (aSSH), and bond SSH (bSSH) models. Each of these models corresponds to a different type of phonon coupling: the optical SSH model involves site-centered optical phonons, the acoustic SSH model deals with acoustic phonons, and the bond SSH model considers bond-centered optical phonons. Although the models treat the lattice coupling differently, they exhibit similar physical behavior at half-filling.

According to the Peierls instability mechanism [2], non-interacting electrons coupled to lattice distortions dimerize into an insulating state. This chapter discusses this type of instability, focusing on three distinct regimes: the adiabatic limit, where phonons are treated as classical variables and the system dimerizes into a Peierls insulator for any value of the Hubbard interaction U [41, 48]; the anti-adiabatic limit, where infinite-frequency phonons lead to an effective electronic Hamiltonian and a competition between the Peierls insulator and an undistorted Mott insulating phase, with a quantum phase transition between them [49, 50]; and the case of finite phonon frequency, where the same Kosterlitz-Thouless transition occurs between the two phases [51, 42, 43].

Overall, this chapter provides a comprehensive analysis of the 1D SSH-Hubbard model at half-filling, emphasizing the interplay between electron-electron interactions and quantum phonon fluctuations in determining the phase diagram.

1.1.2 Variational Monte Carlo Ansatz

Chapters 3 and 4 focus, respectively, on the description of the variational wave function and the details of its implementation within the VMC framework.

In Chapter 3, we define the variational wave function for the SSH-Hubbard model, addressing both the 1D and 2D cases, and introducing several enhancements to the standard Jastrow-Slater approach. The variational wave function is constructed in a hybrid Hilbert space that incorporates both electron and phonon degrees of freedom.

The wave function is analyzed in detail. A standard approach in variational calculations is

the Jastrow-Slater ansatz [52, 53], namely:

$$|\psi_{\text{var}}\rangle = \exp\left\{\frac{1}{2}\sum_{i,j}v_{ij}\hat{n}_i\hat{n}_j\right\}|\psi_0\rangle ,$$
 (1.1)

where v_{ij} are Jastrow variational parameters and the fermionic part $|\psi_0\rangle$ is typically described by the ground state of an auxiliary quadratic BCS-Hamiltonian:

$$\hat{H}_{0} = \sum_{i,j,\sigma} t_{ij} \hat{c}_{i,\sigma}^{\dagger} \hat{c}_{j,\sigma} + \mu \sum_{i,\sigma} \hat{c}_{i,\sigma}^{\dagger} \hat{c}_{i,\sigma} + \sum_{i,j} \Delta_{ij} \hat{c}_{i,\uparrow}^{\dagger} \hat{c}_{j,\downarrow}^{\dagger} + h.c. , \qquad (1.2)$$

where μ , t_{ij} , Δ_{ij} are variational parameters.

However, this method does not directly account for electron-phonon correlations. To address this, we propose an extension to the standard approach by incorporating electron-phonon correlation effects directly into the fermionic part of the wave function. This is achieved through an auxiliary Hamiltonian that depends on the phonon displacements, enabling the inclusion of "backflow" terms in the fermionic wave function [54, 55]. The auxiliary Hamiltonian becomes:

$$\hat{H}_{ep} = \hat{H}_0 + g \sum_{i,\sigma} (X_{i+1} - X_i) \,\hat{c}_{i,\sigma}^{\dagger} \hat{c}_{i+1,\sigma} , \qquad (1.3)$$

where g is a variational parameter. This modification improves the accuracy of the variational wave function by capturing electron-phonon correlations more effectively: the wave function becomes also exact in the adiabatic limit of zero phonon frequency.

Other terms are added to the wave function to properly account for the presence of phonons. An uncorrelated bosonic component is included to capture phonon distortion phenomena. This component is represented as a product of Gaussian functions, one for each harmonic oscillator, with a variational parameter z that controls the dimerization pattern of the phonon displacements, which is crucial for describing the Peierls insulating state.

To account for various correlation effects, several Jastrow factors are introduced: electron-electron, electron-phonon, and phonon-phonon Jastrow terms. The **electron-electron Jastrow** factor shown in Eq. (1.1) is particularly important to describe the Mott insulating phase [52], where double occupancy is suppressed. The **electron-phonon Jastrow** factor significantly improves the accuracy of the trial wave function in the Peierls insulator phase, particularly when the Hubbard interaction U is large, while the **phonon-phonon Jastrow** term allows to reproduce dispersion effects in the bosonic components.

The two-dimensional SSH-Hubbard model on a square lattice is also considered: the corresponding Hamiltonian contains two phonon modes per site, one for each spatial direction. As a result, the variational wave function is also extended to incorporate both x and y phonon coordinates. The specific details of the wave function generalization, adapted for the 2D case, are presented in the final section of Chapter 3.

Chapter 4 focuses on the details of the VMC method, emphasizing its application to electronphonon systems. After introducing the variational principle, which states that the expectation
value of a Hamiltonian \hat{H} with respect to any trial wave function $|\psi_{\text{var}}\rangle$ provides an upper
bound to the true ground-state energy, we demonstrate how to estimate this expectation value
for complex many-body systems using Monte Carlo sampling. The chapter proceeds with a
detailed discussion of the procedure and its specific implementation for systems with coupled
electrons and phonons, including details of the Metropolis algorithm and the energy estimator.
The final section describes the optimization of the variational parameters, which is performed
using the Stochastic Reconfiguration method [56].

1.1.3 1D oSSH-Hubbard model: a variational Monte Carlo study

Chapter 5 is focused on the investigation of the one-dimensional oSSH-Hubbard model employing the generalized Jastrow-Slater wave function that includes backflow effects. To validate our approach, we benchmark our results against density-matrix renormalization group (DMRG) calculations with periodic boundary conditions. The comparison yields an accuracy of approximately 1% for U/t=4 and 2% for U/t=10, resulting in a clear improvement over the simple Jastrow-Slater ansatz.

At half-filling, we correctly identify a quantum phase transition between two insulating phases: a Mott insulator with gapless spin excitations and preserved translational symmetry, and a Peierls insulator, which breaks translational invariance and exhibits a fully gapped excitation spectrum (in agreement with previous numerical studies [42, 43]).

Upon hole doping, the system displays a rich phenomenology. Doping the Mott insulator leads to a Luttinger liquid, characterized by gapless excitations in both spin and charge sectors, consistent with the known physics of the doped Hubbard chain. In contrast, doping the Peierls insulator stabilizes a Luther-Emery liquid, a metallic phase with gapless charge excitations and a robust spin gap. The presence of such a phase, long discussed in the literature but elusive in models with repulsive interactions and only two Fermi points [57, 58, 59, 60, 61, 62], is firmly established here via both variational and DMRG results.

We construct a phase diagram as a function of doping and electron-phonon coupling, identifying the regions where the Luther-Emery phase is stabilized; we further confirm the robustness of this phase through finite-size scaling analyses, showing that the spin gap remains finite in the thermodynamic limit.

Finally, we address an unphysical artifact of the SSH model, namely the possibility of changes in the sign of the hopping amplitude due to large phonon distortions. To this end, we introduce a regularized SSH coupling that preserves the positivity and smoothness of the hopping term. Although this modification prevents unphysical configurations, it does not qualitatively affect the structure of the phase diagram or the stabilization of the Peierls phase.

Overall, our results demonstrate the power of backflow-enhanced VMC in capturing the subtle interplay between electron-electron and electron-phonon interactions in low-dimensional systems, and provide strong evidence for the emergence of a Luther-Emery liquid in the oSSH-Hubbard chain.

1.1.4 Square lattice SSH-Hubbard model at half-filling

Chapter 6 focuses on the two-dimensional version of the SSH-Hubbard model at half-filling, presenting the current understanding from the literature. The phase diagram is well-established from previous exact QMC studies, showing two phases: a Peierls insulator exhibiting bond-order wave (BOW) and an antiferromagnetic (AFM) insulator [44, 45, 46, 47]. The system's phase depends on which interaction scale predominates: either the electron-phonon coupling for the Peierls insulator or the Hubbard interaction for the antiferromagnetic insulator.

As we did for the one-dimensional case, we introduce three distinct ways to implement the SSH coupling: the optical SSH (oSSH), acoustic SSH (aSSH), and bond SSH (bSSH) models, explicitly showing the Hamiltonian of the system in both the adiabatic and anti-adiabatic limits. We observe that the dimerization pattern in the adiabatic limit exhibits peculiar differences depending on the model considered: the aSSH model shows exotic patterns [63, 64, 65, 66], while the optical phonon models display a standard $Q = (\pi, \pi)$ pattern [67, 68].

In the presence of a finite Hubbard interaction U, a transition occurs from the AFM to the BOW phase, regardless of the phonon frequency. The presence of quantum fluctuations due to a finite phonon frequency allows for the existence of an AFM phase even at U=0 for small

values of the electron-phonon coupling [44, 45].

We discuss a few results from the literature regarding the nature of the AFM-BOW transition, including the possibility of a phase-coexistence region in between. This region seems to be absent in the *bSSH*-Hubbard case [44, 45], while it may be present in the *oSSH*-Hubbard model [47].

1.1.5 2D oSSH-Hubbard model: a variational Monte Carlo and Hartree-Fock study

Chapter 7 presents our study on the two-dimensional version of the oSSH-Hubbard model.

First, we assess the accuracy of our wave function by comparing our VMC results at half-filling with those from determinant quantum Monte Carlo (DQMC) simulations [47]. This comparison demonstrates that our wave function is highly accurate and consistent with exact DQMC results for the non-interacting case (U=0), both in the BOW phase and outside of it. As we increase the interaction strength U, for U/t=4 we maintain a reasonable accuracy of less than 2% in energy. The accuracy decreases to approximately 3% for U=6 and reaches up to 5% for U=8.

Next, we focus on the phase diagram at half-filling. Although the accuracy of our variational method decreases for large values of U, it predicts a phase diagram that is in very good agreement with the one obtained from DQMC simulations [47]. We also address the issue of the coexistence between the AFM and BOW phases, presenting some partial results, which are nevertheless consistent with those found by DQMC in Ref. [47]. Besides, our results support the presence of AFM order at U=0 within the oSSH model.

The most important aspect we wish to discuss is the emergence of superconducting phases upon doping the system. In this respect, we begin by performing a Hartree-Fock calculation. We consider the system in the anti-adiabatic limit, where the phonon degrees of freedom become fast and can be integrated out, and we apply the Hartree-Fock method to decouple the effective electronic Hamiltonian in the presence of the Hubbard interaction. The results strongly depend on how the SSH coupling is implemented.

- oSSH-Hubbard: The Hartree—Fock calculation does not reveal d-wave superconductivity. In this case, the terms corresponding to d-wave and extended s-wave superconductivity vanish during the mean-field decoupling, leaving only an on-site s-wave term. This term drives the system into a superconducting phase when the electron-phonon coupling dominates, showing on-site s-wave superconductivity; however, no other superconductive phase appears.
- **bSSH-Hubbard**. It has been suggested that the *bSSH-Hubbard* model exhibits a *d*-wave superconducting phase upon hole doping [39, 40]. Our Hartree-Fock results confirm this hypothesis in the anti-adiabatic limit (at least at the mean-field level), where we identify a phase with on-site *s*-wave superconductivity in the regime of dominant electron-phonon coupling, and a phase where on-site *s*-wave and *d*-wave superconductivity coexist for larger values of *U*.

We observe that, in the anti-adiabatic limit, the aSSH and bSSH models become equivalent. Clearly, the Hartree-Fock result (which holds in the anti-adiabatic limit) does not completely rule out the possibility of d-wave superconductivity in the phase diagram of the oSSH-Hubbard model, but suggests that different implementations of the SSH coupling may lead to distinct phase diagrams when the system is doped away from half-filling. Moreover, it is apparent that using the oSSH version of the model may not be the most effective way to identify a strong d-wave superconducting phase.

Finally, we investigate the oSSH-Hubbard model with hole doping using VMC. First, we analyze the weak-coupling regime with U=0 and large λ . Here, the system is deep in the BOW phase at half-filling, and upon doping we observe the emergence of on-site s-wave superconductivity. The superconductive correlations are similar in magnitude to those found in the attractive Hubbard model at U/t=-2, indicating that the electron-phonon coupling effectively induces an attractive interaction between electrons in this regime.

Then, our focus moves on d-wave superconducting instabilities for large values of U; for this reason, we do not consider charge density wave (CDW) and stripe phases, which strongly compete with d-wave superconductivity and may represent the actual ground state of the Hubbard model at 1/8 hole doping. Since the VMC approach, using a Jastrow-Slater wave function, can describe both stripe and d-wave superconducting phases [69, 70], our aim is to determine whether the inclusion of phonons enhances superconductivity when compared to the VMC solution of the Hubbard model without phonons at the same values of U. At doping $\delta = 1/8$ for U/t = 10 and small electron-phonon coupling, the system develops a dominant d-wave pairing amplitude in the auxiliary Hamiltonian. However, the comparison with the plain Hubbard model at the same U reveals that the latter exhibits stronger and longer-ranged d-wave superconductive correlations. This indicates that the electron-phonon interaction in this regime does not favor—and may even suppress—d-wave superconductivity.

Finally, we consider the case with both large U and large electron-phonon coupling, focusing on points near the AFM-BOW phase boundary. Away from half-filling, although significant superconducting variational parameters are observed in the auxiliary fermionic Hamiltonian of Eq. (1.2), the superconducting correlations are weak and decay rapidly. As a result, the presence of superconductivity in this regime remains uncertain.

Together, these results highlight the delicate interplay between electron-electron and electron-phonon interactions in the oSSH-Hubbard model. While phonon-mediated superconductivity can emerge in the absence of repulsive interactions, strong correlations tend to suppress this tendency or steer the system toward competing orders.

Chapter 2

SSH-Hubbard chain at half-filling

In this chapter, we study the physical properties of the SSH-Hubbard chain at half-filling. The model reveals a rich physics related to the interplay between electron-electron interactions and electron-phonon coupling. We present analytical calculations where possible and discuss selected results from the literature.

We begin by introducing the SSH-Hubbard Hamiltonian in one dimension (Section 2.1) and exploring alternative definitions of electron-phonon coupling in Section 2.2. To provide a physical understanding of the model, Sections 2.3 and 2.4 focus on two limiting cases of the phonon mass: the infinite mass (adiabatic) and vanishing mass (anti-adiabatic) limits, respectively. Finally, Section 2.5 addresses the case of quantum phonons with a finite mass.

The results show that when phonons are treated as classical in the Born-Oppenheimer approximation (i.e., infinite phonon mass, adiabatic limit), the lattice always undergoes a symmetry-breaking distortion that opens an energy gap, leading to a Peierls insulator. In contrast, for quantum phonons with finite mass m (and even for $m \to 0$ in the anti-adiabatic limit), the competition between the Hubbard interaction U and the electron-phonon coupling α leads to two distinct phases: an undistorted Mott insulating phase for large U and a Peierls insulator when α dominates. This demonstrates how the competition between these phases is strongly influenced by the quantum nature of the phonons.

2.1 SSH-Hubbard chain

We consider an L-site chain with periodic boundary conditions (PBC), where optical phonons are modeled as L quantum harmonic oscillators, each centered on a site and with no dispersion. The harmonic oscillators, with frequency ω and ionic mass m, are coupled to the electrons via SSH coupling α , which modulates the electron hopping amplitudes [19, 20]. The bare electron hopping amplitude is t, and the resulting Hamiltonian is:

$$\hat{H} = -t \sum_{i,\sigma} \left[1 - \alpha \left(\hat{x}_{i+1} - \hat{x}_i \right) \right] \left(\hat{c}_{i,\sigma}^{\dagger} \hat{c}_{i+1,\sigma} + \hat{c}_{i+1,\sigma}^{\dagger} \hat{c}_{i,\sigma} \right) + \sum_{i} \left[\frac{\hat{p}_i^2}{2m} + \frac{1}{2} m \omega^2 \hat{x}_i^2 \right] , \qquad (2.1)$$

where $\hat{c}_{i,\sigma}^{\dagger}$ creates an electron at site *i* with spin σ and \hat{x}_i , \hat{p}_i are the position and momentum operators of the phonon describing the ion at site *i*, satisfying the usual commutation relation:

$$[\hat{x}_j, \hat{p}_k] = i\hbar \delta_{jk} \ . \tag{2.2}$$

We consider an on-site Hubbard interaction with strength U that shall be added to \hat{H} , namely:

$$\hat{H}_U = U \sum_i \hat{n}_{i,\uparrow} \hat{n}_{i,\downarrow} . \tag{2.3}$$

An important dimensionless parameter for quantifying the e-ph interaction is:

$$\lambda = \frac{t\alpha^2}{m\omega^2} \ . \tag{2.4}$$

The Hamiltonian of Eq (2.1) incorporates the same type of electron-phonon coupling introduced by Su, Schrieffer, and Heeger to describe the behavior of electrons in long-chain polyenes [19]. In this model, at half-filling, electrons are subject to the Peierls instability [2], leading to the formation of dimerization patterns, corresponding to the x-coordinate of the oscillators acquiring a finite staggered expectation value: $\langle x_i \rangle = (-1)^j \Delta$.

Performing a large-U expansion on the Hamiltonian of Eq. (2.1), a Spin-Peierls Heisenberg model with quantum phonons is obtained, resulting in the following Hamiltonian:

$$\hat{H} = J \sum_{i}^{L} \left[1 - \alpha \left(\hat{x}_{i+1} - \hat{x}_{i} \right) \right] \hat{\vec{S}}_{i} \cdot \hat{\vec{S}}_{i+1} + \sum_{i} \left[\frac{\hat{p}_{i}^{2}}{2m} + \frac{1}{2} m \omega^{2} \hat{x}_{i}^{2} \right] , \qquad (2.5)$$

where $J = \frac{4t^2}{U}$ and each site hosts a spin-1/2 operator $\hat{\vec{S}}_i = (\hat{S}_i^x, \hat{S}_i^y, \hat{S}_i^z)$. This model has been widely studied numerically [49, 71, 72], particularly due to its connection with the spin-Peierls compound CuGeO₃ [12, 13, 73].

2.2 Alternative definitions of SSH-Hamiltonians

Now, we discuss different choices to account for the presence of phonons in a simple lattice model.

We will refer to oSSH the choice of considering decoupled harmonic oscillators to account for optical phonon modes with no dispersion as we did in Eq. (2.1).

Another natural choice would be to introduce dispersion in the harmonic oscillators to mimic acoustic phonons. We will call such choice aSSH, and the corresponding Hamiltonian would take the following form:

$$\hat{H} = -t \sum_{i,\sigma} \left[1 - \alpha \left(\hat{x}_{i+1} - \hat{x}_i \right) \right] \left(\hat{c}_{i,\sigma}^{\dagger} \hat{c}_{i+1,\sigma} + \hat{c}_{i+1,\sigma}^{\dagger} \hat{c}_{i,\sigma} \right) + \sum_{i} \left[\frac{\hat{p}_i^2}{2m} + \frac{1}{2} m \omega^2 \left(\hat{x}_{i+1} - \hat{x}_i \right)^2 \right] . \tag{2.6}$$

A third option, frequently used in previous studies also for computational efficiency — since density-matrix renormalization group and quantum Monte Carlo simulations converge more easily with this type of coupling — is to consider dispersionless, decoupled harmonic oscillators; however, instead of associating each oscillator with a lattice site, it is linked to the bond between adjacent sites. We call this choice bSSH, where b stands for bond; the resulting Hamiltonian would be:

$$\hat{H} = -t \sum_{i,\sigma} \left[1 - \alpha \left(\hat{x}_{(i,i+1)} \right) \right] \left(\hat{c}_{i,\sigma}^{\dagger} \hat{c}_{i+1,\sigma} + \hat{c}_{i+1,\sigma}^{\dagger} \hat{c}_{i,\sigma} \right) + \sum_{i} \left[\frac{\hat{p}_{(i,i+1)}^{2}}{2m} + \frac{1}{2} m \omega^{2} \left(\hat{x}_{(i,i+1)} \right)^{2} \right]. \tag{2.7}$$

We notice that the three Hamiltonians of Eqs. (2.1), (2.6) and (2.7) are not related in any simple way by a canonical transformation. However, a thorough comparative study of these models in the absence of interaction (U=0) was performed using exact determinant quantum Monte Carlo [74]. According to Ref. [74], at half-filling the oSSH and aSSH models are remarkably similar (showing quantitative agreement in their correlation functions), while the similarity with the bSSH model is only qualitative. As the system is doped away from half filling, each model may display distinct behaviors.

Ref. [74] also suggests that the correct way to compare the three models would be to fix the dimensionless parameter λ shown in Eq. (2.4), ensuring it is properly defined for each model. Denoting the couplings with subscripts "o", "a" and "b" for the oSSH, aSSH, and bSSH models respectively, the equivalence reads:

$$\frac{t\alpha_o^2}{m_o\omega_o^2} \sim \frac{t\alpha_a^2}{4m_a\omega_a^2} \sim \frac{t\alpha_b^2}{4m_b\omega_b^2} \ . \tag{2.8}$$

We observe that the bSSH model in Eq. (2.7) exhibits a peculiar behavior compared to the oSSH and aSSH models: the average phonon displacement $\Delta L = \langle \sum_i \hat{x}_i \rangle$ is always zero in both the oSSH and aSSH models (even in the presence of distorted phases). In contrast, in the bSSH model, ΔL can vary as a function of α unless an external constraint is enforced, meaning that distortion patterns can lead to the stretching of the chain. Clearly, if one does not need to address specifically the issue of stretching chains, this may be an undesired effect. This is also the reason why Ref. [74] found that only the oSSH and aSSH models exhibited quantitative agreement at half-filling.

2.3 Adiabatic limit

In the adiabatic limit, corresponding to the Born-Oppenheimer approximation, the phonons become classical degrees of freedom:

$$m \to \infty$$
 $\omega \to 0$ with $K = m\omega^2 = const$. (2.9)

Applying this limit to Eq. (2.1), including also the Hubbard interaction term \hat{H}_U , the Hamiltonian reduces to:

$$\hat{H} = -t \sum_{i,\sigma} \left[1 - \alpha \left(x_{i+1} - x_i \right) \right] \left(\hat{c}_{i,\sigma}^{\dagger} \hat{c}_{i+1,\sigma} + \hat{c}_{i+1,\sigma}^{\dagger} \hat{c}_{i,\sigma} \right) + \frac{1}{2} K \sum_{i} x_i^2 + U \sum_{i} \hat{n}_{i,\uparrow} \hat{n}_{i,\downarrow} , \quad (2.10)$$

where the coordinates x_i are now classical variables acting as external parameters in the fermionic Hamiltonian. Hence, the ground-state wave function depends parametrically on the set $\{x_i\}$, which must be optimized.

Instead of optimizing each x_i coordinate independently, one can take inspiration from the fact that electronic systems of this kind at half-filling are subject to the Peierls instability [2] and impose an ansatz for the dimerization pattern of ionic displacements controlled by a single parameter Δ :

$$x_i = \frac{1}{2}(-1)^{i+1}\Delta \quad \to \quad x_{i+1} - x_i = (-1)^i\Delta \ .$$
 (2.11)

We say that the ground state of the system is a Peierls insulator if the optimal value of Δ which minimizes the energy is finite (clearly, this analysis holds only at half-filling).

We observe that all three choices of phonon Hamiltonian of Eq. (2.1), (2.6) and (2.7) (respectively oSSH, aSSH and bSSH) trivially coincide in the adiabatic limit when considering an ansatz as the one of Eq. (2.11). The corresponding Hamiltonians are identical when applying the following equivalences: $K_o = K_b = 4K_a$ and $2\alpha_o = 2\alpha_a = \alpha_b$. This also furnishes a nice explanation for why the equivalence of Eq. (2.8) works: it becomes exact in the adiabatic limit.

2.3.1 Non-interacting fermions in the adiabatic limit: U=0

For the case of non-interacting fermions (U = 0), an analytical solution can be found. In this section, we will first show explicitly how the Hamiltonian can be brought into diagonal form and

derive its energy spectrum. Next, we will demonstrate that its ground state is always a Peierls insulator (Δ >0) for any finite value of the electron-phonon coupling α . We will then characterize the ground state by showing that it displays a bond-order wave order parameter, and that both the energy gap and the order parameter are proportional to the value of Δ . Finally, we will compute a few static correlation functions.

By considering the dimerization pattern of Eq. (2.11), we can write the Hamiltonian of Eq. (2.10) in the case U = 0 as follows:

$$\hat{H} = -t \sum_{i=1}^{L} \sum_{\sigma} \left[1 - \alpha \Delta (-1)^{i} \right] \left(\hat{c}_{i,\sigma}^{\dagger} \hat{c}_{i+1,\sigma} + \hat{c}_{i+1,\sigma}^{\dagger} \hat{c}_{i,\sigma} \right) + \frac{1}{8} NK\Delta^{2} , \qquad (2.12)$$

where we consider L, the number of sites of the chain, to be even.

At this point, we recognize the Hamiltonian of the well-known electronic SSH model [75] by separating creation and annihilation operators on even and odd sites of the chain as:

$$\hat{a}_{i,\sigma} \equiv \hat{c}_{2i,\sigma} \qquad \hat{b}_{i,\sigma} \equiv \hat{c}_{2i+1,\sigma} \ . \tag{2.13}$$

The Hamiltonian is then expressed as follows:

$$\hat{H} = -t \sum_{i=1}^{L/2} \sum_{\sigma} \left[1 - \alpha \Delta \right] \left(\hat{a}_{i,\sigma}^{\dagger} \hat{b}_{i,\sigma} + \hat{b}_{i,\sigma}^{\dagger} \hat{a}_{i,\sigma} \right)$$

$$- t \sum_{i=1}^{L/2} \sum_{\sigma} \left[1 + \alpha \Delta \right] \left(\hat{b}_{i,\sigma}^{\dagger} \hat{a}_{i+1,\sigma} + \hat{a}_{i+1,\sigma}^{\dagger} \hat{b}_{i,\sigma} \right) + \frac{1}{8} NK\Delta^{2} . \tag{2.14}$$

Next, we express the Hamiltonian in Fourier space, noting that, since the primitive cell contains two sites, the Brillouin zone is folded and the momentum index k spans the reduced interval $[-\pi/2, \pi/2)$. For this reason, the Fourier transform of the operators $\hat{a}_{j,\sigma}$ and $\hat{b}_{j,\sigma}$ is defined as follows:

$$\hat{a}_{j,\sigma} = \sqrt{\frac{2}{L}} \sum_{k=-\pi/2}^{\pi/2 - 2\pi/L} e^{2ikj} \hat{a}_{k,\sigma} , \qquad \hat{b}_{j,\sigma} = \sqrt{\frac{2}{L}} \sum_{k=-\pi/2}^{\pi/2 - 2\pi/L} e^{2ikj} \hat{b}_{k,\sigma} . \qquad (2.15)$$

In this representation, the Hamiltonian takes the form of a quadratic operator:

$$\hat{H} = \sum_{k=-\pi/2}^{\pi/2 - 2\pi/L} \sum_{\sigma} \left(\hat{a}_{k,\sigma}^{\dagger} \quad \hat{b}_{k,\sigma}^{\dagger} \right) \mathbb{H}(k) \begin{pmatrix} \hat{a}_{k,\sigma} \\ \hat{b}_{k,\sigma} \end{pmatrix} + \frac{1}{8} NK\Delta^2 , \qquad (2.16)$$

with the matrix $\mathbb{H}(k)$ defined as:

$$\mathbb{H}(k) = \begin{pmatrix} 0 & -t \left[1 - \alpha \Delta + (1 + \alpha \Delta) e^{-2ik} \right] \\ -t \left[1 - \alpha \Delta + (1 + \alpha \Delta) e^{+2ik} \right] & 0 \end{pmatrix} . \tag{2.17}$$

Its eigenvalues are given by:

$$\epsilon_{\pm}(k) = \pm 2t\sqrt{1 - (1 - \alpha^2 \Delta^2)\sin^2 k} = \pm 2t\sqrt{\cos^2 k + \alpha^2 \Delta^2 \sin^2 k}$$
 (2.18)

One can readily observe that a finite value of Δ corresponds to a gapped spectrum of the Hamiltonian. Specifically, $\epsilon_{\pm}(k)$ vanishes at $k=\pm\pi/2$ only for $\Delta=0$. For $\Delta\neq0$, $\epsilon_{\pm}(k)$ acquires a value proportional to Δ at $k=\pm\pi/2$ and never vanishes for all other values of k.

Given the expression for $\epsilon_{\pm}(k)$, we can compute the total energy of the system at half filling. In that case, only the lower band $\epsilon_{-}(k)$ is occupied. Thus, the energy of the system in the thermodynamic limit is expressed as follows:

$$\frac{E^{tot}(\Delta)}{L} = \frac{K}{8} \Delta^2 + \frac{1}{\frac{L}{2}} \sum_{k=-\pi/2}^{\pi/2 - 2\pi/L} \epsilon^-(k) \quad \xrightarrow{L \to \infty} \quad \frac{K}{8} \Delta^2 + \frac{1}{\pi} \int_{-\pi/2}^{\pi/2} dk \ \epsilon^-(k) \ . \tag{2.19}$$

More explicitly, we can write:

$$\frac{E^{tot}(\Delta)}{L} = \frac{K}{8} \Delta^2 - \frac{2t}{\pi} \int_{-\pi/2}^{\pi/2} dk \sqrt{1 - [1 - (\alpha \Delta)^2] \sin^2(k)} = \frac{K}{8} \Delta^2 - \frac{4t}{\pi} \mathbb{E}\left[\sqrt{1 - (\alpha \Delta)^2}\right] , \quad (2.20)$$

where $\mathbb{E}[z]$ refers to the complete elliptic integral of the second kind:

$$\mathbb{E}[z] \equiv \int_0^{\pi/2} dx \sqrt{1 - z^2 \sin^2(x)} \ . \tag{2.21}$$

The total energy per site as a function of Δ exhibits a double-well shape, as shown in Fig. 2.1 for the case t = 1, $\alpha = 0.3$, K = 0.1, indicating that the system always lowers its energy by transitioning into a dimerized state.

2.3.1.1 Peierls transition in the thermodynamic limit

We aim to show that, given the expression for the energy of a half-filled system in the thermodynamic limit of Eq. (2.20), the system behaves as a Peierls insulator for any value of $\alpha > 0$.

Since we are interested in finding the minimum of the total energy as a function of Δ , we compute its derivative and set it to zero:

$$\frac{d}{d\Delta} \frac{E^{tot}(\Delta)}{L} = \frac{K}{4} \Delta - \frac{4t}{\pi} \frac{\mathbb{E}[\sqrt{1 - (\alpha \Delta)^2}] - \mathbb{E}[\sqrt{1 - (\alpha \Delta)^2}]}{\sqrt{1 - (\alpha \Delta)^2}} \frac{d}{d\Delta} \sqrt{1 - (\alpha \Delta)^2} = 0 , \qquad (2.22)$$

where $\mathbb{F}[z]$ corresponds to the complete elliptic integral of the first kind:

$$\mathbb{F}[z] \equiv \int_0^{\pi/2} \frac{dx}{\sqrt{1 - z^2 \sin^2(x)}} , \qquad (2.23)$$

and, to compute the derivative inside Eq. (2.22), we made use of the following relation between the integrals:

$$\frac{d}{dz}\mathbb{E}[z] = \frac{\mathbb{E}[z] - \mathbb{F}[z]}{z} \ . \tag{2.24}$$

We can factor out Δ from Eq. (2.22), obtaining as a result:

$$\left(\frac{K}{4} + \frac{4t\alpha^2}{\pi} \frac{\mathbb{E}[\sqrt{1 - (\alpha\Delta)^2}] - \mathbb{E}[\sqrt{1 - (\alpha\Delta)^2}]}{1 - (\alpha\Delta)^2}\right) \Delta = 0.$$
(2.25)

Apart from the trivial solution $\Delta=0$, we need to check for which values of Δ the expression inside the parentheses vanishes. To do so, the expansion of the elliptic integrals around z=1 comes into hand:

$$\mathbb{E}[z] \approx 1 + o(1) \text{ for } z \to 1; \qquad \mathbb{F}[z] \approx -\frac{1}{2}\ln(1-z) + \ln(4) + o(1) \text{ for } z \to 1.$$
 (2.26)

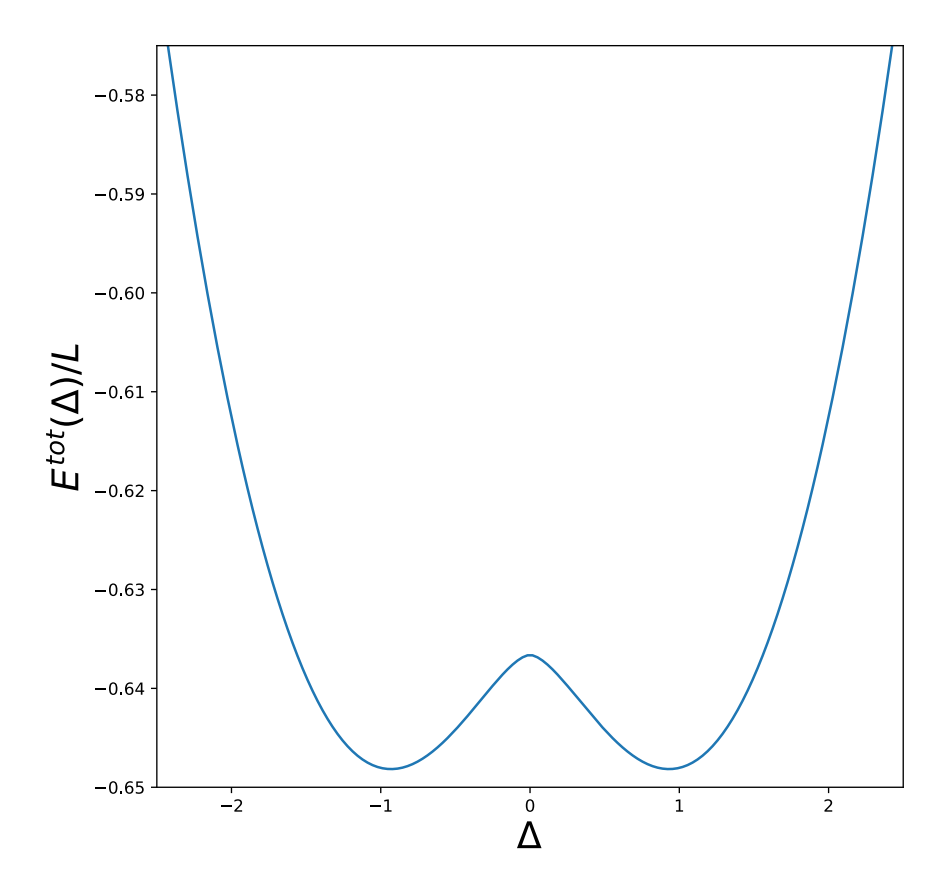


Figure 2.1: Total energy per site as a function of the dimerization parameter Δ for the SSH model in the adiabatic limit (see Eq. (2.20)). The plot is shown for t = 1, $\alpha = 0.3$, K = 0.1.

Thus, the solution for Eq. (2.25) in the case of $\Delta \to 0$ can be written as:

$$\frac{\pi K}{16t\alpha^2} + \frac{1 - \ln(4) + \ln\left(1 - \sqrt{1 - (\alpha\Delta)^2}\right)/2}{1 - (\alpha\Delta)^2} = 0.$$
 (2.27)

Exploiting the fact that $\Delta \to 0$, we can perform additional simplification:

$$-\frac{1}{2}\ln\left(\frac{\alpha^2\Delta^2}{2}\right) = \frac{\pi K}{16t\alpha^2} + 1 - \ln(4) \ . \tag{2.28}$$

This leads to the result:

$$\Delta = \frac{4\sqrt{2}}{\alpha \ e} \exp\left(-\frac{\pi K}{16t\alpha^2}\right). \tag{2.29}$$

In this way, we show that the non-interacting system is unstable towards dimerization, since the value of Δ that minimizes the ground state energy is finite for any value of $\alpha > 0$.

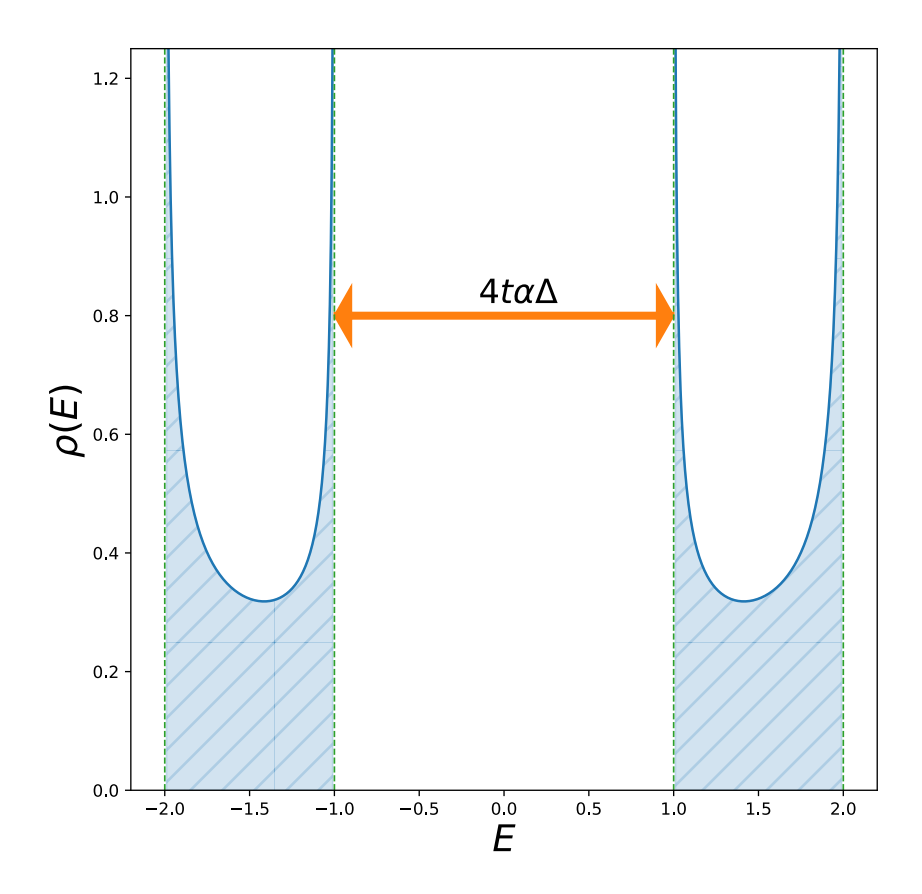


Figure 2.2: Density of states $\rho(E)$ for the SSH model in the adiabatic limit, see Eq. (2.12). The plot is shown for t=1 and $\alpha\Delta=0.5$: the energy gap $\Delta E=4t\alpha\Delta$ is indicated by the orange arrow.

2.3.1.2 Density of states and energy gap

From the Hamiltonian spectrum $\epsilon_{\pm}(k)$, Eq. (2.18), we can derive the density of states. First, we compute the following derivative:

$$\frac{d\epsilon_{\pm}(k)}{dk} = \pm \frac{2t\left(\alpha^2 \Delta^2 - 1\right)\sin k \cos k}{\sqrt{1 - (1 - \alpha^2 \Delta^2)\sin^2 k}} = \frac{4t^2\left(\alpha^2 \Delta^2 - 1\right)\sin k \cos k}{\epsilon_{\pm}(k)} \ . \tag{2.30}$$

We observe that, having defined $E = \pm 2t\sqrt{1 - (1 - \alpha^2 \Delta^2)\sin^2 k}$, two simple relations hold:

$$\sin^2(k) = \frac{4t^2 - E^2}{4t^2(1 - \alpha^2 \Delta^2)}; \qquad \cos^2(k) = \frac{E^2 - 4t^2 \alpha^2 \Delta^2}{4t^2(1 - \alpha^2 \Delta^2)}. \tag{2.31}$$

It is now easy to invert the expression of Eq. (2.30) to find $\frac{dk(E)}{dE}$, namely:

$$\left| \frac{dk}{d\epsilon_{+}(k)} \right| = \left| \frac{dk}{d\epsilon_{-}(k)} \right| = \frac{|E|}{\sqrt{(4t^2 - E^2)(E^2 - 4t^2\alpha^2\Delta^2)}} \ . \tag{2.32}$$

The density of states is computed as follows:

$$\rho(E) = \int_{-\pi/2}^{\pi/2} \frac{dk}{2\pi} \left[\delta(\epsilon_{+}(k) - E) + \delta(\epsilon_{-}(k) - E) \right] =$$

$$= \frac{1}{2\pi} \left| \frac{dk}{d\epsilon_{+}(k)} \right| + \frac{1}{2\pi} \left| \frac{dk}{d\epsilon_{-}(k)} \right| = \frac{|E|}{\pi \sqrt{(4t^{2} - E^{2})(E^{2} - 4t^{2}\alpha^{2}\Delta^{2})}} . \tag{2.33}$$

Assuming $\alpha^2 \Delta^2 < 1$ (otherwise the electrons hopping amplitude between neighboring sites would change sign, which is unphysical), the domain of $\rho(E)$ is $\mathcal{D} = (-2t, -2t\alpha\Delta) \cup (2t\alpha\Delta, 2t)$. Thus, we can clearly see that the model displays an energy gap ΔE proportional to the dimerization parameter Δ , namely:

$$\Delta E = 4t\alpha \Delta \ . \tag{2.34}$$

The density of states $\rho(E)$ and the energy gap ΔE are shown in Fig. 2.2 for the case t=1, $\alpha \Delta = 0.5$.

We have shown in Eq. (2.29) that the optimal value of Δ , in the limit of small α and Δ , is given by $\Delta \propto \exp\left(-\frac{\pi K}{16t\alpha^2}\right)/\alpha$. Combining this with the expression for the energy gap from Eq. (2.34), we observe that the energy gap opens in a non-analytical way as a function of the coupling. For small values of α , the following relation holds:

$$\Delta E \approx \frac{16t\sqrt{2}}{e} \exp\left(-\frac{\pi K}{16t\alpha^2}\right)$$
 (2.35)

Both Eq. (2.33) and Eq. (2.20) are consistent with the density of states and total energy found by Su, Schrieffer and Heeger in Ref. [20].

2.3.1.3 Ground state wave function

The quadratic Hamiltonian of the SSH model expressed in Eq. (2.16) can be brought into diagonal form with the knowledge of the unitary matrix U_k that diagonalizes $\mathbb{H}(k)$. The procedure is the following:

$$\hat{H} = \sum_{k} \sum_{\sigma} \left(\hat{a}_{k,\sigma}^{\dagger} \quad \hat{b}_{k,\sigma}^{\dagger} \right) U_{k} U_{k}^{\dagger} \mathbb{H}(k) U_{k} U_{k}^{\dagger} \begin{pmatrix} \hat{a}_{k,\sigma} \\ \hat{b}_{k,\sigma} \end{pmatrix} =
= \sum_{k} \sum_{\sigma} \left[\left(\hat{a}_{k,\sigma}^{\dagger} \quad \hat{b}_{k,\sigma}^{\dagger} \right) U_{k} \right] \left[U_{k}^{\dagger} \mathbb{H}(k) U_{k} \right] \left[U_{k}^{\dagger} \begin{pmatrix} \hat{a}_{k,\sigma} \\ \hat{b}_{k,\sigma} \end{pmatrix} \right] =
= \sum_{k} \sum_{\sigma} \left(\hat{\gamma}_{k,\sigma}^{\dagger} \quad \hat{\zeta}_{k,\sigma}^{\dagger} \right) \begin{pmatrix} \epsilon^{-}(k) & 0 \\ 0 & \epsilon^{+}(k) \end{pmatrix} \begin{pmatrix} \hat{\gamma}_{k,\sigma} \\ \hat{\zeta}_{k,\sigma} \end{pmatrix} ,$$
(2.36)

where $\hat{\gamma}_{k,\sigma}$ and $\hat{\zeta}_{k,\sigma}$ are new fermionic operators, related to the old ones by the relations:

$$\begin{pmatrix} \hat{\gamma}_{k,\sigma} \\ \hat{\zeta}_{k,\sigma} \end{pmatrix} = U_k^{\dagger} \begin{pmatrix} \hat{a}_{k,\sigma} \\ \hat{b}_{k,\sigma} \end{pmatrix} \; ; \qquad \qquad \begin{pmatrix} \hat{a}_{k,\sigma} \\ \hat{b}_{k,\sigma} \end{pmatrix} = U_k \begin{pmatrix} \hat{\gamma}_{k,\sigma} \\ \hat{\zeta}_{k,\sigma} \end{pmatrix} \; . \tag{2.37}$$

We can give an explicit expression for the matrix U_k as follows:

$$U_k = \frac{1}{\sqrt{2}} \begin{pmatrix} -r_k^* & r_k^* \\ 1 & 1 \end{pmatrix} , \qquad (2.38)$$

where we introduced the variable r_k , defined as follows:

$$r_k \equiv \frac{-t \left[1 - \alpha \Delta + (1 + \alpha \Delta) e^{+2ik}\right]}{\epsilon^+(k)} = \frac{\alpha \Delta - 1 - (1 + \alpha \Delta) e^{+2ik}}{2\sqrt{1 - (1 - \alpha^2 \Delta^2) \sin^2 k}} . \tag{2.39}$$

 r_k is actually a phase, since $|r_k|^2 = 1$.

For a system with L electrons, the ground state is obtained by filling the lower energy band $\epsilon^-(k)$ with L/2 spin-up and L/2 spin-down electrons, namely:

$$|GS\rangle = \prod_{k} \hat{\gamma}_{k,\uparrow}^{\dagger} \hat{\gamma}_{k,\downarrow}^{\dagger} |0\rangle = |GS_{\uparrow}\rangle \otimes |GS_{\downarrow}\rangle .$$
 (2.40)

Once we have an explicit expression for the ground state, we can compute relevant correlation functions and observables.

2.3.1.4 Bond-order wave order parameter

We define a bond-order wave (BOW) order parameter as follows:

$$\hat{m}_{BOW} \equiv \frac{1}{L} \sum_{i=1}^{L} (-1)^i \left[\sum_{\sigma} \left(\hat{c}_{i,\sigma}^{\dagger} \hat{c}_{i+1,\sigma} + \hat{c}_{i+1,\sigma}^{\dagger} \hat{c}_{i,\sigma} \right) \right] . \tag{2.41}$$

The fact that the value of $\langle GS|\hat{m}_{BOW}|GS\rangle$ tends to a constant in the thermodynamic limit indicates the presence of an ordered phase.

Following the same steps used to derive Eq. (2.14), we can express \hat{m}_{BOW} in terms of the operators $\hat{a}_{k,\sigma}$ and $\hat{b}_{k,\sigma}$:

$$\hat{m}_{BOW} \equiv \frac{1}{L} \sum_{k} \sum_{\sigma} \left[\hat{a}_{k,\sigma}^{\dagger} \hat{b}_{k,\sigma} \left(1 - e^{-2ik} \right) + \hat{b}_{k,\sigma}^{\dagger} \hat{a}_{k,\sigma} \left(1 - e^{2ik} \right) \right] . \tag{2.42}$$

By using Eq. (2.37), we first express $\hat{a}_{k,\sigma}$ and $\hat{b}_{k,\sigma}$ in terms of the new fermionic operators. Then, when averaging over the ground state of Eq. (2.40), a few simplifications occur, yielding:

$$\langle GS|\hat{m}_{BOW}|GS\rangle = -\frac{2}{L} \sum_{k} Re \left[r_k \left(1 - e^{-2ik} \right) \right] = \frac{8t\alpha \Delta}{L} \sum_{k} \frac{\sin^2(k)}{\epsilon^+(k)}$$

$$\xrightarrow{L \to \infty} \frac{4t\alpha \Delta}{\pi} \int_{-\pi/2}^{\pi/2} dk \frac{\sin^2(k)}{\epsilon_+(k)} . \qquad (2.43)$$

Now, instead of numerically evaluating this expression, we observe that it is directly related to the value of Δ that minimizes the energy of the ground state. We note that, by explicitly rewriting Eq. (2.25), one can obtain a relation satisfied by the optimal dimerization parameter Δ in the thermodynamic limit, namely:

$$\frac{\pi}{16\ t\ \lambda} = \int_{-\pi/2}^{\pi/2} dk \frac{\sin^2(k)}{\epsilon_+(k)} \ , \tag{2.44}$$

where $\lambda = (t\alpha^2)/K$ and the only point where the parameter Δ appears is inside $\epsilon_+(k)$ at the denominator.

It is then straightforward to observe that the BOW order parameter is directly proportional to the displacement parameter Δ and, by inspecting Eq. (2.34), also to the energy gap, namely:

$$\langle GS|\hat{m}_{BOW}|GS\rangle = \frac{\alpha\Delta}{4\lambda} , \qquad \Delta E = 16 \ t \ \lambda \langle GS|\hat{m}_{BOW}|GS\rangle .$$
 (2.45)

2.3.1.5 Charge and spin static correlation functions

We define the Fourier transform of the density operator as follows:

$$\hat{n}_{q} = \frac{1}{\sqrt{L}} \sum_{j} e^{-ijq} \hat{n}_{j} = \frac{1}{\sqrt{L}} \sum_{j} e^{-ijq} \left(\hat{n}_{j\uparrow} + \hat{n}_{j\downarrow} \right) = \hat{n}_{q\uparrow} + \hat{n}_{q\downarrow} , \qquad (2.46)$$

where we emphasize that \hat{n}_q is the sum of two spin-resolved density operators. We now express this operator in terms of the fermionic operators $\hat{\gamma}_{k,\sigma}$ and $\hat{\zeta}_{k,\sigma}$. First, we observe that $\hat{n}_{q,\sigma}$ can be expressed as follows:

$$\hat{n}_{q,\sigma} = \frac{1}{\sqrt{L}} \sum_{k} \left[\hat{a}_{k-q,\sigma}^{\dagger} \hat{a}_{k,\sigma} + e^{-iq} \left(\hat{b}_{k-q,\sigma}^{\dagger} \hat{b}_{k,\sigma} \right) \right] . \tag{2.47}$$

Using Eq. (2.37) to write the old fermionic operators in terms of the new ones, we obtain:

$$\hat{n}_{q\sigma} = \frac{1}{2\sqrt{L}} \sum_{k} \left[r_{k-q} r_{k}^{*} \left(-\hat{\gamma}_{k-q,\sigma}^{\dagger} + \hat{\zeta}_{k-q,\sigma}^{\dagger} \right) \left(-\hat{\gamma}_{k,\sigma} + \hat{\zeta}_{k,\sigma} \right) + e^{-iq} \left(\hat{\gamma}_{k-q,\sigma}^{\dagger} + \hat{\zeta}_{k-q,\sigma}^{\dagger} \right) \left(\hat{\gamma}_{k,\sigma} + \hat{\zeta}_{k,\sigma} \right) \right].$$

$$(2.48)$$

The charge structure factor is then defined as:

$$N(q) \equiv \langle GS | \hat{n}_{-q} \hat{n}_q | GS \rangle = \langle GS | (\hat{n}_{-q,\uparrow} + \hat{n}_{-q,\downarrow}) (\hat{n}_{q,\uparrow} + \hat{n}_{q,\downarrow}) | GS \rangle . \tag{2.49}$$

We see that four spin-dependent terms contribute to N(q). However, cross-spin terms vanish due to the factorized ground state structure: $|GS\rangle = |GS_{\uparrow}\rangle \otimes |GS_{\downarrow}\rangle$. Thus, only the terms $\hat{n}_{-q,\sigma}\hat{n}_{q,\sigma}$ remain and we obtain:

$$N(q) = \sum_{\sigma} \langle GS | \hat{n}_{-q,\sigma} \hat{n}_{q,\sigma} | GS \rangle = \sum_{\sigma} \langle GS_{\sigma} | \hat{n}_{-q,\sigma} \hat{n}_{q,\sigma} | GS_{\sigma} \rangle . \qquad (2.50)$$

For $q \neq 0$, the operator $\hat{n}_{q,\sigma}$ acting on the ground state simplifies as:

$$\hat{n}_{q\sigma} |GS_{\sigma}\rangle = \sum_{s} \left[+r_{s-q} r_{s}^{*} \left(-\hat{\mathcal{Y}}_{s-q,\sigma}^{\dagger} + \hat{\zeta}_{s-q,\sigma}^{\dagger} \right) \left(-\hat{\gamma}_{s,\sigma} + \hat{\zeta}_{s,\sigma}^{\dagger} \right) + e^{-iq} \left(\hat{\mathcal{Y}}_{s-q,\sigma}^{\dagger} + \hat{\zeta}_{s-q,\sigma}^{\dagger} \right) \left(\hat{\gamma}_{s,\sigma} + \hat{\zeta}_{s,\sigma}^{\dagger} \right) \right] \left(\prod_{k=-\pi/2}^{\pi/2 - 2\pi/L} \hat{\gamma}_{k,\sigma}^{\dagger} \right) |0\rangle = \sum_{s} \left(-r_{s-q} r_{s}^{*} + e^{-iq} \right) \hat{\zeta}_{s-q,\sigma}^{\dagger} \hat{\gamma}_{s,\sigma} |GS_{\sigma}\rangle .$$
(2.51)

An analogous simplification holds for the term $\langle GS_{\sigma}|\,\hat{n}_{-q,\sigma}$ and, therefore, the expectation value $\langle GS|\hat{n}_{-q,\sigma}\hat{n}_{q,\sigma}|GS\rangle$ is expressed as follows:

$$\langle GS|\hat{n}_{-q\sigma}\hat{n}_{q\sigma}|GS\rangle = \frac{1}{4L}\sum_{t,s} \left(-r_{t+q}r_t^* + e^{iq}\right) \left(-r_{s-q}r_s^* + e^{-iq}\right) \langle GS|\,\hat{\gamma}_{t+q,\sigma}^{\dagger}\hat{\zeta}_{t,\sigma}\hat{\zeta}_{s-q,\sigma}^{\dagger}\hat{\gamma}_{s,\sigma}\,|GS\rangle$$

$$(2.52)$$

One can easily compute the matrix element in the previous equation, obtaining:

$$\langle GS | \hat{\gamma}_{t+q,\sigma}^{\dagger} \hat{\zeta}_{t,\sigma} \hat{\zeta}_{s-q,\sigma}^{\dagger} \hat{\gamma}_{s,\sigma} | GS \rangle = \delta_{t,s-q}$$
 (2.53)

Therefore, the full charge structure factor reads:

$$N(q) = \langle GS | \hat{n}_{-q} \hat{n}_{q} | GS \rangle = 2 \langle GS | \hat{n}_{-q\uparrow} \hat{n}_{q\uparrow} | GS \rangle = \frac{1}{2} - \frac{1}{L} \sum_{s=-\pi/2}^{\pi/2 - 2\pi/L} \operatorname{Re} \left\{ r_{s}^{*} r_{s-q} e^{iq} \right\} =$$

$$= \frac{1}{2} - \frac{2t^{2}}{L} \sum_{s} \frac{\cos(q) \left(1 + \alpha^{2} \Delta^{2} \right) + \cos(2s - q) \left(1 - \alpha^{2} \Delta^{2} \right)}{\epsilon^{+}(s) \epsilon^{+}(s - q)}$$
(2.54)

Using trigonometric identities, one can show that $N(q=\pi)=1$ for all values of $\alpha\Delta$. We define the spin structure factor as $S(q)=\langle GS|\hat{S}^z_{-q}\hat{S}^z_q|GS\rangle$, with:

$$\hat{S}_q^z = \frac{1}{\sqrt{L}} \sum_j e^{-ijq} \hat{S}_j^z = \frac{1}{\sqrt{L}} \sum_j e^{-ijq} \left(\hat{n}_{j\uparrow} - \hat{n}_{j\downarrow} \right) = \hat{n}_{q,\uparrow} - \hat{n}_{q,\downarrow}$$
 (2.55)

Since $S(q) = \langle GS | \hat{S}^z_{-q} \hat{S}^z_q | GS \rangle = \langle GS | (\hat{n}_{-q,\uparrow} - \hat{n}_{-q,\downarrow}) (\hat{n}_{q,\uparrow} - \hat{n}_{q,\downarrow}) | GS \rangle$, the cross terms between different spin components vanish—just as in the charge case—leading to:

$$S(q) = N(q) = \langle GS | \hat{n}_{-q,\uparrow} \hat{n}_{q,\uparrow} | GS \rangle + \langle GS | \hat{n}_{-q,\downarrow} \hat{n}_{q,\downarrow} | GS \rangle$$
 (2.56)

In Fig. 2.3, we show the charge structure factor N(q) for the ground state of the Hamiltonian in Eq. (2.12) for t=1, K=0.1 and various values of α . For each value of α , the optimal value of Δ is obtained by numerically minimizing Eq. (2.20). The structure factor is then computed on a L=100 lattice using Eq. (2.54). For $\alpha=0.125$, the optimal value of Δ is so small (5×10^{-4}) that the structure factor appears to be almost gapless. Changing α , the structure factor interpolates between the case of free fermion, where $N(q)=1-|q-\pi|/\pi$, and the limit of very large Δ , where $N(q)=1-\cos^2{(q/2)}$.

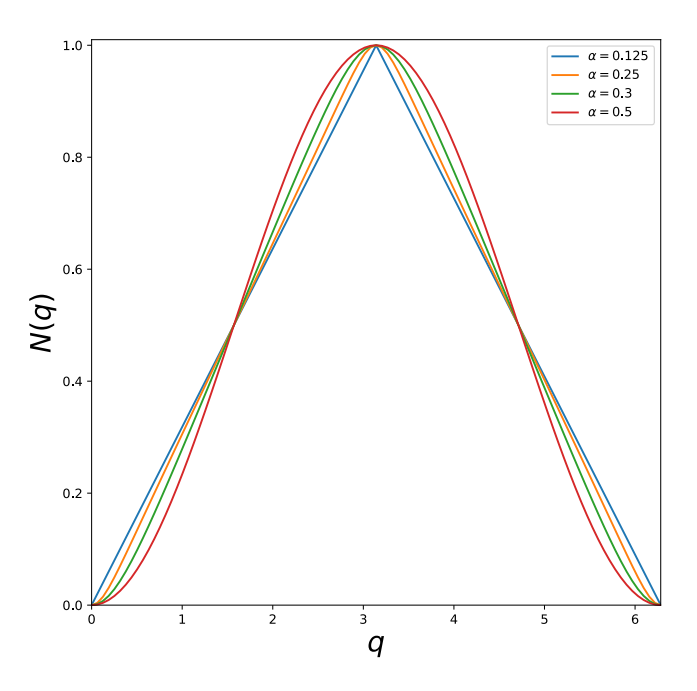


Figure 2.3: Charge structure factor N(q) for the ground state of the SSH Hamiltonian, Eq. (2.12), with t = 1, K = 0.1 and various values of α .

2.3.2 Interacting fermions in the adiabatic limit: U>0

Taking into account the Hubbard interaction U, the adiabatic limit can no longer be solved by a simple analytic treatment. Although the phonon degrees of freedom remain classical, after performing the substitution $x_i = (-1)^{i+1} \Delta/2$ shown in Eq. (2.11) into the Hamiltonian of Eq. (2.10), the resulting Hamiltonian becomes:

$$\hat{H} = -t\sum_{i}^{L} \sum_{\sigma} \left[1 - \alpha \Delta (-1)^{i} \right] \left(\hat{c}_{i,\sigma}^{\dagger} \hat{c}_{i+1,\sigma} + \hat{c}_{i+1,\sigma}^{\dagger} \hat{c}_{i,\sigma} \right) + \frac{1}{8} NK\Delta^{2} + U\sum_{i} \hat{n}_{i,\uparrow} \hat{n}_{i,\downarrow} . \quad (2.57)$$

Since the electrons are interacting, it is not straightforward to determine whether the dimerized state (with a finite value of Δ) is always favored, or if there exists a regime where an undistorted state with $\Delta = 0$ prevails.

This model was first studied using the unrestricted Hartree-Fock approximation [76], reporting the presence, for sufficiently large values of U, of an undistorted spin-density-wave (SDW) state with $\langle n_{i,\sigma} \rangle = 1/2 + \sigma \; (-1)^i \; \delta^{SWF}$. A subsequent analysis by Baereswyl and Maki [48], using a variational approximation (specifically a Gutzwiller wave function and an expansion valid for $U/(4t) \lesssim 1$), found no evidence of a SDW state, agreeing well with Hirsch's exact Monte Carlo calculation performed for a very large value of the harmonic oscillator mass term (K=0.25 and $M\approx 230$, close to the adiabatic limit) [41]. Both Monte Carlo calculations and the Gutzwiller wave function agree that a small value of the Hubbard interaction ($U/t \lesssim 1$) actually favours the dimerized state, leading to an increase in the dimerization parameter Δ compared to the non-interacting U=0 case. The dimerization parameter Δ reaches a maximum around $U/(4t) \sim 1$ and decreases for higher interaction values.

In the large-U limit, the model of Eq. (2.57) becomes equivalent to a spin-Peierls Heisenberg model, with the following Hamiltonian:

$$\hat{H} = J \sum_{i}^{L} \left[1 - \alpha \Delta (-1)^{i} \right] \hat{\vec{S}}_{i} \cdot \hat{\vec{S}}_{i+1} + \frac{1}{8} N K \Delta^{2} , \qquad (2.58)$$

where $J=\frac{4t^2}{U}$ and each site hosts a spin-1/2 operator $\hat{\vec{S}}_i=\left(\hat{S}_i^x,\hat{S}_i^y,\hat{S}_i^z\right)$. This model has been widely studied [77, 78], and it was established that the spin part of the Hamiltonian has an energy per site that scales as $-J\Delta^{4/3}$ in the thermodynamic limit [79]. Since the function $-J\ c\ \Delta^{4/3}+\frac{1}{8}K\Delta^2$ always has a minimum at a finite value of Δ , the ground state of the spin-Peierls Heisenberg model of Eq. (2.58) always exhibits dimerization in the thermodynamic limit, for any finite value of α .

The conclusion drawn from these studies is that the model in Eq. (2.57) does not support undistorted phases, even in the presence of a large Hubbard interaction U. Although this conclusion is not a rigorous proof, it naturally follows from the fact that the model seems to always favor dimerization, both for finite values of U/t and in the large-U limit.

2.4 Anti-adiabatic limit

In the anti-adiabatic limit, the phonon mass becomes negligible, and the phonon degrees of freedom can be effectively integrated out:

$$m \to 0 \qquad \omega \to \infty \qquad \text{with} \quad K = m\omega^2 = const \ .$$
 (2.59)

In this section, we first consider the bSSH model, as it is the simplest and most instructive case for performing the anti-adiabatic limit. Next, we address the aSSH and oSSH models. Finally,

we discuss the physical properties of the models in the anti-adiabatic limit, both in the absence and in the presence of Hubbard interaction U. Although the effective Hamiltonians derived in this section are valid for any doping level, the analysis of physical properties will focus exclusively on the half-filling regime.

To perform this limit, it is convenient to switch to an imaginary-time action formalism, which naturally shows how the bosonic fields are integrated out, leaving an effective electronic interaction. First, we define the electronic action in the absence of phonons, which we will refer to as $S_0[\bar{\psi}, \psi]$, namely:

$$S_0[\bar{\psi}, \psi] = \int d\tau \sum_{i} \left[\bar{\psi} \partial_{\tau} \psi - t B_{i,i+1} \right] , \qquad (2.60)$$

where $B_{i,j} = \sum_{\sigma} (\bar{\psi}_{i\sigma} \psi_{j\sigma} + \text{h.c.})$ represents the electronic hopping term.

2.4.1 Anti-adiabatic limit for the bSSH chain

The imaginary-time action for the bSSH model, which includes electron hopping, phonon kinetic and potential energy, and electron-phonon coupling, is given by:

$$S[\bar{\psi}, \psi, x] = S_0[\bar{\psi}, \psi] + \int d\tau \sum_{i} \left[\frac{m}{2} (\partial_{\tau} x_{(i,i+1)})^2 + \frac{K}{2} x_{(i,i+1)}^2 + t\alpha \ x_{(i,i+1)} B_{i,i+1} \right] , \quad (2.61)$$

where $x_{(i,i+1)}$ is the phonon displacement field (in the *bSSH* model, each pair of nearest neighbors (i, i+1) corresponds to a variable $x_{(i,i+1)}$, which is bond-centered) and $B_{i,j}$ is the electronic hopping term defined above.

In the anti-adiabatic limit, the phonon kinetic term vanishes, allowing us to integrate out the phonons. It is sufficient to complete the square for each $x_{(i,i+1)}$ term to see that the $x_{(i,i+1)}$ fields get integrated out:

$$\int \mathcal{D}\bar{\psi}\mathcal{D}\psi\mathcal{D}x \ e^{-S[\bar{\psi},\psi,x]} = \int \mathcal{D}\bar{\psi}\mathcal{D}\psi \ e^{-S_0[\bar{\psi},\psi]} \int \mathcal{D}x \Big(\prod_i e^{-\int d\tau \frac{K}{2} \left[x_{(i,i+1)} + \frac{t\alpha}{K}B_{i,i+1}\right]^2} e^{\int d\tau \frac{t^2\alpha^2}{2K}B_{i,i+1}^2} \Big),$$
(2.62)

This results in an effective electronic interaction mediated by phonons:

$$S_{\text{eff}}[\bar{\psi}, \psi] = S_0[\bar{\psi}, \psi] - \int d\tau \sum_i \frac{t^2 \alpha^2}{2K} B_{i,i+1}^2 = \int d\tau \sum_i \left[\bar{\psi} \partial_\tau \psi - t B_{i,i+1} - \frac{t^2 \alpha^2}{2K} B_{i,i+1}^2 \right]. \quad (2.63)$$

The interaction term $B_{i,i+1}^2$ can be rewritten in terms of spin and pairing operators, respectively:

$$\hat{S}_{j}^{\alpha} = \frac{1}{2} \sum_{\sigma,\sigma'} \hat{c}_{j,\sigma}^{\dagger} \tau_{\sigma,\sigma'}^{\alpha} \hat{c}_{j,\sigma'}^{\dagger} ; \qquad \hat{\Delta}_{j} = \hat{c}_{j,\downarrow} \hat{c}_{j,\uparrow} . \qquad (2.64)$$

It can be easily checked that the following equality holds:

$$\hat{B}_{ij}^{2} = \sum_{\sigma,\sigma'} \left(\hat{c}_{i\sigma}^{\dagger} \hat{c}_{j\sigma} + \hat{c}_{j\sigma}^{\dagger} \hat{c}_{i\sigma} \right) \left(\hat{c}_{i\sigma'}^{\dagger} \hat{c}_{j\sigma'} + \hat{c}_{j\sigma'}^{\dagger} \hat{c}_{i\sigma'} \right) =
= -4 \hat{\vec{S}}_{i} \cdot \hat{\vec{S}}_{j} - \hat{n}_{i} \hat{n}_{j} + 2 \left(\hat{\Delta}_{i}^{\dagger} \hat{\Delta}_{j} + \hat{\Delta}_{j}^{\dagger} \hat{\Delta}_{i} \right) + \hat{n}_{i} + \hat{n}_{j} .$$
(2.65)

Hence, we obtain the effective Hamiltonian for the bSSH model in the anti-adiabatic limit,

namely:

$$\hat{H}_{AA}^{bSSH} = -t \sum_{i,\sigma} (\hat{c}_{i,\sigma}^{\dagger} \hat{c}_{i+1,\sigma} + \text{h.c.}) - \frac{t^{2} \alpha^{2}}{2K} \sum_{i} (\hat{B}_{i,i+1})^{2} =
= -t \sum_{i,\sigma} (\hat{c}_{i,\sigma}^{\dagger} \hat{c}_{i+1,\sigma} + \text{h.c.}) +
+ \frac{2t^{2} \alpha^{2}}{K} \sum_{i} \left[\hat{\vec{S}}_{i} \cdot \hat{\vec{S}}_{i+1} + \frac{1}{4} \hat{n}_{i} \hat{n}_{i+1} - \frac{1}{2} \left(\hat{\Delta}_{i}^{\dagger} \hat{\Delta}_{i+1} + \hat{\Delta}_{i+1}^{\dagger} \hat{\Delta}_{i} \right) \right].$$
(2.66)

We can notice that the presence of phonons effectively generates an antiferromagnetic spin exchange term $(\hat{\vec{S}}_i \cdot \hat{\vec{S}}_{i+1})$ and an attractive pairing interaction of the form $-(\hat{\Delta}_i^{\dagger} \hat{\Delta}_{i+1} + \text{h.c.})$.

2.4.2 Anti-adiabatic limit for the aSSH chain

We note that, for the aSSH model, following a procedure similar to the one shown in the previous section, the resulting effective interaction turns out to be exactly the same as in Eq. (2.66). The imaginary-time action for the aSSH model is given by:

$$S[\bar{\psi}, \psi, x] = S_0[\bar{\psi}, \psi] + \int d\tau \sum_{i,\nu} \left[\frac{m}{2} (\partial_\tau x_i)^2 + \frac{K}{2} (x_{i+1} - x_i)^2 + t\alpha (x_{i+1} - x_i) B_{i,i+1} \right], \quad (2.67)$$

where x_i is the phonon displacement field (site-centered in this case).

Although it would be straightforward to perform a treatment analogous to Eq. (2.62) to integrate out the phonons, namely by writing:

$$\int \mathcal{D}\bar{\psi}\mathcal{D}\psi\mathcal{D}x \ e^{-S[\bar{\psi},\psi,x]} = \int \mathcal{D}\bar{\psi}\mathcal{D}\psi \ e^{-S_0[\bar{\psi},\psi]} \int \mathcal{D}x \Big(\prod_i e^{-\int d\tau \frac{K}{2} \left[x_{i+1} - x_i + \frac{t\alpha}{K}B_{i,i+1}\right]^2} e^{\int d\tau \frac{t^2\alpha^2}{2K}B_{i,i+1}^2}\Big),$$
(2.68)

the fact that the integral of the quadratic term $\int \mathcal{D}x \prod_i e^{-\int d\tau \frac{K}{2} \left[x_{i+1} - x_i + \frac{t\alpha}{K} B_{i,i+1}\right]^2}$ gives a constant result independent of $\frac{t\alpha}{K} B_{i,i+1}$ is less trivial in this case. A careful treatment would require switching to k-space and treating the term with zero momentum separately, since the dispersion relation of acoustic phonons is $\omega(k) \propto |\sin(k/2)|$, which vanishes at k = 0. However, the resulting effective Hamiltonian turns out to be the same as in Eq. (2.66) [80, 81].

2.4.3 Anti-adiabatic limit for the oSSH chain

Integrating out the phonons in the anti-adiabatic limit requires a slightly more complex calculation for the case of the oSSH Hamiltonian rather than the straightforward case of the oSSH model. The imaginary-time action for the oSSH model is given by:

$$S[\bar{\psi}, \psi, x] = S_0[\bar{\psi}, \psi] + \int d\tau \sum_i \left[\frac{m}{2} (\partial_\tau x_i)^2 + \frac{K}{2} x_i^2 + t\alpha (x_{i+1} - x_i) B_{i,i+1} \right], \qquad (2.69)$$

where x_i is the site-centered phonon displacement field.

The most simple way to integrate out the phonons in the case of vanishing mass m = 0 relies on the following identity [47]:

$$\sum_{i} (x_{i+1} - x_i) B_{i,i+1} = \sum_{i} x_i (B_{i-1,i} - B_{i,i+1}).$$
(2.70)

Thanks to this identity, completing the square for each x_i is straightforward. The path integral $\int \mathcal{D}\bar{\psi}\mathcal{D}\psi\mathcal{D}xe^{-S[\bar{\psi},\psi,x]}$ can then be written as:

$$\int \mathcal{D}\bar{\psi}\mathcal{D}\psi \ e^{-S_0[\bar{\psi},\psi]} \int \mathcal{D}x \Big(\prod_i e^{-\int d\tau \frac{K}{2} \big[x_i + \frac{t\alpha}{K}(B_{i-1,i} - B_{i,i+1})\big]^2} e^{\int d\tau \frac{t^2\alpha^2}{2K}(B_{i-1,i} - B_{i,i+1})^2} \Big).$$
(2.71)

Hence, we obtain the effective Hamiltonian:

$$\hat{H}_{AA}^{oSSH} = -t \sum_{i,\sigma} (\hat{c}_{i,\sigma}^{\dagger} \hat{c}_{i+1,\sigma} + \text{h.c.}) - \frac{t^2 \alpha^2}{2K} \sum_{i} (\hat{B}_{i-1,i} - \hat{B}_{i,i+1})^2 =$$

$$= \sum_{i} \left[-t \hat{B}_{i,i+1} - \frac{t^2 \alpha^2}{K} (\hat{B}_{i,i+1})^2 + \frac{t^2 \alpha^2}{2K} (\hat{B}_{i-1,i} \hat{B}_{i,i+1} + \hat{B}_{i,i+1} \hat{B}_{i-1,i}) \right]. (2.72)$$

We can compare the results of performing the anti-adiabatic limit for the oSSH model with those for the bSSH model discussed in Section 2.4.1, in particular by examining the effective Hamiltonians obtained after integrating out the phonons: Eqs. (2.66) and (2.72). In both cases, a term of the form $-(\hat{B}_{i,i+1})^2$ is generated, which, as discussed in Eq. (2.66), leads to an effective antiferromagnetic spin exchange term and an attractive pairing interaction. However, for the oSSH case, an additional term of the form $\hat{B}_{i-1,i}\hat{B}_{i,i+1}$ is generated. This term has the same amplitude but the opposite sign compared to the squared hopping term, introducing a distinct feature in the effective Hamiltonian.

2.4.4 Physical properties in the anti-adiabatic limit for U=0

After performing the anti-adiabatic limit, an effective electronic Hamiltonian remains. However, integrating out the phonon degrees of freedom generates interactions within the resulting electronic model, making it more challenging to investigate the nature of the insulating state at half-filling.

We first focus on the case of absence of Hubbard interaction (U=0). Using a field theory approach combined with renormalization group techniques [80], Fradkin and Hirsch demonstrated that the system remains in a dimerized ground state at half-filling for any value of the coupling constants, confirming that dimerization persists despite the phonon-induced interactions. Their study focused on the bSSH and aSSH models in the anti-adiabatic limit, namely on the effective electronic Hamiltonian of Eq. (2.66).

A subsequent work by Zhang et al. numerically confirmed Fradkin's prediction using density-matrix renormalization group (DMRG) [81]. They showed that, even in the anti-adiabatic limit, a linear relationship exists between the energy gap and the BOW order parameter. This relationship is reminiscent of Eq. (2.45) which holds in the adiabatic limit, although with a different proportionality constant, indicating similar underlying physics despite the complexity introduced by the interactions.

2.4.5 SSH-Hubbard model in the anti-adiabatic: U > 0

When the Hubbard interaction U is included, the situation becomes more intriguing. One possible approach is to first take the large-U limit and then perform the anti-adiabatic limit (as we did in this section) on the effective Spin-Peierls Heisenberg Hamiltonian given in Eq. (2.5). This procedure has been employed in various works [49, 82], resulting in an effective J_1 - J_2 Heisenberg Hamiltonian:

$$\hat{H} = J_1 \sum_{i} \hat{\vec{S}}_{i} \cdot \hat{\vec{S}}_{i+1} + J_2 \sum_{i} \hat{\vec{S}}_{i} \cdot \hat{\vec{S}}_{i+2} . \tag{2.73}$$

The couplings J_1 and J_2 are given by $J_1/J = 1 + J\alpha^2/2K$ and $J_2/J = J\alpha^2/4K$, where $J = 4t^2/U$, while α and K represent the electron-phonon coupling and the phonon spring constant respectively. The J_1 - J_2 Heisenberg chain has been extensively studied, and it is well known that when the ratio J_2/J_1 exceeds a critical value of 0.241167(5), a phase transition occurs from a spin-liquid (gapless) state to a dimerized (gapped) state. This implies that, for any value of K, there is a critical value for the electron-phonon coupling that allows the transition from a dimerized Peierls state to an undistorted state. The undistorted state is adiabatically connected to the ground state of the one-dimensional S - 1/2 Heisenberg chain, characterized by gapless spin excitations and quasi-long-range spin order (true antiferromagnetic order is prevented by the Mermin–Wagner theorem, which forbids breaking of SU(2) symmetry at zero temperature in one dimension).

The case of finite Hubbard interaction U has been studied less frequently. Nevertheless, a work by Zhang et al. [50] demonstrated that a sufficiently large value of U can drive the system described by Eq. (2.66) from a Peierls insulator to a Mott insulator, characterized by gapless spin excitations and the absence of BOW.

Although the one-dimensional SSH model (in the absence of interaction) tends to stabilize a dimerized BOW phase in both the adiabatic and anti-adiabatic limits, the fact that the Hubbard interaction can turn a 1D Peierls insulator into a Mott insulator in the anti-adiabatic limit, but not in the adiabatic one, reveals the crucial role of quantum phonons in the competition between the distorted and undistorted phases.

2.5 Finite Phonon mass case

We now review results from previous studies on the SSH-Hubbard model with fully quantum phonons of finite mass m.

At half-filling, several works agree on the point that two distinct phases can be stabilized depending on the dominant interaction. When the electron-electron interaction prevails, the system enters a Mott insulating phase, which features no lattice distortions and gapless spin excitations. In contrast, when the electron-phonon coupling dominates, a Peierls insulating phase emerges, characterized by lattice distortions, BOW, and a fully gapped excitation spectrum.

In the following subsections, we begin by discussing the historical results on the stability of the two phases and the transition between them (Sec. 2.5.1). Then, we examine numerical and analytical results in the large-U limit, corresponding to the Spin-Peierls model (Sec. 2.5.2), before concluding with a focus on numerical results for finite values of U (Sec. 2.5.3).

2.5.1 Early studies on the SSH-Hubbard Model

Hirsch was among the first to employ Monte Carlo techniques to study the sign-problem-free half-filled model in 1983 [41]. He was able to study relatively small rings (N=24 sites) and argued that a sufficiently large Hubbard interaction U would suppress Peierls dimerization. His argument relied on the large-U limit of the model, which is mapped to an effective Spin-Peierls Heisenberg Hamiltonian, see Eq. (2.5), which in turn can be mapped to spinless fermions via a Jordan-Wigner transformation. Fradkin and Hirsch previously demonstrated, using renormalization group arguments, that the spinless SSH model cannot sustain dimerization at any finite phonon frequency ω , undergoing a Kosterlitz-Thouless transition to an undimerized phase when the electron-phonon coupling α is smaller than a frequency-dependent critical value $\alpha^*(\omega)$ [80].

2.5.2 Spin-Peierls Heisenberg model in the large-U limit

The large-U limit problem has been extensively studied via the effective Spin-Peierls Heisenberg Hamiltonian of Eq. (2.5), with minor variations depending on the type of phonon coupling (acoustic, optical, or bond-centered). Citro, Orignac and Giamarchi [51] employed bosonization and renormalization group techniques to derive an explicit expression for the energy gap at the transition, confirming that the dimerized-undimerized transition belongs to the Berezinskii-Kosterlitz-Thouless (BKT) universality class. The presence of the Mott insulating an Peierls insulating phases had been numerically confirmed earlier: Bursill et al. [49] used DMRG to study a Spin-Peierls Heisenberg model with oSSH coupling, while Sandvik and Campbell [72] used sign-problem-free quantum Monte Carlo to analyze an analogous model with oSSH coupling. Both works identified a transition point at finite electron-phonon coupling strength. Analogous results have been found in a study that used a flow equation approach to map the system onto an effective magnetic problem [83].

2.5.3 Numerical results on SSH-Hubbard model

The finite-U case with quantum phonons has been studied in a limited number of works. Ref. [42] employed stochastic series expansion quantum Monte Carlo to study the model with bSSH coupling of Eq. (2.7), while Ref. [43] used continuous-time quantum Monte Carlo method to study both the cases of bSSH and aSSH couplings, Eq. (2.7) and Eq. (2.6), respectively. Both studies included on-site Hubbard interaction U and a (small) nearest-neighbor interaction term $V\sum_{j}\hat{n}_{j}\hat{n}_{j+1}$, confirming the presence of a direct transition between Mott and Peierls insulating phases.

Regarding the transition point between the phases, it can be observed that, for a fixed Hubbard interaction U>0, the critical value α_c of the electron-phonon coupling at which the system transitions from a Mott insulator to a Peierls insulator is a monotonically increasing function of the phonon frequency ω . This has been demonstrated numerically in Ref. [84] for U/t=4, for both the aSSH and oSSH models. In the case of small ω (and consequently large phonon mass m), the system approaches the adiabatic limit, where the Mott insulating phase disappears, and α_c tends to zero. As ω increases, one approaches the anti-adiabatic limit, where the Mott insulating phase remains stable from $\alpha=0$ up to a large critical value α_c .

Notably, Pearson et al. [84, 85] conducted studies first on a Spin-Peierls Heisenberg Hamiltonian and subsequently on a SSH-Hubbard Hamiltonian with a phonon energy term interpolating continuously between the oSSH and aSSH couplings. The conclusion of both works is that the dimerized phase associated with acoustic phonons (aSSH coupling) is less robust against quantum fluctuations, favoring the Mott phase over a broader region of the phase diagram.

Chapter 3

Variational wave function for SSH-Hubbard model

In this chapter, we define the variational wave function that we employ to study the SSH-Hubbard model, leaving the discussion of the optimization procedure and the details of variational Monte Carlo for the next chapter.

We begin by demonstrating how the number of parameters in the *SSH* Hamiltonian can be reduced by introducing rescaled variables to describe the phonon degrees of freedom (Sec. 3.1). The variational wave function of the model is expressed in terms of these new rescaled phononic variables.

The most important part of the chapter follows in Sec. 3.2, where we define the variational wave function and describe the Hilbert space in which it is constructed. We then provide a detailed analysis of the wave function components. First, we focus on the antisymmetric fermionic part, discussing the improvements made over a simple Slater determinant. Next, we present the uncorrelated bosonic part of the wave function, which captures the presence of bond-order wave. Finally, we discuss the various Jastrow factors that account for correlation effects both among the electrons and between electrons and phonons.

Throughout the chapter, we focus on the 1D SSH-Hubbard model, with Sec. 3.3 extending the variational wave function to the 2D case.

3.1 Simplified SSH Hamiltonian with rescaled phonon coordinates

Our variational Monte Carlo study of the SSH-Hubbard model focuses on the oSSH version, which involves dispersion-less harmonic oscillators coupled to each site of the chain, as given by Eq. (2.1). For convenience, we rewrite the Hamiltonian for the 1D case here, as we will perform a few steps to reduce the number of parameters it contains:

$$\hat{H} = -t \sum_{i,\sigma} \left[1 - \alpha \left(\hat{x}_{i+1} - \hat{x}_i \right) \right] \left(\hat{c}_{i,\sigma}^{\dagger} \hat{c}_{i+1,\sigma} + \hat{c}_{i+1,\sigma}^{\dagger} \hat{c}_{i,\sigma} \right) + \sum_{i} \left[\frac{\hat{p}_i^2}{2m} + \frac{1}{2} m \omega^2 \hat{x}_i^2 \right] + U \sum_{i} \hat{n}_{i,\uparrow} \hat{n}_{i,\downarrow} ,$$

$$(3.1)$$

where $\hat{c}_{i,\sigma}^{\dagger}$ creates an electron on site i with spin σ , and \hat{x}_i , \hat{p}_i are the position and momentum operators of the phonon describing the ion at site i. The parameter t is the bare electron hopping amplitude, and U represents the on-site Hubbard interaction. The harmonic oscillators have frequency ω and ionic mass m, while α is the electron-phonon SSH coupling.

The displacements and conjugate momenta of the harmonic oscillators satisfy the usual commutation relation:

$$[\hat{x}_j, \hat{p}_k] = i\hbar \delta_{jk} . \tag{3.2}$$

We observe that the ground state of the free-bosonic problem (in the case t = U = 0) is given by a product of identical Gaussian wave functions, each centered around one site:

$$\psi_{Gaussian}(x) \propto \exp\left\{-\frac{m\omega}{2\hbar}x^2\right\}.$$
(3.3)

Now, we define new rescaled variables for the phonons in the following way:

$$\hat{X}_i = \sqrt{\frac{m\omega}{\hbar}} \hat{x}_i \quad ; \qquad \qquad \hat{P}_i = \sqrt{\frac{1}{m\omega\hbar}} \hat{p}_i \quad . \tag{3.4}$$

Their commutation relation is therefore:

$$\left[\hat{X}_i, \hat{P}_i\right] = i \ . \tag{3.5}$$

Therefore, the Hamiltonian of the system becomes:

$$\hat{H} = -t \sum_{i} \left[1 - \tilde{\alpha} \left(\hat{X}_{i+1} - \hat{X}_{i} \right) \right] \left(\hat{c}_{i}^{\dagger} \hat{c}_{i+1} + \hat{c}_{i+1}^{\dagger} \hat{c}_{i} \right) + \frac{\hbar \omega}{2} \sum_{i} \left[\hat{P}_{i}^{2} + \hat{X}_{i}^{2} \right] + U \sum_{i} \hat{n}_{i,\uparrow} \hat{n}_{i,\downarrow} , \quad (3.6)$$

where $\tilde{\alpha}$ is the rescaled version of α , which has absorbed the extra prefactor brought by the new displacement operator, and is defined as follows:

$$\tilde{\alpha} = \alpha \sqrt{\frac{\hbar}{m\omega}} \ . \tag{3.7}$$

Using these new units, the Gaussian wave function for the ground state of the non-interacting bosonic problem acquires a simple form:

$$\psi_{Gaussian}(X) \propto \exp\left\{-\frac{1}{2}X^2\right\}.$$
(3.8)

At last, the dimensionless parameter λ described in Eq. (2.4), gets a simple expression in terms of $\tilde{\alpha}$, namely:

$$\lambda = \frac{t\alpha^2}{m\omega^2} = \frac{t\tilde{\alpha}^2}{\hbar\omega} \tag{3.9}$$

After this procedure, the mass of the phonons has been completely reabsorbed. Thus, we can simply work with the following values being specified:

- t
- *U*
- ħω
- $\tilde{\alpha}$ or λ

Since the Hamiltonian in Eq. (3.6) allows us to perform simulations by specifying only the phonon frequency $\hbar\omega$, we explain how the adiabatic and anti-adiabatic limits of the phonon degrees of freedom are defined for this Hamiltonian in Appendix A.

3.2 Variational wave function definition

We define the wave function in a Hilbert space that contains both electron and phonon configurations. However, while the electronic degrees of freedom are described in terms of creation and annihilation operators in second quantization, we decide to describe the harmonic oscillators in terms of their displacement operators, working in first quantization and in a continuum basis. Therefore, the Hilbert space is defined by the following quantum states:

$$|X; n_{\sigma}\rangle = |X\rangle \otimes |n_{\sigma}\rangle = \bigotimes_{j} |X_{j}\rangle \otimes |n_{j,\sigma}\rangle ,$$
 (3.10)

where the local Hilbert space of electrons is made by four states, namely:

$$|n_{j,\sigma}\rangle = \left\{ |0\rangle , \hat{c}_{j,\uparrow}^{\dagger}|0\rangle , \hat{c}_{j,\downarrow}^{\dagger}|0\rangle , \hat{c}_{j,\uparrow}^{\dagger}\hat{c}_{j,\downarrow}^{\dagger}|0\rangle \right\} ; \tag{3.11}$$

while the local Hilbert space of bosonic coordinates is defined by:

$$\hat{X}_j | X_j \rangle = X_j | X_j \rangle \qquad X_j \in (-\infty, \infty) , \qquad (3.12)$$

where \hat{X}_j is the position operator for the harmonic oscillator at site j, defined in Eq. (3.4). The variational wave function we use is defined in the Hilbert space of Eq. (3.10) as follows:

$$\langle X; n_{\sigma} | \Psi_{\text{var}} \rangle = \mathcal{J}_{\text{ee}}(n_{\sigma}) \, \mathcal{J}_{\text{pp}}(X) \, \mathcal{J}_{\text{ep}}(X, n_{\sigma}) \, \left(\langle X | \Psi_{\text{p}} \rangle \, \langle X; n_{\sigma} | \Psi_{\text{e}} \rangle \right) \,,$$
 (3.13)

where $\langle X; n_{\sigma} | \Psi_{\rm e} \rangle$ represents the fermionic determinant part, which is antisymmetric with respect to the fermionic coordinates, and depends directly on the phonon state $|X\rangle$. The term $\langle X | \Psi_{\rm p} \rangle$ describes a non-interacting bosonic state. The remaining three terms are Jastrow factors: $\mathcal{J}_{\rm ee}(n_{\sigma})$, $\mathcal{J}_{\rm pp}(X)$, and $\mathcal{J}_{\rm ep}(X, n_{\sigma})$, which account for electron-electron, phonon-phonon, and electron-phonon correlation effects, respectively.

All terms that appear inside Eq. (3.13) contain variational parameters that must be optimized in order to provide an approximate description of the ground state. In this chapter, we focus on the precise description of the ansatz itself, leaving for the next chapter the optimization procedure and the details of variational Monte Carlo that allow to compute relevant expectation values.

We notice that one could have used a second-quantization notation also to deal with the bosonic degrees of freedom, namely by defining a local space for the harmonic oscillators of the form:

$$|b_j^n\rangle = \frac{1}{\sqrt{n}} \left(\hat{b}_j^{\dagger}\right)^n |0\rangle \quad \text{with} \quad \hat{b}_j^{\dagger} = \frac{1}{\sqrt{2}} \left(\hat{X}_j - i\hat{P}_j\right) ,$$
 (3.14)

obtained by repeatedly applying a construction operator \hat{b}_{j}^{\dagger} to the vacuum, with \hat{X}_{j} and \hat{P}_{j} defined in Eq. (3.4). This choice is perfectly legitimate, and typically employed when using density-matrix renormalization group (DMRG) to optimize a Matrix Product State (MPS) variational ansatz. However, our variational wave function will benefit from the fact that the bosons are described as continuous variables and by the fact that their displacement coordinate is diagonal in the basis of our choice: evaluating the variational wave function of Eq. (3.13) on the local Hilbert space of Eq. (3.14) would not be feasible, in particular for the term $\langle X; n_{\sigma} | \Psi_{\rm e} \rangle$.

3.2.1 Slater Determinant with phonon-backflow terms

In a conventional Jastrow-Slater approach, as has been done multiple times in the past for this and other electron-phonon systems (such as the Hubbard-Holstein model) [53, 86, 87, 88], one could design a variational wave function where the antisymmetric part is given by a pair-product state, independent of the phonon degrees of freedom, namely:

$$|\Psi_{\rm e}\rangle = \exp\left(\sum_{i,j} f_{i,j} \hat{c}_{i,\uparrow}^{\dagger} \hat{c}_{j,\downarrow}^{\dagger}\right) |0\rangle ,$$
 (3.15)

where the values $f_{i,j}$ can either be independent variational parameters or be determined from the diagonalization of an auxiliary quadratic BCS-Hamiltonian \hat{H}_0 , which itself contains some variational parameters to be optimized. The form of \hat{H}_0 is:

$$\hat{H}_0 = \sum_{i,j,\sigma} t_{ij} \hat{c}_{i,\sigma}^{\dagger} \hat{c}_{j,\sigma} + \mu \sum_{i,\sigma} \hat{c}_{i,\sigma}^{\dagger} \hat{c}_{i,\sigma} + \sum_{i,j} \Delta_{ij} \hat{c}_{i,\uparrow}^{\dagger} \hat{c}_{j,\downarrow}^{\dagger} + h.c. , \qquad (3.16)$$

where the hopping $(t_{ij} = t_{ji}^*)$ and pairing $(\Delta_{ij} = \Delta_{ji})$ amplitudes are variational parameters, as well as the chemical potential μ .

If one were to consider a variational wave function of the form described in Eq. (3.13) and use a pair-product ansatz as Eq. (3.15) for the antisymmetric part, the term $\langle X; n_{\sigma} | \Psi_{\rm e} \rangle$ would lose its dependence on the phonon configuration $|X\rangle$. The downside of this approach is that, in this case, correlation effects between electronic and phonon degrees of freedom would only be captured by the term $\mathcal{J}_{\rm ep}(X,n_{\sigma})$. If this term were to vanish, the trial wave function would factorize into two terms: $\langle X; n_{\sigma} | \Psi_{\rm var} \rangle = \langle X | \phi_{phonon} \rangle \ \langle n_{\sigma} | \varphi_{electrons} \rangle$.

Previous variational Monte Carlo calculations on the SSH-Hubbard chain, using a wave function with the fermionic part given by Eq. (3.13), demonstrated that the presence of the term $\mathcal{J}_{\text{ep}}(X, n_{\sigma})$ was not crucial for obtaining a valid description of the physical system. When this term was eliminated, the quality of the results remained similar. For this reason, we concluded that a new way to incorporate electron-phonon correlations within the variational wave function was needed.

Our idea is to add a direct contribution from the phonon degrees of freedom inside the pair function of Eq. (3.15), such that electron-phonon correlation effects are already included within the fermionic part of the wave function. This is achieved by considering an auxiliary Hamiltonian that parametrically depends on the phonon displacements:

$$\hat{H}_{\text{ep}} = \hat{H}_{0} + \sum_{i,m,\sigma} g_{m} (X_{i+m} - X_{i}) \hat{c}_{i,\sigma}^{\dagger} \hat{c}_{i+m,\sigma} + \sum_{i,m} h_{m} (X_{i+m} - X_{i}) \hat{c}_{i,\uparrow}^{\dagger} \hat{c}_{i+m,\downarrow}^{\dagger} + h.c. , \quad (3.17)$$

where $g_m = g_{-m}$ and $h_m = -h_{-m}$ are variational parameters for $m = \pm 1$ and ± 3 (suitable for a possible bond dimerization), and $\{X_j\}$ are the phonon displacements in the configuration $|X\rangle$. In this way, $\langle X; n_{\sigma} | \Psi_e \rangle$ depends upon the actual phonon configuration. This introduces a sort of "backflow" within the electronic part of the variational wave function.

In the standard continuum case, the term "backflow" refers to a trial wave function in which the effective position of each electron (from which the Slater determinant is constructed) depends on the positions of all other electrons [89, 90, 91]. On the lattice, this approach has been extended by constructing single-particle orbitals or pairing functions that explicitly depend on the many-body electron configuration [54, 55]. In our case, the backflow correlations involve both electrons and phonons.

The reason why we expect this ansatz to effectively capture electron-phonon correlation effects within the SSH-Hubbard model is that the term with coefficient g_1 in Eq. (3.17) has

exactly the same form as the SSH coupling appearing in the physical Hamiltonian of the model in Eq. (3.6). For this reason, if one considered the adiabatic limit in which the phonon displacements $\{X_j\}$ become classical coordinates, the ground state of the Hamiltonian \hat{H}_{ep} coincides with the exact ground state of the physical SSH Hamiltonian at U=0 for any fixed value of the phonon displacements $\{X_j\}$, which should only be minimized classically.

3.2.2 Non-interacting bosonic state

The non-interacting bosonic state, represented by the term $\langle X|\Psi_{\rm p}\rangle$ in Eq. (3.13), is given by the following expression:

$$\langle X|\Psi_{\rm p}\rangle = \prod_{j} \exp\left\{-\frac{\Omega}{2} \left[X_j - z \ (-1)^j\right]^2\right\},$$
 (3.18)

where X_j denotes the position operator of the jth phonon coordinate within $|X\rangle$, while Ω and z are variational parameters.

The most significant variational parameter is z, which controls the staggered phonon displacement. This parameter closely resembles the variational parameter Δ introduced in Section 2.3 to describe the dimerization of the SSH model in the adiabatic limit. A finite value of Δ corresponded to the system showing a dimerization pattern of the ionic displacements, resulting in a Peierls insulating state.

In the adiabatic limit described in Section 2.3, since the phonons were treated as classical degrees of freedom, the substitution $x_j \to (-1)^j \Delta/2$ could be made directly in the Hamiltonian. In the present case, where the phonons are modeled as quantum harmonic oscillators, we introduce the parameter z into the wave function. A finite value of z shifts the center of the Gaussian wave function of each harmonic oscillator in a staggered manner by an amount z. The average value of the \hat{X}_j operator in the wave function of Eq. (3.18) satisfies the same relation as in the adiabatic limit, namely:

$$\langle \Psi_{\mathbf{p}} | \hat{X}_j | \Psi_{\mathbf{p}} \rangle = (-1)^j \ z \ . \tag{3.19}$$

3.2.3 Jastrow factors

The three Jastrow factors that appear inside the variational wave function of Eq. (3.13) are described as follows:

$$\mathcal{J}_{ee}(n_{\sigma}) = \exp\left\{\frac{1}{2}\sum_{i,j}v_{ij}(n_i-1)(n_j-1)\right\},$$
 (3.20)

$$\mathcal{J}_{pp}(X) = \exp\left\{\frac{1}{2}\sum_{i,j}u_{ij}X_iX_j\right\},\tag{3.21}$$

$$\mathcal{J}_{\text{ep}}(X, n_{\sigma}) = \exp \left\{ \sum_{i,j} w_{ij} (n_i - 1)(n_j - 1)(X_i - X_j) \right\},$$
 (3.22)

where the pseudo-potentials v_{ij} , u_{ij} , and w_{ij} are variational parameters, with $v_{ji} = v_{ij}$, $u_{ji} = u_{ij}$, and $w_{ji} = -w_{ij}$.

We observe that, in principle, the pseudo-potentials can be optimized as independent parameters for each pair of sites (i, j) in the lattice. However, to reduce the number of variational parameters, some symmetries can be implemented. In our variational Monte Carlo calculations, we imposed both translation and reflection symmetries for the Jastrow factors, which ensures

that the variational parameter associated with sites (i, j) depends only on the lattice distance between site i and site j.

The density-density Jastrow factor $\mathcal{J}_{\text{ee}}(n_{\sigma})$ captures correlation effects arising from a large Hubbard interaction U, which disfavors double occupancy and thus modulates electronic charge fluctuations. This term is especially relevant for describing the Mott insulating phase, where the Fourier transform of the pseudo-potential v_q scales as $v_q \approx 1/q^2$ for small momenta q [52].

The phonon-phonon Jastrow factor $\mathcal{J}_{pp}(X)$ is designed to capture correlation effects between phonons that go beyond the simple non-interacting term described in Eq. (3.18).

On the other hand, the electron-phonon Jastrow factor $\mathcal{J}_{ep}(X, n_{\sigma})$ becomes particularly important in the regime where both U and λ are large. It enables the capturing of correlations between the electronic charge and phonon displacements that go beyond the expressive power of the fermionic ansatz $\langle X; n_{\sigma} | \Psi_{e} \rangle$ that includes phonon-backflow effects.

It is important to note that the term $(n_i-1)(n_j-1)$ inside the electron-electron and electronphonon Jastrow factors cannot be simply replaced with $n_i n_j$. In the case of $\mathcal{J}_{ep}(X, n_{\sigma})$, we found that the optimal value of the parameters w_{ij} , with the term defined as in Eq. (3.22), led to a better variational energy compared to the same wave function with the term defined as $n_i n_j$ and the parameters undergoing a new optimization.

3.3 Variational wave function for 2D SSH-Hubbard model

In this section, we will first show how to generalize the SSH-Hubbard Hamiltonian to a square lattice geometry and then provide a variational wave function that is a straightforward generalization of the one of Sec. 3.2. Next, we will focus on some peculiarities of the 2D wave function.

3.3.1 SSH-Hubbard Hamiltonian on the square lattice

The natural generalization of the SSH-Hubbard model to a two-dimensional square lattice simply requires to consider phonons along both the x and y directions. Consequently, each Einstein dispersionless phonon is modeled as a quantum harmonic oscillator attached to each site. In this case, each site hosts two phonon modes: one for the x direction and another for the y direction. The Hamiltonian of the system for the case of the oSSH model is then:

$$\hat{H} = -t \sum_{R,\sigma} \left[1 - \tilde{\alpha} \left(\hat{X}_{R+e_x} - \hat{X}_R \right) \right] \left(\hat{c}_{R,\sigma}^{\dagger} \hat{c}_{R+e_x,\sigma} + \hat{c}_{R+e_x,\sigma}^{\dagger} \hat{c}_{R,\sigma} \right) +$$

$$- t \sum_{R,\sigma} \left[1 - \tilde{\alpha} \left(\hat{Y}_{R+e_y} - \hat{Y}_R \right) \right] \left(\hat{c}_{R,\sigma}^{\dagger} \hat{c}_{R+e_y,\sigma} + \hat{c}_{R+e_y,\sigma}^{\dagger} \hat{c}_{R,\sigma} \right) +$$

$$+ \frac{\hbar \omega}{2} \sum_{R} \left[\hat{P}_{x,R}^2 + \hat{X}_R^2 \right] + \frac{\hbar \omega}{2} \sum_{R} \left[\hat{P}_{y,R}^2 + \hat{Y}_R^2 \right] + U \sum_{R} \hat{n}_{R,\uparrow} \hat{n}_{R,\downarrow} ,$$

$$(3.23)$$

where the sum over $R = (R_x, R_y)$ runs over all lattice sites, e_x and e_y are unit displacement vectors in the x and y directions, respectively, and the operator $\hat{c}_{R,\sigma}^{\dagger}$ creates an electron on site R with spin σ . As before, U represents the on-site Hubbard interaction and t is the bare electron hopping amplitude. The operators \hat{X}_R and \hat{Y}_R are the position operators of the harmonic oscillators attached to site R, accounting for the optical phonon modes in the x and y directions, respectively. Their conjugate momenta are $\hat{P}_{x,R}$ and $\hat{P}_{y,R}$, and together they satisfy the following commutation relations:

$$\left[\hat{X}_{R}, \hat{P}_{x,S}\right] = \left[\hat{Y}_{R}, \hat{P}_{y,S}\right] = i\delta_{R,S} \qquad \left[\hat{X}_{R}, \hat{P}_{y,S}\right] = \left[\hat{Y}_{R}, \hat{P}_{x,S}\right] = 0. \tag{3.24}$$

For simplicity, we are already working with rescaled variables for the phonons, as defined in Eq. (3.4) for the one-dimensional case. Hence, the Hamiltonian in Eq. (3.24) only requires the phonon frequency and the electron-phonon coupling $\tilde{\alpha}$ to be specified. Finally, we note that the phonon frequency and the electron-phonon coupling are assumed to be equal in both the x and y directions.

3.3.2 Variational wave function on the square lattice

The definition of the Hilbert space in the square lattice case closely follows the construction presented in Sec. 3.2. The Hilbert space includes both electron and phonon configurations: the former described in terms of creation and annihilation operators in second quantization, the latter characterized by their displacement operators. The quantum state that we use to describe the Hilbert space is given by:

$$|X;Y;n_{\sigma}\rangle = |X\rangle \otimes |Y\rangle \otimes |n_{\sigma}\rangle = \bigotimes_{R} |X_{R}\rangle \otimes |Y_{R}\rangle \otimes |n_{R,\sigma}\rangle ,$$
 (3.25)

where the local Hilbert space of electrons is defined as in Eq. (3.11), and the local Hilbert space for bosonic coordinates is defined in terms of the eigenvalues of the \hat{X}_R and \hat{Y}_R position operators.

The variational wave function is defined as follows:

$$\langle X; Y; n_{\sigma} | \Psi_{\text{var}} \rangle = \mathcal{J}_{\text{ee}}(n_{\sigma}) \, \mathcal{J}_{\text{pp}}(X, Y) \, \mathcal{J}_{\text{ep}}(X, Y, n_{\sigma}) \, \left(\langle X; Y | \Psi_{\text{p}} \rangle \, \langle X; Y; n_{\sigma} | \Psi_{\text{e}} \rangle \right) \,, \quad (3.26)$$

where $\langle X; Y; n_{\sigma} | \Psi_{\rm e} \rangle$ represents the fermionic determinant part, which also depends on the phonon state $|X; Y\rangle$. The term $\langle X; Y | \Psi_{\rm p} \rangle$ describes a non-interacting bosonic state, and the remaining three terms are Jastrow factors.

The determinant term $\langle X; Y; n_{\sigma} | \Psi_{e} \rangle$ is the straightforward generalization of the one-dimensional term, which is defined to be the ground state of an auxiliary Hamiltonian that explicitly depends on the phonon configuration as shown in Eq. (3.17). In this case, also the Y coordinates are included: in the following equation we show how the hopping term g is modified when added to the auxiliary BCS quadratic Hamiltonian \hat{H}_{0} :

$$\hat{H}_{\rm ep} = \hat{H}_0 + \sum_{R,\sigma} g \left(X_{R+e_x} - X_R \right) \hat{c}_{R,\sigma}^{\dagger} \hat{c}_{R+e_x,\sigma} + \sum_{R,\sigma} g \left(Y_{R+e_y} - Y_R \right) \hat{c}_{R,\sigma}^{\dagger} \hat{c}_{R+e_y,\sigma} , \qquad (3.27)$$

where the usual BCS auxiliary Hamiltonian \hat{H}_0 in this case contain pairing terms that can be divided into s-wave and d-wave pairing channels, namely:

$$\hat{H}_{0} = \sum_{R,S,\sigma} t_{RS} \hat{c}_{R,\sigma}^{\dagger} \hat{c}_{S,\sigma} + \mu \sum_{R,\sigma} \hat{c}_{R,\sigma}^{\dagger} \hat{c}_{R,\sigma} +
+ \sum_{R} \Delta_{0} \hat{c}_{R,\uparrow}^{\dagger} \hat{c}_{R,\downarrow}^{\dagger} + h.c. +
+ \sum_{R} \Delta_{s} \left(\hat{c}_{R,\uparrow}^{\dagger} \hat{c}_{R+e_{x},\downarrow}^{\dagger} + \hat{c}_{R,\uparrow}^{\dagger} \hat{c}_{R+e_{y},\downarrow}^{\dagger} \right) + h.c. +
+ \sum_{R} \Delta_{d} \left(\hat{c}_{R,\uparrow}^{\dagger} \hat{c}_{R+e_{x},\downarrow}^{\dagger} - \hat{c}_{R,\uparrow}^{\dagger} \hat{c}_{R+e_{y},\downarrow}^{\dagger} \right) + h.c. ,$$
(3.28)

with Δ_0 , Δ_s and Δ_d being superconducting variational parameters, together with the conventional t_{RS} and μ terms.

The non-interacting bosonic state $\langle X; Y | \Psi_{\rm p} \rangle$ is defined in close analogy to its 1D counterpart of Eq. (3.18), specifically:

$$\langle X; Y | \Psi_{\mathbf{p}} \rangle = \prod_{R} \exp \left\{ -\frac{\Omega_x}{2} \left[X_R - z_x \cos(Q_x \cdot R) \right]^2 \right\} \exp \left\{ -\frac{\Omega_y}{2} \left[Y_R - z_y \cos(Q_y \cdot R) \right]^2 \right\},$$
(3.29)

where the x and y phonon coordinates are controlled by different variational parameters, Ω_x and Ω_y , which determine the width of the Gaussians, and z_x and z_y , which specify the displacement of their centers. This expression is written in a more general form with respect to the 1D case, allowing for different bond-order wave patterns depending on the two-dimensional vectors Q_x and Q_y . For the half-filling case, the possible values of the two components of Q_x are restricted to either 0 or π . The same holds true for Q_y .

Apart from the density-density Jastrow factor $\mathcal{J}_{ee}(n_{\sigma})$, which is defined exactly as in Eq. (3.22), the other two Jastrow factors are slightly modified in the 2D case.

The phonon-phonon Jastrow factor $\mathcal{J}_{pp}(X,Y)$ is a product of two independent terms, namely:

$$\mathcal{J}_{pp}(X,Y) = \exp\left\{\frac{1}{2}\sum_{R,S}u_{RS}^{xx}X_{R}X_{S}\right\}\exp\left\{\frac{1}{2}\sum_{R,S}u_{RS}^{yy}Y_{R}Y_{S}\right\},$$
 (3.30)

where the parameters u_{RS}^{xx} and u_{RS}^{yy} are optimized independently. We also tried to add a mixed term $\sum_{R,S} u_{RS}^{xy} X_R Y_S$, but it did not contribute to lower the energy of the variational wave function, so we discarded it.

In the exact same way, the electron-phonon Jastrow factor $\mathcal{J}_{ep}(X, Y, n_{\sigma})$ is the product of two independent factors for the phonons in the x and y directions, namely:

$$\mathcal{J}_{ep}(X, Y, n_{\sigma}) = \exp\left\{ \sum_{R,S} w_{R,S}^{x}(n_{R} - 1)(n_{S} - 1)(X_{R} - X_{S}) \right\}$$

$$\cdot \exp\left\{ \sum_{R,S} w_{R,S}^{y}(n_{R} - 1)(n_{S} - 1)(Y_{R} - Y_{S}) \right\},$$
(3.31)

with independent parameters $w_{R,S}^x$ and $w_{R,S}^y$.

For computational reasons, all the variational parameters inside the Jastrow terms (namely v, u^{xx} , u^{yy} , w^x and w^y) have been considered respecting reflection symmetry and translational symmetry in the x and y direction independently, allowing for the breaking of rotational symmetry.

3.3.2.1 External antiferromagnetic field for the auxiliary Hamiltonian

The two-dimensional Hubbard model at half-filling displays antiferromagnetic order with ordering vector $Q^{AFM} = (\pi, \pi)$, for this reason we may be interested in inserting an external antiferromagnetic field within the auxiliary quadratic Hamiltonian \hat{H}_0 . Inserting an antiferromagnetic ordering vector requires to break SU(2) invariance of the model by favoring a particular direction. A straightforward choice would be to direct the external field in the z-direction for the spin operators, namely:

$$\hat{H}_{B^z} = \hat{H}_0 + B^z \sum_{R} \cos\left(Q^{AFM} \cdot R\right) \left[\hat{c}_{R,\uparrow}^{\dagger} \hat{c}_{R,\uparrow} - \hat{c}_{R,\downarrow}^{\dagger} \hat{c}_{R,\downarrow}\right] , \qquad (3.32)$$

where B^z is the variational parameter representing the external antiferromagnetic field.

However, the most effective way to give a variational description of antiferromagnetism in the square-lattice Hubbard model corresponds to consider the direction of the external antiferromagnetic field to lie in the x-direction for the spin operators, namely:

$$\hat{H}_{B^x} = \hat{H}_0 + B^x \sum_{R} \cos\left(Q^{AFM} \cdot R\right) \left[\hat{c}_{R,\uparrow}^{\dagger} \hat{c}_{R,\downarrow} + \hat{c}_{R,\downarrow}^{\dagger} \hat{c}_{R,\uparrow}\right] , \qquad (3.33)$$

where B^x is the variational parameter representing the external antiferromagnetic field. In order to obtain a correct description of the antiferromagnetic system, an additional Jastrow factor that is linked to the correlation between spin operators must be added, namely:

$$\mathcal{J}_{S^zS^z}(n_\sigma) = \exp\left\{\sum_{R,S} J_{R,S} S_R^z S_S^z\right\}, \qquad (3.34)$$

where the value of S_R^z is defined by the eigenvalue of the operator $\hat{S}_R^z = \hat{c}_{R,\uparrow}^\dagger \hat{c}_{R,\uparrow} - \hat{c}_{R,\downarrow}^\dagger \hat{c}_{R,\downarrow}$, diagonal in the Hilbert space in which we are working.

In the case of a BCS auxiliary Hamiltonian \hat{H}_{ep} which includes pairing terms (e.g. Δ_0), we employ a particle-hole transformation for computational reasons to write the Hamiltonian in terms of new fermionic operators. This allows us to express its ground state as a determinant, avoiding the need for Bogoliubov transformations. The procedure is described in detail in the first section of Appendix B.

However, a downside of using a particle-hole transformation is that we cannot simultaneously include the BCS-pairing terms Δ_0 , Δ_s , Δ_d , and the external antiferromagnetic field B^x in the auxiliary Hamiltonian \hat{H}_{ep} .

Therefore, when considering antiferromagnetic solutions in our variational Monte Carlo study of the 2D Hubbard SSH model, we will need to exclude pairing terms in the auxiliary Hamiltonian \hat{H}_{ep} . It is important to note that the presence of backflow terms of the form g is unaffected by the external magnetic field, and only the terms h will be eliminated.

Chapter 4

Variational Monte Carlo

In this chapter, we focus on variational Monte Carlo by first describing the variational principle, on which variational Monte Carlo is based, in Section 4.1; next, we briefly introduce variational Monte Carlo in general terms focusing on the Metropolis algorithm, Section 4.2. Then, we discuss the details of our implementation for electron-phonon systems, including details regarding the Metropolis algorithm and the local energy, Section 4.3. At last, we describe the optimization procedure, which is based on the Stochastic Reconfiguration technique, Section 4.4. Specific details regarding the computation of derivatives are discussed in Appendix B. We refer to the book in Ref. [92] for a detailed discussion about Variational Monte Carlo and interacting electronic systems.

4.1 Variational principle

Variational methods in quantum mechanics are based on the so-called variational principle. For a general interacting quantum system described by a Hermitian Hamiltonian \hat{H} in a Hilbert space \mathcal{H} , at least in principle, we can always find a basis of the Hilbert space given by the eigenstates of \hat{H} :

$$\hat{H} |\phi_m\rangle = E_m |\phi_m\rangle . \tag{4.1}$$

We consider a variational state $|\psi_{\text{var}}\rangle$ that we wish to use to approximate the ground state $|\phi_0\rangle$ of \hat{H} . The variational energy E_{var} is defined as:

$$E_{\text{var}} = \frac{\langle \psi_{\text{var}} | \hat{H} | \psi_{\text{var}} \rangle}{\langle \psi_{\text{var}} | \psi_{\text{var}} \rangle} . \tag{4.2}$$

Clearly, $|\psi_{\text{var}}\rangle$ can be expanded on the basis of eigenvectors of \hat{H} , namely:

$$|\psi_{\text{var}}\rangle = \sum_{m} a_m |\phi_m\rangle$$
 (4.3)

Considering a normalized variational state requires an additional constraint:

$$\langle \psi_{\text{var}} | \psi_{\text{var}} \rangle = \sum_{m} |a_m|^2 = 1 .$$
 (4.4)

The variational wave function is progressively more accurate as a_0 approaches the value of 1, becoming exact in the case $a_0 = 1$.

We can substitute Eq. (4.3) into the expression for the variational energy $E_{\rm var}$, obtaining:

$$E_{\text{var}} = \sum_{m} E_m |a_m|^2 \ge E_0 \sum_{m} |a_m|^2 = E_0 ,$$
 (4.5)

where, exploiting the normalization condition on $|\psi_{\text{var}}\rangle$ and the fact that E_0 is the lowest eigenvalue, we show that E_{var} represents an upper bound to the exact ground-state energy E_0 . The quality of the approximation can be measured in terms of the energy difference between E_{var} and E_0 , namely:

$$E_{\text{var}} - E_0 = \sum_{m>0} (E_m - E_0) |a_m|^2 \ge (E_1 - E_0) \sum_{m>0} |a_m|^2 = (E_1 - E_0) \left(1 - |a_0|^2\right) , \quad (4.6)$$

where we again used the fact that the eigenvalues are ordered and the normalization condition on $|\psi_{\text{var}}\rangle$.

Inspecting Eq. (4.6), we can observe that it relates the value of $|a_0|^2$ to the variational energy and the energy gap $E_1 - E_0$ between the ground state and the first excited state of the system, namely:

 $|a_0|^2 \ge 1 - \frac{E_{\text{var}} - E_0}{E_1 - E_0}$ (4.7)

Therefore, as the error made by the variational energy with respect to the ground state $E_{\text{var}} - E_0$ decreases with respect to the energy gap $E_1 - E_0$, the variational state $|\psi_{\text{var}}\rangle$ is guaranteed to provide a better approximation of the ground state $|\phi_0\rangle$.

4.2 Variational Monte Carlo

Once the variational principle is established, the main challenge is to compute the variational energy efficiently. This is where Markov chain Monte Carlo (MCMC) comes into play. In this section, we first briefly explain how Monte Carlo sampling can be used to approximate the variational energy. Then, we show how the Metropolis algorithm can be employed to sample a given probability distribution. Finally, we discuss a few peculiarities of its implementation.

4.2.1 Monte Carlo sampling

In order to obtain an estimate of the variational energy, the idea is to insert a resolution of the identity $\sum_{x} |x\rangle \langle x| = 1$ over the entire Hilbert space in the definition of the variational energy Eq. (4.2), namely:

$$E_{\text{var}} = \frac{1}{\langle \psi_{\text{var}} | \psi_{\text{var}} \rangle} \sum_{x} \langle \psi_{\text{var}} | x \rangle \langle x | \hat{H} | \psi_{\text{var}} \rangle . \tag{4.8}$$

This expression cannot be evaluated exactly for large systems, since the dimension of the Hilbert space that appears in the sum grows exponentially with the system size. However, we can multiply and divide the right-hand side of the equation by the same term $\langle x|\psi_{\rm var}\rangle$, isolating two terms:

$$E_{\text{var}} = \sum_{x} \frac{|\langle x | \psi_{\text{var}} \rangle|^2}{\langle \psi_{\text{var}} | \psi_{\text{var}} \rangle} \frac{\langle x | \hat{H} | \psi_{\text{var}} \rangle}{\langle x | \psi_{\text{var}} \rangle} = \sum_{x} P(x) \mathcal{E}_L(x) . \tag{4.9}$$

The first term P(x) in the sum corresponds to the normalized squared modulus of the wave function on configuration $|x\rangle$, the second term $\mathcal{E}_L(x)$ is typically referred to as the local energy.

The key is to interpret Eq. (4.9) as the average value of the quantity $\mathcal{E}_L(x)$, weighted over the probability distribution P(x). To compute it, it would be sufficient to randomly draw Mindependent configurations that are distributed according to the probability distribution P(x)and average the local energy for each of them, namely:

$$E_{\text{var}} \approx \frac{1}{M} \sum_{x \sim P(x)}^{M} \mathcal{E}_L(x) \ .$$
 (4.10)

According to the Central Limit Theorem, the error made by approximating E_{var} in this way scales as $1/\sqrt{M}$, where M is the number of sampled used, independently of the dimension of the original Hilbert space.

4.2.2 The Metropolis algorithm

At this point, we only need to specify how to sample configurations from a probability distribution P(x). This task is accomplished using the Metropolis algorithm [93]. The procedure requires to start from a certain configuration $|x\rangle$ and propose a new configuration $|x'\rangle$ according to a certain transition kernel k(x', x). The configuration $|x'\rangle$ is then accepted with probability:

$$A(x',x) = \min\left\{1, \frac{P(x')k(x,x')}{P(x)k(x',x)}\right\} . \tag{4.11}$$

The procedure is then repeated to create a Markov chain. The algorithm allows to sample a probability distribution P(x) without explicitly computing its normalization, which disappears in the acceptance probability relation.

If the transition kernel is symmetric, i.e., k(x', x) = k(x, x') (which will always be the case in our implementation), the transition probability simplifies to:

$$A(x',x) = \min\left\{1, \frac{P(x')}{P(x)}\right\}$$
 (4.12)

Thus, to perform a Metropolis step, it is sufficient to evaluate the probability distribution at the two configurations $|x\rangle$ and $|x'\rangle$ and draw a random number η uniformly distributed in [0,1). If $\eta < \frac{P(x')}{P(x)}$, the move is accepted; otherwise, it is rejected. The Metropolis algorithm ensures that, after a transient regime, the chain of configurations drawn in this way will sample the probability distribution P(x).

Moreover, the Metropolis algorithm can be restated in terms of the logarithm of the probability distribution $\ln P(x)$ instead of P(x). Given the monotonicity of the function \ln , it is equivalent to extract a random number u uniformly distributed in [0,1) and compute the acceptance probability by: $\ln(1-u) < \ln P(x') - \ln P(x)$. This is useful because it allows us to work directly with the logarithm of the wave function, computing the logarithm of the unnormalized probability distribution as $\ln P(x) = 2 \ln |\psi(x)|$.

4.2.3 Details about Variational Monte Carlo implementation

The enforcement of projectors that reduce the Hilbert space to a specific subspace (such as a sector with fixed magnetization or with fixed number of electrons) is usually trivially implemented within variational Monte Carlo. It is sufficient to initialize the Markov chain from a configuration that lies within the target subspace and ensure that the configurations proposed during the Metropolis steps remain within this subspace.

The main issue is that the configurations drawn by the Metropolis algorithm are correlated with each other. A common solution to reduce autocorrelation effects is to compute observables not at every step of the Metropolis algorithm, but after a certain number of proposed steps, usually proportional to the system size. This technique is referred to as sparse averaging.

Finally, when estimating error bars, autocorrelation effects should be accounted for by using methods such as binning averaging [94].

4.3 Variational Monte Carlo for electron-phonon systems

In the case of the SSH-Hubbard model described by Eq. (3.6), considering a variational wave function as described in the previous chapter, defined on the Hilbert space in Eq. (3.10), we can explicitly write the form of the variational energy estimator and provide a detailed description of the local energy term. We remind that the Hilbert space we consider is defined as:

$$|X; n_{\sigma}\rangle = |X\rangle \otimes |n_{\sigma}\rangle = \bigotimes_{j} |X_{j}\rangle \otimes |n_{j,\sigma}\rangle ,$$
 (4.13)

where the electronic local state is defined in terms of creation operators acting on the vacuum, while the local bosonic state is represented by the continuous eigenvalue X_j of the position operator \hat{X}_j .

A resolution of the identity in this specific Hilbert space is written as:

$$\sum_{n_{\sigma}} \int dX |n_{\sigma}, X\rangle \langle n_{\sigma}, X| = 1, \qquad (4.14)$$

where the sum extends over all electron configurations and the integral is over all phonon displacements.

The variational energy is therefore written as:

$$E_{\text{var}} = \frac{\langle \Psi_{\text{var}} | \hat{H} | \Psi_{\text{var}} \rangle}{\langle \Psi_{\text{var}} | \Psi_{\text{var}} \rangle} = \sum_{n_{\sigma}} \int dX \underbrace{\frac{|\langle X; n_{\sigma} | \Psi_{\text{var}} \rangle|^{2}}{\langle \Psi_{\text{var}} | \Psi_{\text{var}} \rangle}}_{P(X; n_{\sigma})} \underbrace{\frac{\langle X; n_{\sigma} | \hat{H} | \Psi_{\text{var}} \rangle}{\langle X; n_{\sigma} | \Psi_{\text{var}} \rangle}}_{\mathcal{E}_{L}(X; n_{\sigma})}, \tag{4.15}$$

where $P(X; n_{\sigma})$ is the probability distribution given by the square amplitude of the wave function, and $\mathcal{E}_L(X; n_{\sigma})$ is the local energy term. Both quantities are expressed in terms of the configuration state $|X; n_{\sigma}\rangle$.

4.3.1 Metropolis algorithm details

All simulations have been performed working within a reduced Hilbert subspace of fixed electron number and zero magnetization, namely $\sum_{j} n_{j,\uparrow} = \sum_{j} n_{j,\downarrow} = N_e/2$. Therefore, the system is always initialized in an initial configuration $|n_{\sigma}, X\rangle$ that satisfies the above constraints. At each Metropolis step, one of the following updating schemes is randomly selected:

- Electron hopping move: The next configuration is proposed by randomly selecting an electron and a direction, then moving the electron to its nearest neighbor site in that direction. If the move violates the Pauli exclusion principle, it is rejected directly; otherwise, it is accepted or rejected according to the Metropolis criterion.
- Electron spin-flip move: The next configuration is proposed by randomly selecting an electron and a direction. If, on its nearest neighbor site in that direction, there is an electron with opposite spin, the two electrons swap places. The move is accepted or rejected according to the Metropolis criterion (it is rejected immediately if the initial configuration does not involve exactly two electrons with opposite spin, one on each site).
- **Phonon move:** A lattice site j is randomly selected, and a random number Δ is drawn, uniformly distributed within the interval $[-\Delta_{\max}, \Delta_{\max}]$. The proposed move is $X_j \mapsto X_j + \Delta$, with the acceptance probability computed using the Metropolis algorithm.

4.3.2 Local energy term

The local energy $\mathcal{E}_L(X; n_{\sigma})$ for a given local configuration $|X; n_{\sigma}\rangle$ consists of two contributing terms, which are obtained by splitting the Hamiltonian of Eq. (3.6) in the following way:

$$\hat{H} = \underbrace{-t\sum_{i} \left[1 - \tilde{\alpha} \left(\hat{X}_{i+1} - \hat{X}_{i}\right)\right] \left(\hat{c}_{i}^{\dagger} \hat{c}_{i+1} + \hat{c}_{i+1}^{\dagger} \hat{c}_{i}\right) + U\sum_{i} \hat{n}_{i,\uparrow} \hat{n}_{i,\downarrow}}_{\hat{H}^{\text{phon}}} + \underbrace{\frac{\hbar \omega}{2} \sum_{i} \left[\hat{P}_{i}^{2} + \hat{X}_{i}^{2}\right]}_{\hat{H}^{\text{phon}}}.$$

$$(4.16)$$

Thus, the local energy of Eq. (4.9) can be written as:

$$\mathcal{E}_{L}(X; n_{\sigma}) = \frac{\langle X; n_{\sigma} | \hat{H}^{\text{elec}} | \Psi_{\text{var}} \rangle}{\langle X; n_{\sigma} | \Psi_{\text{var}} \rangle} + \frac{\langle X; n_{\sigma} | \hat{H}^{\text{phon}} | \Psi_{\text{var}} \rangle}{\langle X; n_{\sigma} | \Psi_{\text{var}} \rangle} = \mathcal{E}^{\text{elec}}(X; n_{\sigma}) + \mathcal{E}^{\text{phon}}(X; n_{\sigma}) \quad (4.17)$$

First, we focus on the electronic term $\mathcal{E}^{\text{elec}}(X; n_{\sigma})$. Notice that the Hubbard interaction term is trivial, as it acts by leaving the state $|x\rangle$ unchanged; hence, its contribution only accounts for the number of doubly occupied sites times U. On the other hand, the hopping term is diagonal in the phonon coordinates (one can replace the operators $\hat{X}_{i+1} - \hat{X}_i$ it contains with their eigenvalues $X_{i+1} - X_i$), but it acts non-trivially in the electronic space. Thus, it can be computed as follows by inserting a resolution of the identity:

$$\mathcal{E}^{\text{elec}}(X; n_{\sigma}) = \frac{\langle X; n_{\sigma} | \hat{H}^{\text{elec}} | \Psi_{\text{var}} \rangle}{\langle X; n_{\sigma} | \Psi_{\text{var}} \rangle} = \sum_{n_{\sigma}'} \langle X; n_{\sigma} | \hat{H}^{\text{elec}} | X; n_{\sigma}' \rangle \frac{\langle X; n_{\sigma}' | \Psi_{\text{var}} \rangle}{\langle X; n_{\sigma} | \Psi_{\text{var}} \rangle} , \qquad (4.18)$$

where the configurations n'_{σ} over which the sum runs are those connected to the local configuration n_{σ} by the hopping Hamiltonian within \hat{H}^{elec} , and $\langle X; n_{\sigma} | \hat{H}^{\text{elec}} | X; n'_{\sigma} \rangle$ is the corresponding matrix element. Since the Hamiltonian is local, the number of configurations n'_{σ} scales with the size of the lattice, making the calculation feasible.

Lastly, the term $\mathcal{E}^{\text{phon}}(X; n_{\sigma})$ does not depend on the local electronic configuration. The potential energy term $\frac{\hbar \omega}{2} \sum_{i} \hat{X}_{i}^{2}$ is particularly simple, as it is diagonal in the basis we are using. Its contribution is obtained by replacing the operators \hat{X}_{i} with their eigenvalues X_{i} . The kinetic term requires computing the second derivative of the wave function, since the operator \hat{P}_{i}^{2} acts as $-\frac{\partial^{2}}{\partial X_{i}^{2}}$ in the basis we are considering.

Thus, the term that needs to be computed is:

$$\mathcal{E}^{\text{phon}}(X; n_{\sigma}) = \frac{\langle X; n_{\sigma} | \hat{H}^{\text{phon}} | \Psi_{\text{var}} \rangle}{\langle X; n_{\sigma} | \Psi_{\text{var}} \rangle} = \frac{\hbar \omega}{2} \left[\sum_{i} X_{i}^{2} + \frac{1}{\Psi_{\text{var}}(X; n_{\sigma})} \sum_{i} \frac{\partial^{2} \Psi_{\text{var}}(X; n_{\sigma})}{\partial X_{i}^{2}} \right] . \quad (4.19)$$

Considering a generic wave function $\psi(X; n_{\sigma})$ defined for the local configuration $|X; n_{\sigma}\rangle$, we observe that, by working with the logarithm of the wave function instead of the wave function itself, the following equality holds:

$$\frac{1}{\psi(X; n_{\sigma})} \frac{\partial^{2} \psi(X; n_{\sigma})}{\partial X_{j}^{2}} = \frac{\partial^{2} \ln \psi(X; n_{\sigma})}{\partial X_{j}^{2}} + \left(\frac{\partial \ln \psi(X; n_{\sigma})}{\partial X_{j}}\right)^{2} , \qquad (4.20)$$

where the logarithm is defined in the complex plane, ensuring there are no issues with its domain. By considering the gradient operation $(\nabla_X)_j = \frac{\partial}{\partial X_j}$ and expressing the operator inside the local energy as a Laplacian, i.e., $\Delta_X = \sum_i \frac{\partial^2}{\partial X_i^2}$, the previous equality can be rewritten as:

$$\frac{1}{\psi(X; n_{\sigma})} \Delta_X \psi(X; n_{\sigma}) = \Delta_X \ln \psi(X; n_{\sigma}) + \left\| \nabla_X \ln \psi(X; n_{\sigma}) \right\|^2. \tag{4.21}$$

The variational wave function described in the previous chapter is real, with its sign fully determined by the fermionic part, and all other terms being positive definite by definition. It is given as a product of various components: Jastrow factors, non-interacting bosonic terms, and the fermionic antisymmetric part. We now consider a generic wave function expressed as the product of several terms:

$$\psi(X; n_{\sigma}) = \prod_{\alpha} \varphi_{\alpha}(X; n_{\sigma}) \qquad \to \qquad \ln \psi(X; n_{\sigma}) = \sum_{\alpha} \ln \varphi_{\alpha}(X; n_{\sigma}) , \qquad (4.22)$$

where the logarithm is defined in the complex plane.

Taking the logarithm of the wave function from Eq. (4.22), we can express its gradient and Laplacian as follows:

$$\nabla_X \ln \psi(X; n_\sigma) = \sum_{\alpha} \frac{1}{\varphi_\alpha(X; n_\sigma)} \nabla_X \varphi_\alpha(X; n_\sigma) . \tag{4.23}$$

$$\Delta_X \ln \psi(X; n_{\sigma}) = \sum_{\alpha} \frac{1}{\varphi_{\alpha}(X; n_{\sigma})} \Delta_X \varphi_{\alpha}(X; n_{\sigma}) - \sum_{\alpha} \left\| \frac{1}{\varphi_{\alpha}(X; n_{\sigma})} \nabla_X \varphi_{\alpha}(X; n_{\sigma}) \right\|^2. \tag{4.24}$$

Thus, if the wave function $\psi(X; n_{\sigma})$ has a product form as described in Eq. (4.22), the Laplacian in logarithmic form expressed in Eq. (4.21) can be written as:

$$\frac{1}{\psi(X; n_{\sigma})} \Delta_{X} \psi(X; n_{\sigma}) = \sum_{\alpha} \frac{1}{\varphi_{\alpha}(X; n_{\sigma})} \Delta_{X} \varphi_{\alpha}(X; n_{\sigma}) +
- \sum_{\alpha} \left\| \frac{1}{\varphi_{\alpha}(X; n_{\sigma})} \nabla_{X} \varphi_{\alpha}(X; n_{\sigma}) \right\|^{2} +
+ \left\| \sum_{\alpha} \frac{1}{\varphi_{\alpha}(X; n_{\sigma})} \nabla_{X} \varphi_{\alpha}(X; n_{\sigma}) \right\|^{2}.$$
(4.25)

From this expression, we observe that for each wave function component, we only need to compute its gradient and Laplacian divided by the component itself.

Applying Eq. (4.25) to the wave function described in the previous chapter, one can compute the kinetic term in the local energy. However, the evaluation of the gradient and Laplacian is a straightforward calculation in the case of the non-interacting bosonic term and the Jastrow factors contributions; the case of the fermionic part of the ansatz (which depends on the position operators X_j) is much more complicated. For this reason, this case is treated in detail in Appendix B.

4.4 Optimization method: Stochastic Reconfiguration

After having shown how to compute the energy of a variational state within the variational Monte Carlo framework, the next step is to explain how the variational parameters are optimized. This optimization allows us to obtain the best possible representation of the true ground state within the variational space, specifically the one that minimizes the variational energy.

The optimization is performed using the Stochastic Reconfiguration method [56], which is an improved version of gradient descent. The key feature of Stochastic Reconfiguration is that it preconditions the gradient by multiplying it with a preconditioner matrix, allowing for a faster convergence. This section provides a brief overview of the Stochastic Reconfiguration method; for a more detailed description see Ref. [92]. In Section 4.4.1, we describe the local operators used to compute the gradient and the preconditioner matrix. In Section 4.4.2, we present the

gradient descent method, and in Section 4.4.3, we discuss Stochastic Reconfiguration. Since we are working with a real-valued wave function (as opposed to a complex one), all the equations will be presented accordingly.

4.4.1 Local operators

The local operators used to estimate the gradient and the preconditioner are defined for each variational parameter α_k as follows:

$$\hat{O}_{k} | X; n_{\sigma} \rangle = O_{k}(X; n_{\sigma}) | X; n_{\sigma} \rangle
O_{k}(X; n_{\sigma}) = \frac{1}{\Psi_{\text{var}}(X; n_{\sigma})} \frac{\partial \Psi_{\text{var}}(X; n_{\sigma})}{\partial \alpha_{k}} .$$
(4.26)

The quantities $O_k(X; n_{\sigma})$ are functions of the local configuration $|X; n_{\sigma}\rangle$, and they can be expressed analytically for variational parameters associated with Jastrow factors and the non-interacting bosonic state. The case of the determinant part of the wave function is more complex, and the local operators are computed by means of backward automatic differentiation, which is described in the Appendix B.

For each parameter α_k , the average value of \hat{O}_k over the variational wave function can be computed as follows:

$$\bar{O}_{k} = \frac{\langle \Psi_{\text{var}} | \hat{O}_{k} | \Psi_{\text{var}} \rangle}{\langle \Psi_{\text{var}} | \Psi_{\text{var}} \rangle} = \sum_{n_{\sigma}} \int dX \underbrace{\frac{|\langle X; n_{\sigma} | \Psi_{\text{var}} \rangle|^{2}}{\langle \Psi_{\text{var}} | \Psi_{\text{var}} \rangle}}_{P(X; n_{\sigma})} O_{k}(X; n_{\sigma}) . \tag{4.27}$$

This expression offers a significant simplification compared to Eq. (4.15) for the estimator of the variational energy, mainly because each operator \hat{O}_k is local. As a result, in order to estimate \bar{O}_k , one only needs to sample configurations from $P(X; n_{\sigma})$ using the Metropolis algorithm and compute the average of $O_k(X; n_{\sigma})$ over all configurations.

4.4.2 Gradient descent

If one were to apply plain gradient descent, only the derivative of the variational energy with respect to the variational parameters would be required. Therefore, one would need an estimator for the following quantity:

$$f_k = -\frac{\partial E_{\text{var}}}{\partial \alpha_k} = -\frac{\partial}{\partial \alpha_k} \frac{\langle \psi_{\text{var}} | \hat{H} | \psi_{\text{var}} \rangle}{\langle \psi_{\text{var}} | \psi_{\text{var}} \rangle} , \qquad (4.28)$$

where $|\psi_{\text{var}}\rangle$ depends on the variational parameters α .

The correct expression for f_k is given as follows:

$$f_{k} = -\frac{2 \langle \psi_{\text{var}} | \hat{H} \left(\hat{O}_{k} - \bar{O}_{k} \right) | \psi_{\text{var}} \rangle}{\langle \psi_{\text{var}} | \psi_{\text{var}} \rangle} =$$

$$= -2 \sum_{n_{\sigma}} \int dX \underbrace{\frac{|\langle X; n_{\sigma} | \Psi_{\text{var}} \rangle|^{2}}{\langle \Psi_{\text{var}} | \Psi_{\text{var}} \rangle}}_{P(X; n_{\sigma})} \mathcal{E}_{L}(X; n_{\sigma}) \left(O_{k}(X; n_{\sigma}) - \bar{O}_{k} \right) =$$

$$= 2 \left[E_{\text{var}} \bar{O}_{k} - \sum_{n_{\sigma}} \int dX \ P(X; n_{\sigma}) \mathcal{E}_{L}(X; n_{\sigma}) O_{k}(X; n_{\sigma}) \right] , \qquad (4.29)$$

where $\mathcal{E}_L(X; n_{\sigma})$ is the local energy. In order to estimate f_k , at each configuration $|X; n_{\sigma}\rangle$ sampled via the Metropolis algorithm, one needs to store the following:

- the local energy $\mathcal{E}_L(X; n_\sigma)$, whose average returns the estimate for E_{var} ;
- the local operators $O_k(X; n_\sigma)$, whose average returns the estimate for \bar{O}_k ;
- the product $\mathcal{E}_L(X; n_\sigma)O_k(X; n_\sigma)$, whose average, having subtracted the product $E_{\text{var}} \bar{O}_k$, returns the estimate for f_k .

Performing gradient descent only requires imposing a learning rate γ (usually between 10^{-1} and 10^{-4}) and updating the parameters according to f_k , i.e.:

$$\alpha_k' = \alpha_k + \gamma \ f_k \ . \tag{4.30}$$

The procedure can then be iterated until convergence.

4.4.3 Stochastic Reconfiguration

Stochastic Reconfiguration significantly improves the convergence speed of gradient descent by applying a preconditioner matrix to f_k before updating the parameters. In this section, we will not derive the method from first principles or discuss it in detail. Instead, we will focus on how the algorithm works and how it is implemented in our case.

In order to apply Stochastic Reconfiguration, together with the estimate for f_k computed in the gradient descent case, one also needs to compute the Fisher information matrix S of the variational parameters with respect to the variational wave function. The Fisher information matrix is defined as:

$$S_{kk'} = \frac{\langle \psi_{\text{var}} | \left(\hat{O}_{k} - \bar{O}_{k} \right) \left(\hat{O}_{k'} - \bar{O}_{k'} \right) | \psi_{\text{var}} \rangle}{\langle \psi_{\text{var}} | \psi_{\text{var}} \rangle} =$$

$$= \sum_{n_{\sigma}} \int dX \underbrace{\frac{|\langle X; n_{\sigma} | \Psi_{\text{var}} \rangle|^{2}}{\langle \Psi_{\text{var}} | \Psi_{\text{var}} \rangle}}_{P(X; n_{\sigma})} \left(O_{k}(X; n_{\sigma}) - \bar{O}_{k} \right) \left(O_{k'}(X; n_{\sigma}) - \bar{O}_{k'} \right) =$$

$$= \left[\sum_{n_{\sigma}} \int dX \ P(X; n_{\sigma}) O_{k}(X; n_{\sigma}) O_{k'}(X; n_{\sigma}) \right] - \bar{O}_{k} \bar{O}_{k'} . \tag{4.31}$$

In order to estimate $S_{kk'}$, at each configuration $|X; n_{\sigma}\rangle$ sampled via the Metropolis algorithm, one needs to store in a matrix all the products $O_k(X; n_{\sigma})O_{k'}(X; n_{\sigma})$. By subtracting the contribution $\bar{O}_k\bar{O}_{k'}$ from their average, one obtains an estimator for $S_{kk'}$.

The matrix $S_{kk'}$ can be interpreted as a covariance matrix of the operators \hat{O}_k evaluated on the wave function $|\Psi_{\text{var}}\rangle$, and it is positive definite by definition. However, since we are computing an estimate of $S_{kk'}$ via Monte Carlo sampling, the positive definiteness may not be guaranteed due to the sampling error. To ensure that the matrix is invertible, a small bias ϵ (of the order of 10^{-2} to 10^{-5}) is added to the diagonal of $S_{kk'}$, obtaining:

$$\widetilde{S}_{kk'} = S_{kk'} + \epsilon \ \delta_{kk'} \tag{4.32}$$

The Stochastic Reconfiguration method can now be applied by performing gradient descent using the matrix \widetilde{S}^{-1} as a preconditioner, i.e.:

$$\alpha_k' = \alpha_k + \gamma \sum_{k'} \widetilde{S}_{kk'}^{-1} f_{k'} , \qquad (4.33)$$

where γ is the learning rate.

An alternative approach is to consider the imaginary-time Schrödinger equation. If it were possible to evolve the variational state exactly in imaginary time, the exact ground state of the system would be reached. By minimizing the difference between the infinitesimal evolution in imaginary time and the evolution of the variational state within the variational space, one derives equations of motion for the variational parameters. The Stochastic Reconfiguration method is equivalent to discretizing these equations using the Euler method, with the discretization time step equal to the learning rate γ .

Thus, Stochastic Reconfiguration provides the closest approximation to imaginary-time evolution within the variational space, leading to significantly faster convergence.

Chapter 5

1D oSSH-Hubbard model: a variational Monte Carlo study

In this chapter, we present our variational Monte Carlo (VMC) study of the oSSH-Hubbard chain, including results at both half-filling and upon hole doping. To validate our VMC results, we compare them with density-matrix renormalization group (DMRG) [95] calculations performed on the same system under periodic boundary conditions, wherever possible.

We begin by benchmarking the VMC method against DMRG in Section 5.1. Following that, in Section 5.2, we focus on the half-filling regime, providing a phase diagram and presenting several correlation functions. The main part of the chapter is dedicated to the analysis of the doped system in Section 5.3, where we demonstrate the presence of a Luther-Emery liquid phase, characterized by gapless charge excitations and gapped spin excitations. Finally, in Section 5.4, we explore the effects of modifying the SSH coupling to prevent unphysical behaviors and discuss the associated results.

Throughout this study, we use t as the energy scale and, unless otherwise stated, set $\hbar\omega = t$. Different values of the phonon energy have also been considered, but they do not affect the qualitative results.

5.1 Benchmark against DMRG calculations

First, we assess the accuracy of our variational wave function by comparing its energy with DMRG results. We aim to quantify the improvement achieved by including phonon-backflow terms in the antisymmetric part of the wave function over a simple Jastrow-Slater ansatz. We consider a chain of L=50 sites with electrons coupled to phonons, described by the oSSH-Hubbard Hamiltonian in Eq. (3.6) with $\hbar\omega=t$, and work within the half-filling regime: $\sum_i n_{i,\uparrow} = \sum_i n_{i,\downarrow} = L/2$.

5.1.1 Details about DMRG implementation

In the DMRG calculations, a truncation of the Hilbert space of the phonon is required. Bosonic degrees of freedom must be described using creation and annihilation operators, as shown in Eq. (3.14), but their occupancy cannot be unbounded (for computational reasons). Thus, we set a maximum occupancy of 10 bosons per site, which is considerably larger than the average occupancy. Considering the electron-phonon Hamiltonian with periodic boundary conditions, the energy is optimized using the DMRG algorithm implemented in the ITensor library [96] for a matrix product state (MPS) [97] which, for computational efficiency, does not assume translational symmetry.

Optimizing an MPS ground state with periodic boundary conditions requires very high bond dimensions and extensive optimization. The accuracy of the DMRG calculations is verified by evaluating the variance of the total energy, which remains below $0.007t^2$ for all DMRG results presented in this section. The bond dimension of the MPS is always above $\chi = 1200$, reaching $\chi = 2400$ in some cases.

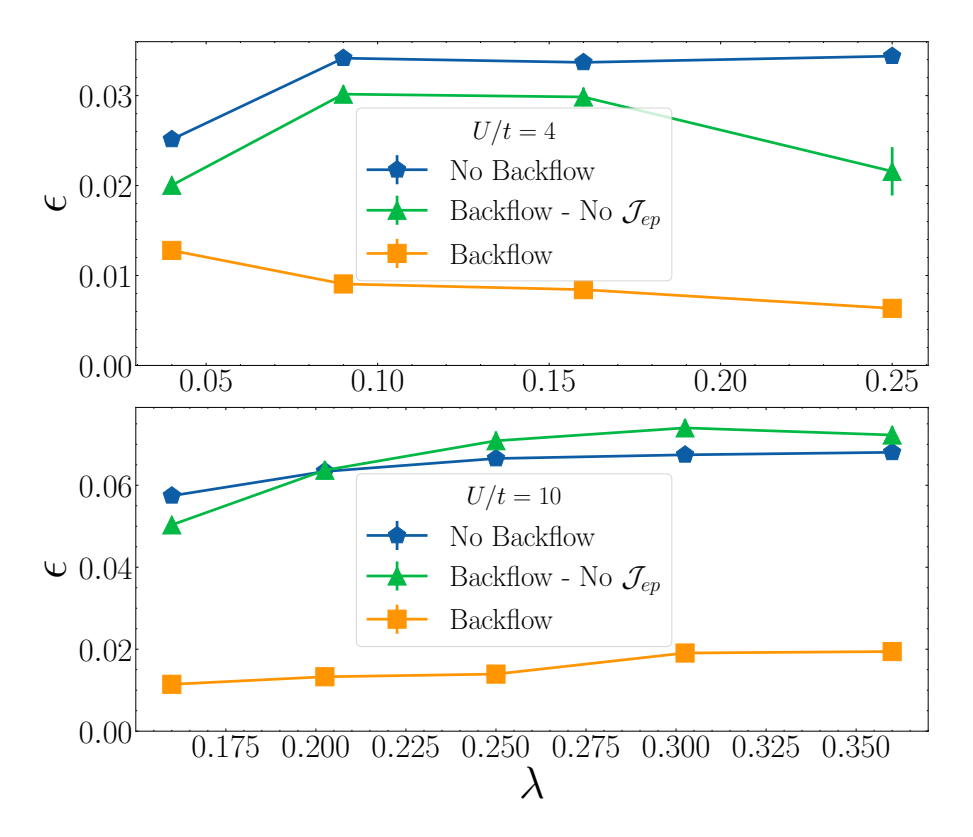


Figure 5.1: Accuracy of the variational energy with respect to DMRG, $\epsilon = (E-E_{DMRG})/|E_{DMRG}-\hbar\omega/2|$ on L=50 sites for $\hbar\omega = t=1$. The simplest wave function, for which the electronic part is obtained from the auxiliary Hamiltonian (3.16), is denoted by blue points; the best one with backflow correlations generated by Eq. (3.17), is represented by orange points; an intermediate case, with backflow correlations, but without electron-phonon Jastrow factor \mathcal{J}_{ep} , is also reported for comparison (green points). Results are shown for U/t=4 (upper panel) and U/t=10 (lower panel), as a function of λ .

5.1.2 Benchmark results

The energy accuracy is defined as:

$$\epsilon = \frac{E_{\text{VMC}} - E_{\text{DMRG}}}{|E_{\text{DMRG}} - \hbar\omega/2|} , \qquad (5.1)$$

where the term $\hbar\omega/2$ is subtracted from the denominator to account for any global energy shift in the Hamiltonian. The value of ϵ is reported for U/t=4 and U/t=10 in Fig. 5.1, where the electron-phonon coupling λ is varied, and $\hbar\omega=t=1$ is fixed.

We compare three different wave functions: the full wave function of Eq. (3.13) described in Section 3.2, a conventional Jastrow-Slater wave function with no phonon-backflow effect, and a wave function that includes phonon-backflow but lacks the electron-phonon Jastrow term \mathcal{J}_{ep} (i.e., where only the phonon-backflow terms inside the determinant enable correlation effects between electrons and phonons).

The best wave function, which includes both backflow correlations and Jastrow factors, achieves high accuracy ($\epsilon \approx 0.01$ for U/t = 4 and $\epsilon \approx 0.02$ for U/t = 10), significantly improving over the standard wave function without backflow terms. Since the backflow wave function is exact in the adiabatic limit ($\omega \to 0$) with U = 0, its accuracy is expected to decrease as U increases. However, the observed increase from $\epsilon \approx 0.01$ to ≈ 0.02 is still a notable achievement.

Interestingly, the electron-phonon Jastrow factor \mathcal{J}_{ep} , as defined in Eq. (3.22), plays a crucial role in the variational optimization. A substantial deterioration in accuracy is observed when this term is removed. For U/t=10, the accuracy of the backflow state without \mathcal{J}_{ep} is comparable to the standard Jastrow-Slater ansatz with no backflow but including \mathcal{J}_{ep} .

5.2 Half-filling results

In this section, we discuss the results at half-filling, focusing on our best variational Ansatz with backflow correlations. The properties of the SSH-Hubbard chain at half-filling have been extensively described in Chapter 2. We showed that, for a finite phonon frequency ω , varying the electron-electron repulsion U and the electron-phonon interaction λ leads to a ground state that is either a Mott insulator (uniform) or a Peierls insulator (dimerized). We will begin by presenting the phase diagram of the system and then focus on two representative points: one corresponding to the Mott insulator and one to the Peierls insulator. For these points, we will calculate and show a few correlation functions to better characterize the phases.

5.2.1 Phase diagram

Within our approach, the presence of a finite lattice distortion is indicated by the stabilization of a finite parameter z in Eq. (3.18), which describes a dimerized pattern around which the phonon displacements are distributed. In this case, the translational symmetry is explicitly broken in the variational wave function, and dimerization can also be detected by calculating the bond-order parameter:

$$B_{\rm e} = \frac{1}{L} \sum_{j=1}^{L} \sum_{\sigma} (-1)^j \langle \hat{c}_{j,\sigma}^{\dagger} \hat{c}_{j+1,\sigma} + \hat{c}_{j+1,\sigma}^{\dagger} \hat{c}_{j,\sigma} \rangle, \tag{5.2}$$

where the expectation value is taken over the variational state $|\Psi_{\text{var}}\rangle$.

The results are summarized in the phase diagram shown in Fig. 5.2, where we fix $\hbar\omega/t=1$. In this diagram, the trivial limits are $\lambda=0$, corresponding to the Mott insulator with no electron-phonon coupling, and U=0, corresponding to the Peierls insulator. The transition between these two phases is of the Kosterlitz-Thouless type [51]. As a result, it is extremely difficult to pinpoint the exact location of this transition in numerical calculations, since the spin gap of the Peierls phase is exponentially small near the transition. This issue is especially relevant in the vicinity of the non-interacting limit, $U=\lambda=0$, where large clusters are required to detect the tiny dimerization that exists as $\lambda\to 0$. Nevertheless, well away from the non-interacting limit, our variational approach can effectively distinguish between the two regimes: with and without bond order.

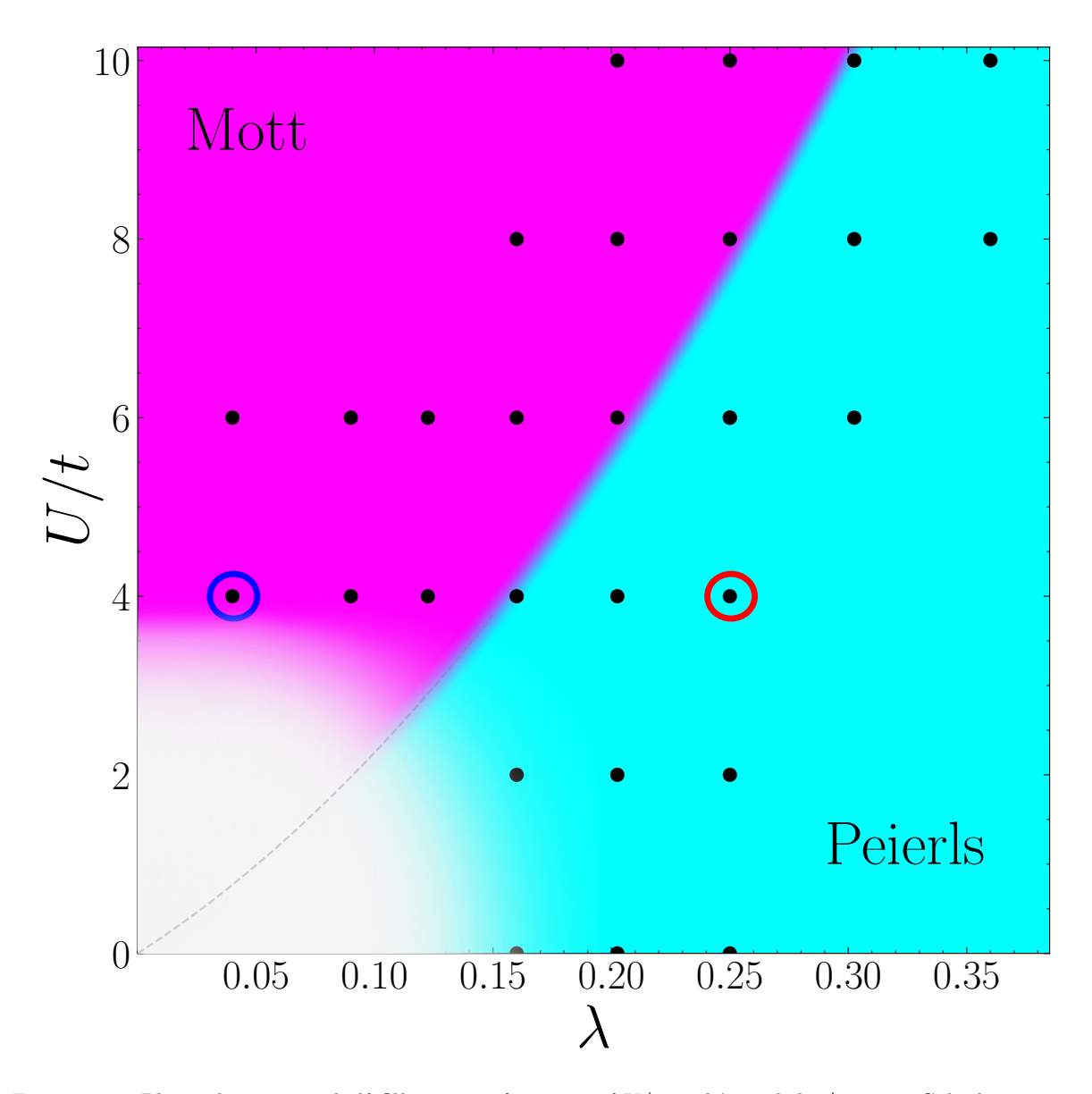


Figure 5.2: Phase diagram at half-filling as a function of U/t and λ with $\hbar\omega/t=1$. Calculations are performed on a chain with L=50 sites at the points marked by filled black circles. For $U/t\to 0$ and $\lambda\to 0$, distinguishing between Mott and Peierls insulators becomes extremely difficult, as indicated by the white region. The blue and red circles denote two points that will be examined in more detail in the following sections.

5.2.2 Static structure factors definition

The nature of the ground state can be inferred from equal-time correlation functions. We begin by defining the density, spin, and bond operators at site j as follows:

$$\hat{n}_j = \sum_{\sigma} \hat{c}^{\dagger}_{j,\sigma} \hat{c}_{j,\sigma}, \tag{5.3}$$

$$\hat{S}_{j}^{z} = \sum_{\sigma} s_{\sigma} \hat{c}_{j,\sigma}^{\dagger} \hat{c}_{j,\sigma}, \qquad (5.4)$$

$$\hat{b}_j = \sum_{\sigma} \left(\hat{c}_{j,\sigma}^{\dagger} \hat{c}_{j+1,\sigma} + \text{h.c.} \right), \tag{5.5}$$

where $s_{\sigma} = 1$ for spin-up and $s_{\sigma} = -1$ for spin-down.

Next, we define the density, spin, and bond structure factors as:

$$N(q) = \frac{1}{L} \sum_{m,j} e^{iq(m-j)} \langle \hat{n}_m \hat{n}_j \rangle, \qquad (5.6)$$

$$S(q) = \frac{1}{L} \sum_{m,j} e^{iq(m-j)} \langle \hat{S}_m^z \hat{S}_j^z \rangle, \qquad (5.7)$$

$$B(q) = \frac{1}{L} \sum_{m,j} e^{iq(m-j)} \langle \hat{b}_m \hat{b}_j \rangle.$$
 (5.8)

Structure factors provide valuable insights into the system's instabilities and the presence of gapless excitations.

Considering a generic operator \hat{O}_j and the corresponding structure factor $\mathcal{O}(q)$, the presence of long-range order with a given momentum Q for a certain correlation function [i.e., $\langle \hat{O}_m \hat{O}_n \rangle \sim C \ e^{iQ(m-n)}$ as $(m-n) \to \infty$] determines a peak at q=Q in the corresponding structure factor. The value of $\mathcal{O}(q=Q)$ will diverge with the system size L as $\mathcal{O}(Q) \sim C \ L$ and can be considered as an order parameter.

Power-law correlations in real space imply cusps in momentum space and the existence of gapless excitations in the corresponding sector. More specifically, for $\langle \hat{O}_m \hat{O}_n \rangle \sim \frac{e^{iQ(m-n)}}{|m-n|^{\alpha}}$ with $\alpha > 1$, there will be a divergence in the derivatives of $\mathcal{O}(q)$, which manifests as a cusp at q = Q. Slower power-law decays imply both singularities in the derivatives and a sublinear divergence of the structure factor with system size. For instance, $\langle \hat{O}_m \hat{O}_n \rangle \sim \frac{e^{iQ(m-n)}}{|m-n|}$ leads to $\mathcal{O}(Q) \sim \ln(L)$, and $\langle \hat{O}_m \hat{O}_n \rangle \sim \frac{e^{iQ(m-n)}}{|m-n|^{\alpha}}$ with $\alpha < 1$ corresponds to $\mathcal{O}(Q) \sim L^{1-\alpha}$.

In contrast, exponential decay of correlations in real space leads to smooth behavior in momentum space and gapped excitations.

For small values of q, the charge and spin structure factors exhibit specific scaling behaviors related to the spectrum of variational excited states of the form $|\Psi_{\text{var}}^q\rangle = \hat{n}_q |\Psi_{\text{var}}\rangle$, where $\hat{n}_q = \sum_j e^{iqj} \hat{n}_j$. Specifically:

- If $N(q) \sim q$ for $q \to 0$, the variational state $|\Psi_{\text{var}}^q\rangle$ has a vanishing energy for q = 0 in the thermodynamic limit, indicating a gapless charge excitation spectrum.
- If $N(q) \sim q^2$ for $q \to 0$, the charge excitation channel is gapped at q = 0.

The same applies to S(q), with a smooth quadratic decay in q for gapped spin excitations.

5.2.3 Mott and Peierls insulating states

We select two representative points from the phase diagram in Fig. 5.2, marked by the small blue and red circles. The results for U/t=4 are shown in Fig. 5.3 for two different regimes: $\lambda=0.04$ (Mott insulator, blue circle) and $\lambda=0.25$ (Peierls insulator, red circle). DMRG results, obtained on the same cluster size and optimized for the Hamiltonian with periodic boundary conditions, are also included for comparison.

The distinction between Mott and Peierls states is most clearly observed in the bond structure factor, which shows a huge peak at $q=\pi$ (i.e., $B(\pi)\approx 30$) in the Peierls case. This peak, which diverges with increasing system size, indicates the presence of dimerization. In the variational approach, this peak at $q=\pi$ arises due to the stabilization of a finite phonon parameter z [see Eq. (3.18)], representing a finite lattice distortion. In contrast, within the Mott state, $B(\pi)$ is much smaller, though it still exhibits a cusp that diverges logarithmically with system size. Since both the Mott and Peierls insulators exhibit a peak at $q=\pi$ in the bond structure factor $B(q=\pi)$, the presence of a Peierls phase is more readily identified by examining the parameter z [or equivalently $B_{\rm e}$, as defined in Eq. (5.2)] rather than considering the bond structure factor B(q) alone.

Next, we turn to the density and spin correlations. In both insulating phases, the density structure factor N(q) is smooth and shows quadratic behavior for small q, i.e., $N(q) \propto q^2$, indicating that charge excitations are gapped. For the spin structure factor, S(q) is also smooth and quadratic around the origin in the Peierls phase, suggesting gapped spin excitations. However, in the Mott phase S(q) is linear for small q and features a peak at $q = \pi$, which is expected to diverge logarithmically with system size, signaling the presence of gapless spin excitations.

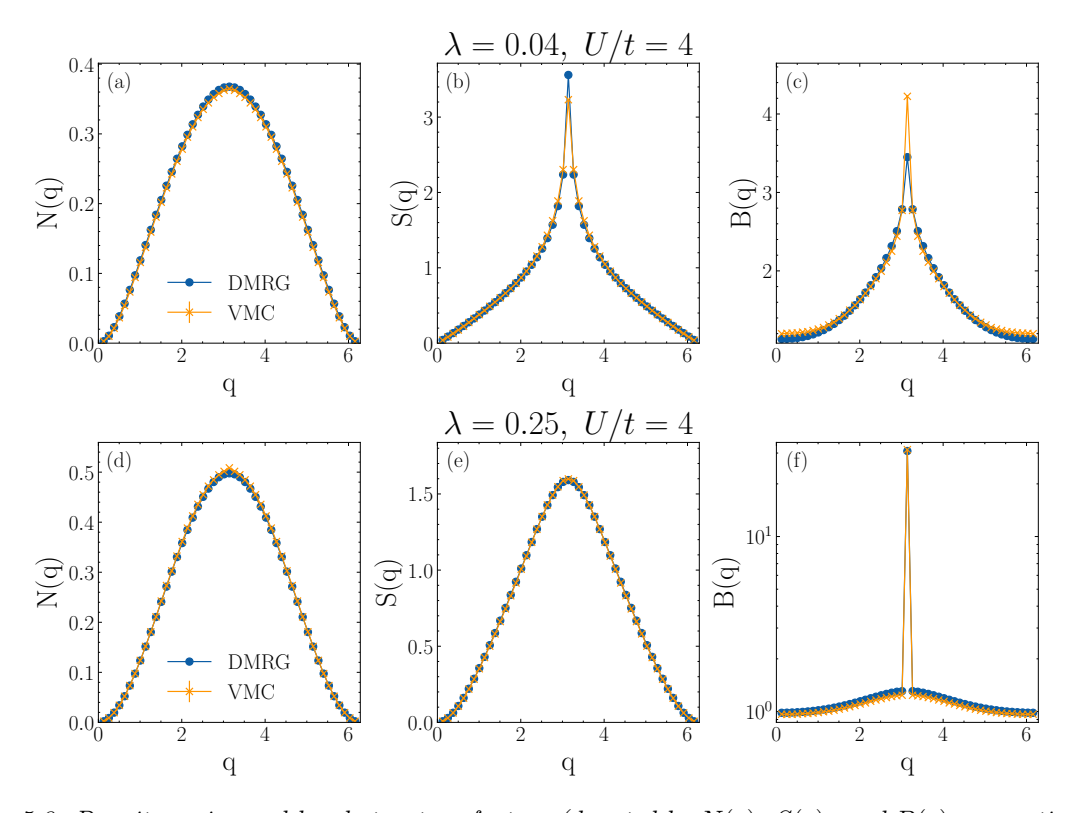


Figure 5.3: Density, spin, and bond structure factors (denoted by N(q), S(q), and B(q), respectively) at half-filling for L=50 sites, with U/t=4 and $\lambda=0.04$ (upper panels) and $\lambda=0.25$ (lower panels). The phonon energy is set to $\hbar\omega/t=1$. In each panel, variational results from the backflow wave function are compared to the ones obtained by DMRG calculations (optimized for the Hamiltonian with periodic boundary conditions).

5.3 Results away from half-filling

In this section, we investigate the behavior of the ground state in the doped regime, where the number of electrons N_e is less than the system size L, and the doping is defined as $\delta = 1 - N_e/L$. Throughout, we restrict our study to the subspace where the total spin projection is zero, i.e., $\sum_i \hat{S}_i^z = 0$, which implies $\sum_i n_{i,\uparrow} = \sum_i n_{i,\downarrow} = N_e/2$.

5.3.1 Doping the Mott insulator

Let us begin by doping the Mott insulator. In the Hubbard model, when only nearest-neighbor hopping t and the U-interaction are present, with no phonons included, the system enters a Luttinger liquid phase upon doping, characterized by gapless modes in both the charge and spin sectors. In this case, real-space correlations decay as a power law, and the corresponding structure factors show cusps at $q = 2k_F$ in momentum space, where $k_F = \frac{\pi(1-\delta)}{2}$.

These features are also present when phonons are included, as long as the Mott insulator remains stabilized at half-filling. The results for the doped Mott insulator are shown in Fig. 5.4, where we take the same parameters as in the Mott insulating state presented in the upper panel of Fig. 5.3; we consider three different doping levels, each requiring a new optimization procedure, and display the corresponding structure factors. The data reveal the characteristic cusps at $q = 2k_F$ in the variational calculations of both the density structure factor N(q) and the spin structure factor S(q). Notably, these cusps are less prominent in the density correlations obtained via DMRG, particularly as the system approaches half-filling. Nevertheless, the linear behavior of N(q) for small values of q strongly indicates the presence of gapless charge modes, confirming the metallic nature of the doped Mott state, even though the singularities at $q = 2k_F$ are less pronounced compared to those in the backflow wave function.

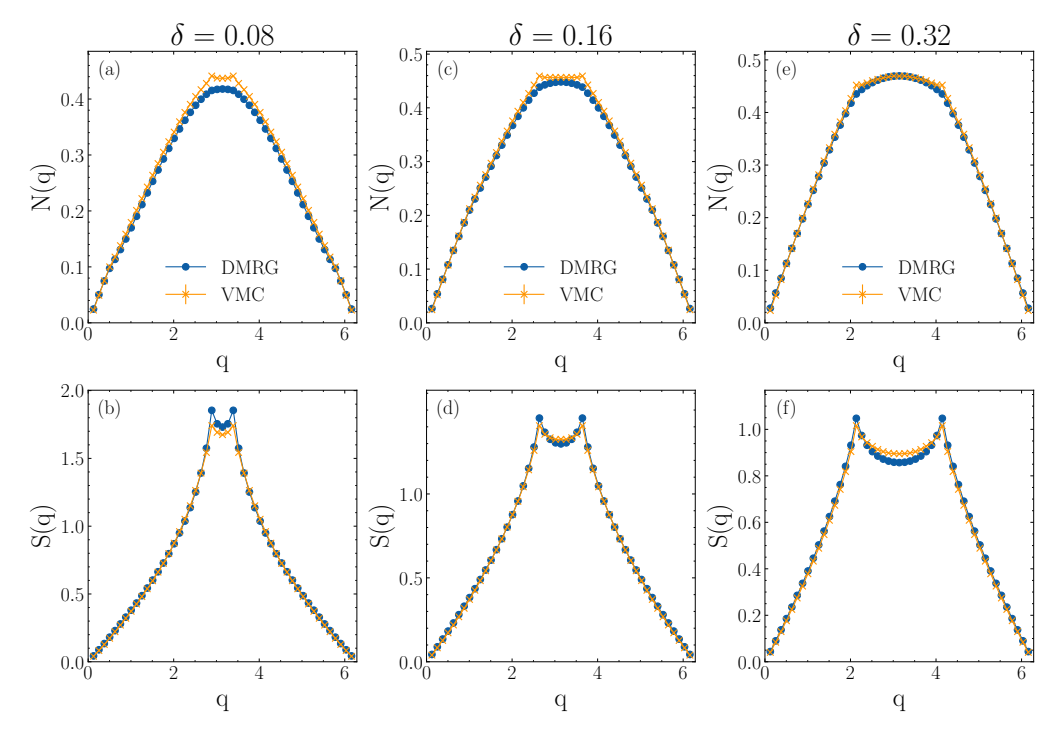


Figure 5.4: Density and spin structure factors for a chain with L=50 sites at various dopings δ , for U/t=4 and $\lambda=0.04$ (with $\hbar\omega/t=1$). At half-filling ($\delta=0$), the ground state is a Mott insulator. DMRG results (optimized for the Hamiltonian with periodic boundary conditions) are shown for comparison.

DMRG calculations become significantly more demanding in the doped regime compared to half-filling. However, the variance of the total energy remains consistently below $0.09t^2$.

5.3.2 Doping the Peierls insulator

The most interesting behavior is observed when doping the Peierls insulator. For small doping δ , the system transitions into a Luther-Emery liquid. Indeed, for $\delta > 0$ the system immediately turns into a metal, but the spin gap remains finite close to half-filling. As δ increases, the spin gap gradually decreases, eventually leading to a Luttinger liquid for sufficiently large doping.

This observation is particularly significant because the Luther-Emery state has been identified in repulsive models without phonons, emerging from a spin-gapped and dimerized insulator [57, 58, 59, 60, 61]. However, its stabilization has been argued to depend on the presence of multiple Fermi points in the non-interacting band structure. Only one notable exception to this has to be signaled: Ref. [62] suggested that the Luther-Emery liquid may emerge from doping an insulating phase with bond order obtained within a single-band Hubbard model in presence of both on-site and nearest-neighbor interactions.

In our case, the band structure is trivial, with only two Fermi points, and the spin gap is opened by the electron-phonon coupling. The Luther-Emery phase has remained elusive in the context of the SSH model with interacting electrons. To the best of our knowledge, only an early study [35], employing bosonization and renormalization-group methods, showed that a spin-gapped metal can emerge near half-filling due to phonon-assisted backward scattering.

The density and spin structure factors for the doped Peierls insulator are presented in Fig. 5.5, where we consider three different doping levels and show the corresponding structure factors (as before, we take the same parameters of the Peierls insulating state presented in the lower panel of Fig. 5.3, we consider three different doping levels, each requiring a new optimization procedure, and display the corresponding structure factors). The results show that a smooth S(q) persists in the doped system for small values of δ , before cusps appear at $q = 2k_F$. The existence of this spin-gapped metal is confirmed by DMRG calculations.

Interestingly, the Luther-Emery phase in the SSH-Hubbard model has not been observed before in other numerical studies, although its stability extends down to the U=0 limit. Evidence for this phase is shown in Fig. 5.6, where $\lambda=0.16$ and $\delta=0.08$ demonstrate the presence of a spin-gapped metal. Although determining the exact power-law decay of correlation functions is challenging due to their oscillatory behavior, bond-bond correlations appear to dominate in the Luther-Emery phase.

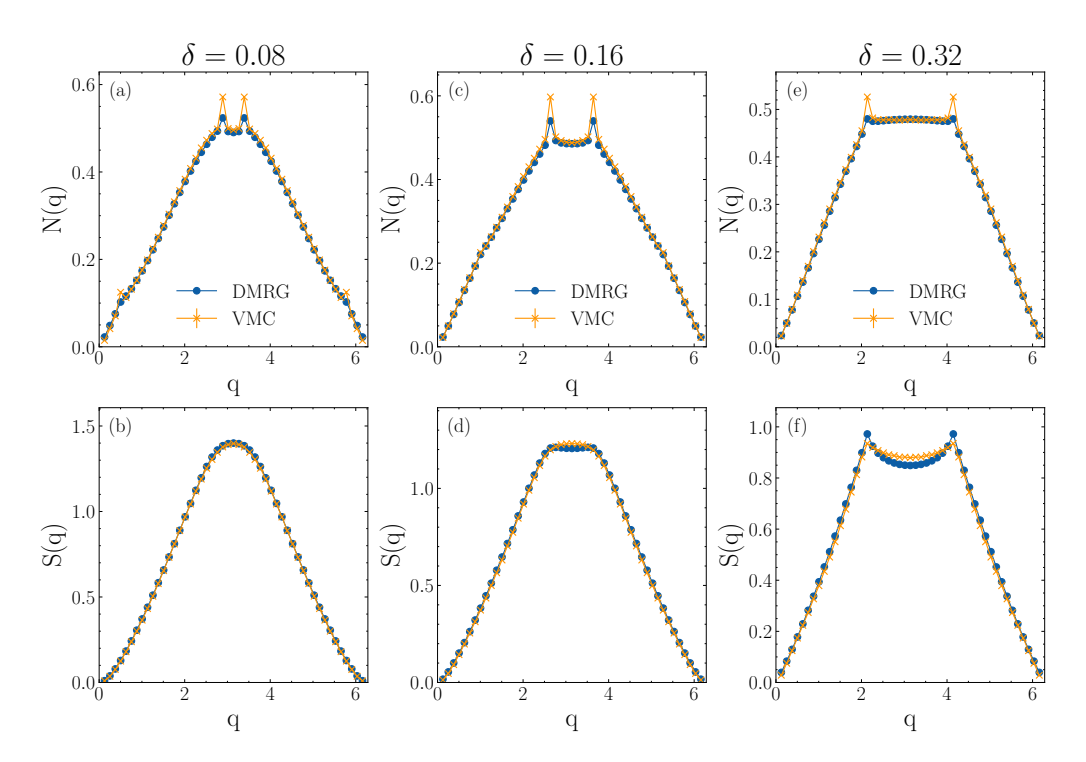


Figure 5.5: The same as in Fig. 5.4, but for U/t=4 and $\lambda=0.25$. At half-filling, the ground state is a Peierls insulator.

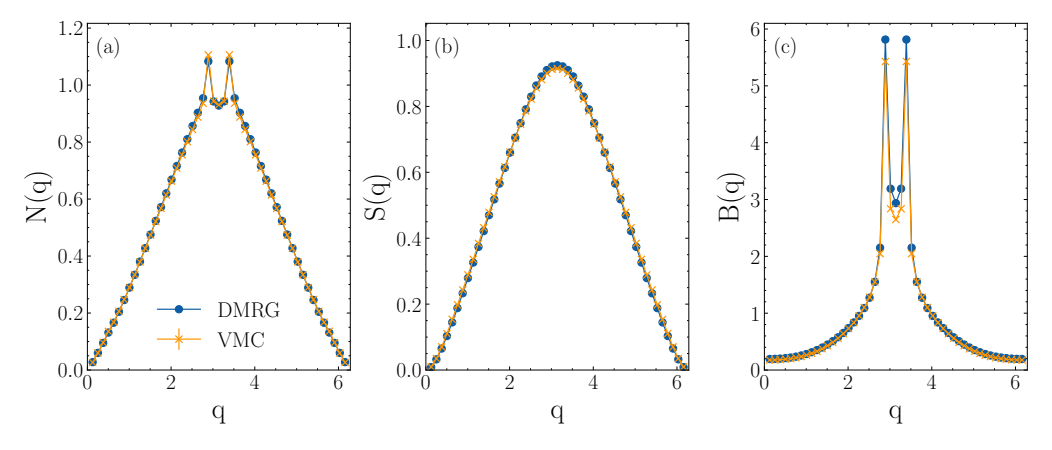


Figure 5.6: Density, spin, and bond structure factors for a chain with L=50 sites at $\delta=0.08$, for U=0 and $\lambda=0.16$ (with $\hbar\omega/t=1$). DMRG results (optimized for the Hamiltonian with periodic boundary conditions) are shown for comparison.

5.3.3 Luther-Emery Liquid: Phase Diagram, Phase Separation, and Size Scaling

By analyzing the singularities in the spin structure factor, we are able to construct a phase diagram as a function of electron doping δ . Specifically, we focus on the case where λ is varied and U/t=4 is fixed, as shown in Fig. 5.7. At $\delta=0$, the system is either a Mott insulator or a Peierls insulator. Upon introducing doping, a Luther-Emery metal emerges from doping the Peierls insulator at sufficiently large λ . As the doping concentration increases further, the system transitions into a Luttinger liquid, characterized by gapless spin excitations.

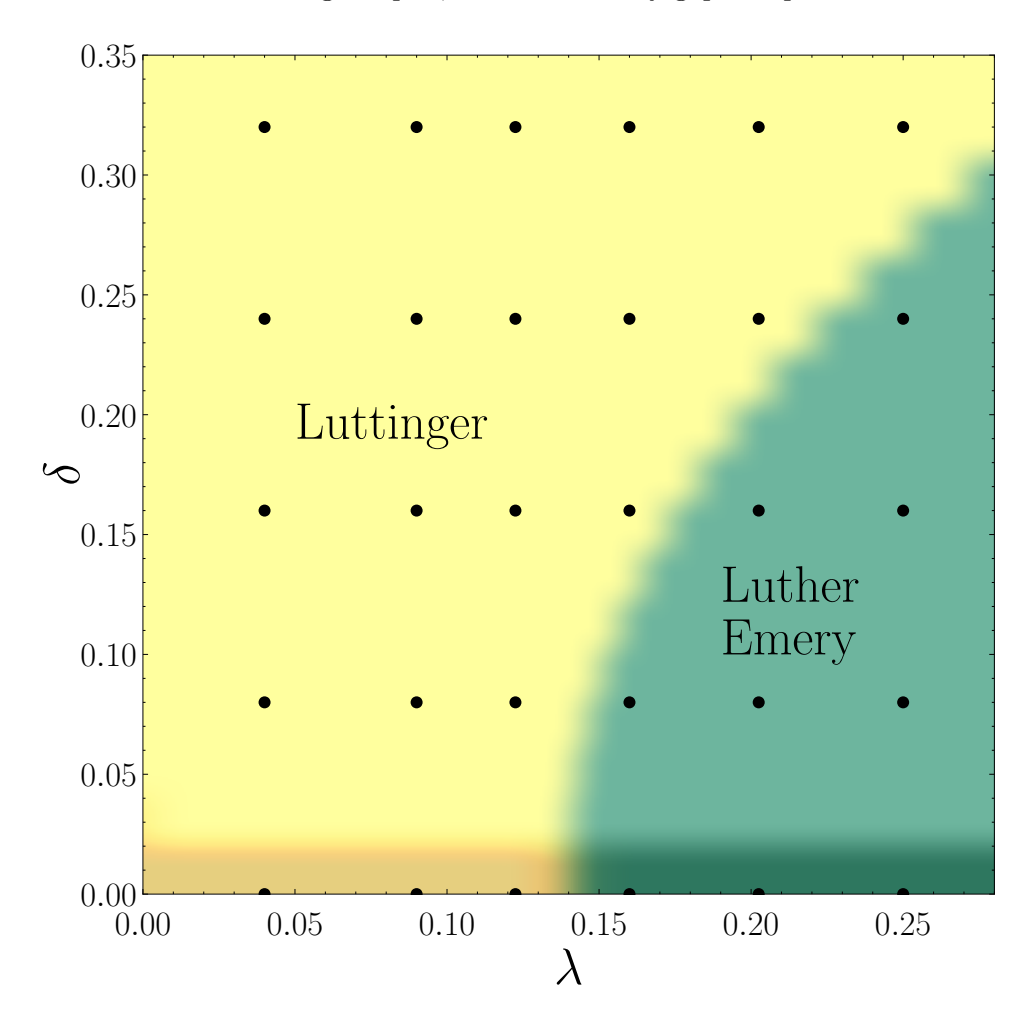


Figure 5.7: Phase diagram at U/t=4 as a function of λ and δ with $\hbar\omega/t=1$. Calculations are performed on a chain with L=50 sites, with data points represented by filled circles. The system is insulating at $\delta=0$, indicated by the shaded region at the bottom of the figure. For finite values of δ , a transition is observed from a Luttinger liquid to a Luther-Emery metallic phase.

To confirm the stability of the Luther-Emery phase and ensure that the spin gap persists as the system size increases, we perform a size-scaling analysis at $\lambda=0.25$ and $\delta=0.15$, which lies within the Luther-Emery phase. The structure factors for chains of length $L=40,\,80,$ and 120 are shown in Fig. 5.8. Remarkably, the spin structure factor does not exhibit significant changes with system size, which indicates the stability of the Luther-Emery phase even for large systems, and eventually in the thermodynamic limit.

For U/t = 4, we rule out the presence of phase separation in both the Luttinger and Luther-Emery phases within the λ and δ range shown in Fig. 5.7. This conclusion is supported by DMRG simulations, which yield the expected convex behavior of the energy as a function of electron doping. VMC results, although very accurate for the Peierls insulator, show a tiny region of phase separation near half-filling in the Luther-Emery phase. However, this is mainly due to the different accuracy of VMC energies, which is very high in the Peierls insulator and slightly worse for small values of δ , while still capturing the correct physical behavior.

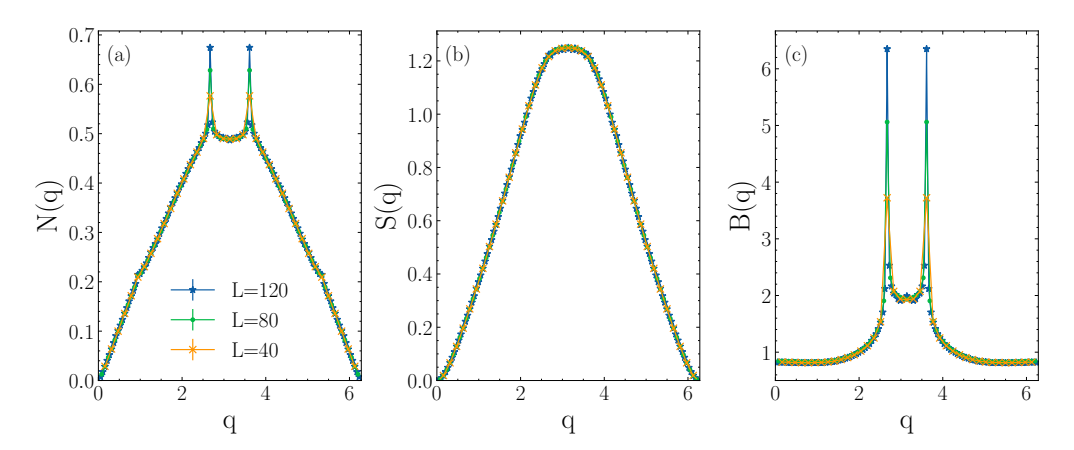


Figure 5.8: Density, spin, and bond structure factors for a Luther-Emery metal at $\lambda=0.25$ and $\delta=0.15$. The quantities are shown for chains of length $L=40,\,80,\,$ and 120. No significant changes are observed in the spin structure factors, confirming that the Luther-Emery liquid survives in the large-chain limit. The peaks of the charge and bond structure factors at $2k_F$ diverge sub-linearly with the system size.

5.4 Changing the SSH Coupling to prevent sign changes of the hopping amplitude

In this section, we address the issue of sign changes in the hopping amplitudes when modeling electron-phonon coupling through SSH-like terms. In the original SSH model, the electron-phonon interaction is linear, meaning that the hopping amplitude between neighboring sites i and i+1 depends linearly on the displacement between neighboring phonon sites. Specifically, the hopping amplitude is given by:

$$t\left[1 - \alpha(x_{i+1} - x_i)\right]$$
 (5.9)

However, this linear dependence can lead to unphysical behavior when the term $\alpha(x_{i+1} - x_i)$ becomes too large. In particular, two related problems may arise:

- A milder issue occurs when $\alpha(x_{i+1} x_i)$ becomes large but remains smaller than 1. In this case, the linear coupling loses its validity, and non-linear terms would be necessary to maintain a correct description of the physical system.
- A more severe issue arises when $\alpha(x_{i+1}-x_i)$ exceeds 1, which causes the hopping amplitude to become negative. This would imply that electrons are unable to move from one site to the next, which is clearly unphysical.

These problems become particularly relevant when the system enters the Peierls insulating phase in the SSH-Hubbard model at half-filling. In this phase, characterized by bond-order wave (BOW) formation, the phonon distortions lead to $\langle x_i \rangle = (-1)^i \Delta$, where the value of Δ increases as the BOW grows. This behavior is illustrated in Fig. 5.9, which shows the observable $\alpha \langle \Delta x \rangle = \alpha \sum_{i}^{even} \langle \hat{x}_{i+1} - \hat{x}_i \rangle$ as a function of λ for U/t = 4 at half-filling, based on data from our VMC

simulations for a L=50 oSSH-Hubbard chain. As the system enters the Peierls phase, $\alpha \langle \Delta x \rangle$ increases rapidly, soon exceeding 1, which leads to sign changes of the hopping amplitudes in a significant fraction of configurations sampled during the Monte Carlo simulation.

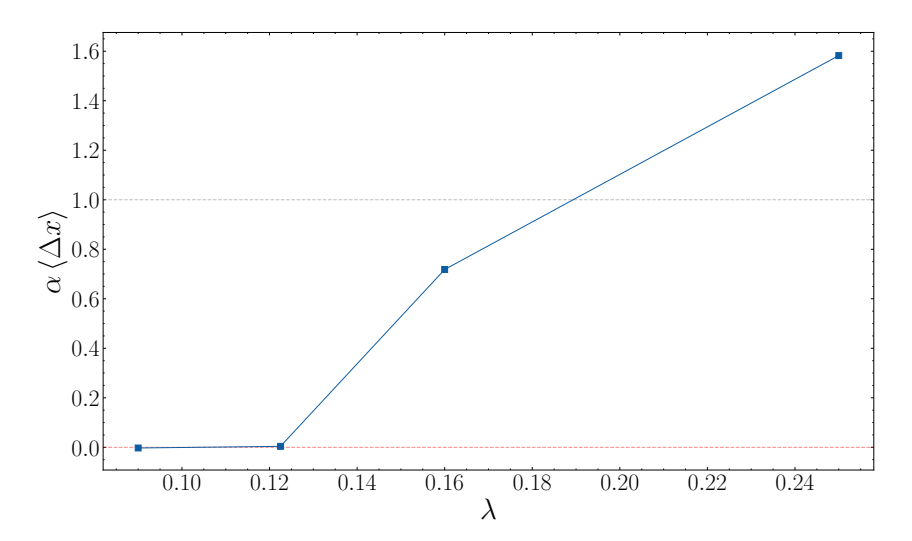


Figure 5.9: VMC results for a L=50 chain, showing $\alpha \langle \Delta x \rangle = \alpha \sum_{i}^{even} \langle \hat{x}_{i+1} - \hat{x}_i \rangle$ as a function of λ for U/t=4 at half-filling. The points shown here correspond to the same points displayed in the phase diagram of Fig. 5.2 at U/t=4. The Peierls transition occurs between $\lambda=0.12$ and $\lambda=0.16$, showing a rapid increase of $\alpha \langle \Delta x \rangle$.

To resolve the sign-change problem, we modify the SSH coupling by introducing a regularized form for the coupling term, ensuring that the hopping amplitude remains positive. The modified Hamiltonian is expressed as:

$$\hat{H} = -t \sum_{i,\sigma} f_{\alpha} \left(\hat{x}_{i+1} - \hat{x}_{i} \right) \left(\hat{c}_{i,\sigma}^{\dagger} \hat{c}_{i+1,\sigma} + \hat{c}_{i+1,\sigma}^{\dagger} \hat{c}_{i,\sigma} \right) . \tag{5.10}$$

Here, the function $f_{\alpha}(x)$ is chosen to maintain a positive, differentiable, and smooth hopping amplitude. Specifically, we define $f_{\alpha}(x)$ as:

$$f_{\alpha}(x) = \begin{cases} 1 - \alpha \cdot x & \text{if } x < 0, \\ \left(1 + \frac{\alpha}{2} \cdot x\right)^{-2} & \text{if } x > 0. \end{cases}$$
 (5.11)

The functional form of $f_{\alpha}(x)$ is illustrated in Fig. 5.10, and its design was inspired by Ref. [74], which discusses the same problem of unphysical sign-change in SSH model.

Our backflow wave function is fully capable of representing the ground state of the modified Hamiltonian in Eq. (5.10) with the same accuracy as when using the original SSH Hamiltonian, at least in principle. The reason is that, since $f_{\alpha}(x)$ is a smooth function, introducing the corresponding backflow term to account for phonon displacements costs the same as the original backflow term in the case of the linear SSH coupling.

The new backflow term corresponds to the ground state of the following auxiliary Hamiltonian (see Eq. (3.17) to compare it with the conventional backflow case):

$$\hat{H}_{ep} = \hat{H}_0 - \sum_{i,\sigma} f_g (x_i - x_{i+1}) \left(\hat{c}_{i,\sigma}^{\dagger} \hat{c}_{i+1,\sigma} + \hat{c}_{i+1,\sigma}^{\dagger} \hat{c}_{i,\sigma} \right) , \qquad (5.12)$$

where f_g has the same functional form shown in Eq. (5.11) and g is a variational parameter.

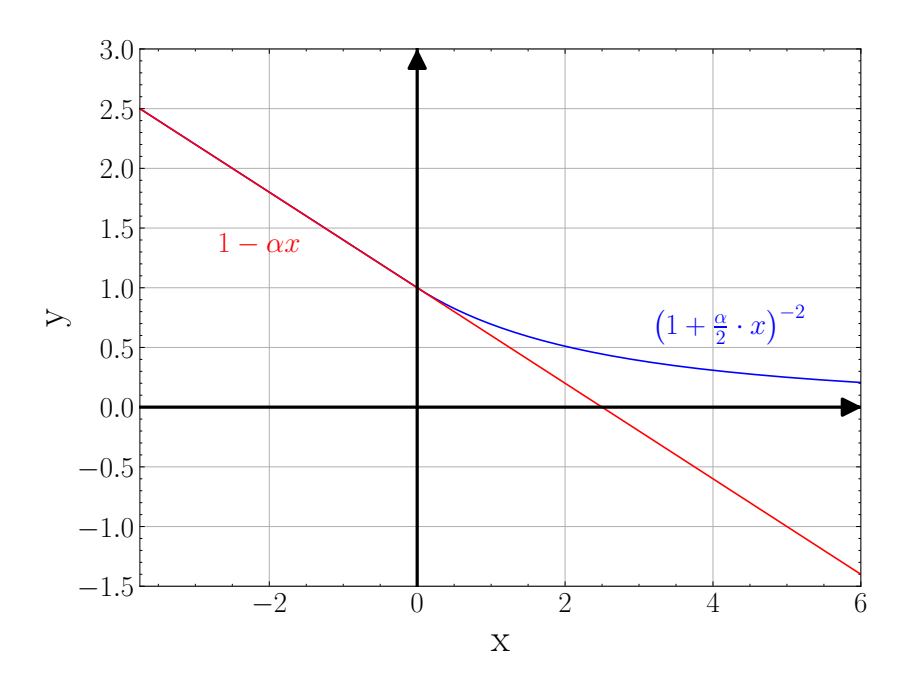


Figure 5.10: Plot of the regularized SSH coupling $f_{\alpha}(x)$ defined in Eq. (5.11) as a function of x. The function ensures that the hopping amplitude remains positive, smooth, and differentiable. In red one can see the original SSH coupling $1 - \alpha x$ and in blue its regularization for x > 0, as described in Eq. (5.11).

In contrast, DMRG methods would struggle with the Hamiltonian in Eq. (5.10), since the method relies on describing bosonic degrees of freedom through creation and annihilation operators [as seen in Eq. (3.14)]. This approach greatly benefits from the linear nature of the $\hat{x}_{i+1} - \hat{x}_i$ term, which can be expressed as a linear combination of four creation and annihilation operators.

The Hamiltonian in Eq. (5.10) can be seen as a regularization of the original oSSH-Hubbard Hamiltonian in Eq. (2.1), since it depends on the same parameter α . It is therefore reasonable to take some points of the phase diagram of Fig. 5.2 and show the corresponding structure factors for the original oSSH-Hubbard Hamiltonian and for the regularized version, where the SSH coupling is given via $f_{\alpha}(x)$ of Eq. (5.11). We also include the DMRG results for the original Hamiltonian to provide an understanding of the bias introduced by our variational wave function.

The results for $t=\hbar\omega=1$, U/t=4, and $\lambda=0.09$ (upper panel, Mott insulator) and $\lambda=0.25$ (lower panel, Peierls insulator) on a L=50 chain are shown in Fig. 5.11. In the Mott insulating phase, the backflow wave function tends to overestimate the peak at $B(q=\pi)$ compared to DMRG results. The regularized Hamiltonian mitigates this effect slightly, but the change is small. In the Peierls insulating phase, the regularized Hamiltonian reduces the BOW strength by slightly lowering the peak at $B(q=\pi)$, but again, the effect is mild.

Overall, we find that preventing sign changes in the SSH coupling does not significantly reduce the strong phonon distortion effect for large λ . The phonon distortion remains nearly identical regardless of the modification, and the phase diagram still contains a large portion of the BOW region that becomes unphysical due to large phonon displacements.

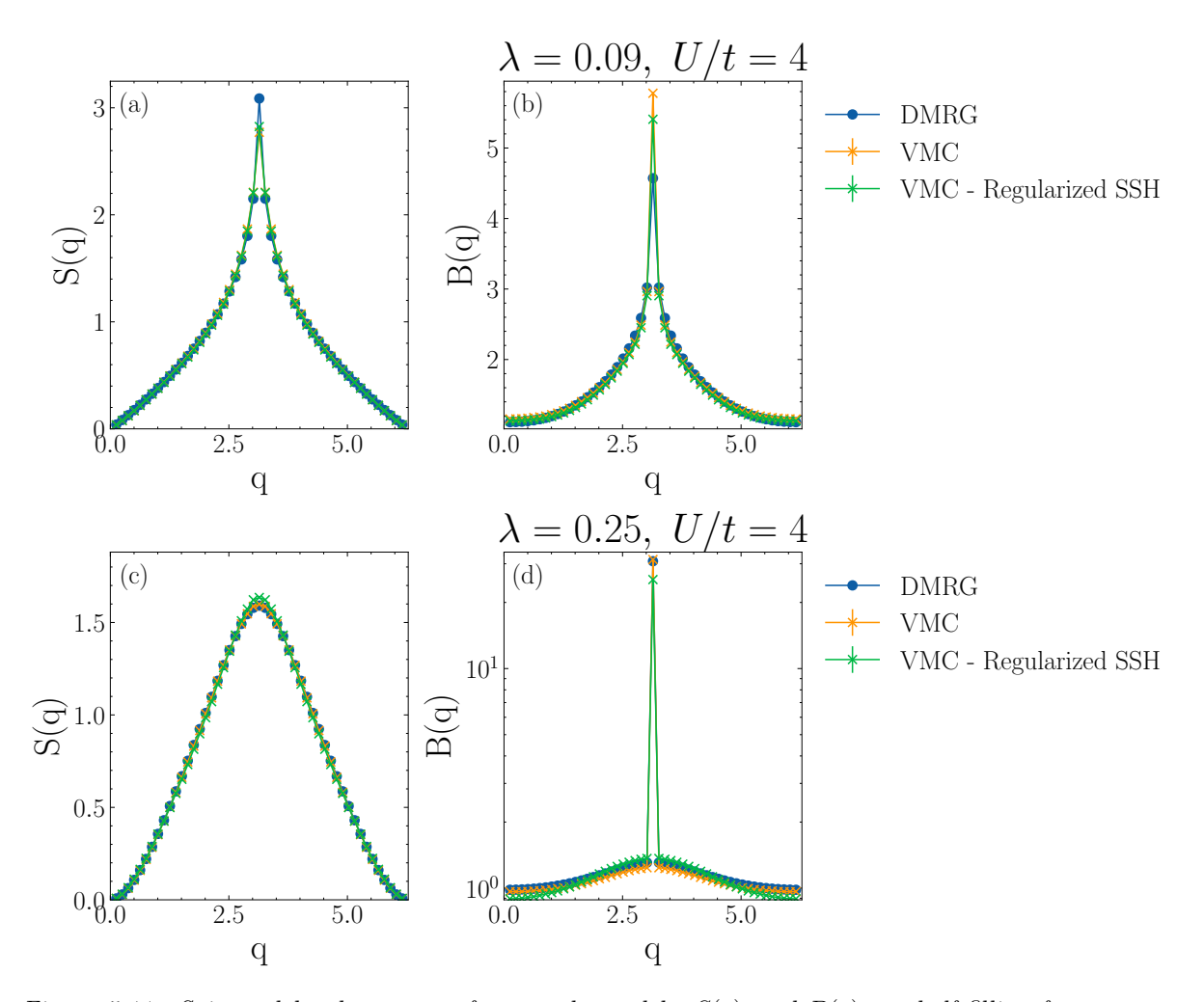


Figure 5.11: Spin and bond structure factors, denoted by S(q) and B(q), at half-filling for a system with L=50 sites. Results are shown for U/t=4 and $\lambda=0.09$ (upper panels) and $\lambda=0.25$ (lower panels), with the phonon energy set to $\hbar\omega/t=1$. The variational results from the backflow wave function are compared to DMRG results, along with results from another backflow wave function optimized for a regularized oSSH Hamiltonian. In this case, the SSH coupling is defined by $f_{\alpha}(x)$ as given in Eq. (5.11).

Chapter 6

Square lattice SSH-Hubbard model at half-filling

In this chapter, we study the physical properties of the SSH-Hubbard model on a square lattice at half-filling. We primarily focus on different implementations of the SSH coupling and on the limiting cases of the model (zero-phonon frequency and infinite frequency). In this way, we provide an overview of the current understanding of this model and discuss various results from the literature.

We begin by introducing the SSH-Hubbard Hamiltonian in two dimensions and exploring alternative definitions of the electron-phonon coupling in Sec. 6.1. Specifically, we consider models for acoustic phonons, site-centered optical phonons, and bond-centered optical phonons, corresponding to the aSSH, oSSH, and bSSH models, respectively. Next, we examine the infinite-mass/zero-frequency (adiabatic) limit in Section 6.2, where we highlight peculiar differences in the dimerization pattern of the aSSH model, in contrast to the similar pattern observed in both the oSSH and bSSH models. We then turn our attention to the anti-adiabatic limit (vanishing mass/infinite frequency) in Section 6.3. Finally, Section 6.4 discusses the case of quantum phonons with finite mass.

In contrast to the one-dimensional case, where for $\omega \to 0$ only a phase with finite lattice distortions is present, on the square lattice an undistorted phase exists when U > 0 for any phonon frequency, even in the adiabatic limit of $\omega \to 0$. The undistorted phase, present when the Hubbard interaction U dominates, is characterized by antiferromagnetic (AFM) order. The other phase displays bond-order wave (BOW) corresponding to finite phonon distortions. The literature suggests that a coexistence region between these two phases may exist.

6.1 The Hamiltonians

We start by presenting the Hamiltonian for the square lattice oSSH-Hubbard model, which incorporates site-centered optical phonons. To extend the SSH-Hubbard model to a two-dimensional square lattice, we introduce phonons along both the x and y directions. In this framework, each site hosts two phonon modes: one corresponding to the x direction and the other to the y direction, with each mode modeled as a quantum harmonic oscillator. The Hamiltonian for the

oSSH-Hubbard model is given by:

$$\hat{H} = - t \sum_{R,\sigma} \left[1 - \alpha \left(\hat{x}_{R+e_x} - \hat{x}_R \right) \right] \left(\hat{c}_{R,\sigma}^{\dagger} \hat{c}_{R+e_x,\sigma} + \hat{c}_{R+e_x,\sigma}^{\dagger} \hat{c}_{R,\sigma} \right) + \\
- t \sum_{R,\sigma} \left[1 - \alpha \left(\hat{y}_{R+e_y} - \hat{y}_R \right) \right] \left(\hat{c}_{R,\sigma}^{\dagger} \hat{c}_{R+e_y,\sigma} + \hat{c}_{R+e_y,\sigma}^{\dagger} \hat{c}_{R,\sigma} \right) + \\
+ \sum_{R} \left[\frac{\hat{p}_{x,R}^2}{2m} + \frac{1}{2} m \omega^2 \hat{x}_R^2 \right] + \sum_{R} \left[\frac{\hat{p}_{y,R}^2}{2m} + \frac{1}{2} m \omega^2 \hat{y}_R^2 \right] + U \sum_{R} \hat{n}_{R,\uparrow} \hat{n}_{R,\downarrow} , \quad (6.1)$$

where R=(i,j) denotes the coordinates of a site on the square lattice, $\hat{c}_{R,\sigma}^{\dagger}$ creates an electron at site R with spin σ , and \hat{x}_R , $\hat{p}_{x,R}$, \hat{y}_R , $\hat{p}_{y,R}$ are the position and momentum operators for the two phonon modes at site R. The usual commutation relations hold:

$$[\hat{x}_R, \hat{p}_{x,S}] = i\hbar \delta_{R,S} , \qquad [\hat{y}_R, \hat{p}_{y,S}] = i\hbar \delta_{R,S} , \qquad (6.2)$$

while all other commutators vanish.

Another possible effective model contains acoustic phonon modes. In this case, the two-dimensional aSSH-Hubbard model is obtained:

$$\hat{H} = -t \sum_{R,\sigma} \left[1 - \alpha \left(\hat{x}_{R+e_x} - \hat{x}_R \right) \right] \left(\hat{c}_{R,\sigma}^{\dagger} \hat{c}_{R+e_x,\sigma} + \hat{c}_{R+e_x,\sigma}^{\dagger} \hat{c}_{R,\sigma} \right) + \\
- t \sum_{R,\sigma} \left[1 - \alpha \left(\hat{y}_{R+e_y} - \hat{y}_R \right) \right] \left(\hat{c}_{R,\sigma}^{\dagger} \hat{c}_{R+e_y,\sigma} + \hat{c}_{R+e_y,\sigma}^{\dagger} \hat{c}_{R,\sigma} \right) + U \sum_{R} \hat{n}_{R,\uparrow} \hat{n}_{R,\downarrow} + \\
+ \sum_{R} \left[\frac{\hat{p}_{x,R}^2}{2m} + \frac{1}{2} m \omega^2 \left(\hat{x}_{R+e_x} - \hat{x}_R \right)^2 \right] + \sum_{R} \left[\frac{\hat{p}_{y,R}^2}{2m} + \frac{1}{2} m \omega^2 \left(\hat{y}_{R+e_y} - \hat{y}_R \right)^2 \right] , \tag{6.3}$$

where the operators are the same as those of the oSSH case.

Finally, the bSSH-Hubbard model is frequently adopted in numerical studies due to its relatively simpler implementation. This model incorporates bond-centered optical phonons:

$$\hat{H} = -t \sum_{R,\sigma} \left[1 - \alpha \, \hat{x}_{(R,R+e_x)} \right] \left(\hat{c}_{R,\sigma}^{\dagger} \hat{c}_{R+e_x,\sigma} + \hat{c}_{R+e_x,\sigma}^{\dagger} \hat{c}_{R,\sigma} \right) + \\
- t \sum_{R,\sigma} \left[1 - \alpha \, \hat{y}_{(R,R+e_y)} \right] \left(\hat{c}_{R,\sigma}^{\dagger} \hat{c}_{R+e_y,\sigma} + \hat{c}_{R+e_y,\sigma}^{\dagger} \hat{c}_{R,\sigma} \right) + U \sum_{R} \hat{n}_{R,\uparrow} \hat{n}_{R,\downarrow} + \\
+ \sum_{R} \left[\frac{\hat{p}_{x,(R,R+e_x)}^2}{2m} + \frac{1}{2} m \omega^2 \hat{x}_{(R,R+e_x)}^2 \right] + \sum_{R} \left[\frac{\hat{p}_{y,(R,R+e_y)}^2}{2m} + \frac{1}{2} m \omega^2 \hat{y}_{(R,R+e_y)}^2 \right] , \tag{6.4}$$

where each phonon mode is attached to a bond between neighboring sites.

In all of these models, a phase transition occurs from the AFM phase to the BOW phase, depending on whether the Hubbard electron-electron interaction or the electron-phonon coupling predominates.

6.2 Adiabatic limit

In this section, we consider the two-dimensional SSH-Hubbard model in the adiabatic limit, where the phonon degrees of freedom are treated as classical variables with infinite mass, i.e., $m \to \infty$ and $\omega \to 0$, while keeping the elastic constant $K = m\omega^2$ finite. This limit was discussed

for the one-dimensional case in Section 2.3. The Hamiltonian of the oSSH model in Eq. (6.2) becomes

$$\hat{H} = -t \sum_{R,\sigma} \left[1 - \alpha \left(x_{R+e_x} - x_R \right) \right] \left(\hat{c}_{R,\sigma}^{\dagger} \hat{c}_{R+e_x,\sigma} + \hat{c}_{R+e_x,\sigma}^{\dagger} \hat{c}_{R,\sigma} \right) +$$

$$- t \sum_{R,\sigma} \left[1 - \alpha \left(y_{R+e_y} - y_R \right) \right] \left(\hat{c}_{R,\sigma}^{\dagger} \hat{c}_{R+e_y,\sigma} + \hat{c}_{R+e_y,\sigma}^{\dagger} \hat{c}_{R,\sigma} \right) +$$

$$+ \sum_{R} \left[\frac{K}{2} x_R^2 + \frac{K}{2} y_R^2 \right] + U \sum_{R} \hat{n}_{R,\uparrow} \hat{n}_{R,\downarrow} ,$$

$$(6.5)$$

where the phonon displacements $\{x_R\}$ and $\{y_R\}$ are classical fields, and the electronic problem depends parametrically on their configuration. As in the one-dimensional case, a common approach is to compare different variational ansätze for the phonon displacements and identify the one yielding the lowest total energy.

6.2.1 Single mode distorsions

A straightforward strategy to determine the distortion pattern favored by the system is to restrict the analysis to single-parameter patterns and compare their energies [see Section 2.3].

An early study by Tang and Hirsch [67] showed that, in the non-interacting limit (U=0), the two-dimensional SSH model is unstable towards a bond-order-wave (BOW) phase. This analysis of the two-dimensional case follows a similar approach to the treatment of the Peierls instability in the one-dimensional SSH model, as presented in Section 2.3.1, but with the additional complexity of considering several dimerization patterns in two dimensions. In each case, the phonon displacement fields in the x and y directions are defined according to the ordering vectors Q^x and Q^y as

$$x_R = \Delta_x \cos(Q^x \cdot R) , \qquad y_R = \Delta_y \cos(Q^y \cdot R) , \qquad (6.6)$$

where Δ_x and Δ_y are variational parameters to be optimized. This ansatz is written here for the oSSH model.

Tang and Hirsch considered the following four single-mode patterns:

Dimerization pattern	Q^x	Q^y	Δ_x	Δ_y
Columnar order in the x-direction	$(\pi,0)$	_	Δ	0
Plaquette order	$(\pi,0)$	$(\pi,0)$	Δ	Δ
(π,π) order in the x-direction	(π,π)	_	Δ	0
Staircase order	(π,π)	(π,π)	Δ	Δ

The columnar and (π, π) orders listed here are taken along the x-direction; an equivalent choice would have been to consider them in the y-direction. The four patterns are illustrated in Fig. 6.1.

Analytical results for U=0 of Ref. [67] show that the (π,π) order is the most energetically favorable. As in the one-dimensional SSH model in the adiabatic limit, dimerization occurs for any non-zero value of the electron-phonon coupling α .

When the on-site Hubbard repulsion U is included, the two-dimensional SSH model enters an undistorted phase in the large-U regime, characterized by AFM order. This behavior contrasts with the one-dimensional case, where the ground state is always dimerized in the adiabatic limit, regardless of the value of the Hubbard interaction U. A subsequent study on the square-lattice SSH-Hubbard model in the adiabatic limit, employing Hartree-Fock and slave boson methods, confirmed the transition from the AFM phase to the (π, π) BOW phase and identified a coexistence region [68].

Finally, we note that the analysis in this section was performed for the oSSH-Hubbard model. However, the ansatz given by Eq. (6.6) can be easily reformulated for both the bSSH and aSSH models. It is important to emphasize that, for any of the four single-mode patterns listed above, the oSSH, bSSH, and aSSH models become equivalent, up to trivial rescaling of α and K, as discussed in Section 2.3 for the one-dimensional case. This equivalence holds only after imposing the single-mode ansatz; the full models are not identical.

Furthermore, while the single-mode analysis correctly captures the dimerization pattern in the oSSH and bSSH models ¹, in the aSSH case the (π, π) configuration represents only a local energy minimum, as shown in the next section.

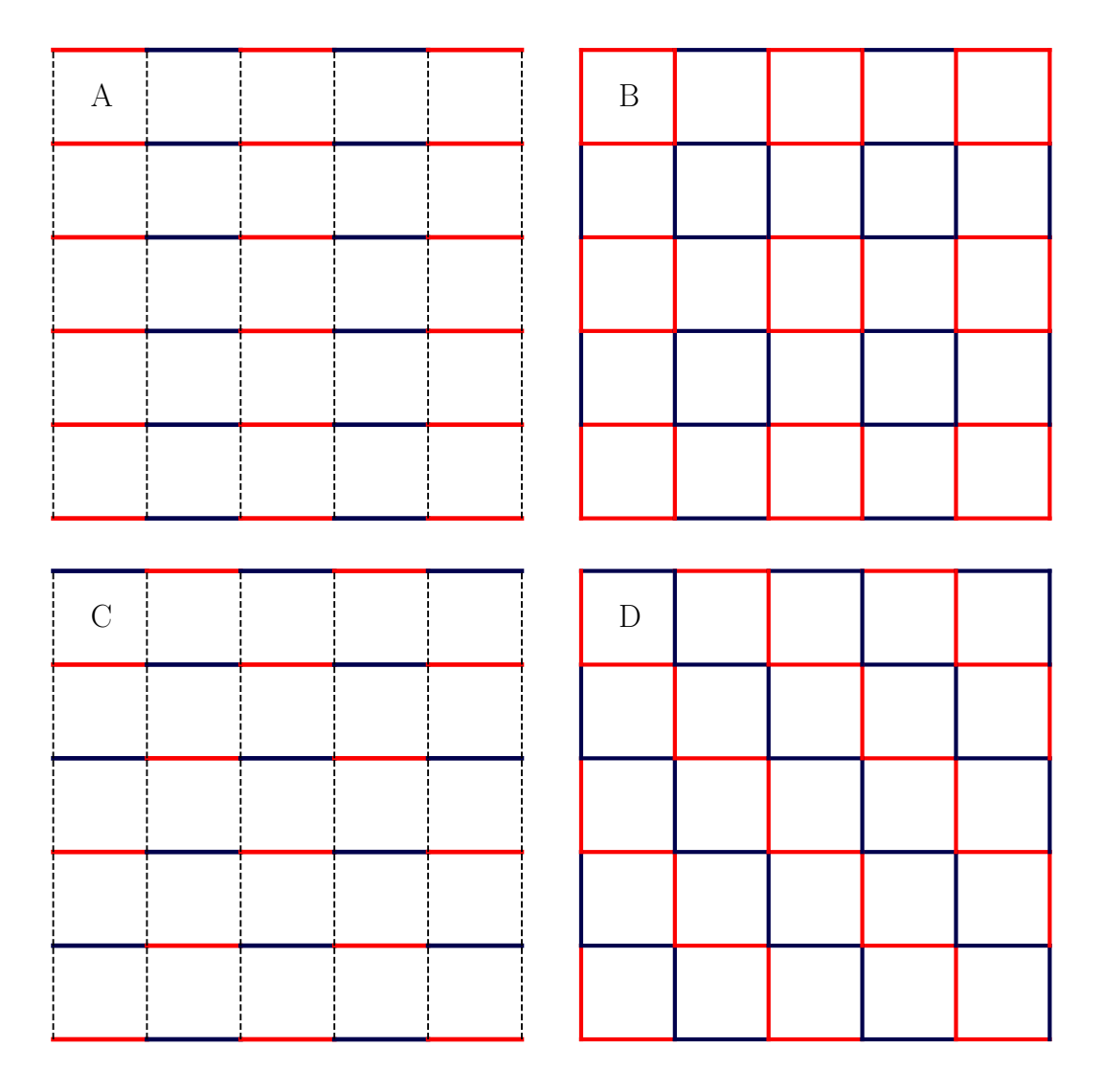


Figure 6.1: Four dimerization patterns on a 6×6 lattice. Bonds crossing the periodic boundaries are not shown. The hopping amplitude on each bond is indicated by color: blue bonds represent short (and stronger) bonds, red bonds represent long (and weaker) bonds, and dotted bonds are undistorted. From left to right and top to bottom: (A) Columnar order, (B) Plaquette order, (C) (π, π) order, and (D) Staircase order.

¹Actually, in the oSSH model, for large values of the coupling α , the favored pattern becomes another single mode ansatz not included in the previous analysis, having $Q_x = (\pi, \pi)$, $Q_y = (0, \pi)$ and finite Δ_x and Δ_y .

6.2.2 Multimode Peierls distortions in the adiabatic limit for the aSSH model

As discussed in the previous section, the single-mode ansatz provides a reliable description of the energetically favored distortion pattern for the oSSH and bSSH models. However, in the case of the aSSH model, this is not the case: as first noted in Ref. [63], the ground state in the adiabatic limit is not a single-mode distortion, but instead exhibits a more complex multimode pattern.

The Hamiltonian of the aSSH model in the adiabatic limit at U=0 is:

$$\hat{H} = -t \sum_{R,\sigma} \left[1 - \alpha \left(x_{R+e_x} - x_R \right) \right] \left(\hat{c}_{R,\sigma}^{\dagger} \hat{c}_{R+e_x,\sigma} + \hat{c}_{R+e_x,\sigma}^{\dagger} \hat{c}_{R,\sigma} \right) + \\
- t \sum_{R,\sigma} \left[1 - \alpha \left(y_{R+e_y} - y_R \right) \right] \left(\hat{c}_{R,\sigma}^{\dagger} \hat{c}_{R+e_y,\sigma} + \hat{c}_{R+e_y,\sigma}^{\dagger} \hat{c}_{R,\sigma} \right) + \\
+ \frac{K}{2} \sum_{R} \left[\left(x_{R+e_x} - x_R \right)^2 + \left(y_{R+e_y} - y_R \right)^2 \right] .$$
(6.7)

A simple way to illustrate the multimode nature of the optimal distortion is to consider a *bimode* ansatz:

$$x_{R+e_x} - x_R = a_Q \cos(Q \cdot R) + a_{Q/2} \cos[(Q \cdot R)/2]$$

$$y_{R+e_y} - y_R = a_Q \cos(Q \cdot R) - a_{Q/2} \cos[(Q \cdot R)/2],$$
(6.8)

where $Q = (\pi, \pi)$ and a_Q , $a_{Q/2}$ are variational parameters. Substituting this ansatz into Eq. (6.7), the resulting tight-binding Hamiltonian can be diagonalized at half filling to evaluate the total energy.

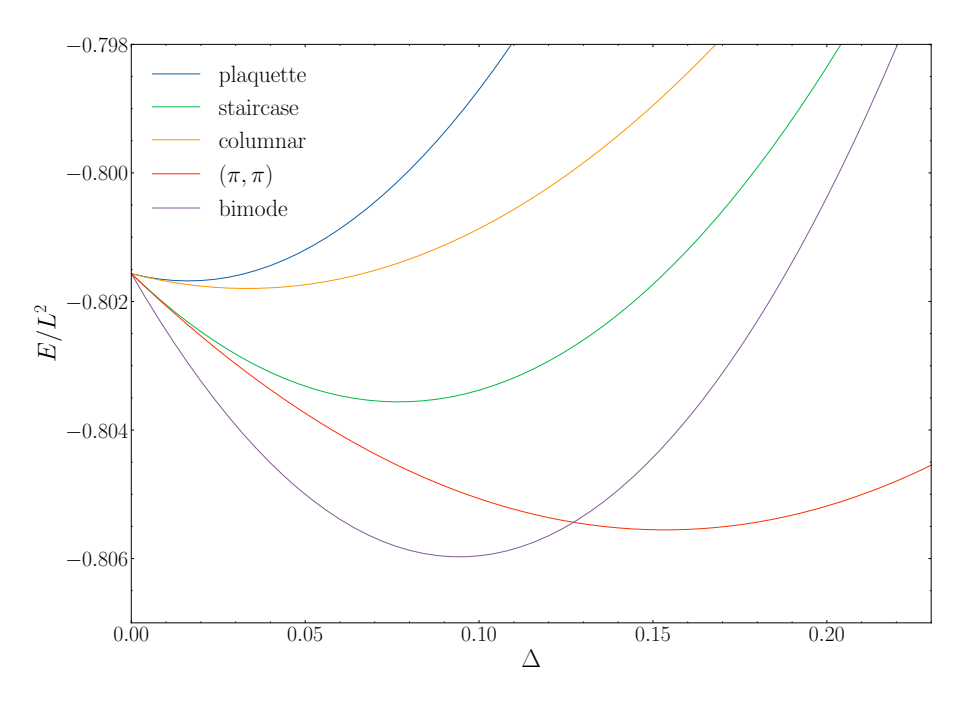


Figure 6.2: Energies per site as a function of Δ for various distortion patterns. The bimode distortion is taken as $a_Q = a_{Q/2} = \Delta$ for simplicity. Results are shown for a $L \times L$ square lattice with L = 12, K = 0.5, and $\alpha = 0.5$, using the Hamiltonian of the aSSH model, Eq. (6.7).

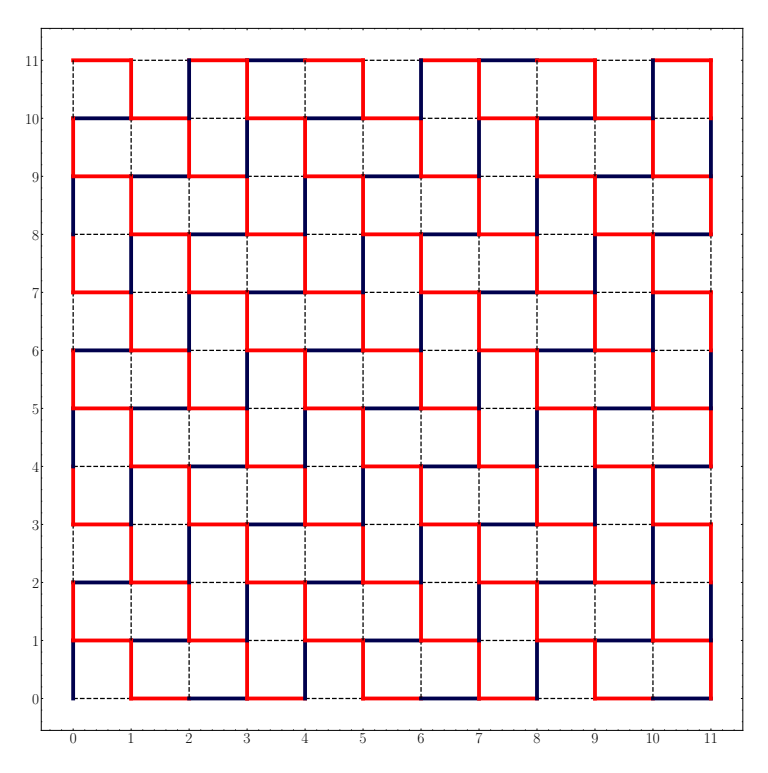


Figure 6.3: Bimode distortion of Eq. (6.8) for $a_Q = a_{Q/2} = \Delta$ on a 12 × 12 lattice. Bonds crossing the periodic boundaries are not shown. Blue bonds represent short bonds (with larger hopping amplitude for electrons), red bonds indicate long bonds (with smaller hopping amplitude), undistorted bonds are represented as dotted lines.

The results in Fig. 6.2 show that, even under the constraint $a_Q = a_{Q/2} = \Delta$, the bimode pattern yields a lower energy than the standard single-mode dimerization on a 12 × 12 lattice. The real-space structure of this bimode distortion is shown in Fig. 6.3.

A key feature of the aSSH model is that only bond differences, such as $x_{R+e_x} - x_R$, enter the Hamiltonian. This motivates the introduction of bond-centered displacement variables:

$$\Delta x_{(R,R+e_x)} = x_{R+e_x} - x_R, \qquad \Delta y_{(R,R+e_y)} = y_{R+e_y} - y_R.$$
 (6.9)

In terms of these variables, Eq. (6.7) can be rewritten as

$$\hat{H} = -t \sum_{R,\sigma} \left[1 - \alpha \Delta x_{(R,R+e_x)} \right] \left(\hat{c}_{R,\sigma}^{\dagger} \hat{c}_{R+e_x,\sigma} + \hat{c}_{R+e_x,\sigma}^{\dagger} \hat{c}_{R,\sigma} \right) +$$

$$- t \sum_{R,\sigma} \left[1 - \alpha \Delta y_{(R,R+e_y)} \right] \left(\hat{c}_{R,\sigma}^{\dagger} \hat{c}_{R+e_y,\sigma} + \hat{c}_{R+e_y,\sigma}^{\dagger} \hat{c}_{R,\sigma} \right) +$$

$$+ \frac{K}{2} \sum_{R} \left[\left(\Delta x_{(R,R+e_x)} \right)^2 + \left(\Delta y_{(R,R+e_y)} \right)^2 \right].$$

$$(6.10)$$

The Hamiltonian of Eq. (6.10) must also satisfy the constraint:

$$\sum_{n=1}^{L} \Delta x_{(R+ne_x, R+ne_x+e_x)} = 0 \quad \forall R,$$

$$\sum_{n=1}^{L} \Delta y_{(R+ne_y, R+ne_y+e_y)} = 0 \quad \forall R,$$

$$(6.11)$$

which ensure that the lattice length is preserved in both directions, i.e., the distortions do not stretch the system.

It is worth noting that, without these constraints, Eq. (6.10) would correspond to the adiabatic limit of the bSSH Hamiltonian. This distinction is crucial, as the multimode behavior discussed here would not apply in that case.

A systematic analysis of multimode distortions in the aSSH model [63] demonstrated that, at U=0, the optimal distortion pattern contains the nesting vector $Q=(\pi,\pi)$ together with additional components parallel to Q. In the thermodynamic limit, this leads to an infinite set of degenerate multimode configurations, each corresponding to a distinct real-space distortion pattern. The simple bimode ansatz shown in Eq. (6.8) can be generalized into a multimode ansatz as

$$x_{R+e_x} - x_R = a_Q \cos(Q \cdot R) + \sum_q a_q \cos(q \cdot R),$$

$$y_{R+e_y} - y_R = a_Q \cos(Q \cdot R) - \sum_q a_q \cos(q \cdot R),$$
(6.12)

where the q vectors can be expressed as $q = \left(\frac{2\pi}{M}, \frac{2\pi}{M}\right)$ with M > 2, and $\{a_q\}$ are variational parameters. This ansatz is suitable for the aSSH model of Eq. (6.7), where only differences like $x_{R+e_x} - x_R$ appear in the Hamiltonian.

Later works, which incorporated Hubbard interaction effects, confirmed this multimode distortion picture. Hartree–Fock calculations [64] found a first-order AFM to BOW transition with no coexistence region, in agreement with results from variational Monte Carlo simulations [65]. Furthermore, in the large-U limit, the effective spin–Peierls model derived from the aSSH Hamiltonian in the adiabatic limit also exhibits multimode distortions, as shown by quantum Monte Carlo (QMC) studies [66].

6.2.3 Excluding multimode distortions for oSSH and bSSH models

We now examine whether multimode distortions could lead to an energetically favorable ground state in the case of SSH coupling with optical phonons. This analysis parallels the multimode study performed for the aSSH model, but is carried out here for the aSSH and bSSH cases.

For the oSSH model, we first considered the following bimode ansatz:

$$x_R = a_Q \cos(Q \cdot R) + a_{Q/2} \cos\left[(Q \cdot R)/2\right]$$

$$y_R = a_Q \cos(Q \cdot R) - a_{Q/2} \cos\left[(Q \cdot R)/2\right].$$
(6.13)

We also considered the distortion pattern of Eq. (6.8), supplemented by the constraints $x_{R=(1,j)} = 0 \ \forall j$ and $y_{R=(j,1)} = 0 \ \forall j$, since Eq. (6.8) specifies only displacement differences rather than absolute displacements. For completeness, a trimode ansatz was also tested, but is not reported here for brevity.

These ansätze were inserted into Eq. (6.6) for U=0, and the resulting tight-binding Hamiltonian was diagonalized at half filling. The dimerization parameters were optimized via a simple gradient descent algorithm, with derivatives computed using backward automatic differentiation (see Appendix B). Across a broad range of K and α , the multimode configurations were consistently found to be energetically sub-optimal, with the (π, π) distortion remaining the most favorable. This confirms the conclusions of Tang and Hirsch for the oSSH model.

The same result, that the multimode ansatz is sub-optimal, also applies to the case of the bSSH model. It is important to note that the bSSH model in the adiabatic limit can be written as the Hamiltonian in Eq. (6.10), but without the global-length constraints discussed

earlier. Therefore, to properly address this case, one should optimize all dimerization ansätze by introducing for each case two additional variational parameters, x_0 and y_0 , representing the average displacement of the x and y phonon modes. After optimization, these offsets were always found to be finite, and the bimode configuration remained energetically sub-optimal. The same outcome was observed when considering a trimode distortion.

Although this does not constitute a formal proof, our results strongly indicate that multimode distortions are not realized in the oSSH and bSSH models. This conclusion is in line with several determinant quantum Monte Carlo (DQMC) studies of the two-dimensional oSSH and bSSH models at finite phonon frequency, which do not impose any specific ansatz for the bosonic wave function or phonon displacements and do not rely on approximations. These works consistently report only a (π, π) BOW phase [46, 44, 45, 47].

Since this thesis focuses on models with optical phonons, we will not pursue the topic of multimode distortions further and restrict our analysis to the possible patterns shown in Fig. 6.1.

Finally, we note that in a study of phonon dispersion in the multimode regime [98], the authors affirm that they could not draw any conclusions about whether multimode degeneracy might be lifted by quantum corrections. To the best of our knowledge, the investigation of multimode patterns in the aSSH model with fully quantum phonons remains an open problem.

6.3 Anti-adiabatic limit

The procedure to derive the anti-adiabatic limit in the square lattice closely follows the treatment presented in Section 2.4. Since the phonon modes along the x and y directions are decoupled, integrating them out corresponds, effectively, to applying the one-dimensional method separately along each direction. For this reason, we do not repeat the detailed steps outlined in Section 2.4, and we directly present the resulting effective Hamiltonians obtained after integrating out the bosonic degrees of freedom in the various models.

For the bSSH model, the effective Hamiltonian reads:

$$\hat{H}_{AA}^{bSSH} = \sum_{R,\nu} \left[-t \hat{B}_{R,R+e_{\nu}} - \frac{t^2 \alpha^2}{2K} \left(\hat{B}_{R,R+e_{\nu}} \right)^2 \right] =$$

$$= -t \sum_{\langle ij \rangle} \hat{B}_{ij} - \frac{t^2 \alpha^2}{2K} \sum_{\langle ij \rangle} \hat{B}_{ij}^2 , \qquad (6.14)$$

where the sum runs over nearest-neighbor pairs $\langle ij \rangle$, and the hopping operator between sites i and j is defined as $\hat{B}_{ij} = \sum_{\sigma} (\hat{c}^{\dagger}_{i\sigma} \hat{c}_{j\sigma} + \text{h.c.})$. Using Eq. (2.65), the squared hopping term can be rewritten in terms of spin and pairing operators:

$$\hat{S}_{j}^{\alpha} = \frac{1}{2} \sum_{\sigma,\sigma'} \hat{c}_{j,\sigma}^{\dagger} \tau_{\sigma,\sigma'}^{\alpha} \hat{c}_{j,\sigma'}^{\dagger} ; \qquad \hat{\Delta}_{j} = \hat{c}_{j,\downarrow} \hat{c}_{j,\uparrow} . \qquad (6.15)$$

Hence, the effective Hamiltonian in Eq. (6.14) can be rewritten as:

$$\hat{H}_{AA}^{bSSH} = -t \sum_{\langle ij \rangle \sigma} (\hat{c}_{i\sigma}^{\dagger} \hat{c}_{j\sigma} + \text{h.c.}) + \frac{2t^2 \alpha^2}{K} \sum_{\langle ij \rangle} \left[\hat{\vec{S}}_i \cdot \hat{\vec{S}}_j + \frac{1}{4} \hat{n}_i \hat{n}_j - \frac{1}{2} \left(\hat{\Delta}_i^{\dagger} \hat{\Delta}_j + \hat{\Delta}_j^{\dagger} \hat{\Delta}_i \right) \right]. \quad (6.16)$$

The antiferromagnetic spin exchange term, $\hat{\vec{S}}_i \cdot \hat{\vec{S}}_j$, indicates that an AFM phase can be induced by high-frequency phonons via SSH coupling, even in the absence of a Hubbard interaction [44]. We remark that for the aSSH model, the effective interaction in the anti-adiabatic limit turns out to be identical to that in Eq. (6.14).

The oSSH model case is slightly more difficult. The integration of the phonon degrees of freedom, as detailed in Section 2.4.3, leads to a more complex effective Hamiltonian:

$$\hat{H}_{AA}^{\text{oSSH}} = -t \sum_{R,\nu,\sigma} (\hat{c}_{R,\sigma}^{\dagger} \hat{c}_{R+e_{\nu},\sigma} + \text{h.c.}) - \frac{t^{2}\alpha^{2}}{2K} \sum_{R,\nu} (\hat{B}_{R,R+e_{\nu}} - \hat{B}_{R,R-e_{\nu}})^{2} =$$

$$= \sum_{R,\nu} \left[-t \hat{B}_{R,R+e_{\nu}} - \frac{t^{2}\alpha^{2}}{K} (\hat{B}_{R,R+e_{\nu}})^{2} + \frac{t^{2}\alpha^{2}}{2K} (\hat{B}_{R,R+e_{\nu}} \hat{B}_{R,R-e_{\nu}} + \hat{B}_{R,R-e_{\nu}} \hat{B}_{R,R+e_{\nu}}) \right] ,$$
(6.17)

where the sum over ν runs over the two spatial directions, x and y, and the hopping operator \hat{B}_{ij} is defined as above.

Comparing Eq. (6.17) with Eq. (6.14), we observe the emergence of an additional term with coefficient $t^2\alpha^2/(2K)$ in the oSSH case. This term, which has the opposite sign with respect to the squared hopping term in the bSSH model, may frustrate the antiferromagnetic coupling and counteract the attractive pairing interaction mediated by the \hat{B}_{ij}^2 terms.

These models have not been extensively investigated in the literature. Most studies have focused on the doped regime, exploring whether this type of effective phonon-mediated electronic interaction can support superconducting phases. An early work by Hirsch [99] suggested that the ground state of the Hamiltonian in Eq. (6.16) could be superconducting under electron doping.

More recently, a study employing density-matrix renormalization group techniques investigated the same Hamiltonian on cylindrical geometries in the large-U limit—i.e., the corresponding t-J model [100]. The authors reported the absence of a superconducting phase unless a frustrating next-nearest-neighbor hopping term t' was introduced.

A few additional studies have considered a Hamiltonian closely related to Eq. (6.16), derived from the anti-adiabatic limit of a model in which the SSH coupling was accompanied by phonons that coupled the x and y directions. In these cases, the effective Hamiltonian was found to support a d-wave superconducting phase [27, 101, 102].

6.4 Finite-frequency phonon results

In the literature, a few numerical studies on the SSH-Hubbard model with fully quantum phonons at half-filling have been performed, all relying on QMC methods: finite temperature determinant Quantum Monte Carlo (DQMC) and zero temperature projector Quantum Monte Carlo. This is possible because the system is sign-problem free at half-filling for any value of the Hubbard interaction U

Most studies have focused on the bSSH-Hubbard model. All results agree on the existence of a zero-temperature quantum phase transition from an AFM state to a BOW dimerized state. The BOW phase displays (π, π) order, as predicted by Tang and Hirsch in the adiabatic limit [67]; the corresponding pattern is shown in Fig. 6.1 (panel C). A phase diagram showing phase boundaries for U=0 and U=8 is taken from Ref. [103] and shown in Fig. 6.4.

An important feature emerging from QMC results is that, for U=0 and finite phonon frequency, weak electron–phonon coupling induces an AFM phase [44, 45, 46]. In fact, at U=0, the symmetry group of the bSSH Hamiltonian is O(4), making the AFM phase degenerate with a charge-density wave (CDW) and an s-wave superconducting state. However, as pointed out in Ref. [44], any infinitesimal U>0 lifts this degeneracy in favor of AFM order.

The presence of an AFM phase at U=0 and finite ω contrasts with the adiabatic limit (zero phonon frequency), where the system is always a Peierls insulator at U=0. Nonetheless, the emergence of antiferromagnetism is fully consistent with the effective Hamiltonian of Eq. (6.16), obtained in the anti-adiabatic limit (infinite phonon frequency), which contains an AFM spin-exchange term.

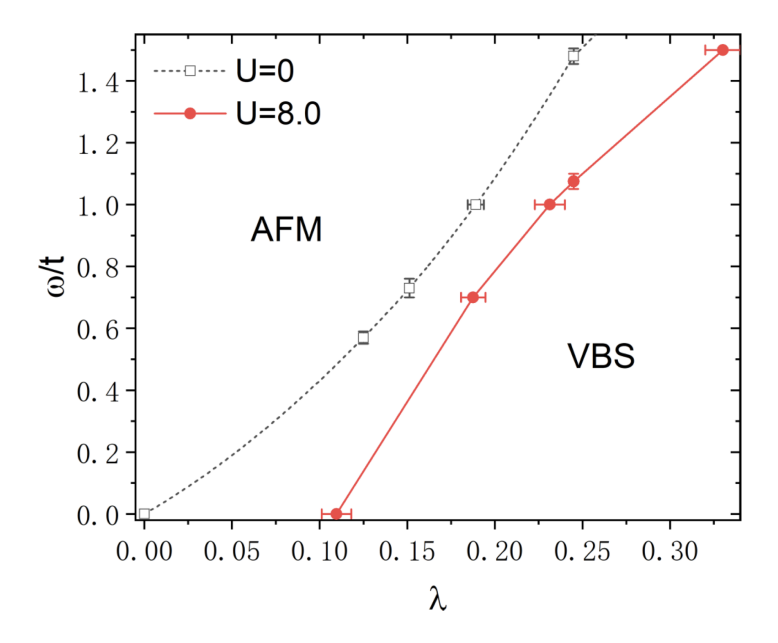


Figure 6.4: Phase diagram taken from Ref. [103] for the bSSH-Hubbard model [see Eq. (6.5)], showing the competing phases as a function of the phonon frequency ω and the electron-phonon coupling λ , for interaction strengths U=0 and U/t=8. Note that the definition of λ used in the figure differs by a rescaling factor from the one adopted in this work; however, the qualitative phase boundaries remain consistent. Two distinct phases are identified: an AFM phase and a Peierls phase characterized by a (π,π) BOW, referred to as a valence bond solid (VBS) in the figure.

The precise nature of the AFM–BOW transition at U=0 is still unclear. The possibility of a deconfined quantum critical point (DQCP) is excluded, since the BOW phase has (π, π) order (a DQCP would have been possible for a transition between AFM and $(\pi, 0)$ columnar BOW [104, 105]). Consequently, the transition is expected to be either first order or accompanied by a coexistence region. Within the bSSH model, no evidence of coexistence has been reported: Ref. [44] suggests a weakly first-order transition, whereas Ref. [45] reports behavior consistent with a continuous transition.

Introducing a finite Hubbard interaction U (favoring the AFM phase), the boundary between the AFM and BOW phases shifts to larger electron-phonon coupling values. The transition in the bSSH-Hubbard model has been reported as direct (without a coexistence region) in Ref. [103], while Ref. [106] suggests that the transition is first-order at large values of U.

The oSSH-Hubbard model with finite-frequency phonons has been studied using DQMC at half filling in Ref. [47]. These results suggest that the AFM-BOW transition may host a coexistence region at finite U. Moreover, AFM correlations at U=0 are substantially weaker than in the bSSH case, consistent with the effective Hamiltonian of Eq. (6.17) in the anti-adiabatic limit, which contains terms that can frustrate phonon-induced AFM coupling. A definitive conclusion regarding the existence of an AFM phase at U=0 for the oSSH model is challenging according to Ref. [47], since the temperatures required to clearly observe the signature of AFM are very low and difficult to reach using DQMC.

Finally, no studies were found that address the two-dimensional aSSH model on the square lattice in the presence of finite phonon frequency. The peculiar feature of the aSSH model in the adiabatic limit—hosting infinitely degenerate multimode distortion patterns—naturally raises the question of whether, and in what manner, quantum fluctuations induced by finite-frequency phonons could lift this degeneracy. As discussed in the previous section, the investigation of multimode patterns in the aSSH model with fully quantum phonons remains an open problem.

Chapter 7

2D oSSH-Hubbard model: a variational Monte Carlo and Hartree-Fock study

In this chapter, we present our analysis of the oSSH-Hubbard model on a square lattice, with results obtained through variational Monte Carlo (VMC) simulations. A Hartree-Fock analysis in the anti-adiabatic limit is also provided.

We employ the Hamiltonian given by Eq. (3.24), which we restate here for clarity:

$$\hat{H} = -t \sum_{R,\sigma} \left[1 - \tilde{\alpha} \left(\hat{X}_{R+e_x} - \hat{X}_R \right) \right] \left(\hat{c}_{R,\sigma}^{\dagger} \hat{c}_{R+e_x,\sigma} + \hat{c}_{R+e_x,\sigma}^{\dagger} \hat{c}_{R,\sigma} \right) +$$

$$- t \sum_{R,\sigma} \left[1 - \tilde{\alpha} \left(\hat{Y}_{R+e_y} - \hat{Y}_R \right) \right] \left(\hat{c}_{R,\sigma}^{\dagger} \hat{c}_{R+e_y,\sigma} + \hat{c}_{R+e_y,\sigma}^{\dagger} \hat{c}_{R,\sigma} \right) +$$

$$+ \frac{\hbar \omega}{2} \sum_{R} \left[\hat{P}_{x,R}^2 + \hat{X}_R^2 \right] + \frac{\hbar \omega}{2} \sum_{R} \left[\hat{P}_{y,R}^2 + \hat{Y}_R^2 \right] + U \sum_{R} \hat{n}_{R,\uparrow} \hat{n}_{R,\downarrow} .$$

$$(7.1)$$

This Hamiltonian is closely related to the oSSH-Hubbard Hamiltonian of Eq. (6.2) by a simple rescaling of the bosonic operators, as discussed in Section 3.1. In our analysis, we will specify the values of the parameters: U/t, $\hbar\omega/t$, and $\lambda = (t\tilde{\alpha}^2)/(\hbar\omega)$.

We begin with Section 7.1, where we demonstrate the accuracy of our variational wave function, which is described in Section 3.3 for the square lattice case, by comparing its energy with that obtained from determinant quantum Monte Carlo (DQMC) in Ref. [47] (A. T. Ly, private communication, March 2025). The results show excellent accuracy for U = 0 across all values of λ , and good accuracy for U/t = 4. The accuracy decreases for larger values of U.

Our variational method at half-filling predicts a phase diagram, shown in Section 7.2, that agrees well with DQMC simulations. The system shows an antiferromagnetic (AFM) undistorted phase for dominant Hubbard interaction U, and a bond-order wave (BOW) phase exhibiting lattice distortions when λ dominates. We also observe a possible phase coexistence region between the AFM and BOW phases, in agreement with DQMC results, although our findings are inconclusive in this regard.

Before exploring the hole-doped regime with VMC, we perform a Hartree-Fock calculation in the anti-adiabatic limit to identify potential superconducting instabilities. Our analysis shows that the oSSH-Hubbard model only exhibits on-site s-wave superconductivity, with no d-wave or extended s-wave terms appearing in the mean-field decoupling. This result contrasts with the bSSH-Hubbard model, where the same Hartree-Fock calculation in the anti-adiabatic limit reveals a d-wave superconducting phase upon hole doping, confirming earlier predictions [39, 40]. Specifically, we observe s-wave superconductivity in the regime dominated by λ , and a coexistence of s-wave and d-wave phases for larger values of U within the bSSH-Hubbard model.

This suggests that different SSH implementations lead to distinct phase diagrams, with the oSSH model potentially being less suitable for identifying d-wave superconductivity.

Finally, we investigate the doped oSSH-Hubbard model using VMC. Our results show that the BOW phase persists up to finite doping and that, for U=0 and doping around $\delta=1/4$, the system exhibits on-site s-wave superconducting correlations. Furthermore, we find that a weak coupling to phonons within the oSSH model at large-U can actually suppress d-wave superconductivity that would otherwise emerge in the pure Hubbard model.

7.1 Comparison with DQMC results

We begin by assessing the accuracy of our variational wave function by comparing its energy with that obtained in Ref. [47] using an exact finite-temperature method. DQMC provides exact sampling of the system's partition function at finite temperature, given by $Z = \text{Tr } e^{-\beta \hat{H}}$, where β is the inverse temperature, and the Hamiltonian \hat{H} includes both bosonic degrees of freedom (to model phonons) and interacting electrons.

The method employs a Hubbard-Stratonovich transformation to account for the U interaction between fermions and applies a Trotter-Suzuki decomposition to exactly sample configurations from the partition function at a given finite temperature. This approach has been adapted to treat electronic systems coupled to bosons [107]. All results we compare with were obtained in the half-filling regime, which is crucial for DQMC to be sign-problem free.

The data we compare with were obtained at a low temperature, ensuring the system is in its ground state, with an inverse temperature $\beta t = 16$ on a 8×8 lattice [47]. Our VMC method, being a ground state method, operates at T = 0, accounting only for quantum fluctuations and not for thermal ones. However, we can still compare our results, obtaining a reasonable figure of merit.

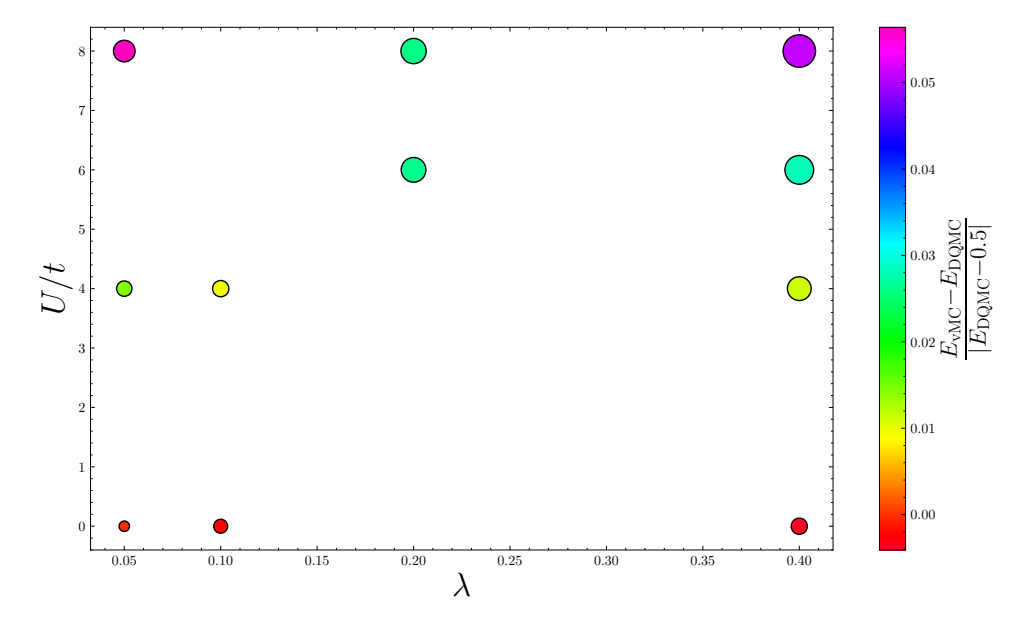


Figure 7.1: Accuracy of the variational energy compared to DQMC results on an 8×8 lattice for $\hbar \omega/t = 0.5$. Points are plotted in the $(\lambda, U/t)$ phase diagram, with color indicating the value of the accuracy ϵ . The size of each point corresponds to the associated error bar. The results are also summarized in Table 7.1.

The energy accuracy is defined as:

$$\epsilon = \frac{E_{\text{VMC}} - E_{\text{DQMC}}}{|E_{\text{DQMC}} - \hbar\omega|} , \qquad (7.2)$$

where the term $\hbar\omega$ is subtracted from the denominator to account for any global energy shift in the Hamiltonian (the zero-point energy of the x and y phonon components is $\hbar\omega/2$ each).

Fig. 7.1 shows the accuracy ϵ , and the results are also reported in Table 7.1, where error bars are included. Our energies coincides (within error bars) with those obtained by DQMC at U=0 for various values of λ , spanning from the undistorted phase to the BOW-distorted phase. The high accuracy is expected for small values of λ , as our wave function is exact in the case of free fermions ($U=\lambda=0$). However, the fact that the accuracy remains unchanged at $\lambda=0.4$ (a point located within the BOW phase) demonstrates that the backflow correlations introduced into the fermionic ansatz accurately capture the electron-phonon physics induced by the SSH coupling.

It is also important to note that our wave function is exact in the adiabatic limit ($\omega \to 0$) at U=0. In our simulations, we set the phonon frequency to $\hbar\omega/t=0.5$ and, as expected, the accuracy decreases as U increases. Nevertheless, maintaining a relative accuracy of around 1.5% at U/t=4 in both the AFM phase (small λ) and the BOW phase (large λ) is a notable achievement.

U/t=0			
λ	ϵ	$\Delta\epsilon$	
0.05	-0.0003	0.002	
0.1	-0.002	0.003	
0.4	-0.0041	0.0044	

U/t=6			
λ	ϵ	$\Delta\epsilon$	
0.2	0.026	0.011	
0.4	0.028	0.014	

U/t=4			
λ ϵ $\Delta\epsilon$			
0.05	0.0145	0.0040	
0.1	0.0098	0.0045	
0.4	0.0111	0.0096	

U/t=8			
λ	ϵ	$\Delta\epsilon$	
0.05	0.056	0.008	
0.2	0.026	0.011	
0.4	0.051	0.018	

Table 7.1: Accuracy of the variational energy compared to DQMC results on an 8×8 lattice for $\hbar\omega/t=0.5$. The accuracy, ϵ , is defined in Eq. (7.2). The data are organized according to different values of U.

7.2 VMC phase diagram at half filling

In this section, we investigate the competition between AFM and BOW phases at half-filling within the two-dimensional oSSH-Hubbard model at $\hbar\omega/t = 0.5$.

Using VMC, we analyze the nature of the AFM-BOW transition, construct the corresponding phase diagram, and explore the possible coexistence of magnetic and bond-ordered phases. We also address the emergence of magnetic order at U=0, highlighting the role of electron-phonon coupling in stabilizing long-range AFM correlations in the absence of Hubbard interactions.

All simulations have been performed on a 8×8 lattice with periodic boundary conditions, apart from a few calculations regarding the presence of AFM at U = 0.

7.2.1 First order AFM-BOW transition

The phase diagram of the two-dimensional oSSH-Hubbard model consists of an undistorted AFM phase and a BOW phase, where the BOW is characterized by lattice distortions. In our initial attempt to characterize the phase diagram, we consider two distinct variational ansätze and observe a first-order transition between them.

The two variational ansätze are realizations of a Jastrow-Slater wave function with phonon backflow terms, as described in Section 3.3. They exhibit the following distinctive features.

- 1. $|\psi_{AFM}\rangle$, which displays AFM order, is characterized by:
 - No phonon distortions. The variational parameters z_x and z_y that appear in the uncorrelated bosonic wave function of Eq. (3.29) are set to zero. These parameters govern the centers of the Gaussian wave functions that model the harmonic oscillators and, thus, do not allow for phonon dimerization when set to zero.
 - External magnetic field B^x . Following Eq. (3.33), an external magnetic field with ordering vector $Q = (\pi, \pi)$ oriented in the x-direction is added to the auxiliary Hamiltonian whose ground state constitutes the antisymmetric part of the wave function. We also tried adding an external magnetic field oriented in the z-direction, but the variational energy was significantly worse.
 - No pairing terms. As discussed in Section 3.3.2.1, given the way in which pairing terms are implemented in the auxiliary Hamiltonian, these cannot be added simultaneously with an in-plane magnetic field. However, backflow terms, such as those in Eq. (3.27), are unaffected by this issue and are added as usual.
 - Spin-spin Jastrow factor. An additional Jastrow factor is introduced to model spin-spin correlations, which are induced by the external magnetic field; see Eq. (3.34).
- 2. $|\psi_{BOW}\rangle$, which displays BOW order, is characterized by:
 - Phonon distortions with ordering vector $Q = (\pi, \pi)$. We tested the four dimerization patterns shown in Fig. 6.1: the pattern with the lowest energy, after a full optimization, is the one with only one phonon specie displaying $Q = (\pi, \pi)$ distortions. For this reason, referring to the phononic wave function of Eq. (3.29), we set $z_y = 0$, $Q_x = (\pi, \pi)$ and optimize the parameter z_x ; the corresponding dimerization pattern is shown in Fig. 6.1 (panel C). This result is in agreement with exact DQMC calculations of Ref. [47], which claim to find the same distortion pattern.
 - No external magnetic field.
 - Pairing terms. Both s-wave and d-wave pairing terms as those shown in Eq. (3.29) are added to the auxiliary Hamiltonian.

By varying λ at a fixed U, the energies of the two ansätze cross, signaling the presence of a first-order phase transition. The energy curves as a function of λ for U/t=4 are shown in Fig. 7.2. The possibility of a phase coexistence region will be discussed later.

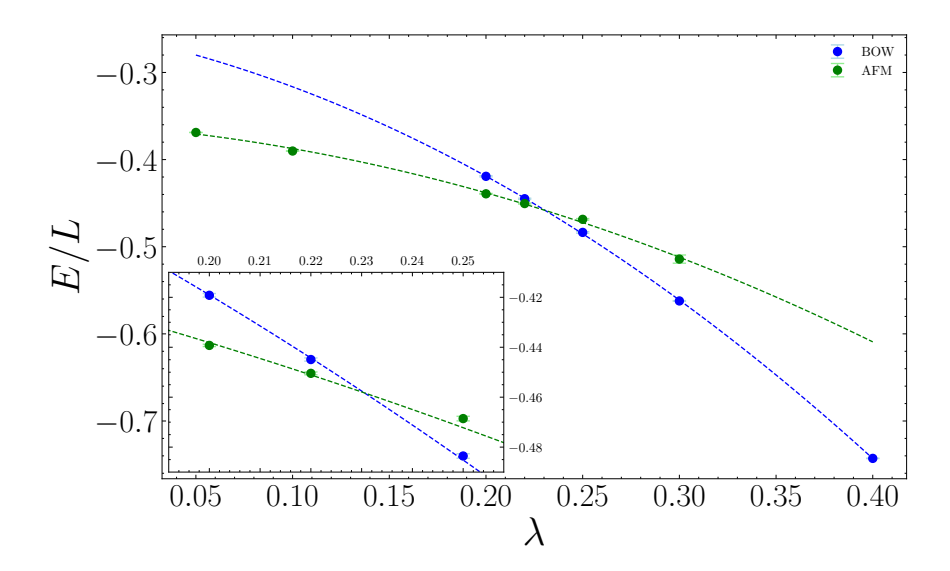


Figure 7.2: Energy comparison between the AFM and BOW phases as a function of λ for U/t=4 in an 8×8 oSSH-Hubbard model at $\hbar\omega/t=0.5$. The energy per site for the two variational ansätze, $|\psi_{AFM}\rangle$ and $|\psi_{BOW}\rangle$, is plotted. Dotted lines represent quadratic fits, included to guide the eye. The inset provides a closer view of the transition point.

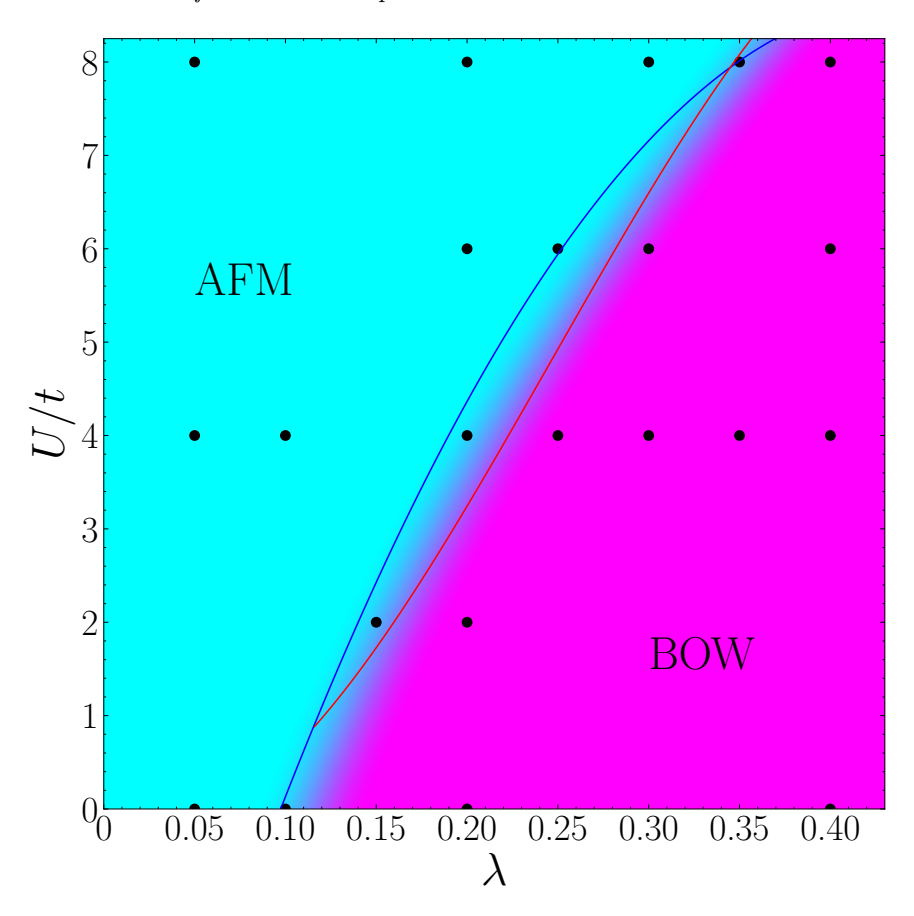


Figure 7.3: Phase diagram of the oSSH-Hubbard model on a 8×8 square lattice at half-filling. Black dots represent the points where our results were obtained, and the two colors correspond to the AFM and BOW phases. The red and blue lines represent the transition points obtained from Ref. [47] by means of DQMC calculations.

7.2.2 Phase diagram

By optimizing the variational solutions $|\psi_{AFM}\rangle$ and $|\psi_{BOW}\rangle$ over a range of values in the (λ, U) plane at $\hbar\omega/t = 0.5$, we can construct a phase diagram for the oSSH-Hubbard model at halffilling. Fig. 7.3 shows the phase diagram, where the black dots represent the points where our results were obtained, and the two colors represent the two different phases. The red and blue lines are taken from the phase diagram of Ref. [47], based on DQMC results. According to Ref. [47], as λ increases from left to right, the red line corresponds to the point where AFM order disappears, while the blue line marks the onset of the BOW phase; a coexistence region is assumed between the two lines by Ref. [47].

We note that, although the accuracy of our wave function decreases when U/t reaches values of 6 or 8, the phase diagram we obtained is in good agreement with the one of Ref. [47], with their transition point marked by the red and blue lines.

To further analyze the results, we pick two points: one within the AFM phase and the other deep within the BOW phase, and show the spin-spin and bond-bond correlations in Fourier space. The correlations are defined as:

$$S(q) = \frac{1}{L} \sum_{R,R'} e^{iq \cdot (R-R')} \langle \hat{S}_R \cdot \hat{S}_{R'} \rangle, \qquad (7.3)$$

$$B^{x}(q) = \frac{1}{L} \sum_{R,R'} e^{iq \cdot (R-R')} \langle \hat{b}_{R}^{x} \hat{b}_{R'}^{x} \rangle, \qquad (7.4)$$

where the local spin and bond operators are defined as follows:

$$\hat{S}_{R}^{\alpha} = \sum_{\sigma,\sigma'} \hat{c}_{R,\sigma}^{\dagger} \tau_{\sigma,\sigma'}^{\alpha} \hat{c}_{R,\sigma'}, \tag{7.5}$$

$$\hat{b}_R^x = \sum_{\sigma} \left(\hat{c}_{R,\sigma}^{\dagger} \hat{c}_{R+e_x,\sigma} + \text{h.c.} \right), \tag{7.6}$$

where τ^{α} denotes one of the three Pauli matrices.

Fig. 7.4 clearly shows that a large peak at $Q = (\pi, \pi)$ determines the described phase. We emphasize that we are representing $B^x(q)$ because we allowed dimerization of the x-phonons; however, we could have chosen the y direction, yielding the same result.

7.2.3 AFM-BOW coexistence

We now briefly address the question of phase coexistence between the AFM and BOW phases. In Ref. [47], the transition points were identified using the following correlation ratios:

$$R_{\text{AFM}} = 1 - \frac{S(Q - \delta_Q)}{S(Q)}, \qquad R_{\text{BOW}} = 1 - \frac{B^x(Q - \delta_Q)}{B^x(Q)},$$
 (7.7)

where $Q=(\pi,\pi)$ is the ordering vector, and δ_Q is the smallest nonzero momentum displacement in the Brillouin zone. In a $l\times l$ lattice, this corresponds to $\delta_Q=(2\pi/l,0)$ or $\delta_Q=(0,2\pi/l)$. In the thermodynamic limit, these ratios tend to 1 in the presence of long-range order, and to 0 in its absence.

When plotting $R_{\rm BOW}$ (or analogously $R_{\rm AFM}$) as a function of a control parameter (e.g., λ), one observes that curves for different system sizes intersect at a common point, marking the location of the phase transition. This method is precisely how Ref. [47] was able to draw the red and blue transition lines shown in the phase diagram of Fig. 7.3, indicating the boundaries where AFM order disappears and BOW order emerges, respectively. Their analysis suggests a narrow coexistence region between the two phases.

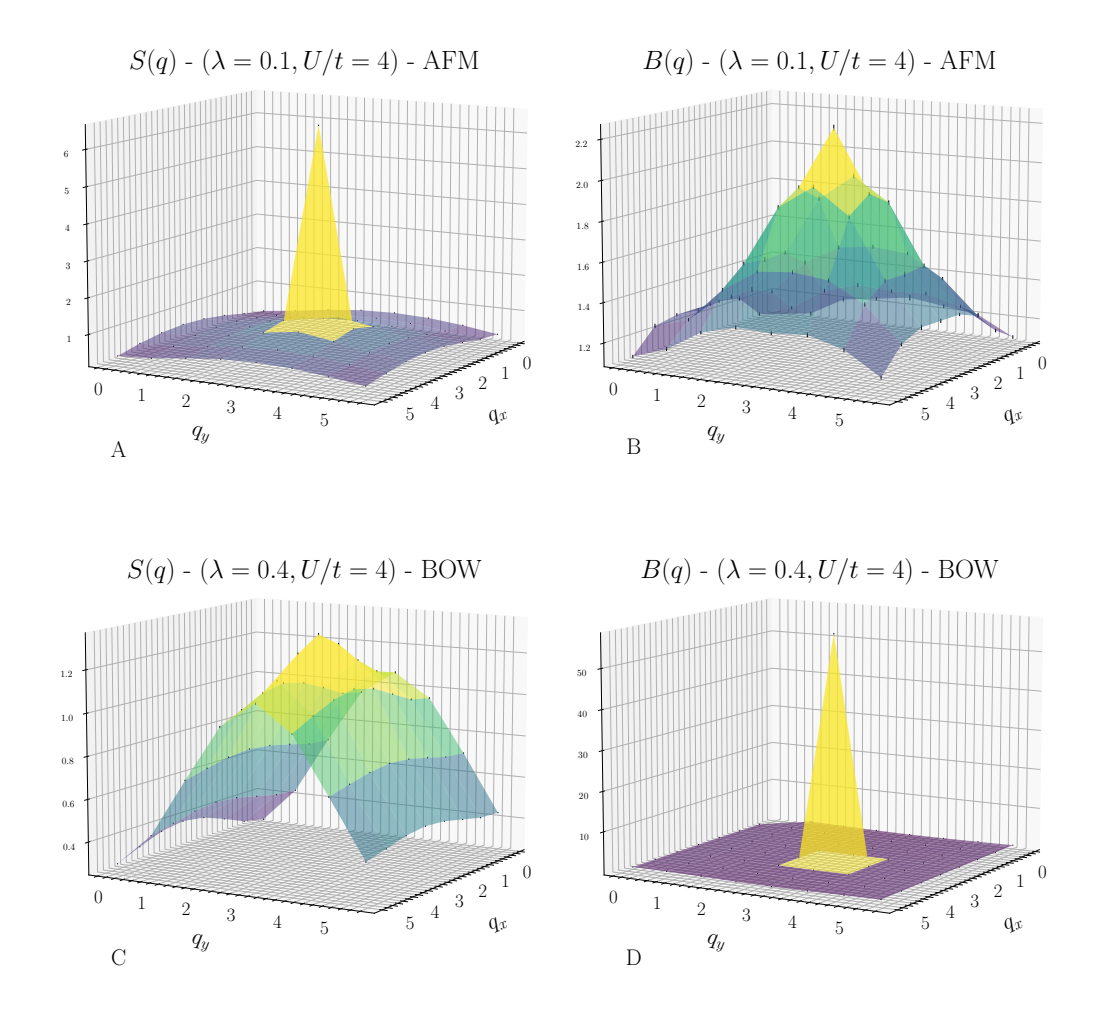


Figure 7.4: Spin-spin and bond-bond correlations in Fourier space within the AFM and BOW phases. Top panels (A and B) show the spin correlation S(q) and bond correlation $B^x(q)$, respectively, for a representative point in the AFM phase with $\lambda = 0.1$ and U/t = 4. Bottom panels (C and D) display the same quantities for a point in the BOW phase, with $\lambda = 0.4$ and U/t = 4. In both cases, the presence or absence of a sharp peak at $Q = (\pi, \pi)$ clearly distinguishes the two phases.

Using VMC and imposing either AFM order or BOW in the wave function, the information which we could extract from the correlation ratio may be significantly biased. As discussed in the previous two sections, our results suggest a first-order transition between the two variational states, $|\psi_{\text{AFM}}\rangle$ and $|\psi_{\text{BOW}}\rangle$, which are not adiabatically connected. Therefore, computing correlation ratios provides limited additional insight: for example, evaluating R_{AFM} for the $|\psi_{\text{AFM}}\rangle$ state would merely confirm the expected presence of long-range AFM order. The most direct and effective method to locate the transition in our variational framework is through energy comparisons, as demonstrated in Fig. 7.2 for the case U/t=4.

We try to address the issue of phase coexistence by considering a different variational ansatz that allows for the coexistence of AFM order and BOW. We refer to this trial wave function as $|\psi_{\text{coexist}}\rangle$, which is characterized by the following features:

- Phonon distortions with ordering vector $Q = (\pi, \pi)$ for the x-phonon component, controlled by a variational parameter z_x in the bosonic wave function.
- External magnetic field B^x along the x-direction, included in the auxiliary Hamiltonian

from which the antisymmetric fermionic part of the wave function is derived [see Eq. (3.33)]. The magnetic field is antiferromagnetic, with ordering vector $Q = (\pi, \pi)$.

- No pairing terms, due to the incompatibility between in-plane magnetic fields and pairing terms in our current implementation of the auxiliary Hamiltonian, as discussed in Section 3.3.2.1.
- Spin-spin Jastrow factor, which models spin correlations induced by the magnetic field (see Eq. (3.34)).

This ansatz can be continuously deformed into $|\psi_{AFM}\rangle$ but not into $|\psi_{BOW}\rangle$, due to the mutual exclusivity of in-plane magnetic fields and pairing terms within our VMC implementation.

Upon optimization, $|\psi_{\text{coexist}}\rangle$ converges to an AFM solution when $z_x \to 0$ and B^x remains finite, and to a BOW solution when $B^x \to 0$ and z_x remains finite. If both z_x and B^x remain non-zero after optimization, the result is a coexistence phase exhibiting both AFM and BOW order

As an illustrative example, we consider the case U/t=4. When optimizing $|\psi_{\text{coexist}}\rangle$ for $\lambda \lesssim 0.2$, the wave function settles into an AFM phase. For larger values of λ , the coexistence solution emerges. Notably, near the transition point identified in Fig. 7.2, the energy of $|\psi_{\text{coexist}}\rangle$ is slightly lower than that of both $|\psi_{\text{AFM}}\rangle$ and $|\psi_{\text{BOW}}\rangle$. However, for even larger values of λ , the coexistence solution persists with an energy slightly higher than that of $|\psi_{\text{BOW}}\rangle$. Table 7.2 reports the variational energies for the 8×8 lattice at U/t=4 and $\hbar\omega/t=0.5$, we can see that the coexistence solution is compatible with the AFM one for $\lambda=0.22$ and has a lower energy than the other two solutions only for $\lambda=0.25$.

U/t = 4				
λ	0.05	0.10	0.20	0.22
AFM	-0.3689 ± 0.0001	-0.3902 ± 0.0001	-0.4393 ± 0.0005	-0.4508 ± 0.0001
coexistence	_	_	_	-0.4510 ± 0.0002
BOW	_	_	-0.4192 ± 0.0007	-0.4449 ± 0.0006

U/t = 4				
λ	0.25	0.30	0.35	0.40
AFM	-0.4686 ± 0.0009	-0.514 ± 0.005	_	_
coexistence	-0.4881 ± 0.0005	-0.5619 ± 0.0002	-0.6464 ± 0.0002	-0.7402 ± 0.0002
BOW	-0.4859 ± 0.0002	-0.5626 ± 0.0001	-0.6479 ± 0.0002	-0.7429 ± 0.0002

Table 7.2: Table showing the energy per site as a function of λ of three variational solutions: $|\psi_{AFM}\rangle$, $|\psi_{coexist}\rangle$, and $|\psi_{BOW}\rangle$. The results are presented for an 8×8 lattice with U/t=4 and $\hbar\omega/t=0.5$. The energies of the AFM and BOW solutions have been previously shown in Fig. 7.2. It can be observed that the coexistence solution is compatible with the AFM solution at $\lambda=0.20$, and it exhibits a lower energy than the other two solutions only for $\lambda=0.25$.

Despite these results being promising, our analysis cannot give a definite conclusion on the possibility of phase coexistence due to the disconnected variational spaces of $|\psi_{\text{coexist}}\rangle$ and $|\psi_{\text{BOW}}\rangle$. Unfortunately, pairing terms are essential to stabilize the BOW solution, and discarding them significantly raises the variational energy. A more complete study would require a unified wave function that includes both pairing terms and in-plane magnetic fields. This would allow a consistent exploration of the full phase diagram using a unique wave function and enabling the use of correlation ratios to precisely locate the boundaries of each phase. As a result, our current analysis cannot fully resolve the nature and the extension of the coexistence region.

7.2.4 Antiferromagnetism at U = 0

The possibility of AFM order in the absence of Hubbard interaction (U=0) has been discussed in earlier studies of two-dimensional SSH models. For instance, exact QMC simulations of the bSSH model reported the emergence of an AFM phase at U=0 for small values of the electron-phonon coupling [44, 45]. A straightforward explanation for this phenomenon lies in the second-order processes induced by the electron-phonon interaction, which give rise to antiferromagnetic exchange interactions. This mechanism is explicitly visible in the effective electronic Hamiltonian derived in the anti-adiabatic limit, where fast phononic degrees of freedom are integrated out, leading to a spin-exchange term, see Eq. (6.16).

The situation for the oSSH model, however, is more intricate. In this case, the effective electronic Hamiltonian in the anti-adiabatic limit includes additional terms that may frustrate antiferromagnetic correlations [see Eq. (6.17)]. In Ref. [47], the authors reported that AFM order could only be detected at finite U; at U=0, the temperature reached in their DQMC simulations was too high to conclusively identify magnetic ordering. Specifically, the AFM correlation ratio $R_{\rm AFM}$ did not display the characteristic size-dependent crossing behavior that signals long-range order. Instead, it decreased with increasing system size for $\lambda \lesssim 0.15$ at U=0, both at $\hbar\omega/t=0.5$ and $\hbar\omega/t=2$, suggesting the absence of detectable AFM order at the simulated temperatures.

Nevertheless, it appears unlikely that the system remains metallic at T=0 without developing some kind of instability when a finite, albeit small, electron-phonon coupling is introduced. Our VMC analysis suggests that an AFM phase indeed exists at U=0. While our method is inherently variational and thus biased by the choice of ansatz, the good agreement in energy with DQMC results at U=0 (see Table 7.1) supports the reliability of our conclusions.

In Fig. 7.5, we compare the behavior of the variational parameter B^x (obtained after fully optimizing the parameters) as a function of system size for U/t=4 and U=0 at $\lambda=0.1$ and $\hbar\omega/t=0.5$. The parameter B^x represents an in-plane magnetic field term in the variational wave function. As shown in the figure, the system clearly develops AFM order at U/t=4, with B^x tending to a finite value in the thermodynamic limit. For U=0, our VMC calculations, within the available cluster, are consistent with a small but finite value in the thermodynamic limit. Moreover, the AFM correlation ratio $R_{\rm AFM}$ increases with system size for $\lambda \lesssim 0.1$, as shown in Fig. 7.6. This strongly suggests the presence of an AFM phase at zero temperature in the oSSH model, even in the absence of a Hubbard interaction.

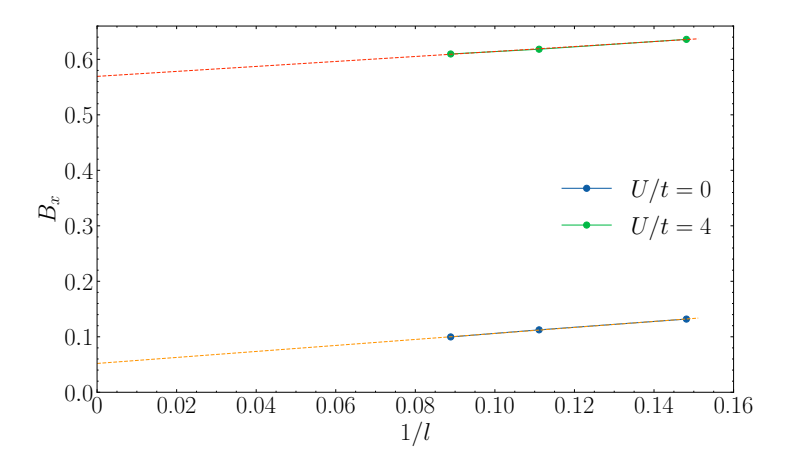


Figure 7.5: Size dependence of the variational magnetic field B^x for $\lambda=0.1$ and $\hbar\omega/t=0.5$, comparing U/t=4 (green points) and U=0 (blue points). Simulations were performed on $l\times l$ lattices, with 1/l shown on the x-axis. The finite values of B^x at U/t=4 provide clear evidence of AFM order in the limit of large l. In contrast, for U=0, the behavior is less conclusive: a linear fit suggests that B^x extrapolates to a small, possibly nonzero value in the thermodynamic limit.

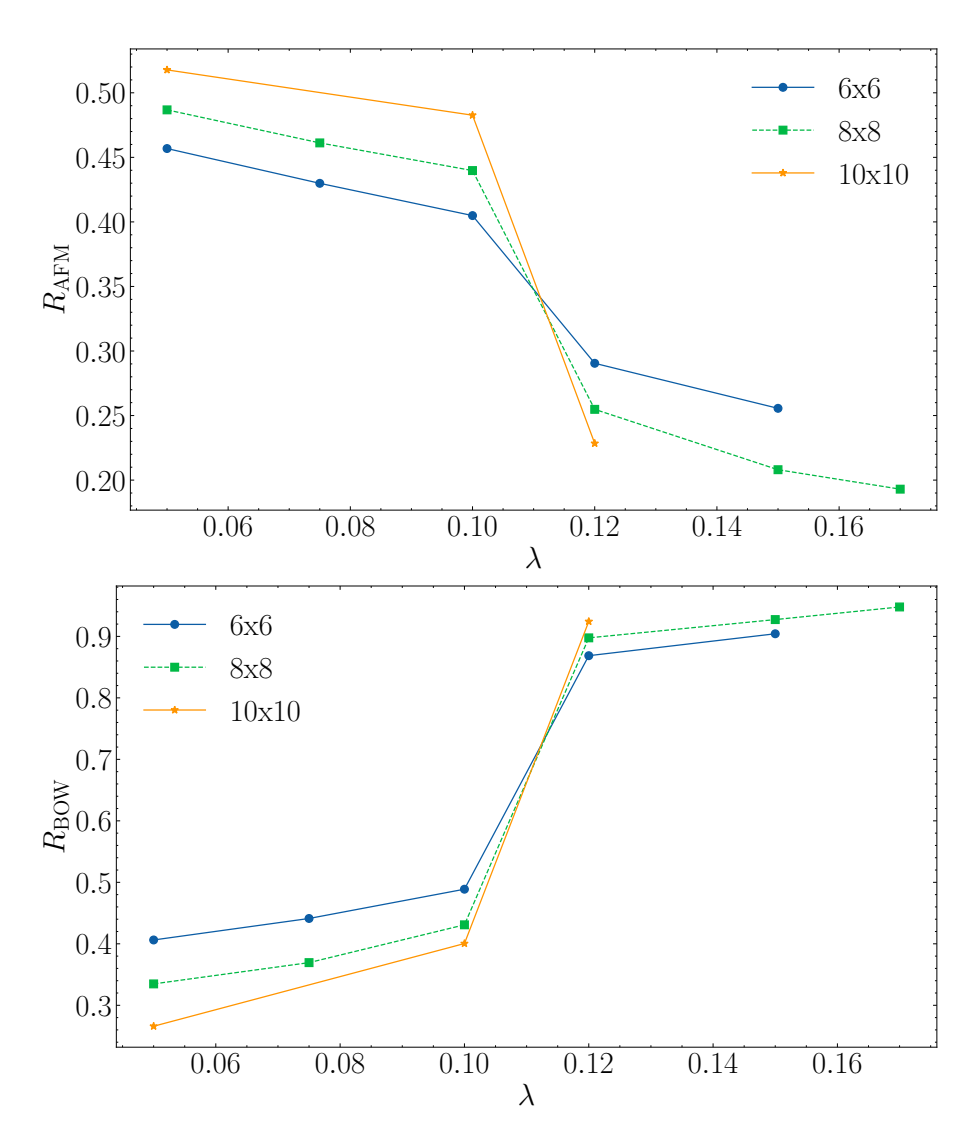


Figure 7.6: Correlation ratio $R_{\rm AFM}$ and $R_{\rm BOW}$ shown for various system sizes as a function of λ for U=0, $\hbar\omega/t=0.5$. The increasing trend of $R_{\rm AFM}$ with size for $\lambda\lesssim 0.1$ supports the existence of long-range AFM order at T=0.

7.3 Superconductive instabilities in the anti-adiabatic limit of the square lattice SSH-Hubbard model: a Hartree-Fock study

In this section, we apply a mean-field analysis to study the effective Hamiltonian of the square lattice SSH-Hubbard model in the anti-adiabatic limit. Our aim is to identify the superconducting instabilities when the system is driven away from half-filling.

We begin by considering the bSSH model in the anti-adiabatic limit, followed by the oSSH model. For convenience, the mean-field treatment will be performed after having expressed the Hamiltonians in k-space.

Hartree-Fock: bSSH-Hubbard model at anti-adiabatic limit 7.3.1

The effective Hamiltonian of the bSSH-Hubbard model, obtained after integrating out the phonons in the anti-adiabatic limit, is given by Eq. (6.14).

For convenience, we rewrite it here and split it into several terms:

$$\hat{H}^{\text{bSSH}} = \hat{H}_0 + U \sum_{i} \hat{n}_{i\uparrow} \hat{n}_{i\downarrow} - g \sum_{R} \left(\hat{B}_{R,R+e_x} \right)^2 - g \sum_{R} \left(\hat{B}_{R,R+e_y} \right)^2 =
= \hat{H}_0 + \hat{H}_U - \hat{H}_q^{x,NN} - \hat{H}_q^{y,NN} ,$$
(7.8)

where \hat{H}_0 represents the non-interacting part of the Hamiltonian, and $\hat{B}_{ij} = \sum_{\sigma} \left(\hat{c}^{\dagger}_{i\sigma} \hat{c}_{j\sigma} + \hat{c}^{\dagger}_{j\sigma} \hat{c}_{i\sigma} \right)$ is the hopping operator connecting sites i and j. The two relevant interaction scales are the Hubbard interaction U and the electron-phonon coupling g. For bSSH phonons, the coupling is given by $g = \frac{t^2 \alpha^2}{2K}$, as derived in Eq. (2.63). The terms $\hat{H}_g^{x,NN}$ and $\hat{H}_g^{y,NN}$ have a negative sign to emphasize that they represent attractive interaction pairing terms.

Expressing the Hamiltonian in k-space

 \hat{H}_0 represents the non-interacting part, given by:

$$\hat{H}_{0} = -t \sum_{R,\sigma} \sum_{\nu} (\hat{c}_{R\sigma}^{\dagger} \hat{c}_{R+e_{\nu},\sigma} + \text{h.c.}) - \mu \sum_{j} \hat{n}_{j} =
= -2t \sum_{k,\sigma} \left[\cos(k_{x}) + \cos(k_{y}) \right] \hat{c}_{k\sigma}^{\dagger} \hat{c}_{k\sigma} - \mu \sum_{k,\sigma} \hat{c}_{k\sigma}^{\dagger} \hat{c}_{k\sigma} ,$$
(7.9)

where μ is the chemical potential, which must be tuned to achieve the desired doping level. H_U is the conventional Hubbard on-site interaction term:

$$\hat{H}_{U} = U \sum_{i} \hat{c}_{i\uparrow}^{\dagger} \hat{c}_{i\uparrow} \hat{c}_{i\downarrow}^{\dagger} \hat{c}_{i\downarrow} = \frac{U}{L} \sum_{k} \sum_{q} \sum_{p} \hat{c}_{k+p,\uparrow}^{\dagger} \hat{c}_{-k+p,\downarrow}^{\dagger} \hat{c}_{-q+p,\downarrow} \hat{c}_{q+p,\uparrow} , \qquad (7.10)$$

where L is the number of sites in the lattice. $\hat{H}_g^{x,NN}$ and $\hat{H}_g^{y,NN}$ represent the nearest neighbor squared hopping terms. These terms can be expressed in momentum space as follows:

$$\hat{H}_{g}^{x,NN} = g \sum_{\sigma,\sigma'} \left(\hat{c}_{i\sigma}^{\dagger} \hat{c}_{i+e_{x},\sigma} + \hat{c}_{i+e_{x},\sigma}^{\dagger} \hat{c}_{i\sigma} \right) \left(\hat{c}_{i\sigma'}^{\dagger} \hat{c}_{i+e_{x},\sigma'} + \hat{c}_{i+e_{x},\sigma'}^{\dagger} \hat{c}_{i\sigma'} \right) =
= \frac{4g}{L} \sum_{k} \sum_{q} \sum_{p} \hat{c}_{k+p,\uparrow}^{\dagger} \hat{c}_{-k+p,\downarrow}^{\dagger} \hat{c}_{-q+p,\downarrow} \hat{c}_{q+p,\uparrow} \left[\cos(2p_{x}) + \cos(k_{x} + q_{x}) \right] +
+ \frac{2g}{L} \sum_{\sigma} \sum_{k} \sum_{q} \sum_{p} \hat{c}_{k,\sigma}^{\dagger} \hat{c}_{k+p,\sigma} \hat{c}_{q,\sigma}^{\dagger} \hat{c}_{q-p,\sigma} \exp\left\{ ik_{x} - iq_{x} + ip_{x} \right\} .$$
(7.11)

A completely equivalent expression holds for the term $\hat{H}_g^{y,NN}$, corresponding to the nearest neighbor squared hopping in the y direction.

7.3.1.2The mean-field Hamiltonian

In order to perform the Hartree-Fock approximation, it is necessary to consider all possible contractions to decouple the interacting Hamiltonian and obtain a new quadratic Hamiltonian H_{MF} , which includes some self-consistent parameters that depend on the ground state $|\psi_{MF}\rangle$ of the mean-field Hamiltonian itself.

The self-consistent parameters are defined by the following equations. First, we focus on conventional terms, which are defined for each spin σ and direction $\nu = \{x, y\}$:

$$n_0^{\sigma} = \frac{1}{L} \sum_{k} \langle \psi_{MF} | \hat{c}_{k\sigma}^{\dagger} \hat{c}_{k\sigma} | \psi_{MF} \rangle \tag{7.12}$$

$$C_{\nu}^{\sigma} = \frac{1}{L} \sum_{k} \cos(k_{\nu}) \langle \psi_{MF} | \hat{c}_{k\sigma}^{\dagger} \hat{c}_{k\sigma} | \psi_{MF} \rangle$$
 (7.13)

$$S_{\nu}^{\sigma} = \frac{1}{L} \sum_{k} \sin(k_{\nu}) \langle \psi_{MF} | \hat{c}_{k\sigma}^{\dagger} \hat{c}_{k\sigma} | \psi_{MF} \rangle$$
 (7.14)

Next, we consider the superconducting terms:

$$\Delta_0 = \frac{1}{L} \sum_{k} \langle \psi_{MF} | \hat{c}_{-k,\downarrow} \hat{c}_{k,\uparrow} | \psi_{MF} \rangle \tag{7.15}$$

$$\Delta_{NN-s} = \frac{1}{2L} \sum_{k} \langle \psi_{MF} | \hat{c}_{-k,\downarrow} \hat{c}_{k,\uparrow} | \psi_{MF} \rangle \left[\cos(k_x) + \cos(k_y) \right]$$
 (7.16)

$$\Delta_{NN-d} = \frac{1}{2L} \sum_{k} \langle \psi_{MF} | \hat{c}_{-k,\downarrow} \hat{c}_{k,\uparrow} | \psi_{MF} \rangle \left[\cos(k_x) - \cos(k_y) \right]$$
 (7.17)

$$\Delta_{\text{Triplet}-\nu} = \frac{1}{L} \sum_{k} \langle \psi_{MF} | \hat{c}_{-k,\downarrow} \hat{c}_{k,\uparrow} | \psi_{MF} \rangle \sin(k_{\nu})$$
 (7.18)

For convenience, we express the superconducting parameters involving terms with $\cos(k_x)$ and $\cos(k_y)$ as nearest-neighbor s-wave and d-wave superconducting parameters, denoted by Δ_{NN-s} and Δ_{NN-d} , respectively. We observe that the superconducting terms Δ_{NN-s} and Δ_{NN-d} correspond to the spin-singlet channel, while $\Delta_{\text{Triplet},x}$ and $\Delta_{\text{Triplet},y}$ belong to the spin-triplet channel

In this particular treatment, we consider a mean-field ground state where the only non-zero correlations are $\langle \psi_{MF} | \hat{c}^{\dagger}_{k\sigma} \hat{c}_{k\sigma} | \psi_{MF} \rangle$, $\langle \psi_{MF} | \hat{c}_{-k,\downarrow} \hat{c}_{k,\uparrow} | \psi_{MF} \rangle$ and $\langle \psi_{MF} | \hat{c}^{\dagger}_{k,\uparrow} \hat{c}^{\dagger}_{-k,\downarrow} | \psi_{MF} \rangle$; all other terms vanish by assumption.

We now show the mean-field decoupling in the case of \hat{H}_U and omit the more involved calculation for $\hat{H}_g^{x,NN}$. In the following equation, the averages are intended to be performed on the mean-field ground state, i.e., $\langle \hat{c}_{-q+p,\downarrow} \hat{c}_{q+p,\uparrow} \rangle = \langle \psi_{MF} | \hat{c}_{-q+p,\downarrow} \hat{c}_{q+p,\uparrow} | \psi_{MF} \rangle$.

$$\frac{U}{L} \sum_{k} \sum_{q} \sum_{p} \hat{c}_{k+p,\uparrow}^{\dagger} \hat{c}_{-k+p,\downarrow}^{\dagger} \hat{c}_{-q+p,\downarrow} \hat{c}_{q+p,\uparrow}$$

$$\frac{HF}{L} \sum_{k} \sum_{q} \sum_{p} \delta_{p,0} \left[\langle \hat{c}_{k+p,\uparrow}^{\dagger} \hat{c}_{-k+p,\downarrow}^{\dagger} \rangle \hat{c}_{-q+p,\downarrow} \hat{c}_{q+p,\uparrow} + \hat{c}_{k+p,\uparrow}^{\dagger} \hat{c}_{-k+p,\downarrow}^{\dagger} \langle \hat{c}_{-q+p,\downarrow} \hat{c}_{q+p,\uparrow} \rangle + \left[\langle \hat{c}_{k+p,\uparrow}^{\dagger} \hat{c}_{-k+p,\downarrow}^{\dagger} \rangle \langle \hat{c}_{-q+p,\downarrow} \hat{c}_{q+p,\uparrow} \rangle \right] + \left[\frac{U}{L} \sum_{k} \sum_{q} \sum_{p} \delta_{q,k} \left[\langle \hat{c}_{k+p,\uparrow}^{\dagger} \hat{c}_{q+p,\uparrow} \rangle \hat{c}_{-k+p,\downarrow}^{\dagger} \hat{c}_{-q+p,\downarrow} + \hat{c}_{k+p,\uparrow}^{\dagger} \hat{c}_{q+p,\uparrow} \langle \hat{c}_{-k+p,\downarrow}^{\dagger} \hat{c}_{-q+p,\downarrow} \rangle + \left[\langle \hat{c}_{k+p,\uparrow}^{\dagger} \hat{c}_{q+p,\uparrow} \rangle \langle \hat{c}_{-k+p,\downarrow}^{\dagger} \hat{c}_{-q+p,\downarrow} \rangle \right] =$$

$$= U \left[\sum_{k} \left(\hat{c}_{k,\uparrow}^{\dagger} \hat{c}_{-k,\downarrow}^{\dagger} \Delta_{0} + \text{h.c.} \right) - L |\Delta_{0}|^{2} + \sum_{k} \sum_{\sigma} \hat{c}_{k,\sigma}^{\dagger} \hat{c}_{k,\sigma} n_{0}^{\overline{\sigma}} - L n_{0}^{\dagger} n_{0}^{\dagger} \right] . \tag{7.19}$$

Thus, the Hartree-Fock approximation allows us to rewrite the interacting Hamiltonian in Eq. (7.8) as a quadratic fermionic Hamiltonian, which contains several parameters that must be determined self-consistently.

We anticipate that, after having completed the self-consistency procedure, all terms of the form S_x^{σ} , S_y^{σ} , $\Delta_{\text{Triplet}-x}$ and $\Delta_{\text{Triplet}-y}$ vanish for all values of the parameters U, g and μ we have considered. Therefore, we will omit these terms in the mean-field Hamiltonian.

Moreover, terms such as n_0^{σ} , C_x^{σ} , and C_y^{σ} correspond to a renormalization of the chemical potential μ and the hopping amplitude t in the non-interacting Hamiltonian \hat{H}_0 , Eq. (7.9). These contributions can therefore be absorbed into a renormalized non-interacting Hamiltonian, which we denote as \hat{H}_0 , that can be explicitly written as:

$$\hat{\tilde{H}}_{0} = \sum_{k,\sigma,\nu} \left[-2t - 8gC_{\nu}^{\bar{\sigma}} - 4gC_{\nu}^{\sigma} \right] \cos(k_{\nu}) \hat{c}_{k\sigma}^{\dagger} \hat{c}_{k\sigma} + \sum_{k,\sigma} \left(-\mu + Un_{0}^{\bar{\sigma}} + 4gn_{0}^{\sigma} - 2g \right) \hat{c}_{k\sigma}^{\dagger} \hat{c}_{k\sigma},$$
 (7.20)

where by $\bar{\sigma}$ we denote the opposite spin.

Therefore, the mean-field Hamiltonian, up to some constant terms such as $L |\Delta_0|^2$, can be expressed in the following way:

$$\hat{H}_{MF}^{\text{bSSH}} = \hat{\tilde{H}}_{0} + (U - 8g) \sum_{k} \left(\hat{c}_{k,\uparrow}^{\dagger} \hat{c}_{-k,\downarrow}^{\dagger} \Delta_{0} + \text{h.c.} \right) +$$

$$- 4g \sum_{k} \left[\hat{c}_{k,\uparrow}^{\dagger} \hat{c}_{-k,\downarrow}^{\dagger} \Delta_{NN-s} \left(\cos k_{x} + \cos k_{y} \right) + \text{h.c.} \right] +$$

$$- 4g \sum_{k} \left[\hat{c}_{k,\uparrow}^{\dagger} \hat{c}_{-k,\downarrow}^{\dagger} \Delta_{NN-d} \left(\cos k_{x} - \cos k_{y} \right) + \text{h.c.} \right] . \tag{7.21}$$

7.3.1.3 Sketch of the self-consistency procedure

To illustrate how the self-consistency procedure works, we start from the mean-field Hamiltonian in Eq. (7.21), which can be written as:

$$\hat{H}_{MF}^{\text{bSSH}} = \sum_{k} \left(\hat{c}_{k,\uparrow}^{\dagger}, \ \hat{c}_{-k,\downarrow} \right) \ \mathbb{H}_{MF}^{k} \left(\begin{array}{c} \hat{c}_{k,\uparrow} \\ \hat{c}_{-k,\downarrow}^{\dagger} \end{array} \right) \ . \tag{7.22}$$

At each momentum k, the problem reduces to diagonalizing the 2×2 matrix \mathbb{H}^k_{MF} . Due to its specific structure, the eigenvalue decomposition reads:

$$\mathbb{U}_k^{\dagger} \, \mathbb{H}_{MF}^k \, \mathbb{U}_k = \begin{bmatrix} \epsilon_k & 0 \\ 0 & -\epsilon_k \end{bmatrix} \,, \tag{7.23}$$

where $\epsilon_k \geq 0$.

Correspondingly, we define new fermionic operators at each k as

$$\begin{pmatrix} \hat{\gamma}_k \\ \hat{\zeta}_k^{\dagger} \end{pmatrix} = \mathbb{U}_k^{\dagger} \begin{pmatrix} \hat{c}_{k,\uparrow} \\ \hat{c}_{-k,\downarrow}^{\dagger} \end{pmatrix} . \tag{7.24}$$

Expressed in terms of these new operators, the mean-field Hamiltonian becomes diagonal:

$$\hat{H}_{MF}^{\text{bSSH}} = \sum_{k} \epsilon_{k} \left(\hat{\gamma}_{k}^{\dagger} \hat{\gamma}_{k} + \hat{\zeta}_{k}^{\dagger} \hat{\zeta}_{k} \right) . \tag{7.25}$$

For the ground state of $\hat{H}_{MF}^{\mathrm{bSSH}}$, the only non-zero two-point correlation functions for the new fermionic operators satisfy

$$\langle \psi_{MF} | \hat{\gamma}_p \hat{\gamma}_k^{\dagger} | \psi_{MF} \rangle = \langle \psi_{MF} | \hat{\zeta}_p \hat{\zeta}_k^{\dagger} | \psi_{MF} \rangle = \delta_{p,k} . \tag{7.26}$$

Thus, using Eq. (7.24) to rewrite the self-consistent parameters as expectation values of $\hat{\gamma}_k$ and $\hat{\zeta}_k$, their evaluation becomes straightforward and the self-consistent cycle simply requires iterating these steps until convergence of all parameters is achieved.

7.3.1.4 Numerical results

By inspecting Eq. (7.21), we can already recognize that for g > U/8 the on-site s-wave superconducting term, corresponding to the parameter Δ_0 , has a negative coefficient. Additionally, for g > U/4, the coefficient of Δ_0 is greater than that of the extended s-wave and d-wave superconducting terms. Consequently, in the regime where $g \gg U$, we expect the system to develop on-site s-wave super-conductivity, which may compete with d-wave and extended s-wave superconductivity in the region around $U/8 \lesssim g \lesssim U/4$. Numerical results confirm this prediction.

We performed the self-consistency calculation on a 20×20 lattice for various doping levels. We observed difficulty in the convergence of variational parameters for $g \lesssim U/8$.

For a doping level $\delta=1-N_e/L=0.25$, the system is dominated by the on-site s-wave superconducting term in the region g>U/8. Fig. 7.7 shows the values of the parameters Δ_0 and Δ_{NN-s} obtained after the self-consistency procedure converged, for different values of U and g. As shown in panel A, Δ_0 dominates in the large-g region. In panel B, one can observe that Δ_{NN-s} becomes progressively more important as g approaches the g=U/8 line, although it remains relatively small (the ratio Δ_0/Δ_{NN-s} never exceeds 0.15 for all points where convergence was achieved). The value of Δ_{NN-d} is always exceedingly small. In the region where the U interaction dominates over g, we were not able to reach convergence, however the superconducting parameters we are considering assume smaller and smaller values as the dominant-U region approaches.

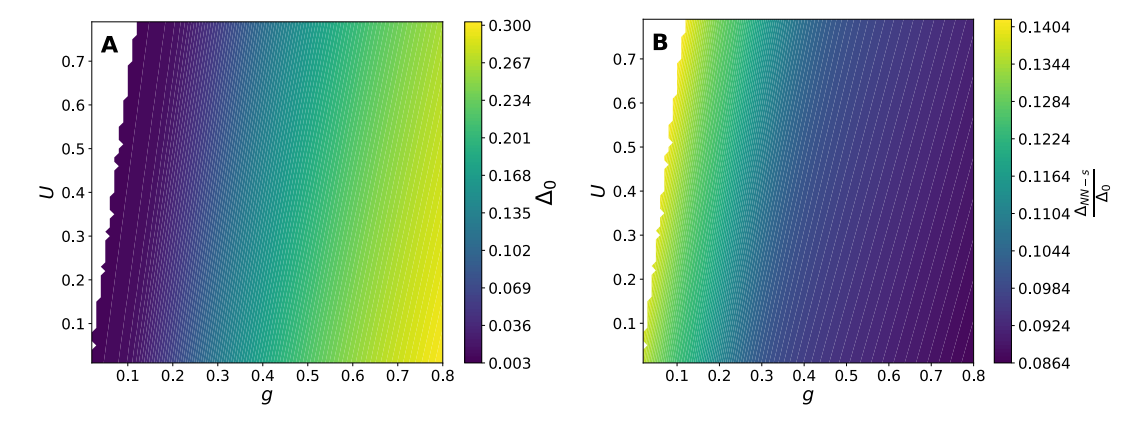


Figure 7.7: $\delta = 0.25$; phase diagram of the mean-field Hamiltonian for the bSSH-Hubbard model in the anti-adiabatic limit, Eq. (7.21). Superconducting self-consistent parameters are shown as a function of U and g. A: On-site s-wave superconducting parameter Δ_0 as a function of U and g, the parameter is larger in the $g \gg U$ region. B: Ratio Δ_{NN-s}/Δ_0 as a function of U and g.

For a lower doping level of $\delta=0.125$, as shown in Fig. 7.8, the system undergoes a transition from the region with g>U/4 where on-site s-wave superconductivity dominates (panel A), to a region where both d-wave superconductivity and on-site s-wave superconductivity coexist for $g\gtrsim U/8$ (panel B). In this region, the value of Δ_{NN-s} is always one order of magnitude

smaller than that of Δ_{NN-d} , as shown in panel C. As in the previous case, the ratio Δ_0/Δ_{NN-s} progressively increases while approaching the g=U/8 line, always remaining quite small (panel D). This result is consistent with previous numerical studies [39, 40], which employed density-matrix renormalization group and functional renormalization group, respectively, to identify a d-wave superconducting phase in the bSSH-Hubbard model.

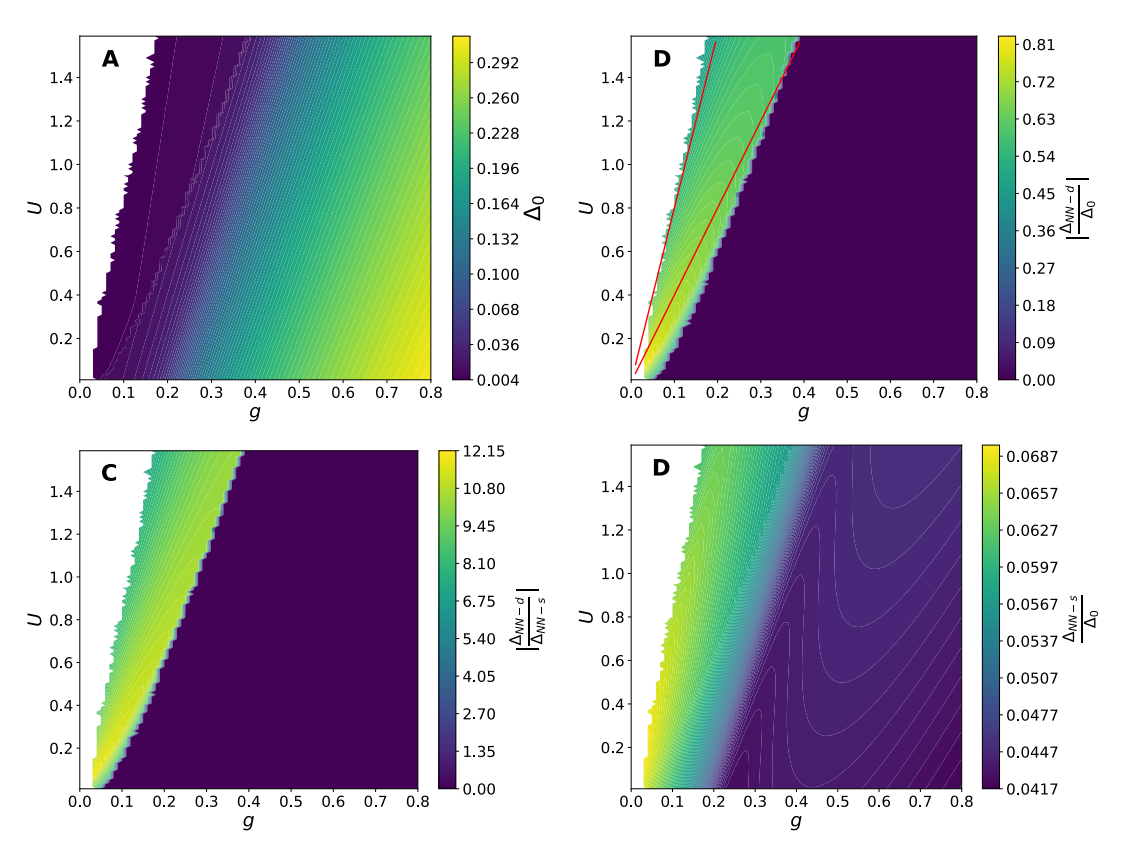


Figure 7.8: $\delta=0.125$, phase diagram of the mean-field Hamiltonian for the bSSH-Hubbard model in the anti-adiabatic limit, Eq. (7.21). A: On-site s-wave superconducting parameter Δ_0 as a function of U and g, the parameter is dominant in the large-g region. B: Ratio $|\Delta_{NN-d}/\Delta_0|$ as a function of U and g, the region of coexistence of d-wave and on-site s-wave superconductivity is clearly visible. The two red lines correspond to g=U/8 and g=U/4. C: Ratio $|\Delta_{NN-d}/\Delta_{NN-s}|$ as a function of U and g. D: Ratio Δ_{NN-s}/Δ_0 as a function of U and g.

7.3.2 Hartree-Fock: oSSH-Hubbard model at anti-adiabatic limit

We now turn to the oSSH case. The effective Hamiltonian, obtained after integrating out the phonons in the anti-adiabatic limit, is given by Eq. (6.17). One can notice that there is one term analogous to the bSSH case (with the same negative sign), along with an additional term with a positive sign. For clarity, we rewrite the Hamiltonian and split it into the following terms:

$$\hat{H}^{\text{oSSH}} = \hat{H}_0 + U \sum_{i} \hat{n}_{i\uparrow} \hat{n}_{i\downarrow} - g \sum_{R} \left(\hat{B}_{R,R+e_x} \right)^2 - g \sum_{R} \left(\hat{B}_{R,R+e_y} \right)^2 +
+ g \sum_{R} \hat{B}_{R-e_x,R} \hat{B}_{R,R+e_x} + g \sum_{R} \hat{B}_{R-e_y,R} \hat{B}_{R,R+e_y} =
= \hat{H}_0 + \hat{H}_U - \hat{H}_g^{x,NN} - \hat{H}_g^{y,NN} + \hat{H}_g^{x,NNN} + \hat{H}_g^{y,NNN} ,$$
(7.27)

where, as before, $\hat{B}_{ij} = \sum_{\sigma} \left(\hat{c}^{\dagger}_{i\sigma} \hat{c}_{j\sigma} + \hat{c}^{\dagger}_{j\sigma} \hat{c}_{i\sigma} \right)$ is the hopping operator connecting sites (i,j), while $\hat{H}^{x,NN}_g$ and $\hat{H}^{y,NN}_g$ are the nearest-neighbor squared hopping terms. The terms $\hat{H}^{x,NNN}_g$ and $\hat{H}^{y,NNN}_g$ correspond to new terms that involve products of two hopping

The terms $\hat{H}_g^{x,NNN}$ and $\hat{H}_g^{y,NNN}$ correspond to new terms that involve products of two hopping terms sharing a site and spanning next-nearest neighbor distances. The interaction strengths depend on the parameters U and g: in the case of oSSH phonons, the coupling g is given by $g = \frac{t^2\alpha^2}{K}$, as derived in Eq. (2.72).

7.3.2.1 The mean-field Hamiltonian

First, we express the Hamiltonian in k-space. Since the term $\hat{H}_g^{x,NN}$ is identical to the one analyzed in the previous section for the bSSH case, the only new contribution not examined earlier is given by $\hat{H}_g^{x,NNN}$, which in momentum space is expressed as:

$$\hat{H}_{g}^{x,NNN} = g \sum_{\sigma,\sigma'} \left(\hat{c}_{i\sigma}^{\dagger} \hat{c}_{i-e_{x},\sigma} + \hat{c}_{i-e_{x},\sigma}^{\dagger} \hat{c}_{i\sigma} \right) \left(\hat{c}_{i\sigma'}^{\dagger} \hat{c}_{i+e_{x},\sigma'} + \hat{c}_{i+e_{x},\sigma'}^{\dagger} \hat{c}_{i\sigma'} \right) =
= \frac{2g}{L} \sum_{k} \sum_{q} \sum_{p} \hat{c}_{k+p,\uparrow}^{\dagger} \hat{c}_{-k+p,\downarrow}^{\dagger} \hat{c}_{-q+p,\downarrow} \hat{c}_{q+p,\uparrow} \left[\cos(2q_{x}) + \cos(2k_{x}) + \right]
+ 2\cos(2p_{x})\cos(k_{x} - q_{x}) +
+ \frac{2g}{L} \sum_{\sigma} \sum_{k} \sum_{q} \sum_{p} \hat{c}_{k,\sigma}^{\dagger} \hat{c}_{k+p,\sigma} \hat{c}_{q,\sigma}^{\dagger} \hat{c}_{q-p,\sigma} \exp\left\{ -ip_{x} \right\} \cos(k_{x} + q_{x})$$
(7.28)

As done in the previous section, we now derive the mean-field Hamiltonian. Apart from the self-consistent parameters defined in Eqs. (7.14)–(7.18), two additional parameters need to be considered in this case:

$$T_{\nu}^{\sigma} = \frac{1}{L} \sum_{k} \cos(2k_{\nu}) \langle \psi_{MF} | \hat{c}_{k\sigma}^{\dagger} \hat{c}_{k\sigma} | \psi_{MF} \rangle$$
 (7.29)

$$\Delta_{NNN-s} = \frac{1}{2L} \sum_{k} \langle \psi_{MF} | \hat{c}_{-k,\downarrow} \hat{c}_{k,\uparrow} | \psi_{MF} \rangle \left[\cos(2k_x) + \cos(2k_y) \right]$$
 (7.30)

As before, we omit the explicit calculation of all contractions for the term $\hat{H}_g^{x,NNN}$ and write the mean-field Hamiltonian neglecting terms involving $\sin(k_x)$ or $\sin(k_y)$, which always vanish at the convergence of the self-consistent cycle.

Once again, we include the contribution of n_0^{σ} , C_x^{σ} , and C_y^{σ} terms into a new renormalized non-interacting Hamiltonian \hat{H}_0 , which is expressed as:

$$\hat{\tilde{H}}_0 = -2t \sum_{k,\sigma,\nu} \cos(k_\nu) \hat{c}_{k\sigma}^{\dagger} \hat{c}_{k\sigma} + \sum_{k,\sigma} \left(-\mu + U n_0^{\bar{\sigma}} + 4g n_0^{\sigma} - 2g \right) \hat{c}_{k\sigma}^{\dagger} \hat{c}_{k\sigma} . \tag{7.31}$$

Remarkably, due to a cancellation between terms with opposite coefficients arising from $\hat{H}_g^{x,NN}$ and $\hat{H}_g^{x,NNN}$, all d-wave and extended s-wave terms vanish. The resulting mean-field Hamiltonian is:

$$\hat{H}_{MF}^{\text{oSSH}} = \hat{H}_{0} + (U - 8g) \sum_{k} \left(\hat{c}_{k,\uparrow}^{\dagger} \hat{c}_{-k,\downarrow}^{\dagger} \Delta_{0} + \text{h.c.} \right) +
+ 2g \sum_{k} \left\{ \hat{c}_{k,\uparrow}^{\dagger} \hat{c}_{-k,\downarrow}^{\dagger} \left[\Delta_{0} \left(\cos 2k_{x} + \cos 2k_{y} \right) + 2\Delta_{NNN-s} \right] + \text{h.c.} \right\} +
+ 2g \sum_{k} \sum_{\sigma} \hat{c}_{k,\sigma}^{\dagger} \hat{c}_{k,\sigma} \left[n_{0}^{\sigma} \left(\cos 2k_{x} + \cos 2k_{y} \right) + T_{x}^{\sigma} + T_{y}^{\sigma} \right]$$
(7.32)

Numerical analysis shows that for this mean-field Hamiltonian, away from half-filling, only onsite s-wave superconductivity appears. The self-consistency procedure is the same as has been described in Sec. 7.3.1.3.

7.3.2.2 Numerical results

The Hamiltonian in Eq. (7.32) is actually simpler than the one from the previous bSSH case. For g > U/8, we expect an on-site s-wave superconducting ground state, since the parameter Δ_0 has a negative coefficient: this is confirmed by our numerical simulations.

We performed the self-consistency calculation on a 20×20 lattice at various doping levels and encountered difficulties in the convergence of the variational parameters for $g \lesssim U/8$.

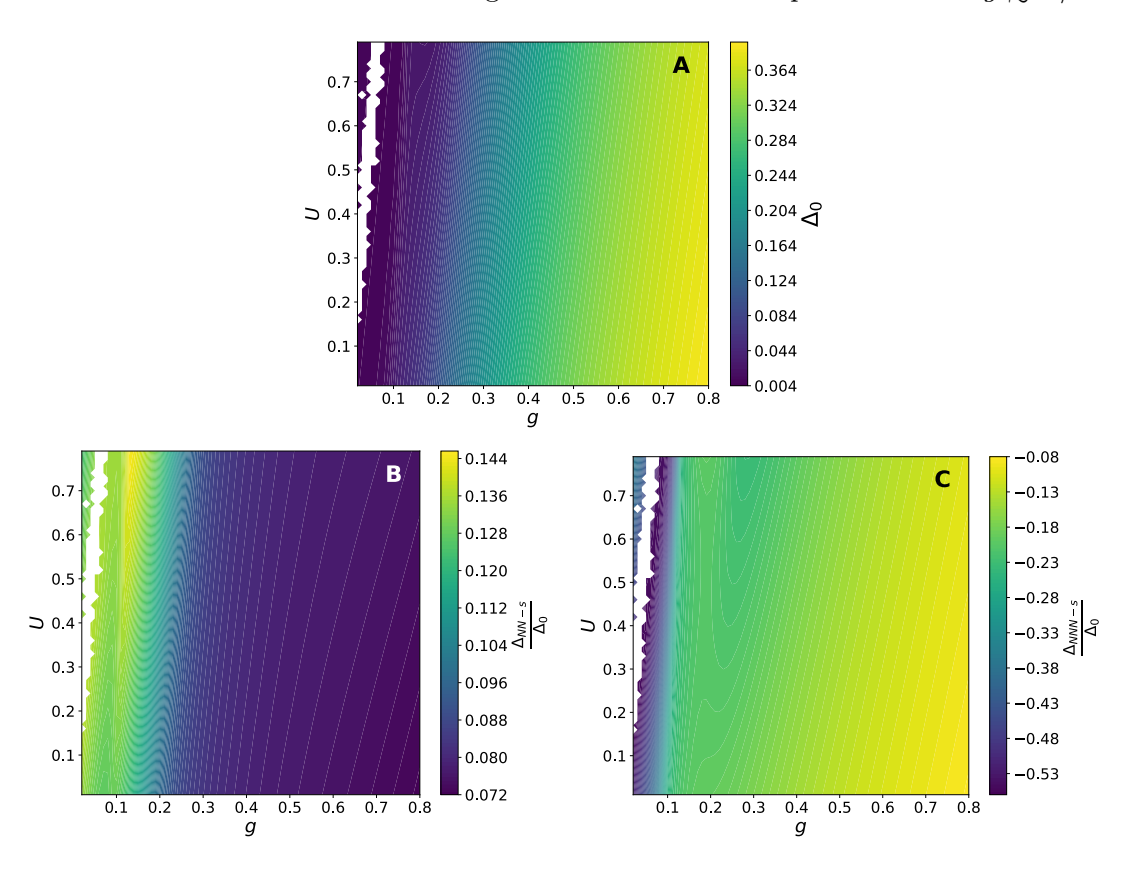


Figure 7.9: $\delta = 0.25$; phase diagram of the mean-field Hamiltonian for the oSSH-Hubbard model in the anti-adiabatic limit, Eq. (7.32). Superconducting self-consistent parameters are shown as a function of U and g.

A: On-site s-wave superconducting parameter Δ_0 as a function of U and g, the parameter is larger in the $g \gg U$ region.

B: Ratio Δ_{NN-s}/Δ_0 as a function of U and g.

C: Ratio Δ_{NNN-s}/Δ_0 as a function of U and g.

For a doping level of $\delta=0.25$, the system is dominated by the on-site s-wave superconducting term in the region g>U/8. Fig. 7.9 shows the values of the parameters Δ_0 , Δ_{NN-s} and Δ_{NNN-s} obtained after the self-consistency procedure converged, for different values of U and g. As shown in panel A, Δ_0 dominates in the large-g region. In panels B and C, we observe that Δ_{NN-s} and Δ_{NNN-s} become progressively closer to Δ_0 in magnitude as g approaches the g=U/8 line. However, since Δ_0 becomes extremely small as the dominant-U region approaches, we would not consider the region $g \lesssim U/8$ to be superconducting. The value of Δ_{NN-d} is always exceedingly small, which is reasonable, given that no d-wave terms appear in the mean-field Hamiltonian.

For a lower doping level of $\delta = 0.125$, as shown in Fig. 7.10, the physical description remains essentially the same, with the panels following the same structure as in Fig. 7.9.

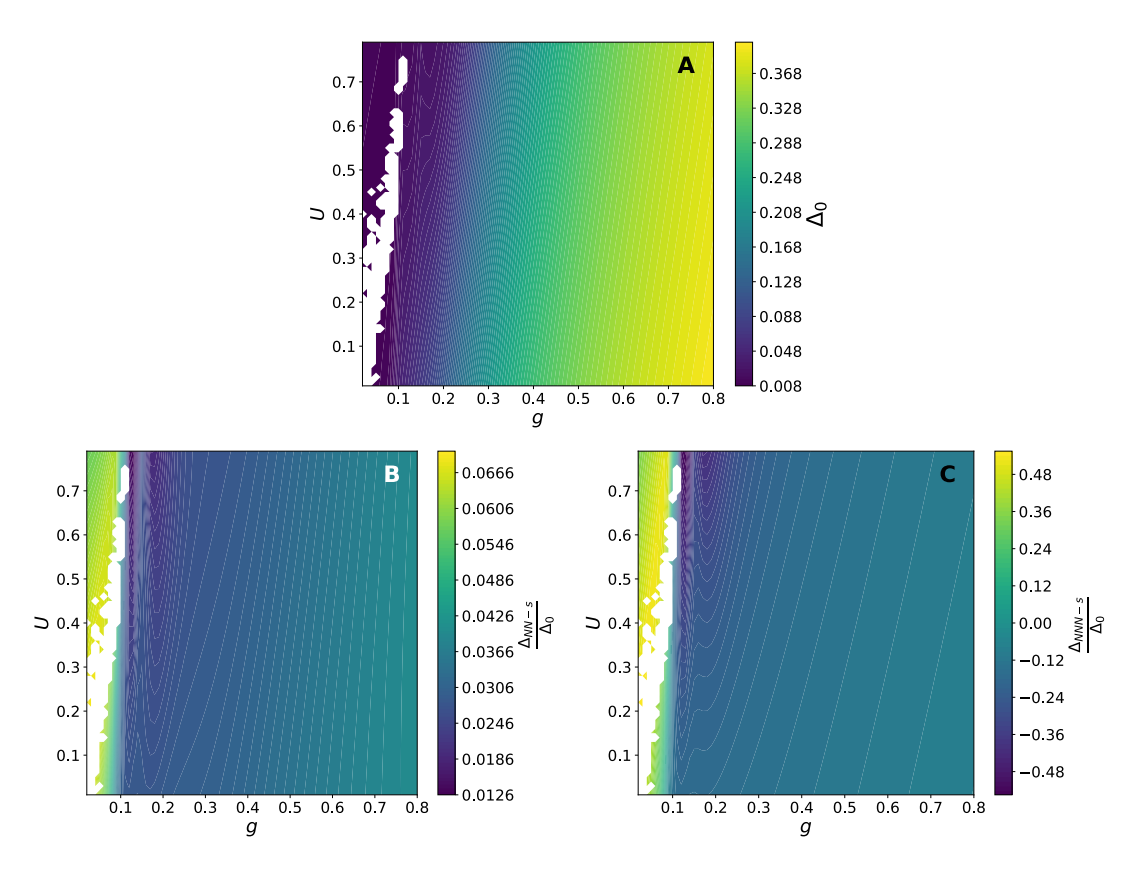


Figure 7.10: $\delta = 0.125$; phase diagram of the mean-field Hamiltonian for the oSSH-Hubbard model in the anti-adiabatic limit, Eq. (7.32). Superconducting self-consistent parameters are shown as a function of U and g.

A: On-site s-wave superconducting parameter Δ_0 as a function of U and g, the parameter is larger in the $g \gg U$ region.

B: Ratio Δ_{NN-s}/Δ_0 as a function of U and g.

C: Ratio Δ_{NNN-s}/Δ_0 as a function of U and g.

7.4 VMC results away from half-filling

In this section, we investigate via VMC the emergence of superconducting correlations in the oSSH-Hubbard model upon hole doping, focusing on the effects of varying the interaction strength U and the electron-phonon coupling λ . The hole doping level is defined as:

$$\delta = 1 - \frac{N_e}{L} \,, \tag{7.33}$$

where N_e is the total number of electrons and $L = l \times l$ is the number of lattice sites. Unless otherwise specified, all results are obtained from VMC simulations on an 8×8 lattice in the $S^z = 0$ sector, with the number of up and down electrons both equal to $N_e/2$.

Section 7.4.1 examines the case of U=0 and large λ , where on-site s-wave pairing emerges upon doping. For U/t=10 and small λ , a dominant d-wave pairing appears, although superconducting correlations are weaker than in the plain Hubbard model, suggesting a slight suppression by the electron-phonon coupling (section 7.4.2). Lastly, for both large U and λ , superconducting correlations remain weak and short-ranged (section 7.4.3). These results suggest that phonons in the oSSH model promote superconductivity in the weakly correlated regime, but do not support robust superconducting phases when the electronic interaction becomes strong.

7.4.1 s-wave superconductivity at U = 0 and large λ

We first examine the emergence of superconductivity away from half-filling at U=0 in the presence of strong electron–phonon coupling. For $\lambda=0.36$ and $\hbar\omega/t=1$, the system lies in the BOW phase at half-filling. Upon hole doping, we observe a progressive melting of the BOW.

The BOW with ordering vector $Q = (\pi, \pi)$ persists up to $\delta = 0.25$. At $\delta = 11/32$, the BOW pattern is fully suppressed, and dominant on-site s-wave superconducting correlations appear. This superconducting tendency is first signaled by the onset of a significant on-site s-wave pairing amplitude Δ_0 in the auxiliary Hamiltonian, see Eq. (3.29). To further describe the superconducting properties, we compute the on-site pair-pair correlation function

$$P_s(R) = \frac{1}{L} \sum_{R'} \langle \psi_{\text{var}} | \hat{\Delta}_{R'+R} \hat{\Delta}_{R'}^{\dagger} | \psi_{\text{var}} \rangle , \qquad (7.34)$$

where $\hat{\Delta}_R = \hat{c}_{R,\downarrow} \hat{c}_{R,\uparrow}$ is the on-site singlet pairing operator. Correlations $P_s(R)$ are evaluated as a function of distance R = (r, 0) and R = (0, r), with $r = 0, 1, \ldots, l - 1$ on an $l \times l$ lattice.

Figure 7.11 shows $P_s(R)$ for the oSSH-Hubbard model at U=0, $\lambda=0.36$, and $\delta=11/32$, compared with results for the attractive Hubbard model at U/t=-2 and the same doping, obtained with a Jastrow-Slater ansatz. The decay of correlations in the oSSH model is comparable with that of the attractive Hubbard model, indicating an effective electron-electron attraction mediated by phonons.

To further explore the connection between the electron-phonon coupling strength λ and the emergence of superconductivity, we analyze a second case with reduced coupling. In Fig. 7.12, we present oSSH-Hubbard results at $\lambda=0.25$ and doping level $\delta=0.25$, showing the same comparison with the attractive Hubbard model at U/t=-2. While both the oSSH-Hubbard and the attractive Hubbard models display comparable superconducting correlations, we observe that the attractive Hubbard model now shows slightly stronger and more slowly decaying correlations than the oSSH case. As expected, the strength of the effective pairing is controlled by λ .

Finally, we remark that the presence of s-wave superconductivity in this regime is consistent with our findings from the Hartree-Fock analysis performed in the anti-adiabatic limit in Section 7.3.2. This conclusion also agrees with a recent DQMC analysis, which reported the presence of s-wave superconductivity within the oSSH model at U=0 under hole doping [28].

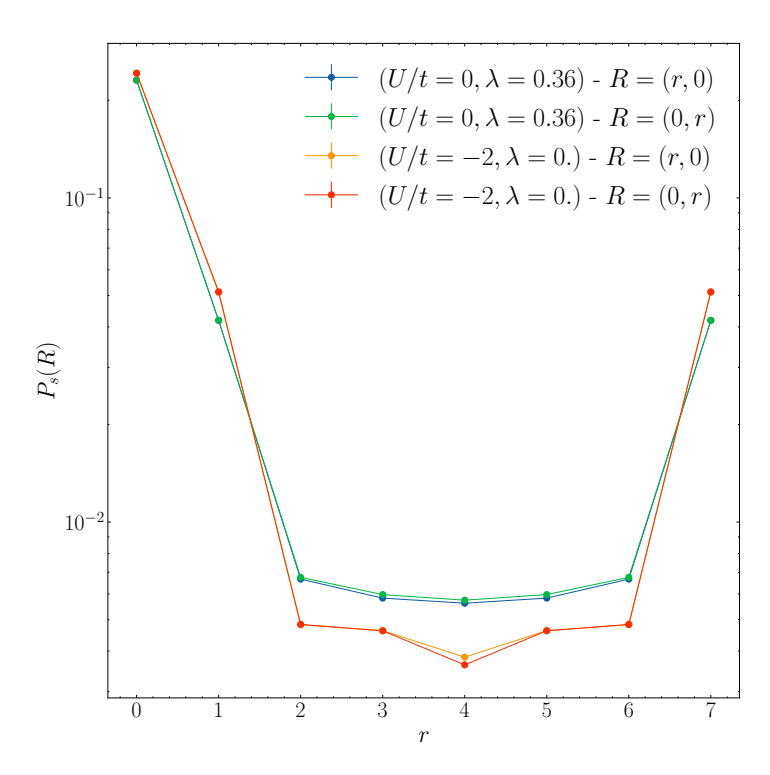


Figure 7.11: On-site s-wave superconducting correlations $P_s(R)$ at $(U=0,\lambda=0.36)$, and $\hbar\omega/t=1$, for doping $\delta=11/32$ (42 electrons on an 8×8 lattice). Results are shown as a function of R=(x,0) and R=(0,x). The variational results for the oSSH-Hubbard model are compared with those from a Jastrow-Slater ansatz for the attractive Hubbard model $(U/t=-2,\lambda=0)$, showing qualitatively similar behavior.

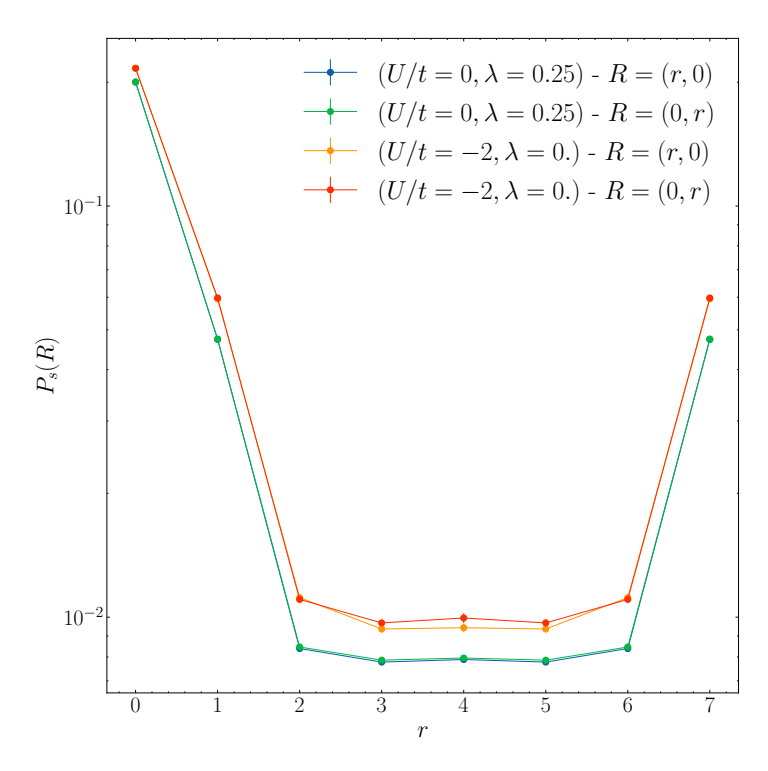


Figure 7.12: On-site s-wave superconducting correlations $P_s(R)$ at U=0, $\lambda=0.25$, and $\hbar\omega/t=1$, for doping $\delta=0.25$ (48 electrons on an 8×8 lattice). The same quantities are shown as in Fig. 7.11. Compared to the attractive Hubbard model at U/t=-2, the oSSH model exhibits slightly faster-decaying correlations, suggesting a reduced effective attractive interaction at lower λ .

7.4.2 Weak d-wave superconductivity at U/t = 10 and small λ

We now investigate the emergence of d-wave superconducting correlations in the strongly correlated regime, considering U/t=10 and a small electron–phonon coupling $\lambda=0.16$ with $\hbar\omega/t=1$. At half-filling, these parameters place the system in the AFM phase, which is also the ground state of the conventional Hubbard model on the square lattice. Upon doping to $\delta=1/8$ (56 electrons on an 8×8 lattice), it is known that by means of a Jastrow-Slater ansatz one can obtain a d-wave superconductive phase in the plain Hubbard model (excluding stripe-like solutions, which we do not consider here).

In our VMC study of the oSSH-Hubbard model at $\delta = 1/8$, the variational wave function develops a finite d-wave pairing amplitude Δ_d in the auxiliary Hamiltonian, as defined in Eq. (3.29), which dominates over the s-wave components. To quantify the superconducting correlations, we evaluate the pair-pair correlation functions:

$$P_{xx}(R) = \frac{1}{L} \sum_{R'} \langle \psi_{\text{var}} | \hat{\Delta}_{x,R'+R} \hat{\Delta}_{x,R'}^{\dagger} | \psi_{\text{var}} \rangle , \qquad (7.35)$$

$$P_{yy}(R) = \frac{1}{L} \sum_{R'} \langle \psi_{\text{var}} | \hat{\Delta}_{y,R'+R} \hat{\Delta}_{y,R'}^{\dagger} | \psi_{\text{var}} \rangle , \qquad (7.36)$$

$$P_{xy}(R) = \frac{1}{L} \sum_{R'} \langle \psi_{\text{var}} | \hat{\Delta}_{x,R'+R} \hat{\Delta}_{y,R'}^{\dagger} | \psi_{\text{var}} \rangle , \qquad (7.37)$$

where the nearest-neighbor singlet pairing operators are defined as:

$$\hat{\Delta}_{x,R}^{\dagger} = \hat{c}_{R,\uparrow}^{\dagger} \hat{c}_{R+e_x,\downarrow}^{\dagger} - \hat{c}_{R,\downarrow}^{\dagger} \hat{c}_{R+e_x,\uparrow}^{\dagger} , \qquad (7.38)$$

$$\hat{\Delta}_{y,R}^{\dagger} = \hat{c}_{R,\uparrow}^{\dagger} \hat{c}_{R+e_y,\downarrow}^{\dagger} - \hat{c}_{R,\downarrow}^{\dagger} \hat{c}_{R+e_y,\uparrow}^{\dagger} . \tag{7.39}$$

In Fig. 7.13, we show the decay of $P_{xx}(R)$ along the x and y directions, i.e., for R = (r, 0) and R = (0, r), with $r \in \{0, \ldots, l-1\}$. We find that $P_{xx}(R)$, $P_{yy}(R)$, and $P_{xy}(R)$ have comparable magnitudes, with $P_{xy}(R)$ carrying the opposite sign—a hallmark of d-wave symmetry.

To assess the relevance of these correlations, we compare our results with those obtained from a plain Hubbard model (with $\lambda=0$ at U/t=10 and the same doping), using a standard Jastrow-Slater wave function. The comparison reveals that the plain Hubbard model exhibits stronger pairing correlations with a slower decay than the oSSH-Hubbard model. This suggests that the electron-phonon interaction in the oSSH-Hubbard model, in this regime, does not significantly enhance d-wave superconductivity; in fact, it may slightly suppress it.

This result may appear counterintuitive, but is actually consistent with previous findings. In Ref. [108], the authors studied the attractive bSSH-Hubbard model using DQMC simulations, which are sign-problem free thanks to the attractive interaction U < 0. They observed that the SSH-type electron-phonon coupling tends to compete with, rather than enhance, the attractive Hubbard interaction both at and away from half-filling.

7.4.3 Preliminary results at large U/t and large lambda

We now examine superconducting correlations near the AFM–BOW phase boundary, focusing on results obtained at U/t=4 and U/t=10 with $\hbar\omega/t=0.5$. Referring to the phase diagram in Fig. 7.3, we selected two representative points close to the transition line: $(U/t=4, \lambda=0.2)$ and $(U/t=10, \lambda=0.35)$. Although both points lie within the AFM phase at half-filling, our variational calculations show that, upon doping to $\delta=1/8$, a BOW solution becomes energetically favorable in both cases.

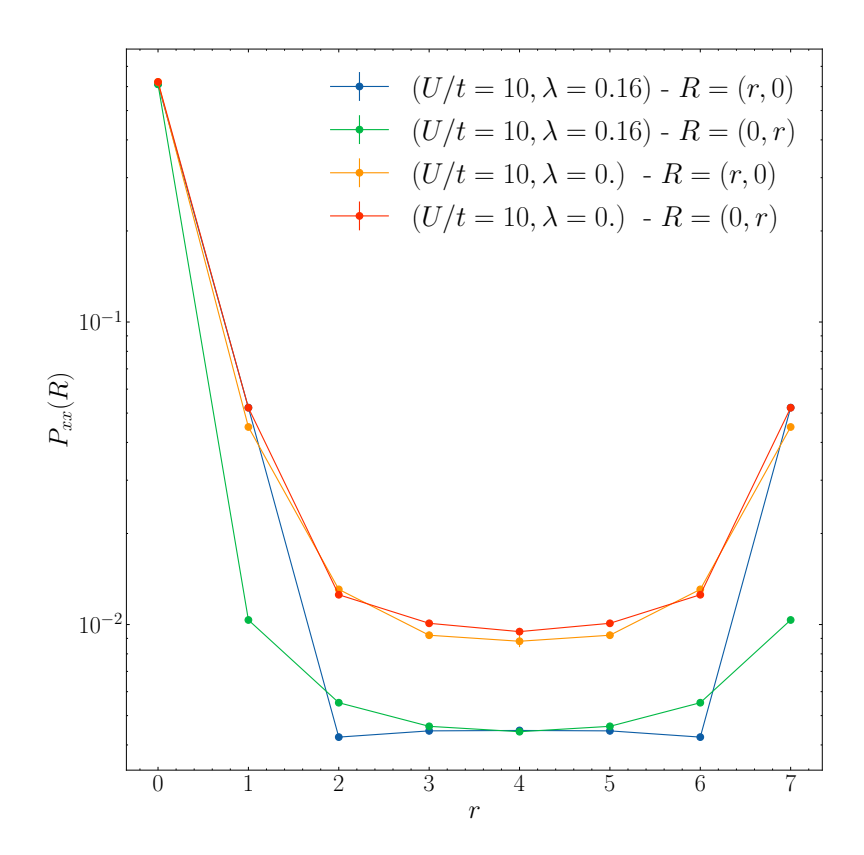


Figure 7.13: Nearest-neighbor superconducting correlations $P_{xx}(R)$ as a function of R=(r,0) and R=(0,r) on an 8×8 lattice at U/t=10, $\lambda=0.16$, and $\hbar\omega/t=1$, with doping $\delta=1/8$. The variational results for the oSSH-Hubbard model are compared with those from a standard Hubbard model ($\lambda=0$) using a Jastrow-Slater wave function. Despite the presence of d-wave pairing in the variational ansatz, the phonon interaction does not enhance superconductivity in this regime.

As the BOW melts with further increasing doping, superconducting variational parameters appear in the auxiliary Hamiltonian. In particular, both the on-site s-wave (Δ_0) and extended s-wave (Δ_s) parameters become finite. Nevertheless, the resulting superconducting correlations remain weak: $P_s(R)$, $P_{xx}(R)$, $P_{yy}(R)$, and $P_{xy}(R)$ decay to values below 10^{-3} , reaching down to 10^{-4} . A possible explanation is that the parameters Δ_0 and Δ_s acquire opposite signs, which may partially cancel their individual contributions to pairing correlations, see Eq. (3.29).

Our results represent a first step toward exploring the superconducting properties of the oSSH-Hubbard model in the regime of simultaneously large U and λ . A systematic study on larger lattices will be necessary to fully characterize the nature of superconductivity in this regime. In any case, the present findings reinforce the picture that has emerged so far: while the oSSH coupling λ alone may favor s-wave superconductivity at U=0 (Section 7.4.1), strong Hubbard interactions compete with this tendency. The d-wave superconductivity observed when U dominates (Section 7.4.2) is not enhanced by a small λ , and when U and λ are comparable near the AFM-BOW transition, their competition is even stronger, resulting in only weak superconducting correlations.

Chapter 8

Conclusions and Future Perspectives

This thesis investigates the impact of quantum phonons on the Hubbard model, focusing on the Su–Schrieffer–Heeger (SSH) coupling. The variational Monte Carlo method employed has proven robust in both one- and two-dimensional lattice models. It provides accurate insights into the interplay between lattice distortions and electronic correlations, revealing the emergence of a rich variety of physical behaviors. In particular, in one-dimensional systems the formation of a Luther–Emery liquid has been demonstrated and benchmarked against density-matrix renormalization group calculations. In one dimension large clusters can be efficiently accessed, allowing for a reliable characterization of the properties of the system in the thermodynamic limit.

In two dimensions, the situation becomes more intriguing and more debated due to the possible stabilization of superconducting states. Variational Monte Carlo calculations are, however, limited to relatively small clusters. An additional complication arises from the fact that the specific implementation of the SSH interaction can significantly affect the physical properties. In particular, the bond-centered SSH (bSSH) and site-centered SSH (oSSH) models, both considering optical phonons, may lead to different outcomes, including distinct phase diagrams in the hole-doped regime. This expectation is supported by a Hartree–Fock calculation we performed in order to gain further insights into the superconducting properties. Future investigations will be necessary to achieve a more comprehensive understanding of these models in the hole-doped regime.

Looking ahead, several directions for future work can be identified.

- **GPU Acceleration:** Migrating the code to GPU-based implementations could significantly speed up diagonalization processes, enabling the simulation of larger system sizes and more complex calculations.
- Incorporating Pairings and Magnetic Fields: In two-dimensional systems, a coexistence of bond-order wave and antiferromagnetic order may occur. To capture this behavior, it is essential to employ a trial wave function that can represent both simultaneously. A more advanced ansatz incorporating pairings and an in-plane magnetic field should therefore be developed. This requires replacing the Slater determinant with a Pfaffian, thus allowing a more accurate description of phase coexistence in the half-filling phase diagram of the oSSH—Hubbard model on the square lattice. Such a wave function would unify the antiferromagnetic, bond-order wave, and coexistence regions within a single variational framework.
- Pairings and In-Plane Magnetic Fields: In two-dimensional systems, a coexistence of bond-order wave and antiferromagnetic order may arise. To capture this behavior, it is crucial to employ a trial wave function capable of representing both simultaneously and

faithfully. A more advanced ansatz incorporating both pairings and an in-plane magnetic field should therefore be developed, replacing the Slater determinant with a Pfaffian. This would enable a unified variational framework for the antiferromagnetic, bond-order wave, and coexistence regions, and allow for a more accurate study of phase coexistence in the half-filling phase diagram of the oSSH-Hubbard model on the square lattice.

- Wave Function Refinement: Further improvements to the trial wave function could be explored by incorporating additional terms inspired by neural-network-based ansätze. In a preliminary study, we tested a phonon-based Restricted Boltzmann Machine preserving lattice translations, added to the variational wave function to extend the description of phonon dispersion beyond the simple Gaussian framework. The results, however, did not show significant quantitative improvements: only in one dimension the variational energy was slightly lowered, and for this reason the ansatz was not included in the final analysis. Nonetheless, more sophisticated architectures, including deep neural networks, remain highly relevant for these systems, and it cannot be excluded that they may yield substantial improvements in two-dimensional studies.
- Putative Superconductive Phase in the Strongly Correlated Regime of the oSSH-Hubbard Model: Further investigations are required to characterize the phase obtained by doping the system in the large-U, strong electron-phonon coupling regime, particularly to clarify the nature of the superconducting phase that may emerge.
- Enhancing d-Wave Superconductivity in the bSSH Model: Implementing a backflow-enhanced variational wave function for this model would enable a more precise search for d-wave superconductivity, providing an instructive comparison with the behavior observed in the oSSH model.
- Multimode Phonon Effects in the aSSH Model: In the adiabatic (Born–Oppenheimer) limit, the distortion pattern of phonons at half-filling leads to an infinitely degenerate ground state in the thermodynamic limit, displaying multimode configurations. A key open question is whether finite-frequency quantum phonons may induce an order-by-disorder mechanism, favoring some patterns over others. Moreover, it remains intriguing to explore whether, and in what form, superconductivity could develop in this model.

In summary, this work contributes to the understanding of SSH-like interactions in strongly correlated systems, while opening several avenues for future research to explore more complex phenomena and further refine our models. The findings presented here lay a solid foundation for future studies on the role of lattice effects in quantum materials.

Acknowledgments

Giunti all'ultima pagina, pare il minimo ringraziare per primo Federico, che mi ha seguito passo passo in questo percorso, mettendosi sempre a disposizione e finendo spesso vittima del mio entusiasmo e delle mie continue domande, che mi hanno portato a invadere il suo ufficio fin troppo spesso. La ricerca scientifica con Federico è un'esperienza unica, fatta di un linguaggio a dir poco colorito, tanta ironia, momenti di sconforto in cui nulla sembra tornare (e in cui lui ha sempre l'aria di prenderla con filosofia) e attimi di gioia per i traguardi raggiunti; porterò nel cuore gli aneddoti, le risate e gli insegnamenti che hanno reso questo cammino così speciale.

Un sentito grazie anche a Michele: al di là della sua disponibilità e cordialità, la sua vastissima conoscenza e comprensione dei modelli di cui ci siamo occupati è stata in più di un'occasione indispensabile per dissipare i dubbi e riportare chiarezza quando tutto sembrava confuso.

Continuando con i collaboratori scientifici, un ringraziamento va anche a Francesco Ferrari, che ha fornito un supporto prezioso nei primi momenti del progetto alla base di questa tesi e che ora ha intrapreso una nuova avventura in azienda, che si spera possa vivere con soddisfazione e serenità. Un grazie a Roberta, con cui è stato un piacere condividere l'ufficio e collaborare al suo articolo in cui, tra fasi note e una fase innominata, ho avuto l'opportunità di avere giusto un assaggio del mondo degli isolanti topologici. Un ringraziamento molto sentito ad Alberto Parola, le cui sortite triestine portano sempre il buonumore, insieme a un sacco di buone idee, pareri scientifici sempre acuti, conditi dal suo impagabile humor. Sembra giusto ringraziare tutte le persone che mi hanno supportato e aiutato nel portare a termine il mio primo lavoro, su tutti Giuseppe, ma anche Guglielmo e Christian. Per finire, sarebbe impossibile non ricordare Sandro: in questi anni, nel corso dei vari progetti, non è stato raro avere la sensazione di stare sulle sue spalle e di portare avanti qualcosa che lui aveva iniziato tanto tempo fa. Pensare di proseguire il cammino che lui aveva tracciato non colma il vuoto della sua assenza, ma rende ancora più evidente il segno profondo che ha lasciato dietro di sé.

Un ringraziamento va anche a Luciano, con cui non ho mai avuto il piacere di collaborare direttamente a qualche articolo: ciò nondimeno, il suo supporto tecnico e i suoi consigli sono stati sempre preziosi, senza contare una notevole quantità di lunghe discussioni scientifiche, sempre stimolanti ed entusiasmanti. Per finire, un ringraziamento a Francesco Tognocchi, con cui ho avuto il piacere di collaborare solamente per un anno: un periodo fatto di interessanti chiacchierate su funzioni theta e traslazioni magnetiche, insieme a divertenti codici in C++, che hanno reso più vivace il mio lavoro quotidiano. Sono certo che i frutti di ciò che abbiamo fatto insieme non tarderanno ad arrivare.

Al di fuori dell'ambito puramente scientifico, per prima va citata senza alcun dubbio Mery. In questo aspetto della vita credo di essere stato molto fortunato, forse più di quanto meritassi. Non so come avrei potuto vivere a Trieste senza di lei: il mio dottorato è stato segnato dalla sua radiosa presenza, dal suo instancabile supporto e dalle sue amorevoli attenzioni. Tutti i traguardi che ho raggiunto portano anche la sua firma, perché senza il suo sostegno non sarebbero stati possibili. Un semplice "grazie" sembra troppo poco nei confronti della persona che ha dato senso e bellezza alla mia vita, e che desidero avere al mio fianco per sempre. Ora che questa parte del

cammino è conclusa, non vedo l'ora di scoprire e vivere insieme il futuro che ci attende.

Al di là di tutto, un ringraziamento a tutta la mia famiglia: ai miei genitori, che mi hanno incoraggiato in tutti questi anni e mi hanno consentito di giungere fino a qui; la sensazione di poter contare sul loro consiglio e sul loro aiuto di fronte a qualsiasi avversità riesce ogni volta a infondere tranquillità alla mia vita. Un grazie a mio fratello, che si sta coraggiosamente avviando sulla strada della fisica, con cui ho passato molte piacevoli ore parlando al telefono in questi anni. Un grazie speciale anche alla Zia Mery, che ci ha sempre regalato il suo affetto e il suo supporto, insieme alla sua compagnia quando è venuta a trovarci a Trieste con Simona; un ringraziamento anche a tutti gli altri miei familiari, tra cui alla nonna Mina, per tutti i discorsi e gli insegnamenti che mi hanno permesso di crescere; alla Zia Chicca, che ha fatto nascere in me il desiderio di seguire la strada della ricerca; e alla nonna Maria: il ricordo del suo amore incondizionato rimane indelebile e sono sicuro che sia molto fiera di me in questo momento. Un grazie anche alla famiglia di Mery, per le serate passate a chiacchierare con Salvatore, le cene sempre abbondanti di Angela che mi hanno fatto sentire accolto e le indimenticabili vacanze in Calabria con tutti i parenti.

Per finire, un ringraziamento a tutti i compagni di viaggio che mi hanno accompagnato nel corso di questi anni: con voi ho condiviso l'ufficio, i banchi delle aule da cui seguire le lezioni, i tavoli della mensa, tanti momenti piacevoli durante e all'infuori dell'orario di lavoro. In ordine di apparizione, i miei compagni di corso alla SISSA, davanti ai quali si apre un futuro radioso fatto di PostDoc in giro per il mondo, insieme ai colleghi del mio anno di fisica statistica. Sono felice dei rapporti che si sono creati e della possibilità di allargare il gruppo anche al di fuori dell'ambito accademico, un gruppo di cui anche Mery si è sentita parte. Per non dimenticare i nomi: Zeno (con Luana), Alessio (insieme ad Arianna), Samuele (con Sandra), Anna e Cristiano, senza contare Matteo, Michele, Maha, Luca e Francesco Gentile. Una menzione speciale va anche ai vari data scientist, tra cui il mitico Riccardo, Vittorio e Mauro, nonché ai biofisici Matteo e Francesco, con cui ho condiviso un divertente progetto extra-accademico in quest'ultimo anno. Dopo il tanto tempo trascorso all'ICTP sarebbe impossibile non ringraziare le persone conosciute lì, tra cui Leonardo, Laria, Walter e Nicholas, oltre ai compagni d'ufficio Marco e Davide, con cui ho condiviso discussioni scientifiche e non, sempre accompagnate da risate e da una piacevole atmosfera.

Credo sia davvero tutto. Spero di non aver dimenticato nessuno; se così fosse, perdonatemi, questi ringraziamenti sono stati scritti di getto in una serata. A tutti, semplicemente: grazie.

Appendix A

Adiabatic and anti-adiabatic limits with simplified SSH Hamiltonian

Within Sec. 3.1, we start from the oSSH Hamiltonian:

$$\hat{H} = -t \sum_{i,\sigma} \left[1 - \alpha \left(\hat{x}_{i+1} - \hat{x}_i \right) \right] \left(\hat{c}_{i,\sigma}^{\dagger} \hat{c}_{i+1,\sigma} + \hat{c}_{i+1,\sigma}^{\dagger} \hat{c}_{i,\sigma} \right) + \sum_{i} \left[\frac{\hat{p}_i^2}{2m} + \frac{1}{2} m \omega^2 \hat{x}_i^2 \right] , \quad (A.1)$$

and show that, by applying a canonical transformation to rescale the coordinates of the phonon degrees of freedom, it can be written as:

$$\hat{H} = -t \sum_{i} \left[1 - \tilde{\alpha} \left(\hat{X}_{i+1} - \hat{X}_{i} \right) \right] \left(\hat{c}_{i}^{\dagger} \hat{c}_{i+1} + \hat{c}_{i+1}^{\dagger} \hat{c}_{i} \right) + \frac{\hbar \omega}{2} \sum_{i} \left[\hat{P}_{i}^{2} + \hat{X}_{i}^{2} \right] , \qquad (A.2)$$

The Hamiltonian in Eq. (A.2) allows us to perform our simulations by specifying only the phonon frequency $\hbar\omega$. However, a slight issue arises. When working with the original Hamiltonian in Eq. (A.1), the adiabatic and anti-adiabatic limits of the phonon degrees of freedom are well-defined in terms of the phonon mass m and frequency ω through Eqs. (2.9) and (2.59). For clarity, we present these two limits again here.

In the adiabatic limit, corresponding to the Born-Oppenheimer approximation, the phonons become classical by acquiring infinite mass:

$$m \to \infty$$
 $\omega \to 0$ with $K = m\omega^2 = const$. (A.3)

In the anti-adiabatic limit, the phonon mass becomes negligible, allowing the phonon degrees of freedom to be effectively integrated out:

$$m \to 0$$
 $\omega \to \infty$ with $K = m\omega^2 = const$. (A.4)

When using the Hamiltonian in Eq. (3.6), where only the phonon frequency needs to be specified, it becomes less straightforward to derive the adiabatic and anti-adiabatic limits. A simple interpretation based on Eqs. (A.3) and (A.4) would suggest that in the adiabatic limit, the phonon frequency tends to zero, while in the anti-adiabatic limit, it tends to infinity. Although this explanation is correct, a simple sketch can help visualize the situation more clearly. In Fig. A.1, we illustrate how, even without knowing the specific values of K and m, but only relying on the relation $K = \omega^2 m$, decreasing ω leads to a region of very large mass, corresponding to the adiabatic limit, while, as $\omega \to \infty$, one approaches a region of vanishing mass, corresponding to the anti-adiabatic limit.

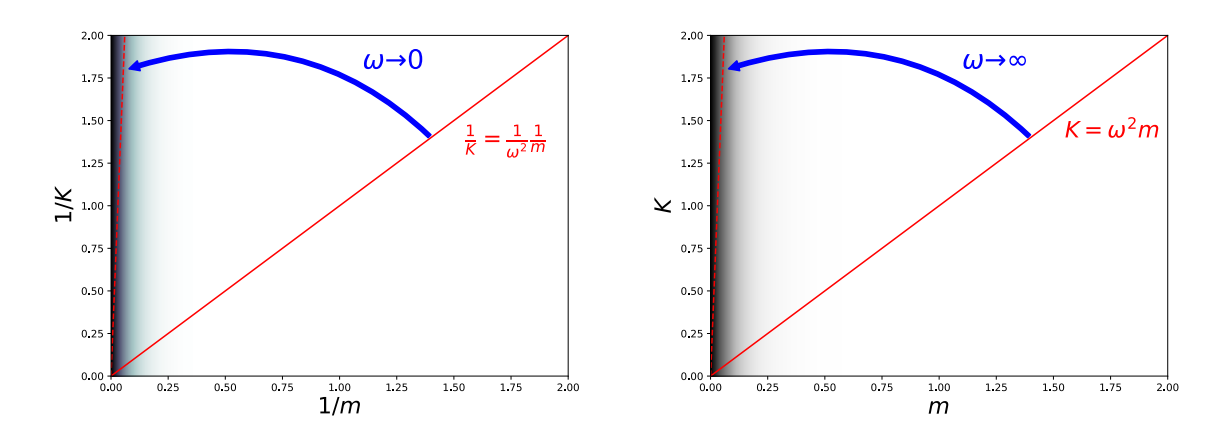


Figure A.1: Visualization of the adiabatic and anti-adiabatic limits (left and right panels, respectively), based on the relation $K = \omega^2 m$. In the left panel, it is shown how, by decreasing the value of ω , the straight line relating 1/K and 1/m approaches the shaded region of infinite mass, corresponding to the adiabatic limit. In the right panel, the same behavior is illustrated as ω increases, where the straight line relating m and K moves closer to the shaded region of vanishing mass, corresponding to the anti-adiabatic limit.

Appendix B

Derivatives of a slater determinant depending on continuous coordinates: automatic differentiation

In this appendix, we focus on the antisymmetric component of the wave function, denoted as $\langle X; n_{\sigma} | \Psi_{\rm e} \rangle$, which is part of the variational wave function defined in Eq. (3.13). Our goal is to show how to compute derivatives for this specific antisymmetric wave function. Specifically, we are interested in:

- First-order derivatives with respect to the variational parameters, which are essential for the optimization procedure, see Eq. (4.26).
- First- and second-order derivatives with respect to the phonon displacements $\{X_j\}$, which are necessary to compute the Laplacian that appears in the phonon part of the local energy, see Eqs. (4.19) and (4.21).

We begin by explicitly defining the wave function and discussing its implementation in Sections B.1 and B.2. For simplicity, we provide an explicit example of the wave function for the one-dimensional case, although extending this treatment to the two-dimensional case is straightforward. (Throughout this analysis, we work within a reduced Hilbert subspace with a fixed electron number and zero magnetization, such that $\sum_{i} n_{i,\uparrow} = \sum_{i} n_{i,\downarrow} = N_e/2$.)

electron number and zero magnetization, such that $\sum_j n_{j,\uparrow} = \sum_j n_{j,\downarrow} = N_e/2$.) In Section B.3, we provide a brief overview of automatic differentiation methods, which can be categorized into forward and backward automatic differentiation. While backward automatic differentiation is more efficient for computing first-order derivatives in our case, the forward method, with appropriate modifications, is well-suited for computing the Laplacian with respect to the phonon displacement coordinates. We refer to this modified method as the Forward Laplacian method.

First, in Section B.4, we demonstrate how backward automatic differentiation can be used to compute first-order derivatives of our wave function. Then, in Section B.5, we show how the same first-order derivatives can be computed using forward automatic differentiation. Finally, in Section B.6, we discuss how the Laplacian can be computed within the framework of automatic differentiation and apply the Forward Laplacian method to our wave function in Section B.7.

B.1 Wave function definition and implementation

We divide this section into two cases: the first considers a wave function that represents the ground state of an auxiliary Hamiltonian without any pairing variational parameters, while the second case includes pairing parameters.

B.1.1 Determinant without pairing terms

Considering a wave function that does not include any pairing variational parameters, the amplitude of a given configuration $|X; n_{\sigma}\rangle$ is computed as follows. First, the non-interacting and real Hamiltonian \hat{H}_{ep} (which explicitly depends on the phonon displacements $\{X_j\}$ in the configuration $|X\rangle$) can be written as:

$$\hat{H}_{ep} = \sum_{i,j,\sigma} t_{ij} \hat{c}_{i,\sigma}^{\dagger} \hat{c}_{j,\sigma} + \mu \sum_{i,\sigma} \hat{c}_{i,\sigma}^{\dagger} \hat{c}_{i,\sigma} + B^{x} \sum_{i} (-1)^{i} \left[\hat{c}_{i,\uparrow}^{\dagger} \hat{c}_{i,\downarrow} + \hat{c}_{i,\downarrow}^{\dagger} \hat{c}_{i,\uparrow} \right] + \\
+ \sum_{i,m,\sigma} g_{m} \left(X_{i+m} - X_{i} \right) \hat{c}_{i,\sigma}^{\dagger} \hat{c}_{i+m,\sigma} ,$$
(B.1)

where the hopping amplitudes $(t_{ij} = t_{ji})$, the chemical potential μ , the external magnetic field B^x and $g_m = g_{-m}$ are real variational parameters.

Next, we introduce a new index I that runs over all lattice sites i and the spin index σ , so that the fermionic operators $\hat{c}_{i,\sigma}^{\dagger}$ can be unified into a new vector \hat{d}_{I}^{\dagger} , defined as:

$$\hat{d}_{I}^{\dagger} = \left(\hat{c}_{1,\uparrow}^{\dagger}, \dots, \hat{c}_{L,\uparrow}^{\dagger}, \hat{c}_{1,\downarrow}^{\dagger}, \dots, \hat{c}_{L,\downarrow}^{\dagger}\right)_{I} \quad \text{with } i \in \{1, \dots, 2L\}.$$
 (B.2)

The Hamiltonian can then be rewritten as a quadratic form:

$$\hat{H}_{\rm ep} = \sum_{I,J} \hat{d}_I^{\dagger} \, \mathbb{H}_{I,J}(X) \, \hat{d}_J \,, \tag{B.3}$$

where $\mathbb{H}_{I,J}(X)$ is a $2L \times 2L$ matrix. To find the ground state, we need to find the matrix $U_{I,\alpha}(X)$ that diagonalizes $H_{I,J}(X)$ (we use the index I to indicate physical sites and the index α to refer to the eigenvalues). In the following, we may omit the explicit dependence on X and write $U_{I,\alpha}$, but one should always bear in mind that the matrix $\mathbb{H}_{I,J}$ depends explicitly on the phonon displacements $\{X_j\}$ in the local configuration $|X\rangle$.

Given that $U^{\dagger} \mathbb{H} U = E$, where $E = \operatorname{diag}(\lambda_0, \lambda_1, \dots, \lambda_{2L})$ is the diagonal matrix of eigenvalues sorted in ascending order, we can rewrite the Hamiltonian \hat{H}_{ep} as:

$$\hat{H}_{\rm ep} = \sum_{I,J} \left(U^{\dagger} \hat{d} \right)_{I}^{\dagger} \left(U^{\dagger} \mathbb{H} U \right)_{I,J} \left(U^{\dagger} \hat{d} \right)_{J} = \sum_{\alpha} \lambda_{\alpha} \, \hat{\phi}_{\alpha}^{\dagger} \hat{\phi}_{\alpha} \,, \tag{B.4}$$

where we define the new fermionic operators $\hat{\phi}_{\alpha}^{\dagger}$ as:

$$\hat{\phi}_{\alpha}^{\dagger} = \sum_{I} U_{I,\alpha} \hat{d}_{I}^{\dagger} . \tag{B.5}$$

The ground state of \hat{H}_{ep} can now be written in terms of these new fermionic operators as:

$$|\psi_0\rangle = \prod_{\alpha=1}^{N_e} \hat{\phi}_{\alpha}^{\dagger} |0\rangle . \tag{B.6}$$

The local state of electrons $|n_{\sigma}\rangle$ can be written as:

$$|n_{\sigma}\rangle = \hat{d}_{R_1}^{\dagger} \hat{d}_{R_2}^{\dagger} \dots \hat{d}_{R_{N_e}}^{\dagger} |0\rangle ,$$
 (B.7)

where R_1, \ldots, R_{N_e} are the sites occupied by electrons in the configuration $|n_{\sigma}\rangle$.

It is not difficult to prove that the matrix element of the state $|\psi_0\rangle$ over the local state $|X; n_{\sigma}\rangle$ is given by the following determinant:

$$\langle X; n_{\sigma} | \Psi_{e} \rangle = \det \left[\widetilde{U}_{R_{i},\alpha}(X) \right] ,$$
 (B.8)

where $\widetilde{U}_{R_i,\alpha}(X)$ is a $N_e \times N_e$ matrix formed by taking the rows R_i and the first N_e columns of the matrix $U_{I,\alpha}(X)$.

B.1.2 Determinant with pairing terms

In the case of a wave function that contains pairing terms, the procedure remains the same. However, in order to write the auxiliary Hamiltonian as a quadratic form, we need to perform a particle-hole transformation. The auxiliary Hamiltonian in the presence of pairing terms reads:

$$\hat{H}_{ep} = \sum_{i,j,\sigma} t_{ij} \hat{c}_{i,\sigma}^{\dagger} \hat{c}_{j,\sigma} + \mu \sum_{i,\sigma} \hat{c}_{i,\sigma}^{\dagger} \hat{c}_{i,\sigma} + \sum_{i,j} \Delta_{ij} \hat{c}_{i,\uparrow}^{\dagger} \hat{c}_{j,\downarrow}^{\dagger} + h.c. +
+ \sum_{i,m,\sigma} g_m (X_{i+m} - X_i) \hat{c}_{i,\sigma}^{\dagger} \hat{c}_{i+m,\sigma} + \sum_{i,m} h_m (X_{i+m} - X_i) \hat{c}_{i,\uparrow}^{\dagger} \hat{c}_{i+m,\downarrow}^{\dagger} + h.c. , (B.9)$$

where the hopping $(t_{ij} = t_{ji})$, pairing $(\Delta_{ij} = \Delta_{ji})$, chemical potential μ and backflow parameters $g_m = g_{-m}$ and $h_m = -h_{-m}$ are all real variational parameters.

We now define a 2L-dimensional vector \hat{d}_{I}^{\dagger} (with index I running over all lattice sites i and the spin index σ), which includes a particle-hole transformation in its definition:

$$\hat{d}_{I}^{\dagger} = \left(\hat{c}_{1,\uparrow}^{\dagger}, \dots, \hat{c}_{L,\uparrow}^{\dagger}, \hat{c}_{1,\downarrow}, \dots, \hat{c}_{L,\downarrow}\right)_{I} \quad \text{with } i \in \{1, \dots, 2L\}.$$
 (B.10)

Since spin-up creation operators are mapped into other creation operators $(\hat{c}_{i,\uparrow}^{\dagger} \to \hat{d}_{i}^{\dagger})$, but spin-down creation operators are mapped into destruction operators $(\hat{c}_{i,\downarrow}^{\dagger} \to \hat{d}_{i+L})$, this transformation maps spin-down states into the vacuum, and vice versa.

If $|0\rangle_j$ is the new vacuum state for the new fermionic operators at site j (i.e., $\hat{d}_j |\widetilde{0}\rangle = \hat{d}_{j+L} |\widetilde{0}\rangle = 0$), the local states are mapped in the following way:

$$|0\rangle_{j} \longrightarrow \hat{d}_{j+L}^{\dagger} |\widetilde{0}\rangle_{j}$$

$$|\uparrow\rangle_{j} = \hat{c}_{j,\uparrow}^{\dagger} |0\rangle_{j} \longrightarrow \hat{d}_{j}^{\dagger} \hat{d}_{j+L}^{\dagger} |\widetilde{0}\rangle_{j}$$

$$|\downarrow\rangle_{j} = \hat{c}_{j,\downarrow}^{\dagger} |0\rangle_{j} \longrightarrow |\widetilde{0}\rangle_{j}$$

$$|\uparrow\downarrow\rangle_{j} = \hat{c}_{j,\uparrow}^{\dagger} \hat{c}_{j,\downarrow}^{\dagger} |0\rangle_{j} \longrightarrow \hat{d}_{j}^{\dagger} |\widetilde{0}\rangle_{j}$$
(B.11)

We can define the occupation number of these new fermionic operators, related to their new vacuum, as the eigenvalues u_I of the operators $\hat{u}_I = \hat{d}_I^{\dagger} \hat{d}_I$.

Since we work with a fixed number of up and down electrons, $\sum_{j} n_{j,\uparrow} = \sum_{j} n_{j,\downarrow} = N_e/2$, expressing these constraints in terms of the occupation numbers of the new fermionic operators yields the following relations:

$$\sum_{j=1}^{L} n_{j,\uparrow} = \sum_{j=1}^{L} u_j = N_e/2 \; ; \qquad \sum_{j=1}^{L} n_{j,\downarrow} = \sum_{j=1}^{L} (1 - u_{j+L}) = N_e/2 \; ; \qquad \sum_{j=1}^{L} u_{j+L} = L - N_e/2 \; .$$
(B.12)

The total occupation of the new fermionic operators is therefore fixed at L independently of the N_e . It is immediate to notice that:

$$\sum_{I=1}^{2L} u_I = L \ . \tag{B.13}$$

At this point, the Hamiltonian \hat{H}_{ep} of Eq. (B.9) can be expressed as a quadratic form in terms of the new particle-hole transformed fermionic operators from Eq. (B.10). All the same steps from Eq. (B.3) to Eq. (B.8) can be followed here, with the key difference being that the local state $|n_{\sigma}\rangle$ should be expressed in terms of the vacuum of the new fermionic operators, as shown in Eq. (B.11). Therefore, the number of rows and columns to be taken from the matrix $U_{I,\alpha}(X)$ is L instead of N_e , with $\widetilde{U}_{R_i,\alpha}(X)$ being a $L \times L$ matrix.

B.2 Recap of wave function computation

In this section, we restate the key steps involved in computing the amplitude of the wave function for a given local configuration $|X; n_{\sigma}\rangle$, using a set of variational parameters, which we denote as α . This procedure is summarized in the simple flow diagram shown in Fig. B.1.

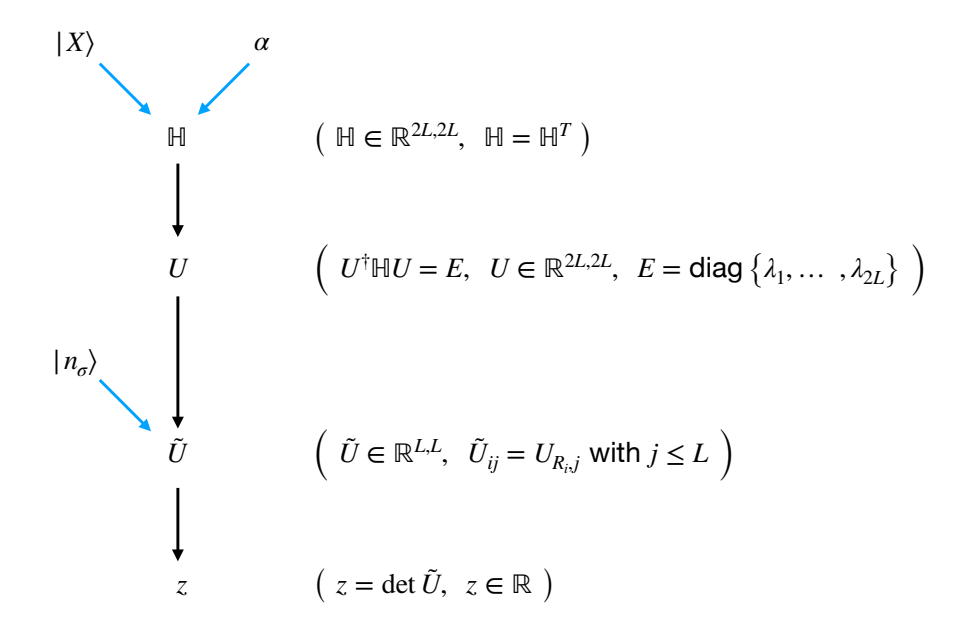


Figure B.1: Flow diagram illustrating the process of computing the amplitude of the wave function given a local configuration and variational parameters.

Our primary goal is to compute the first and second derivatives of $z = \det \widetilde{U}$ (as defined in Fig. B.1) with respect to each coordinate X_j . Additionally, we aim to compute the first derivatives with respect to the variational parameters α .

B.3 Automatic differentiation

Automatic differentiation (AD) is an essential tool in modern computational science, commonly used when calculating derivatives analytically becomes too complex or impractical. It is widely used in machine learning frameworks and is entirely based on the iterative application of the chain rule.

Unlike symbolic differentiation, AD does not require the construction of explicit analytical expressions for derivatives, enabling differentiation through iteration loops with no limitations except for memory usage. For any given function, AD provides the exact value of the derivative at a given point, without the approximations typical of finite difference methods, while keeping the computational cost proportional to the cost of evaluating the function itself.

B.3.1 Types of Automatic Differentiation

There are two primary types of automatic differentiation: forward (also called tangent) and backward (also called adjoint) differentiation.

We consider a function $f: \mathbb{R}^n \to \mathbb{R}^m$ with argument $\mathbf{x} \in \mathbb{R}^n$, whose $m \times n$ -dimensional Jacobian matrix J_f is defined as:

$$(J_f)_{ij} = \frac{\partial f_i(\mathbf{x})}{\partial x_j} \ . \tag{B.14}$$

The choice of which method to use depends on the relationship between m and n:

- Forward (Tangent) Automatic Differentiation: Most efficient when $m \gg n$. Forward AD computes a single column of the Jacobian in one pass, requiring n passes to compute the entire Jacobian.
- Backward (Adjoint) Automatic Differentiation: Most efficient when $n \gg m$. Backward AD computes a single row of the Jacobian in one pass, requiring m passes to compute the entire Jacobian.

In the case where $m \approx n$, both methods have comparable efficiency, in principle. The choice between them depends on the specific function and on the implementation details of automatic differentiation.

Since the wave function amplitude is a scalar value (m=1, real-valued in our case), backward AD is the most efficient method for computing first-order derivatives, both with respect to the variational parameters α and to the phonon displacements $\{X_i\}$.

In the following sections, we will first show how we employ backward automatic differentiation to compute first order derivatives. Next, we will show how the gradient with respect to phonon displacements $\{X_j\}$ can also be computed by forward automatic differentiation. At last, we will focus on how to compute second order derivatives with respect to $\{X_j\}$ by means of a Forward Laplacian method.

B.4 First order derivatives: Backward automatic differentiation

Backward automatic differentiation is particularly useful for computing first-order derivatives of a wave function. The method described below can be used to compute the derivatives of the antisymmetric part of the wave function $\langle X; n_{\sigma} | \Psi_{\rm e} \rangle$ with respect to both the phonon displacements $\{X_j\}$ and the variational parameters α . However, since the procedure for efficiently computing the Laplacian of $\langle X; n_{\sigma} | \Psi_{\rm e} \rangle$ with respect to $\{X_j\}$ automatically provides access to

the gradient, the procedure outlined below will be employed only for the variational parameters α in our numerical implementation.

Backward automatic differentiation operates as follows: we begin by defining the adjoint of the result as $\bar{z} \equiv \frac{\partial z}{\partial z} = 1$. This adjoint, \bar{z} , is then propagated backward through the computational graph shown in Fig. B.1, moving from bottom to top, and ultimately reaching the initial variables at the top of the figure. During this propagation, when the adjoint \bar{U} is computed, it is interpreted as $\bar{U}_{ij} = \frac{\partial z}{\partial U_{ij}}$. Once the adjoint $\bar{\alpha}_k$ is reached, the derivative $\frac{\partial z}{\partial \alpha_k}$ is obtained.

The rules for propagating adjoints for the matrix operations of interest are outlined in Ref. [109]. In our case, the first step is to compute the adjoint of a determinant; since $z = \det \widetilde{U}$, according to Ref. [109] we can write:

$$\tilde{\tilde{U}} = \bar{z} \ z \ \left(\tilde{U}^{-1}\right)^T \tag{B.15}$$

Note that \widetilde{U} is a $L \times L$ matrix (assuming we are working with particle-hole fermions). Then the $2L \times 2L$ matrix \overline{U} is trivially obtained:

$$\bar{U}_{R_i,j} = \bar{\tilde{U}}_{ij} \quad \text{for } i,j \in \{1,L\} ;$$
 $\bar{U}_{i,j} = 0 \quad \text{otherwise} .$ (B.16)

Next, we consider the eigendecomposition of the symmetric matrix \mathbb{H} written as $\mathbb{H}U = \Lambda U$, where $U^{-1} = U^T$ is the orthogonal matrix that performs the decomposition and Λ is the diagonal matrix of eigenvalues, namely $\Lambda = \text{diag}(\lambda_1, \lambda_2, \dots)$. The adjoint $\bar{\mathbb{H}}$ is computed as follows:

$$\bar{\mathbb{H}} = U \left[F \odot \left(U^T \ \bar{U} \right) \right] U^T , \qquad (B.17)$$

where the \odot operation is an element-wise product between matrices (all other operations are standard matrix products), and the antisymmetric matrix F is defined as:

$$F_{ij} = \begin{cases} \frac{1}{\lambda_j - \lambda_i} & \text{if } \lambda_i \neq \lambda_j \\ 0 & \text{if } \lambda_i = \lambda_j \end{cases} , \tag{B.18}$$

where, for computational reasons, in the numerical implementation we set to zero all elements corresponding to eigenvalues closer than a threshold 10^{-11} .

Finally, to propagate the adjoint through the function that returns the matrix \mathbb{H} given the parameters α , we compute:

$$\bar{\alpha}_k = \sum_{ij} \bar{\mathbb{H}}_{ij} \frac{\partial \mathbb{H}_{ij}}{\partial \alpha_k} , \qquad (B.19)$$

where the partial derivatives $\frac{\partial \mathbb{H}_{ij}}{\partial \alpha_k}$ are known analytically.

B.5 First order derivatives: Forward automatic differentiation

In this section, continuing with the wave function shown in Fig. B.1, we discuss how the first-order derivatives (computed in the previous section via backward AD) can also be obtained using a forward automatic differentiation scheme. In particular, we focus on computing the gradient with respect to the coordinates $\{X_i\}$.

Having fixed a certain coordinate X_j with respect to which we want to differentiate, the idea is to initialize a vector of tangent components $\dot{X}_i \equiv \frac{\partial X_i}{\partial X_j} = \delta_{i,j}$ and propagate the tangent \dot{X} by means of the chain rule through all the intermediate steps of the flow diagram in Fig. B.1,

moving from top to bottom. When, at some point in the calculation, one obtains the tangent $\dot{\tilde{U}}$, it corresponds to $\dot{\tilde{U}}_{l,m} = \frac{\partial \tilde{U}_{l,m}}{\partial X_j}$. At the end of the calculation, one obtains the derivative $\dot{z} = \frac{\partial z}{\partial X_j}$. The procedure is then simply repeated by looping over all the phonon coordinates X_j .

The first step is straightforward; it only requires to propagate \dot{X} element by element through the matrix \mathbb{H} :

$$\left(\dot{\mathbb{H}}\right)_{lm} = \sum_{i} \frac{\partial \mathbb{H}_{lm}}{\partial X_{i}} \dot{X}_{i} \qquad \rightarrow \qquad \left(\dot{\mathbb{H}}\right)_{lm} = \frac{\partial \mathbb{H}_{lm}}{\partial X_{j}} , \qquad (B.20)$$

where we made use of the fact that $\dot{X}_i = \delta_{i,j}$, being X_j the coordinate with respect to which we want to differentiate.

Next, to propagate the tangents through the eigendecomposition of the matrix \mathbb{H} , we just need to compute the antisymmetric matrix F defined in Eq. (B.18). Relying on known results regarding the derivative of an eigendecomposition, see Ref. [109], we can find:

$$\dot{U} = U \left[F \odot \left(U^T \dot{\mathbb{H}} \ U \right) \right] , \tag{B.21}$$

where the \odot operation is an element-wise product between matrices. Since the original matrix \mathbb{H} is symmetric, we assume that $U^{-1} = U^T$.

The next step is trivial and only requires extracting the submatrix $\dot{\tilde{U}}$ from the matrix \dot{U} following the definition of \tilde{U} .

$$\left(\dot{\tilde{U}}\right)_{lm} = \left(\dot{U}\right)_{R_l,m} \text{ with } m \le L \ .$$
 (B.22)

Finally, relying on Ref. [109] for the derivative of a determinant, we compute \dot{z} :

$$\dot{z} = z \operatorname{Tr} \left(\widetilde{U}^{-1} \dot{\widetilde{U}} \right) . \tag{B.23}$$

We notice that, in the case of forward automatic differentiation, the procedure involves looping over all coordinates $\{X_j\}$ to compute the gradient. For each coordinate, a different $\dot{\mathbb{H}}$, \dot{U} , $\dot{\widetilde{U}}$, and \dot{z} is computed. However, the entire gradient could have been obtained with a single backward pass, as shown in the previous section.

Specifically, since the adjoint $\bar{\mathbb{H}}$ is the same for all variational parameters, the backward automatic differentiation procedure needs to be performed only once to compute $\bar{\mathbb{H}}$. Once this is done, obtaining the gradient with respect to the coordinates $\{X_l\}$ is straightforward. It only requires computing:

$$\bar{X}_l = \sum_{ij} \bar{\mathbb{H}}_{ij} \frac{\partial \mathbb{H}_{ij}}{\partial X_l} , \qquad (B.24)$$

where the partial derivatives $\frac{\partial \mathbb{H}_{ij}}{\partial X_l}$ are known analytically.

B.6 The Laplacian with Automatic Differentiation: computing the Hessian matrix

In our specific case, we need to compute the Laplacian with respect to the phonon displacements $\{X_j\}$, thus, second-order derivatives are required. In most AD implementations (before July 2023), the Laplacian was computed by first calculating the Hessian matrix and then taking its trace (e.g., this is how the Laplacian calculation is implemented in the "Owl Scientific Computing" library [110, 111]). Although widely used, this method is computationally inefficient, as it involves calculating all mixed derivative terms, which are discarded after the trace is taken.

Consider a function $F: \mathbb{R}^n \to \mathbb{R}$ with argument $\mathbf{x} \in \mathbb{R}^n$. The $n \times n$ -dimensional Hessian matrix is defined as:

$$H_F(\mathbf{x}) = \frac{\partial^2 F(\mathbf{x})}{\partial x_i \partial x_j} \ . \tag{B.25}$$

However, we can define a function $\mathbf{G}: \mathbb{R}^n \to \mathbb{R}^n$ that returns the gradient of F, namely:

$$G_i(\mathbf{x}) = \frac{\partial F(\mathbf{x})}{\partial x_i}$$
 (B.26)

Computing the $n \times n$ -dimensional Jacobian matrix $J_{\mathbf{G}}$ of the function \mathbf{G} is equivalent to computing the Hessian matrix of the initial function F:

$$J_{\mathbf{G}}(\mathbf{x}) = \frac{\partial \mathbf{G}_i(\mathbf{x})}{\partial x_j} = \frac{\partial^2 F(\mathbf{x})}{\partial x_i \partial x_j} = H_F(\mathbf{x}) . \tag{B.27}$$

Therefore, to evaluate the Hessian matrix $H_F(\mathbf{x})$ at a specific point \mathbf{x} , we can apply automatic differentiation twice: the first pass computes the gradient of F at \mathbf{x} , which corresponds to the function $\mathbf{G}(\mathbf{x})$, and the second pass computes its Jacobian $J_{\mathbf{G}}(\mathbf{x})$ at the same point \mathbf{x} .

There are four ways to compute the Hessian, each with different computational efficiencies. The name of each method depends on whether forward or backward AD was employed to compute the gradient and the Hessian, namely: forward-over-forward, forward-over-backward, backward-over-forward, and backward-over-backward. The pros and cons of these methods are discussed in "The Autodiff Cookbook" section of the JAX library [112]. In the JAX library, the "hessian" function explicitly computes the entire Hessian matrix using the forward-over-backward method, where the backward pass is applied first to compute the gradient, followed by the forward pass.

B.7 Forward Laplacian method: directly computing the Laplacian

Although computing the full Hessian and taking its trace is a commonly used method, it is inefficient in our context since we only need the sum of the diagonal elements of the Hessian to compute the Laplacian. A more efficient algorithm, introduced in July 2023 as a preprint and later published in 2024 [113], computes the Laplacian directly without requiring the full Hessian. This method computes the Laplacian in a single forward pass (directly computing first and second derivatives), bypassing the need for mixed derivatives and avoiding the storage of the full Hessian.

Now we extend the treatment of the Section B.5, where we showed a simple forward AD scheme, to directly compute the Laplacian with respect to the coordinates $\{X_j\}$ by means of a single forward pass.

Having fixed a certain coordinate X_j with respect to which we want to differentiate, this time we initialize two vectors of tangent components: $\dot{X}_i = \delta_{i,j}$ and $\ddot{X}_i = \delta_{i,j}$, one for propagating the first and the other for the second derivative. The tangent \ddot{U} will correspond to $\ddot{U}_{l,m} = \frac{\partial^2 U_{l,m}}{\partial X_i^2}$.

B.7.1 Relations among tangents

First, we need to show a few relations regarding the tangents of various matrix operations. We derive all relations regarding second order tangents \ddot{x} . As for the usual tangents \dot{x} , we just show the relations as they are stated in Ref. [109], without deriving them from first principles.

B.7.1.1 Inverse of a matrix

$$C = A^{-1}$$

$$\dot{C} = -A^{-1}\dot{A} A^{-1}. \tag{B.28}$$

B.7.1.2 Determinant of a matrix

$$y = \det A$$

$$\dot{y} = y \operatorname{Tr} \left[A^{-1} \dot{A} \right]$$

$$\ddot{y} = \dot{y} \operatorname{Tr} \left[A^{-1} \dot{A} \right] + y \operatorname{Tr} \left[(\dot{A}^{-1}) \dot{A} \right] + y \operatorname{Tr} \left[A^{-1} \ddot{A} \right] =$$

$$= y \left\{ \left(\operatorname{Tr} \left[A^{-1} \dot{A} \right] \right)^{2} - \operatorname{Tr} \left[A^{-1} \dot{A} A^{-1} \dot{A} \right] + \operatorname{Tr} \left[A^{-1} \ddot{A} \right] \right\} . \tag{B.29}$$

B.7.1.3 Eigendecomposition of a symmetric matrix

Given a real symmetric matrix, $A = A^T$, we define its eigenvalues and eigenvectors according to the relation:

$$Av_i = \lambda_i v_i , \qquad (B.30)$$

where λ_j is the j-th eigenvalue, related to the eigenvector v_j . The eigenvectors v_j are the column of the orthogonal matrix U, with $U^T = U^{-1}$; the eigenvector equation can thus be written as:

$$AU = \Lambda U , \qquad (B.31)$$

where Λ is a diagonal matrix formed by the eigenvalues: $\Lambda = \text{diag}(\lambda_1, \lambda_2, ...)$. We define the F matrix as in Eq. (B.18). According to Ref. [109], the tangents are:

$$\dot{\lambda}_i = v_i^T \dot{A} v_i$$

$$\dot{U} = U \left[F \odot \left(U^T \dot{A} \ U \right) \right] . \tag{B.32}$$

We first compute the tangent of the matrix F of the inverse eigenvalue differences:

$$\dot{F}_{ij} = \begin{cases} \frac{\dot{\lambda}_i - \dot{\lambda}_j}{(\lambda_j - \lambda_i)^2} & \text{if } \lambda_i \neq \lambda_j \\ 0 & \text{if } \lambda_i = \lambda_j \end{cases}$$
(B.33)

Next, we can compute \ddot{U} easily:

$$\ddot{U} = \dot{U} \left[F \odot \left(U^T \dot{A} U \right) \right] + U \left[\dot{F} \odot \left(U^T \dot{A} U \right) \right] +
+ U \left[F \odot \left(U^T \ddot{A} U \right) \right] + U \left[F \odot \left(U^T \dot{A} \dot{U} \right) \right] +
+ U \left[F \odot \left(\left(\dot{U} \right)^T \dot{A} U \right) \right] ,$$
(B.34)

where \dot{A} and \ddot{A} must be given as initial tangents to be propagated, while terms F, \dot{U} , and \dot{F} have been defined above.

B.7.2 Computing the Laplacian for of the wave function

For the specific case of the wave function shown in Fig. B.1, since the SSH coupling is linear with respect to the phonon coordinates, the second derivative of \mathbb{H} with respect to each coordinate X_i is always vanishing. Therefore:

$$\left(\dot{\mathbb{H}}\right)_{lm} = \frac{\partial \mathbb{H}_{lm}}{\partial X_j} \qquad \left(\ddot{\mathbb{H}}\right)_{lm} = \frac{\partial^2 \mathbb{H}_{lm}}{\partial X_j^2} = 0$$
 (B.35)

Computing \dot{U} and \ddot{U} only requires to apply Eqs. (B.32) and (B.34), with the slight simplification that $\ddot{\mathbb{H}} = 0$ in our case.

Obtaining $\hat{\tilde{U}}$ and $\hat{\tilde{U}}$ is trivial and only involves extracting a submatrix:

$$\left(\ddot{\tilde{U}}\right)_{lm} = \left(\ddot{U}\right)_{R_l,m} \text{ with } m \le L ,$$
 (B.36)

the case of $\hat{\tilde{U}}$ has been shown in Eq. (B.22).

At last, one only needs to apply Eq. (B.30) to obtain \dot{z} and \ddot{z} . Looping over all phonon coordinates X_i allows us to compute all derivatives.

Since the quantities that are physically relevant are the first and second derivatives divided by the function itself, we notice that the value of the determinant simplifies when dividing the derivatives by z.

Bibliography

- [1] P. G. de Gennes, Superconductivity of Metals and Alloys. W.A. Benjamin, New York (1966).
- [2] R. Peierls, Quantum Theory of Solids. Clarendon Press, (1955).
- [3] J. Bardeen, L. N. Cooper, and J. R. Schrieffer, *Theory of Superconductivity*. Phys. Rev. 108, 1175 (1957).
- [4] Leon N. Cooper, Bound Electron Pairs in a Degenerate Fermi Gas. Phys. Rev. 104, 1189 (1956).
- [5] Emanuel Maxwell, Isotope Effect in the Superconductivity of Mercury. Phys. Rev. 78, 477 (1950).
- [6] S. A. Kivelson, I. P. Bindloss, E. Fradkin, V. Oganesyan, J. M. Tranquada, A. Kapitulnik, and C. Howald, How to detect fluctuating stripes in the high-temperature superconductors. Rev. Mod. Phys. 75, 1201 (2003).
- [7] Eduardo Fradkin, Steven A. Kivelson, and John M. Tranquada, Colloquium: Theory of intertwined orders in high temperature superconductors. Rev. Mod. Phys. 87, 457 (2015).
- [8] Z. Chen, Y. Wang, S. N. Rebec, T. Jia, M. Hashimoto, D. Lu, B. Moritz, R. G. Moore, T. P. Devereaux, and Z.-X. Shen, Anomalously strong near-neighbor attraction in doped 1D cuprate chains. Science 373, 1235 (2021).
- [9] A. Lanzara, P. V. Bogdanov, X. J. Zhou, S. A. Kellar, D. L. Feng, E. D. Lu, T. Yoshida, H. Eisaki, A. Fujimori, K. Kishio, J. I. Shimoyama, T. Noda, S. Uchida, Z. Hussain, and Z. X. Shen. Evidence for ubiquitous strong electron-phonon coupling in high-temperature superconductors. Nature 412, 510-514 (2001).
- [10] A. J. Berlinsky, T. Tiedje, J. F. Carolan, L. Weiler, and W. Friesen, Evidence for a Peierls Transition in TTF-TCNQ. Bulletin of the American Physical Society 20, 465 (1975)
- [11] H. Morawitz, Orientational Peierls Transition in Quasi One-Dimensional Organic Solids. Phys. Rev. Lett. 34, 1096 (1975).
- [12] Masashi Hase, Ichiro Terasaki, and Kunimitsu Uchinokura, Observation of the spin-Peierls transition in linear Cu_2^+ (spin-1/2) chains in an inorganic compound $CuGeO_3$. Phys. Rev. Lett. 70, 3651 (1993).
- [13] J.P. Boucher and L.P. Regnault, *The Inorganic Spin-Peierls Compound CuGeO*₃. J. Phys. I France 6 1939-1966 (1996).
- [14] M. Lüders, M. A. L. Marques, N. N. Lathiotakis, A. Floris, G. Profeta, L. Fast, A. Continenza, S. Massidda, and E. K. U. Gross, Ab initio theory of superconductivity. I. Density functional formalism and approximate functionals. Phys. Rev. B 72, 024545 (2005).

- [15] Daniel P. Arovas, Erez Berg, Steven Kivelson, and Srinivas Raghu, *The Hubbard Model*. Annual Review of Condensed Matter Physics, Vol. 13:239-274 (2022).
- [16] Mingpu Qin, Thomas Schäfer, Sabine Andergassen, Philippe Corboz, Emanuel Gull, The Hubbard model: A computational perspective. Annual Review of Condensed Matter Physics, Vol. 13:275-302 (2022).
- [17] H. Fröhlich, Electrons in lattice fields. Advances in Physics, Vol. 3:325-361 (1954).
- [18] T. Holstein, Studies of polaron motion: Part I. The molecular-crystal model. Annals of Physics, Volume 8, Issue 3, Pages 325-342 (1959).
- [19] W. P. Su, J. R. Schrieffer, and A. J. Heeger, Solitons in polyacetylene. Phys. Rev. Lett. 42, 1698 (1979).
- [20] W. P. Su, J. R. Schrieffer, and A. J. Heeger, Soliton excitations in polyacetylene. Phys. Rev. B 22, 2099–2111 (1980).
- [21] Martin Hohenadler, Holger Fehske, and Fakher F. Assaad, *Dynamic charge correlations* near the Peierls transition. Phys. Rev. B 83, 115105 (2011).
- [22] Martin Hohenadler, Fakher F. Assaad, and Holger Fehske, Effect of Electron-Phonon Interaction Range for a Half-Filled Band in One Dimension. Phys. Rev. Lett. 109, 116407 (2012).
- [23] Martin Hohenadler, and Fakher F. Assaad, Excitation spectra and spin gap of the half-filled Holstein-Hubbard model. Phys. Rev. B 87, 075149 (2013).
- [24] J. Greitemann, S. Hesselmann, S. Wessel, F. F. Assaad, and M. Hohenadler, *Finite-size effects in Luther-Emery phases of Holstein and Hubbard models*. Phys. Rev. B 92, 245132 (2015).
- [25] Anika Götz, Martin Hohenadler, and Fakher F. Assaad, *Phases and exotic phase transitions of a two-dimensional Su-Schrieffer-Heeger model.* Phys. Rev. B 109, 195154 (2024).
- [26] N. C. Costa, K. Seki, S. Yunoki, and S. Sorella, *Phase diagram of the two-dimensional Hubbard-Holstein model*. Commun Phys 3, 80 (2020).
- [27] F. F. Assaad, and M. Imada, Doping-induced metal-insulator transition in two-dimensional Hubbard and extended Hubbard models. Phys. Rev. B 58, 1845 (1998).
- [28] Andy Tanjaroon Ly, Benjamin Cohen-Stead, Sohan Malkaruge Costa, and Steven Johnston, Comparative study of the superconductivity in the Holstein and optical Su-Schrieffer-Heeger models. Phys. Rev. B 108, 184501 (2023).
- [29] L. Chaix, G. Ghiringhelli, Y. Y. Peng, M. Hashimoto, B. Moritz, K. Kummer, N. B. Brookes, Y. He, S. Chen, S. Ishida, Y. Yoshida, H. Eisaki, M. Salluzzo, L. Braicovich, Z. X. Shen, T. P. Devereaux, and W. S. Lee. *Dispersive charge density wave excitations in Bi₂Sr₂CaCu₂O_{8+δ}*. Nat. Phys. 13, 952 (2017).
- [30] Steve Johnston, Anamitra Mukherjee, Ilya Elfimov, Mona Berciu, and George A. Sawatzky, Charge Disproportionation without Charge Transfer in the Rare-Earth-Element Nickelates as a Possible Mechanism for the Metal-Insulator Transition. Phys. Rev. Lett. 112, 106404 (2014).

- [31] N. Mannella, W. L. Yang, X. J. Zhou, H. Zheng, J. F. Mitchell, J. Zaanen, T. P. Devereaux, N. Nagaosa, Z. Hussain, and Z. X. Shen, *Nodal quasiparticle in pseudogapped colossal mag*netoresistive manganites. Nature 438, 474–478 (2005).
- [32] S. Moser, S. Fatale, P. Krüger, H. Berger, P. Bugnon, A. Magrez, H. Niwa, J. Miyawaki, Y. Harada, and M. Grioni, Electron-Phonon Coupling in the Bulk of Anatase TiO₂ Measured by Resonant Inelastic X-Ray Spectroscopy Phys. Rev. Lett. 115, 096404 (2015).
- [33] N. Driza, S. Blanco-Canosa, M. Bakr, S. Soltan, M. Khalid, L. Mustafa, K. Kawashima, G. Christiani, H-U. Habermeier, G. Khaliullin, C. Ulrich, M. Le Tacon, and B. Keimer, Long-range transfer of electron-phonon coupling in oxide superlattices. Nature Materials 11, 675–681 (2012).
- [34] M. Hohenadler and F. F. Assaad, Peierls to superfluid crossover in the one-dimensional, quarter-filled Holstein model. J. Phys.: Condens. Matter 25 014005 (2012).
- [35] K. Yonemitsu, M. Imada, Spin-gap phase in nearly half-filled one-dimensional conductors coupled with phonons. Phys. Rev. B 54, 2410 (1996).
- [36] Debshikha Banerjee, Jinu Thomas, Alberto Nocera, and Steven Johnston, Ground-state and spectral properties of the doped one-dimensional optical Hubbard-Su-Schrieffer-Heeger model. Phys. Rev. B 107, 235113 (2023).
- [37] Alberto Nocera, John Sous3, Adrian E. Feiguin, and Mona Berciu, *Bipolaron liquids at strong Peierls electron-phonon couplings*. Phys. Rev. B 104, L201109 (2021).
- [38] Debshikha Banerjee, Alberto Nocera, George A. Sawatzky, Mona Berciu, and Steven Johnston, Spectral signatures of residual electron pairing in the extended Hubbard Su-Schrieffer-Heeger model. Phys. Rev. B 111, L241107 (2025).
- [39] Hao-Xin Wang, Yi-Fan Jiang, Hong Yao, Robust d-wave superconductivity from the Su-Schrieffer-Heeger-Hubbard model: possible route to high-temperature superconductivity. Science Bulletin, Volume 70, Issue 14 (2025).
- [40] Qing-Geng Yang, Da Wang, and Qiang-Hua Wang, Functional renormalization group study of the two-dimensional Su-Schrieffer-Heeger-Hubbard model. Phys. Rev. B 106, 245136 (2022).
- [41] J. E. Hirsch, Effect of Coulomb Interactions on the Peierls Instability. Phys. Rev. Lett. 51, 296 (1983).
- [42] Pinaki Sengupta, Anders W. Sandvik, and David K. Campbell, Peierls transition in the presence of finite-frequency phonons in the one-dimensional extended Peierls-Hubbard model at half-filling. Phys. Rev. B 67, 245103 (2003).
- [43] Manuel Weber, Fakher F. Assaad, and Martin Hohenadler, Excitation spectra and correlation functions of quantum Su-Schrieffer-Heeger models. Phys. Rev. B 91, 245147 (2015).
- [44] Xun Cai, Zi-Xiang Li, and Hong Yao, Antiferromagnetism Induced by Bond Su-Schrieffer-Heeger Electron-Phonon Coupling: A Quantum Monte Carlo Study. Phys. Rev. Lett. 127, 247203 (2021).
- [45] A. Götz, S. Beyl, M. Hohenadler, and F. F. Assaad, Valence-bond solid to antiferromagnet transition in the two-dimensional Su-Schrieffer-Heeger model by Langevin dynamics. Phys. Rev. B 105, 085151 (2022).

- [46] Bo Xing, Wei-Ting Chiu, Dario Poletti, R.T. Scalettar, and George Batrouni, *Quantum Monte Carlo Simulations of the 2D Su-Schrieffer-Heeger Model.* Phys. Rev. Lett. 126, 017601 (2021).
- [47] Andy Tanjaroon Ly, Benjamin Cohen-Stead, Steven Johnston, Antiferromagnetic and bond-order-wave phases in the half-filled two-dimensional optical Su-Schrieffer-Heeger-Hubbard model. Phys. Rev. B 111, 245138 (2025).
- [48] D. Baeriswyl and K. Maki, *Electron correlations in polyacetylene*. Phys. Rev. B 31, 6633 (1985).
- [49] Robert J. Bursill, Ross H. McKenzie, and Chris J. Hamer, *Phase Diagram of a Heisenberg Spin-Peierls Model with Quantum Phonons*. Phys. Rev. Lett. 83, 408 (1999).
- [50] Y. Z. Zhang, C. Q. Wu, and H. Q. Lin, Study of the ionic Peierls-Hubbard model using density matrix renormalization group methods. Phys. Rev. B 72, 125126 (2005).
- [51] R. Citro, E. Orignac, and T. Giamarchi, *Adiabatic-anti-adiabatic crossover in a spin-Peierls chain*. Phys. Rev. B 72, 024434 (2005).
- [52] Manuela Capello, Federico Becca, Michele Fabrizio, Sandro Sorella, and Erio Tosatti, *Variational Description of Mott Insulators*. Phys. Rev. Lett. 94, 026406 (2005).
- [53] Seher Karakuzu, Luca F. Tocchio, Sandro Sorella, and Federico Becca, Superconductivity, charge-density waves, antiferromagnetism, and phase separation in the Hubbard-Holstein model. Phys. Rev. B 96, 205145 (2017).
- [54] Luca F. Tocchio, Federico Becca, Alberto Parola, and Sandro Sorella, *Role of backflow correlations for the nonmagnetic phase of the t-t' Hubbard model.* Phys. Rev. B 78, 041101(R) (2008).
- [55] Luca F. Tocchio, Federico Becca, and Claudius Gros, Backflow correlations in the Hubbard model: An efficient tool for the study of the metal-insulator transition and the large-U limit. Phys. Rev. B 83, 195138 (2011).
- [56] Sandro Sorella, Wave function optimization in the variational Monte Carlo method. Phys. Rev. B 71, 241103(R) (2005).
- [57] Michele Fabrizio, Superconductivity from doping a spin-liquid insulator: A simple onedimensional example. Phys. Rev. B 54, 14 (1996).
- [58] S. Daul and R. M. Noack, Ferromagnetic transition and phase diagram of the onedimensional Hubbard model with next-nearest-neighbor hopping. Phys. Rev. B 58, 2635 (1998).
- [59] S. Nishimoto, K. Sano, and Y. Ohta, *Phase diagram of the one-dimensional Hubbard model with next-nearest-neighbor hopping*. Phys. Rev. B 77, 085119 (2008).
- [60] Leon Balents and Matthew P. A. Fisher, Weak-coupling phase diagram of the two-chain Hubbard model. Phys. Rev. B 53, 12133 (1996).
- [61] Yang Shen, Guang-Ming Zhang, and Mingpu Qin, Reexamining doped two-legged Hubbard ladders. Phys. Rev. B 108, 165113 (2023).

- [62] Pinaki Sengupta, Anders W. Sandvik, David K. Campbell, Bond-order-wave phase and quantum phase transitions in the one-dimensional extended Hubbard model. Phys. Rev. B 65, 155113 (2002).
- [63] Yoshiyuki Ono, and Tetsuya Hamano, Peierls Distortion in Two-Dimensional Tight-Binding Model. J. Phys. Soc. Jpn. 69, pp. 1769-1776 (2000).
- [64] Shutaro Chiba, and Yoshiyuki Ono, BOW-SDW Transition in the Two-dimensional Peierls-Hubbard Model. J. Phys. Soc. Jpn. 73, pp. 2777-2780 (2004).
- [65] Yuki Matsumoto, and Akira Terai, Electron correlation effects on multimode Peierls distortion in the two-dimensional electron-lattice system. Phys. Status Solidi C 9, 1183 (2012).
- [66] Shutaro Chiba, and Yoshiyuki Ono, Quantum Monte Carlo study of 2D spin Peierls state with multimode distortions. Physica E, 40, 1092 (2008).
- [67] S. Tang and J. E. Hirsch, *Peierls instability in the two-dimensional half-filled Hubbard model*. Phys. Rev. B 37, 9546 (1988).
- [68] Qingshan Yuan, and Thilo Kopp, Coexistence of the bond-order wave and antiferromagnetism in a two-dimensional half-filled Peierls-Hubbard model. Phys. Rev. B 65, 085102 (2002).
- [69] L.F. Tocchio, A. Montorsi, and F. Becca, Metallic and Insulating Stripes and Their Relation with Superconductivity in the Doped Hubbard Model. SciPost Phys. 7, 21 (2019).
- [70] V. Marino, F. Becca, and L.F. Tocchio, Stripes in the extended t t' Hubbard model: A variational Monte Carlo analysis. SciPost Phys. 12, 180 (2022).
- [71] G. Wellein, H. Fehske, and A. P. Kampf, *Peierls Dimerization with Nonadiabatic Spin-Phonon Coupling*. Phys. Rev. Lett. 81, 3956 (1998).
- [72] Anders W. Sandvik and David K. Campbell, Spin-Peierls Transition in the Heisenberg Chain with Finite-Frequency Phonons. Phys. Rev. Lett. 83, 195 (1999).
- [73] M. Braden, B. Hennion, W. Reichardt, G. Dhalenne, and A. Revcolevschi, *Spin-Phonon Coupling in CuGeO*₃. Phys. Rev. Lett. 80, 3634 (1998).
- [74] Malkaruge Costa, B. Cohen-Stead, A. T. Ly, J. Neuhaus, and S. Johnston, Comparative determinant quantum monte carlo study of the acoustic and optical variants of the suschrieffer-heeger model. Phys. Rev. B 108, 165138 (2023).
- [75] N. Batra and G. Sheet, Physics with coffee and doughnuts. Resonance 25, 765 (2020).
- [76] K. R. Subbaswamy and M. Grabowski, Bond alternation, on-site Coulomb correlations, and solitons in polyacetylene. Phys. Rev. B 24, 2168 (1981).
- [77] F. D. M. Haldane, Spontaneous dimerization in the S=1/2 Heisenberg antiferromagnetic chain with competing interactions. Phys. Rev. B 25, 4925(R) (1985).
- [78] A. M. Tsvelik, Spectrum of magnetic excitations in the spin-Peierls state. Phys. Rev. B 45, 486 (1992).
- [79] M. C. Cross and Daniel S. Fisher, A new theory of the spin-Peierls transition with special relevance to the experiments on TTFCuBDT. Phys. Rev. B 19, 402 (1979).

- [80] E. Fradkin, J. E. Hirsch, *Phase diagram of one-dimensional electron-phonon systems. I.* The Su-Schrieffer-Heeger model. Phys. Rev. B 27, 1680 (1983).
- [81] Y. Z. Zhang, C. Q. Wu, and H. Q. Lin, bond-order wave and energy gap in a one-dimensional bond-charge attraction model. Phys. Rev. B 66, 035115 (2002).
- [82] A. Weiße, G. Wellein, H. Fehske, Quantum lattice fluctuations in a frustrated Heisenberg spin-Peierls chain. Phys. Rev. B 60, 6566 (1999).
- [83] Carsten Raas, Ute Löw, and Götz S. Uhrig, Rainer W. Kühne, Spin-phonon chains with bond coupling. Phys. Rev. B 65, 144438 (2002).
- [84] Christopher J. Pearson, William Barford, and Robert J. Bursill, Quantized lattice dynamic effects on the Peierls transition of the extended Hubbard-Peierls model. Phys. Rev. B 83, 195105 (2011).
- [85] Christopher J. Pearson, William Barford, and Robert J. Bursill, *Quantized lattice dynamic effects on the spin-Peierls transition*. Phys. Rev. B 82, 144408 (2010).
- [86] Hiroshi Watanabe, Kazuhiro Seki, and Seiji Yunoki, Charge-density wave induced by combined electron-electron and electron-phonon interactions in 1T-TiSe₂: A variational Monte Carlo study. Phys. Rev. B 91, 205135 (2015).
- [87] Takahiro Ohgoe and Masatoshi Imada, Competition among Superconducting, Antiferromagnetic, and Charge Orders with Intervention by Phase Separation in the 2D Holstein-Hubbard Model. Phys. Rev. Lett. 119, 197001 (2017).
- [88] Francesco Ferrari, Federico Becca, and Roser Valentí, Spin-phonon interactions on the kagome lattice: Dirac spin liquid versus valence-bond solids. Phys. Rev. B 109, 165133 (2024).
- [89] R. P. Feynman and Michael Cohen, Energy Spectrum of the Excitations in Liquid Helium. Phys. Rev. 102, 1189 (1956).
- [90] Michael A. Lee, K. E. Schmidt, and M. H. Kalos, and G. V. Chester, Green's Function Monte Carlo Method for Liquid ³He. Phys. Rev. Lett. 46, 728 (1981).
- [91] K. E. Schmidt, Michael A. Lee, and M. H. Kalos, and G. V. Chester, *Structure of the Ground State of a Fermion Fluid.* Phys. Rev. Lett. 47, 80 (1981).
- [92] Federico Becca, Sandro Sorella, Quantum Monte Carlo Approaches for Correlated Systems. Cambridge University Press (2017).
- [93] N. Metropolis, A. W. Rosenbluth, M. N. Rosenbluth, and A. H. Teller, Equation of State Calculations by Fast Computing Machines. The Journal of Chemical Physics 21 (6), 1087-1092 (1953)
- [94] V. Ambegaokar and M. Troyer, Estimating errors reliably in Monte Carlo simulations of the Ehrenfest model. Am. J. Phys. 78, 150 (2009).
- [95] S. R. White, Density matrix formulation for quantum renormalization groups. Phys. Rev. Lett. 69, 2863 (1992).
- [96] Matthew Fishman, Steven R. White, E. Miles Stoudenmire, *The ITensor Software Library for Tensor Network Calculations*. SciPost Phys. Codebases 4 (2022).

- [97] Guifré Vidal, Efficient Classical Simulation of Slightly Entangled Quantum Computations. Phys. Rev. Lett. 91, 147902 (2003).
- [98] Shutaro Chiba, and Yoshiyuki Ono, *Phonon Dispersion Relations in Two-dimensional Peierls Phase*. J. Phys. Soc. Jpn. 73, pp. 2473-2479 (2004).
- [99] J. E. Hirsch, Antiferromagnetic singlet pairs, high-frequency phonons, and superconductivity. Phys. Rev. B 35, 8726 (1987).
- [100] Xin Lu, Huaiming Guo, Wei-Qiang Chen, D. N. Sheng, and Shou-Shu Gong, Tuning competition between charge order and superconductivity in the square-lattice t-t'-J model. Phys. Rev. B 111, 035139 (2025).
- [101] F. F. Assaad, M. Imada, and D. J. Scalapino, Quantum Transition between an Antiferromagnetic Mott Insulator and $d_{x^2-y^2}$ Superconductor in Two Dimensions. Phys. Rev. Lett. 77, 4592 (1996).
- [102] F. F. Assaad, M. Imada, and D. J. Scalapino, Charge and spin structures of a $d_{x^2-y^2}$ superconductor in the proximity of an antiferromagnetic Mott insulator. Phys. Rev. B 56, 15001 (1997).
- [103] Xun Cai, Zi-Xiang Li, and Hong Yao, Robustness of antiferromagnetism in the Su-Schrieffer-Heeger Hubbard model. Phys. Rev. B 106, L081115 (2022).
- [104] Michael Levin and T. Senthil, Deconfined quantum criticality and Néel order via dimer disorder. Phys. Rev. B 70, 220403(R) (2004).
- [105] T. Senthil, A. Vishwanath, L. Balents, S. Sachdev, and M. P. A. Fisher, *Deconfined quantum critical points*. Science 303, 1490, (2004).
- [106] Chunhan Feng, Bo Xing, Dario Poletti, Richard Scalettar, and George Batrouni, Phase diagram of the Su-Schrieffer-Heeger-Hubbard model on a square lattice. Phys. Rev. B 106, L081114 (2022).
- [107] Benjamin Cohen-Stead, Owen Bradley, Cole Miles, George Batrouni, Richard Scalettar, and Kipton Barros, Fast and scalable quantum Monte Carlo simulations of electron-phonon models. Phys. Rev. E 105, 065302 (2022).
- [108] Bo Xing, Chunhan Feng, Richard Scalettar, G. George Batrouni, and Dario Poletti, Attractive Su-Schrieffer-Heeger-Hubbard model on a square lattice away from half-filling. Phys. Rev. B 108, L161103 (2023).
- [109] Michael B. Giles An extended collection of matrix derivative results for forward and reverse mode algorithmic differentiation. Report no. 08/01 Oxford University Computing Laboratory (2008).
- [110] Liang Wang, Owl: A General-Purpose Numerical Library in OCaml. arXiv:1707.09616 (2017).
- [111] Liang Wang, Owl-OCaml scientific and engineering computing. http://github.com/owlbarn (Accessed 2025-06-25).
- [112] James Bradbury, Roy Frostig, Peter Hawkins et al., JAX: composable transformations of Python+NumPy programs. http://github.com/jax-ml/jax (2018).
- [113] Li, R., Ye, H., Jiang, D. et al. A computational framework for neural network-based variational Monte Carlo with Forward Laplacian. Nature Machine Intelligence 6, 209–219 (2024).